Marcus Vinícius Canhoto Alves

MODELAGEM NUMÉRICA DO ESCOAMENTO TRANSIENTE CHURN-ANULAR EM TUBULAÇÕES VERTICAIS E SUA APLICAÇÃO NA SIMULAÇÃO DE CARGA DE LÍQUIDO EM POÇOS DE GÁS

Tese submetida ao Programa de Pós-Graduação em Engenharia Mecânica da Universidade Federal de Santa Catarina para a obtenção do Grau de Doutor em Engenharia Mecânica.
Orientador: Prof. Jader Riso Barbosa Jr.

Florianópolis
2014

Marcus Vinícius Canhoto Alves

MODELAGEM NUMÉRICA DO ESCOAMENTO TRANSIENTE CHURN-ANULAR EM TUBULAÇÕES VERTICAIS E SUA APLICAÇÃO NA SIMULAÇÃO DE CARGA DE LÍQUIDO EM POÇOS DE GÁS
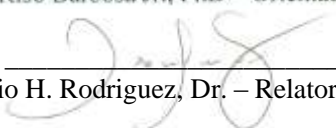
Esta Tese foi julgada adequada para obtenção do Título de Doutor em Engenharia Mecânica e aprovada em sua forma final pelo Programa de Pós-Graduação em Engenharia Mecânica da Universidade Federal de Santa Catarina.

Florianópolis, 30 de Julho de 2014.

_____
Prof. Armando Albertazzi Gonçalves Jr., Dr.
Coordenador do Curso

Banca Examinadora:

Prof. Jader Riso Barbosa Jr., PhD – Orientador (UFSC)

_____
Prof. Oscar Mauricio H. Rodriguez, Dr. – Relator (USP – São Carlos)

Prof. Eugênio Spanó Rosa, PhD (UNICAMP – Campinas)

Prof. Amir Martins de Oliveira Jr, PhD (UFSC)

Prof. Emilio Ernesto Paladino, Dr. (UFSC – Joinville)

Prof. Marintho Bastos Quadri, PhD (EQA – UFSC)

"A man should do the best he can, with what he has available, at that time and place." – Theodore Roosevelt as the 26th President of the United States of America

This work is dedicated to my Parents who inspired me into curiosity, ingenuity and have ever supported my decisions.

Acknowledgments

I would like to thank to my beloved Roberta, for her love and patience.

I would like to thank to my Family, Oswaldo, Sônia and Paulo, for everything.

I would like to thank to Prof. Jader Barbosa, for his supervision, advice, partnership, patience and for offering me this very interesting study subject. I hope this partnership can endure for the years to come.

Prof. Alvaro Prata deserves a special thanks, for the inspiration, patience and the invitation to work at POLO in 2005.

To the Federal University of Santa Catarina and the Department of Mechanical Engineering for the opportunity.

To the Brazilian Research and Development Council - CNPq for both the PhD Scholarship at UFSC and for the one year internship scholarship at the Texas A&M University - US. (grants:142781/2008-8 and 201817/2010-1, respectively).

To Profª Gioia Falcone who welcome me at the Texas A&M University.

To the private sponsors of this research Petrobras, RWE and Shell.

To CENAPAD Campinas at UNICAMP for granting access to their supercomputing facilities were most of results were obtained.

To God for once more allowing me to achieve my goals.

x

Contents

List of Figures

List of Tables

List of Symbols

Roman

Symbol	Description	SI Unit
a	Sound Speed	[m s^{-2}]
A	Area	[m^2]
AAD	Absolute Average Deviation used for comparison	[-]
$Bias$	Systematic Difference used for comparison	[-]
c_p	Isobaric Heat Capacity	[J kg^{-1} K^{-1}]
c	Experimental Constant in Eq. 2.1	[-]
C	Droplet Concentration	[-]
e	Specific Internal Energy	[J kg^{-1}]
ef	Entrained Fraction	[-]
d_T	Pipe Diameter	[m]
F	Force	[N m^{-3}]
f	Friction Factor	[-]
g	Gravity acceleration	[m s^{-2}]
G	Mass Flux	[kg m^{-2} s^{-1}]
h	Specific Enthalpy	[J kg^{-1}]
i	Index of the Space Discretization	[-]
j	Index of the Time Discretization	[-]
k	Deposition Coefficient	[-]
Ku_g	Kutateladze Number	[-]
L	Pipe Length	[m]
m	Experimental Constant in Eq. 2.1	[-]
n	Number of Nodes in the Numerical Grid	[-]
N	Number of Values compared with the statistical parameters	[-]
M	Mass Flux	[kg m^3 s^{-1}
p	Absolute Pressure	[Pa]
s	Specific Entropy	[J kg^{-1} K^{-1}]
t	Time Variable	[s]

Symbol	Description	SI Unit
T	Temperature	[K]
r	Radius Coordinate in Eq. (3.72)	[m]
R	Normalized Residuum	[-]
Re	Reynolds Number	[-]
RMS	Root Mean Squared Difference used for comparison	[-]
u	Velocity	[m s^{-1}]
x	Quality	[-]
y	Boundary Layer Corrdinate	[m]
z	Spatial Variable	[m]

Matrices and Vectors

Symbol	*Description*	*SI Unit*
$\mathbf{A}$	Coefficient Block Matrix in (4.43)	Several
$\vec{B}$	Source Term Vector in (4.43)	Several
$\vec{C}$	Source Term Vector in (3.31)	Several
$\vec{D}$	Source Term Vector in (3.33)	Several
$\mathbf{E}$	Coefficient Matrix in (3.31)	Several
$\mathbf{F}$	Coefficient Matrix in (3.31)	Several
$\mathbf{G}$	Coefficient Matrix in (3.33)	Several
$\mathbf{I}$	Identidy Matrix	[-]
$\mathbf{\Lambda}$	Eigenvalues Diagonal Matrix	Several
$\vec{U}$	Unknown Variables Vector in (3.32)	Several
$\vec{T}$	Eigenvectors of Matrix $\mathbf{G}$	Several
$\mathbf{T}$	Eigenvectors Transformation Matrix of Matrix $\mathbf{G}$	Several

Greek

Symbol	Description	SI Unit
α	Volumetric Fraction	[-]
β	Isothermal Compressibility	$[\text{K}^{-1}]$
δ	Boundary Layer Heigth	[m]
λ	Eigenvalues of Matrix **G**	$[\text{m s}^{-1}]$
μ	Dynamic Viscosity	[Pa s]
σ	Surface Tension	$[\text{N m}^{-1}]$
τ	Shear Stress	[Pa]
ϕ	Auxiliary Variable in the Discretization	[-]
ψ	Auxiliary Variable in the Discretization	[-]
ρ	Density	$[\text{kg m}^3]$

Subscripts

Symbol	Description	SI Unit
annular	Indicates Annular Flow Pattern	[-]
c	Core Phase Descriptor Subscript	[-]
churn	Indicates Churn Flow Pattern	[-]
crit	Indicates Critical Value	[-]
e	Droplet (Entrained) Phase Descriptor Subscript	[-]
f	Film Phase Descriptor Subscript	[-]
g	Gas Phase Descriptor Subscript	[-]
i	Denotes the Number of the Eigenvalue and associated Eigenvector of Matrix **G**	[-]
k	Phase Descriptor Subscript	[-]
l	Liquid Phase Descriptor Subscript	[-]
S	Indicates Superficial Value	[-]

Superscripts

Symbol	Description	SI Unit
$comp$	Indicates Compressibility Influence	[-]
Δp	Indicates Interfacial Pressure Difference Influence	[-]
I	Indicates the Current Iteration	[-]
in	Indicates the Pipe Inlet	[-]
int	Indicates Interfacial Term	[-]
J	Indicates the Current Time Step	[-]
$-$	Indicates Coefficient Matrix associated with the Positive Eigenvalues	[-]
nv	Indicates Non-Viscous Term	[-]
out	Indicates the Pipe Outlet	[-]
$+$	Indicates variable associated with the Boundary Layer when used with a scalar number; Indicates Coefficient Matrix associated with the Positive Eigenvalues.	[-]
T	Indicates Transpose Matrix	[-]
$*$	Indicates Dimensionless Variable; Except with the variable u^* in Eqs. (3.65) to (3.69) when it denotes the friction velocity.	[-]
vm	Indicates Virtual Mass Influence	[-]
w	Indicates Wall Term	[-]
-1	Indicates Invese Matrix	[-]

Resumo

Na produção de gás natural, é de grande importância que todo e qualquer líquido presente no poço seja carregado pelo gás até o separador. O acúmulo de líquido no poço devido à perda de capacidade do gás em arrastá-lo decorre do próprio envelhecimento do reservatório, mas também da sensibilidade das propriedades dos hidrocarbonetos a variações de pressão e temperatura durante transientes de produção. Desta forma, a redução da quantidade de movimento do gás ascendente gera um escoamento oscilatório do líquido que, ao se acumular no poço, aumenta sua queda de pressão, reduzindo assim, ou até mesmo interrompendo, a produção.

A fim de abordar o fenômeno acima descrito, denominado carga de líquido (liquid loading), é necessário compreender a interação entre o poço e a região adjacente do reservatório. Adicionalmente, é necessário possuir ferramentas capazes de resolver o escoamento bifásico no poço em função tanto do espaço quanto do tempo. Embora a literatura seja rica em trabalhos sobre escoamentos gás-líquido em canais verticais, estes resultam, em sua maioria, em correlações empíricas ou modelos simplificados para o cálculo da queda de pressão e das frações volumétricas das fases em condições de regime permanente. Mesmo que tais relações sirvam de critério para a ocorrência do fenômeno de liquid loading, elas não possibilitam a descrição da sequência de eventos que levam à transição entre os regimes de escoamento unidirecional ascendente e oscilatório.

Este trabalho apresenta um modelo diferencial unidimensional para o cálculo do escoamento gás-líuido transiente em tubos verticais com altas frações de gás (padrões anular e churn). Equações de conservação de natureza hiperbólica para a massa, quantidade de movimento e energia são propostas para as fases gasosa e líquida, a qual é dividida entre os campos de filme contínuo e gotículas arrastadas pelo núcleo de gás. Relações de fechamento para o cálculo do atrito na parede e na interface do filme, além de expressões para as taxas de entranhamento e deposição de gotículas, foram obtidas da literatura. Um algoritmo de solução por diferenças finitas baseado no método da separação da matriz de coeficientes foi implementado a fim de melhor lidar com variações

acentuadas no domínio espaço-temporal, tais como ondas de pressão e de retenção de fases. Os resultados do modelo foram comparados com dados experimentais de regime permanente obtidos de oito referências da literatura, somando mais de 1300 pontos para o gradiente de pressão, a vazão do filme de líquido e a retenção gasosa. Para estas variáveis, a concordância entre o modelo e os dados foi em margens inferiores a ± 20%. O modelo foi avaliado também contra dados experimentais para escoamentos gás-líquido transientes em um tubo vertical de 42 m de comprimento e diâmetro de 0,049 m (Waltrich, 2012). Transientes induzidos por variações de pressão e de vazão de líquido na seção de testes foram simulados, conferindo níveis de concordância entre dados experimentais e modelo matemático também inferiores a ± 20%.

Abstract

In the production of natural gas, it is essential that all liquids are carried upwards by the flowing gas up to the separator. The accumulation of liquid in the well and the decrease in the gas capability to lift the liquid are natural processes associated with the ageing of the reservoir itself, but are also related to sensitivity of the properties of hydrocarbons to pressure and temperature variations during transient production. At a given point, a reduction in the gas momentum gives rise to an oscillatory motion of the liquid, which increases the pressure drop in the well, thereby reducing or even interrupting the production prematurely.

To understand the phenomenon of liquid loading described above, it is necessary to understand the interaction between the well and the near wellbore region of the reservoir. Additionally, mathematical tools are needed to solve the two-phase flow of gas and liquid in the time and space domains. Despite the large number of works on gas-liquid flows in vertical channels available in the literature, these are mostly either empirical correlations or simplified models for the calculation of pressure drop and phase fractions at steady state. Although simple relationships serve as criteria for the occurrence of liquid loading, they fail to describe the sequence of events that lead to the transition between the unidirectional and bidirectional (oscillatory) flow regimes.

This work presents a one-dimensional differential model for calculating gas-liquid transient flow in vertical tubes with high gas fractions (annular and churn flow patterns). Hyperbolic conservation equations for mass, momentum and energy are proposed for the gas and liquid phases, which is split between a continuous film and droplets entrained in the gas core. Closure relationships to calculate the wall and interfacial friction and the rates of droplet entrainment and deposition were obtained from the literature. A finite-difference solution algorithm based on the Split Coefficient Matrix Method was implemented to deal with sharp variations in the spatial and temporal domain, such as pressure and phases holdup waves. The model results were compared with steady-state experimental data from eight different sources, totaling more than 1300 data points for pressure gradient, liquid film

flow rate and gas holdup. For these variables, the agreement between the model and the data was within less than ± 20%. The model was also compared against experimental data for transient gas-liquid flows in a 42-m long, 0.049-m ID vertical tube (WALTRICH, 2012). Pressure and flow rate-induced transients were simulated, with levels of agreement between the experimental data and the mathematical model also smaller than ± 20%.

1   *INTRODUCTION*

1.1   BACKGROUND

Gas-liquid two-phase flows are widely encountered in industry and engineering systems. Wet gas risers, steam generators, chemical reactors and heat exchangers, such as falling film evaporators and condensers, are common examples. Although the majority of two-phase equipment is designed taking into account their operation at steady state, knowledge of the two-phase flow behavior in transient situations is important for predicting critical operating conditions, such as start up or shut down of a plant or equipment, or emergency procedures involving the loss of coolant in nuclear power stations.

The process of liquid loading in mature gas wells (vertical or slightly inclined) includes a number of transient phenomena in different time scales. Liquid loading is an undesirable process initiated when, due to a decrease in gas flow rate or an increase in liquid content in the well, the momentum of the flowing gas becomes insufficient to carry all liquids to the surface, and some begin to flow downwards. Liquids in the wellbore may originate from (1) condensation of water vapor along the well, (2) condensate drop-out in the near-wellbore region of the reservoir in the wellbore, as both pressure and temperature decrease from bottomhole to surface (retrograde condensation), or (3) intake of formation water due to a decline in reservoir pressure.

The larger hydrostatic head due to a higher liquid content in the well — aggravated by the oscillatory motion of the liquid — increases the backpressure on the reservoir. Intake of liquid from the well into the near-wellbore region of the reservoir results in the well becoming unloaded again (and capable of transporting the liquids to the surface). However, the natural reduction of the reservoir potential with time means that the liquid loading cycle will repeat itself several times, thus exposing the typical intermittent response of liquid loaded gas wells (FALCONE; BARBOSA, 2013; VEEKEN; BELFROID, 2010). Figure 1.1

shows a plot of well performance data as a function of time, revealing
the occurrence of liquid loading in a real gas well (SUTTON *et al.*, 2003).
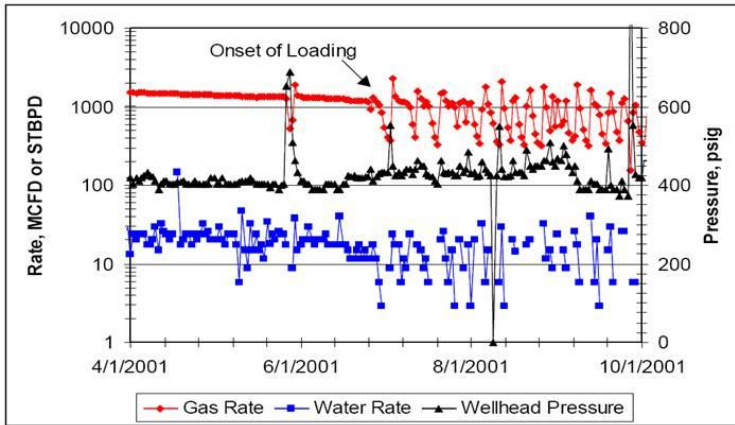
Figure 1.1 – Well performance data indicating the occurrence of liquid
loading (SUTTON *et al.*, 2003).

Currently, the methods for diagnosing and predicting liquid load-
ing are based on steady-state (nodal) analyses (LEA *et al.*, 2003). Nimwe-
gen *et al.* (2013) used a nodal approach to describe the flow instabilities
associated with liquid loading in gas wells. Figure 1.2 illustrates the
occurrence of liquid loading using the inflow and tubing performance
curves. The former represents the bottom hole pressure as a function
of the gas flow rate from the reservoir to the bottom of the well and
the latter relates the bottom hole pressure and the rate at which the
gas flows in the production tubing. The intersection between the two
curves is the production operating point. In order to maintain a sta-
ble operating condition, production should be at a gas flow rate higher
than that corresponding to the minimum bottom hole pressure. At gas
flow rates lower than that associated with the minimum, production is
unstable and subjected to liquid loading in the wellbore.

From a fluid flow perspective, prediction of liquid loading requires
understanding the characteristics of two-phase flow patterns and the
transitions between them. In other words, it is necessary to predict the
transition from an acceptable flow regime (annular flow) to an unac-
ceptable one (churn flow), which triggers liquid loading in the well. The
region of minimum bottom hole pressure in the tubing performance
curve corresponds roughly to the transition between upward annular
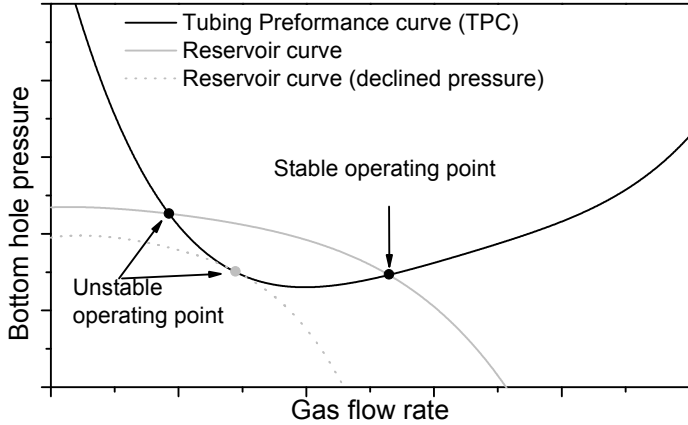
Figure 1.2 – Tubing and inflow performance curves illustrating stable and unstable operating points (reproduced from Nimwegen *et al.* (2013)).

flow and churn-annular flow; a flow regime marked by oscillations and changes of direction of the velocity in the liquid film adjacent to the wall (HEWITT *et al.*, 1985). In the churn flow region, the behavior of the total pressure gradient is such that it decreases with the superficial gas velocity, whereas in annular flow the pressure gradient increases with the superficial gas velocity.

In spite of their widespread use in the oil industry, nodal analyses cannot deal with the time-dependent character of the phenomena that take place in the wellbore during liquid loading, such as the gradual buildup of a liquid column and the associated increase in back pressure on the formation. The methods used to estimate the critical gas velocity and the onset of liquid loading (SUTTON *et al.*, 2010) are not capable of modeling the two-phase flow in the wellbore. They simply provide criteria to assess for what value of gas velocity liquid fallback may begin to occur in the well. A more reliable approach to accurately model the physics of liquid loading would be to use a transient multiphase flow wellbore model that includes the transient features of the near-wellbore region of the reservoir as boundary conditions. This dynamic, integrated modelling approach is essential to investigate the loading-

unloading sequence described previously (FALCONE; BARBOSA, 2013).

1.2   OBJECTIVES

The objective of this thesis is to extend a transient model for gas-liquid two-phase flows in vertical pipes with special emphasys on the churn and annular flow patterns and the transition between them, which is one of the critical aspects of the prediction of the onset of liquid loading in gas wells.

The model is based on a one-dimensional, three-field formulation consisting of a system of hyperbolic partial differential equations. The HyTAF (Hyperbolic Transient Annular Flow) code, developed specifically for this project, makes use of a finite-difference based solution algorithm derived from the Split Coefficient Matrix Method (SCMM) of Chakravarthy *et al.* (1980) to deal with sharp discontinuities such as shocks and void waves.

A number of secondary objectives of the present work have been outlined as follows:

- Carry out an extensive validation of the numerical model with experimental data gathered from the literature on churn and annular flows in vertical pipes at both steady-state and transient conditions;

- Evaluate the performance of closure relationships for the interfacial friction factor in both churn and annular flows;

- Through numerical analyses of different scenarios, gain some understanding of the physical phenomena associated with transient annular flows, and to provide new insights into the problem of liquid loading in vertical gas wells.

The long term objective of this research is to develop a model for the complete coupled flow of hydrocarbons in the production well. Capable of simulating the flow all the way from the reservoir up to the well head. Several chalenges must be overcame to achieve this goal, mainly: the characterization of two-phase flow in the well (which is the subject of this thesis); the two-phase flow in the reservoir and the coupling between the two (which will be adressed in future works). These developments will alow for a better understanding of the liquid loading phenomenon.

1.3 STRUCTURE OF THE THESIS

This thesis is organized as follows. Chapter 2 presents a review of the literature on gas-liquid two-phase flows at high gas fractions, specifically churn and annular flows; and the mathematical methods employed in the simulation of these flow patterns.Chapter 3 describes the three-field model and the closure relationships needed to simulate churn and annular flows under transient conditions. Chapter 4 presents the numerical solution of the model described in Chapter 3, along with a grid sensitivity analysis. Chapter 5 presents the validation of numerical model against experimental data for both steady-state and transitn conditions. Hypothetical cases are also presented in order to gain some understanding of transient phenomena triggered by changes in boundary conditions that resemble those of a well under liquid loading. Chapter 6 presents the main conclusions and reconmendeations for future works.

2   LITERATURE REVIEW

This chapter presents a review of previous works on two-phase flows with high gas volume fractions in vertical pipes. In the first section, a physical description of the flow patterns is presented, emphasizing the main areas of contribution of the present work. Next, the mathematical models derived for steady-state annular and churn flows are reviewed. The mathematical methods utilized to simulate the transient annular and churn flow are then reviewed in the context of their application in two-phase flows. Experimental works on annular and churn flows, which have been used to validate the present mathematical model, are described at the end of the chapter.

2.1   TWO-PHASE FLOW PATTERNS

The flow patterns generally associated with high gas volume fraction in gas-liquid two-phase flows are the plug (slug), churn and annular flows, in order of increasing gas superficial velocity as seen in Fig. (2.1).

In slug flow, the gas flows as elongated bullet-shaped bubbles (Taylor bubbles) with a falling film around them, and as dispersed bubbles in upward-flowing liquid slugs between Taylor bubbles. A slug unit cell is composed of a Taylor bubble and a slug of liquid (COLLIER; THOME, 1994). In annular flow the upward flowing liquid is split between a thin climbing film on the tube wall and into droplets that are entrained in the gas core. The high velocity gas disturbs the film surface and forms waves that are the source of the entrained droplets. After being accelerated by the gas core, the droplets eventually redeposit back on the film at a distance downstream of the point where they were created (HEWITT; HALL-TAYLOR, 1970; AZZOPARDI, 2006). In vertical channels, the average thickness of the liquid film is uniform with respect to
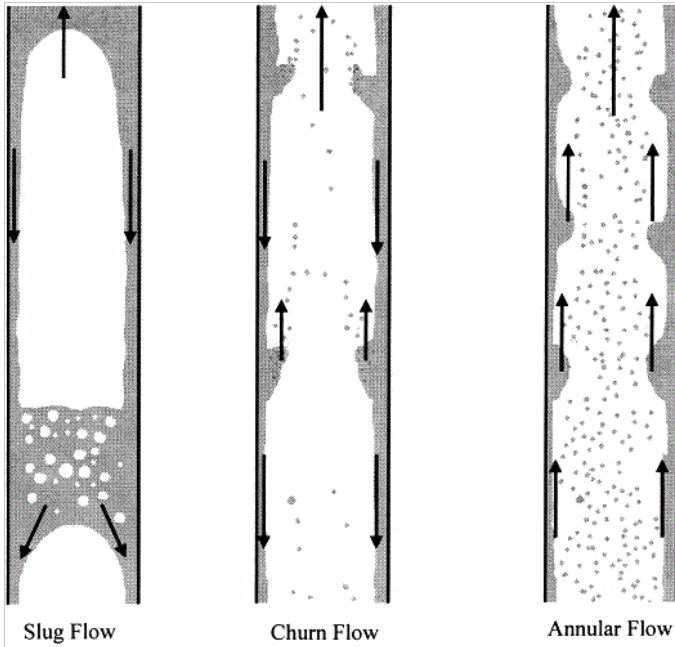
Figure 2.1 – Schematic representation of gas-liquid flow patterns in a vertical pipe. Arrows indicate the direction of the gas and liquid phases. In slug flow, a falling liquid film is established around a rising Taylor bubble and the motion of the liquid slug is in the upward direction. In churn flow, the motion of the liquid substrate between waves is in the downward direction (WATSON; HEWITT, 1999).

the tube perimeter, whereas in horizontal pipes the film is thicker at the bottom due to gravity.

The churn flow pattern arises from the breakup of the Taylor bubbles and collapse of liquid slugs as the gas superficial velocity increases. Changes in the liquid film velocity direction are typical in churn flow. The upward liquid transport is accomplished by large waves and there is considerable entrainment in the gas core (AZZOPARDI, 2006).

2.1.1 Annular Flow

The annular flow pattern is the most important of all due to its practical applications, where in most cases both phases flow in the

turbulent regime with a high fraction of the liquid phase dispersed as droplets in the gas core. The generation of droplets, their behavior while moving through the gas core and their deposition on the liquid film are key factors in the development of models for heat, mass and momentum transfer in annular flow.

In 'ideal annular flow' there is no liquid entrainment and the interface is smooth. However, this type of flow is rarely encountered in practice because interfacial waves and droplet entrainment are already observed at relatively small flow rates. The pioneering models for annular flow developed in the 1950's and 1960's presented simple analytical solutions for ideal annular flow. Although the direct application of these solutions is limited, their development has provided valuable insights into the modeling of annular flow because of the introduction of basic concepts, such as the triangular relationship between the film flow rate, film thickness and pressure gradient (HEWITT, 1961), which are employed in phenomenological models to this date.

The classical approach to annular flow is to divide the domain into three flowing fields: a liquid film near the wall, a continuous gas core, and some liquid droplets dispersed in the gas. The structure of the liquid film in annular flow is a complex combination of disturbances of different wavelengths and amplitudes. Although the smaller wavelengths are present in almost all combinations of gas and liquid mass fluxes, only above a critical liquid film Reynolds number, the long, high amplitude disturbance waves start to form. The shearing of the gas over the disturbance waves on the liquid film generates the droplets. Azzopardi and Whalley (1980) investigated the droplet generation process and concluded that the appearance of disturbance waves in the film are strongly correlated to the entrainment of droplets in the gas core.

More recent observations (ALEKSEENKO et al., 2012) used a high-speed modification of the laser-induced fluorescence (LIF) technique to conduct experiments vertical pipe with downward annular flow. The evolution of the instantaneous distribution of the local film thickness was investigated over a small spatial domain with high sampling frequency. The results confirmed the results pointed by previous works (as pointed above), in particular disturbance waves were confirmed to form full rings around the pipe's circumference and it's height to vary across this direction. This heterogeneity affects the formation of the ripple waves, which are generated with higher frequency and amplitude where the disturbance waves have it's maximum height. This heterogeneity also influences the circumferential size of the ripples, being defined by the characteristic length of non-uniformity in the disturbance

waves. Alekseenko *et al.* (2012) also point that without liquid entrainment, primary and secondary waves (analogue to disturbance and ripple waves) are not ring shaped, as described by previous works (OHBA; NAGAE, 1993), however, the circumferential size of primary waves is greater than that of secondary waves.

2.1.2   Churn Flow

Churn flow occurs after the rupture of the Taylor bubbles characteristic of slug flow with the increase in superficial gas velocity. Inversions of the liquid film flow direction can be detected through a direct observation of the flow. Although the term churn flow has been used to describe two-phase flows with these features for a long time (HEWITT; HALL-TAYLOR, 1970) some of its fundamental characteristics have not yet been thoroughly investigated (AZZOPARDI, 2012).

Visual observations performed by Hewitt *et al.* (1985) revealed the physical characteristics of churn flow and its resemblance to the annular flow pattern, as both have a continuous gas core with some entrained liquid and a continuous liquid film near the tube wall (thicker in the case of churn flow). Despite the many similarities, there are important differences between the two flow patterns that deserve to be highlighted:

1. The breakup of the Taylor bubbles in slug flow is followed by a steep increase in the pressure gradient due to interfacial friction (OWEN, 1986; COSTIGAN, 1997; WALTRICH, 2012; YUAN *et al.*, 2013; SKOPICH *et al.*, 2013). In churn flow, the total pressure gradient decreases with increasing gas superficial velocity, which is opposite to what happens in annular flow;

2. The physical mechanism of churn flow as established by Hewitt *et al.* (1985) is such that the liquid is transported upwards by big waves that collect the falling liquid film above the wave and discharge liquid in the form of a new film below the wave (see Fig 2.1). These waves originate similarly to those causing the flooding phenomenon in counter-current gas-liquid flow;

3. The big flooding waves breakup with evolution of a significant fraction of the liquid mass flux as droplets and liquid filaments in the gas core. Different authors observed that the liquid entrainment is higher in churn flow and goes through a minimum before increasing again in annular flow. (WALLIS, 1969; GOVAN, 1990; BARBOSA *et al.*, 2001b; van't Westende, 2008; van der Meulen, 2012)

2.1.3 Churn-Annular Transition

Starting from a stabilized churn flow condition, if the gas velocity is increased, the higher momentum flux of the gas increases the interfacial drag, which reduces the directional oscillations of the liquid film. Eventually, as the film becomes thinner and the liquid film turns unidirectional, disturbance waves appear and the pressure gradient starts to increase monotonically with the gas superficial velocity. This qualitative description of the churn-annular transition points to several possible transition criteria as follows,

1. The point of total flow reversal, i.e., the point at which the gas superficial velocity is high enough to carry all the liquid film upwards;

2. The point of minimum pressure gradient;

3. The point of zero average wall shear stress, as this average wall shear stress is negative in churn flow and positive in annular flow;

4. The point at which the local wall shear stress becomes continuously positive, which occurs when the liquid film flux is entirely in upflow.

According to Barbosa Jr. (2010), of all the above criteria, the one most commonly applied to correlate the churn-annular transition is the flow reversal criterion due to its easy experimental observation and simple relationship that defines it. The flow reversal criterion of Wallis (1969) is based on the Hewitt and Wallis (1963) flooding correlation given by,

$$\left(u_{gS}^{*}\right)^{0.5} + m(u_{lS}^{*})^{0.5} \approx C \qquad (2.1)$$

where m and C are constants that depend on the geometry of the test section, but are roughly equal to unity for conditions typical of a long tube. The dimensionless superficial velocities are defined as,

$$u_{gS,lS}^{*} = u_{gS,lS}\sqrt{\frac{\rho_{g,l}}{gd_T\left(\rho_l - \rho_g\right)}} \qquad (2.2)$$

where $u_{gS,lS}^{*}$ is the local dimensionless superficial velocity, $\rho_{g,l}$ is the local density, g is the local gravitational acceleration and d_T is the pipes internal diameter.

The flow reversal transition was found to be relatively insensitive to the liquid superficial velocity, taking place at an approximately constant gas superficial velocity. Thus

$$u_{gS}^* \approx 1.0 \qquad\qquad (2.3)$$

at the point of flow reversal.

Equation (2.3) correlates well the flow reversal in tubes smaller than 50 mm. For larger diameter tubes, droplet entrainment from the wave tips may occur before the waves themselves are transported (HEWITT, 2010). In this case, an alternative correlation for the flooding velocity that does not take into account the tube diameter has been suggested. This has been attributed to Puskina and Sorokin (1969) and is written in terms of the Kutateladze number for the gas,

$$Ku_g = \left[\frac{u_{gS}^4 \rho_g^2}{g\sigma \left(\rho_l - \rho_g \right)} \right]^{0.25} \approx 3.2 \qquad\qquad (2.4)$$

Equation (2.4) is similar to the well known Turner *et al.* (1969) criterion for the liquid loading critical velocity in vertical wells. In the Turner criterion, $Ku_g = 3.67$. The assumptions involved in the Turner *et al.* (1969) criterion are discussed in Lea *et al.* (2003).

2.2 ANNULAR AND CHURN FLOW MODELING

There is no universal model for two-phase flows of industrial relevance. The governing equations are complex and cannot be solved in a straightforward way, even when one-dimensional flow is assumed. Simplified forms of the governing equations derived from the phenomenological models involve closure relationships with empirical parameters that are often not valid outside the bounds of the original experiments.

Experiments go hand to hand with the development of prediction methods for annular and churn flows. In one-dimensional models, semiempirical correlations are needed for wall and interfacial friction factors and rates of droplet entrainment and deposition.

2.2.1 Annular Flow Modeling

At steady-state, a triangular relationship has been established between the liquid film thickness, the film flow rate and the pressure gradient (HEWITT, 1961). This initially involved the assumption of log-law velocity profile in the liquid film and a specific relationship for the interfacial shear stress.

The most common and simpler approach to calculate the interfacial shear stress has been to assume that the liquid film acts as an equivalent pipe roughness, with an interfacial friction factor proportional to the mean liquid film thickness (WALLIS, 1969; WHALLEY; HEWITT, 1978; BELT *et al.*, 2009). Different forms of the interfacial friction factor have been proposed to take into account the suppression of turbulence in the gas core due to the presence of liquid droplets (OWEN, 1986).

Turbulence modification in the liquid film in comparison with single-phase in pipes has been dealt with through modified log-law relationships for film velocity (DOBRAN, 1983; JENSEN, 1987) or turbulent eddy diffusivities for heat and momentum transfer for algebraic turbulence models (CIONCOLINI; THOME, 2011).

Semi-empirical correlations for the rates of droplet entrainment and deposition per unit pipe surface area have been proposed since the early 1970's. A survey of the methods available until the late 1980's was presented by Owen (1986).

Droplet deposition rates are correlated as the product of a deposition coefficient and the homogeneous core droplets concentration. The droplet deposition coefficient was found to depend on physical properties of the two phases (viscosity, density and surface tension) and on the droplet concentration itself (WHALLEY *et al.*, 1974; MCCOY; HANRATTY, 1977; WHALLEY; HEWITT, 1978).

Empirical correlations for the droplet entrainment rate based on a dimensionless group relating the interfacial shear stress, the film thickness and the surface tension were proposed by Hutchinson and Whalley (1973), Tatterson (1975) and Whalley and Hewitt (1978). Dallman (1978) was the first to take into account the critical film mass flow rate below which no entrainment occurs in the entrainment rate correlation.

Through the late 1980's and early 1990's, more experimental data were incorporated into the correlation data banks to improve their predictive capabilities. Schadel *et al.* (1990) determined the rates of droplet atomization and deposition for air-water flows in vertical tubes with different diameters. They concluded that the atomization rate varied linearly with gas velocity and liquid film flow rate. The deposition rate was found to vary linearly with droplet concentration at low concentrations but was insensitive to changes in droplet concentration at high concentrations.

Hewitt and Govan (1990) (also Govan *et al.* (1988)) presented a set of correlations for deposition and entrainment rates in annular flow based on 2354 data points from 32 sources. The model was incorporated into the Harwell code and validated against steady-state adiabatic

flows, flows with phase change (evaporating and condensing) and post-dryout flows. For the latter, there was still a dependence of the model results on the value of the liquid entrained fraction at the onset of annular flow. This issue was addressed a few years later by Barbosa (2001), who correlated the liquid entrained fraction at the churn-annular transition and computed the critical heat flux (film dryout) for pure fluids and mixtures using an extended version of the Hewitt and Govan (1990) rate correlations.

Nigmatulin *et al.* (1996) reviewed the data for entrainment and deposition rates in gas-liquid and vapor-liquid annular flows from three different sources: Rachkov (1979), Netunaev (1982) and Hewitt and Govan (1990). A new expression for the entrainment and deposition rate is presented and compared with the data. This new correlation uses the same parameters as the first one, differing only by a gas core velocity term that appears in the new correlation but is not present in the derived by Hewitt and Govan (1990). Both correlations show significant spreading and the authors do not drawn any definitive conclusion about the application of either correlation. Each correlation presented better results when compared to the dataset from which they were originated.

Kataoka *et al.* (2000)investigated entrainment rate in annular flow using ideas similar to those of Nigmatulin *et al.* (1996) and proposed a correlation that takes into account the momentum flux in the gas core. The correlation was based on experimental data for entrained fraction and in a force balance through the wavy interface. The correlation successfully captured the trends in the entrained fraction data from the experiments of Gill *et al.* (1962) and Cousins *et al.* (1965). No correlation for deposition rate was presented.

Lopez de Bertodano *et al.* (2001) performed experiments using air and water and Freon-133 in a 10-mm ID vertical tube. In these experiments, the influence of surface tension and density ratio effects on the entrainment rate were investigated. A new correlation was presented for the entrainment rate based on a Kelvin-Helmholtz instability analysis of the liquid film surface. The new correlation was not compared with data from the literature. However, the authors considered it to represent their own data reasonably. They also advised against the application of their correlation for highly viscous fluids and large diameter pipes, as the correlation did not take those effects into account.

Okawa and Kataoka (2005) developed correlations for entrainment and deposition rates based on air-water data from the literature. The deposition rate correlation was developed to was developed to obey two empirical rules: (i) the deposition is independent of concentration and

more influenced by the gas velocity at low concentrations, and (ii) the deposition rate is dependent on the concentration at high concentrations. For correlating the entrainment rate, the ratio of the interfacial shear force to the surface tension force acting on the surface of liquid film was corroborated as been the primary factor governing the phenomenon (as in Hewitt and Govan (1990)). The correlation was tested against air-water and high pressure steam-water data showing a satisfactory behavior.

Simpler correlations for the entrained liquid fraction (as opposed to separate relationships for entrainment and deposition rates) have been proposed by a number of authors (ISHII; GROLMES, 1975; HOLOWACH *et al.*, 2002; SAWANT *et al.*, 2009; CIONCOLINI; THOME, 2010). The biggest advantage of this approach is the simplicity of an algebraic formulation. However, entrained liquid fraction correlations fail to capture the liquid entrainment behavior under hydrodynamic non-equilibrium conditions, and are insensitive to variations of the liquid entrainment fraction at the onset of annular flow (initial condition). For this reason, they cannot be employed in a model such as the one proposed in this thesis.

The works described above on droplet entrainment were based on steady-state conditions. To the author's knowledge, the only study devoted to entrainment in transient flows was conducted by Langner and Mayinger (1979). The entrained liquid mass flow rate was estimated with an axial-viewing method in a 0.014-m ID 5-m long heated test section using R-12. Pressure-induced transient tests were conducted in an attempt to simulate the behavior of the liquid phase in annular flow following a loss-of-coolant accident (LOCA) in a boiling-water nuclear reactor.

The entrained liquid mass flow measurements were made in the annular flow regime immediately prior to the film dryout for different depressurization rates. At low depressurization rates (small break), the "quasi-stationary" behavior of decreasing entrainment liquid mass flow rate at high void fractions was observed, which is consistent with the fact that the entrainment rate per unit pipe surface area decreases when the film flow rate falls below a critical value.

At high depressurization rates, flow acceleration was so strong and interfacial shear stress forces were so large that liquid droplets were torn away even from the very thin films, which resulted in an increase of the entrained liquid mass flow rate until the film dryout point. Langner and Mayinger (1979) reported that, as a result of the sudden increase of the liquid entrained fraction, the reduction of the film thickness was very significant and there was a very short annular flow period for

large break areas (high expansion rates). Due to the inherent lack of accuracy of the experimental method, the agreement with theoretical predictions was rather poor.

A number of mechanistic models that make use of the closure relationships for interfacial friction and droplet interchange at steady-state have been proposed and verified against experimental data. The works of Owen (1986), Govan (1990) and Barbosa (2001) summarize some of earlier annular flow models, such as the Harwell HANA code.

Fu and Klausner (1997) developed a model for vertical annular flow with convective heat transfer. Mass, momentum and energy equations were solved for the liquid film thickness, pressure drop and wall temperature (to determine the heat transfer coefficient). The results were compared to experimental data for pressure drop and heat transfer coefficient from the open literature. The authors concluded that the model was an useful tool in predicting evaporative heat transfer in the purely convective regime.

Alipchenkov *et al.* (2002, 2004) developed a one-dimensional three-fluid model for two-phase flows which is based on the equations of conservation of mass, momentum and energy for the gas phase, dispersed phase (droplets) and liquid film. The model includes an equation for the number density of particles of the dispersed phase, which is used to determine the average particle size. The calculation results are compared with experimental data for the entrainment coefficient, film and droplet flow rates, film thickness, pressure drop and droplet size. The agreement was reasonable (mostly in the $\pm$ 30 % deviation range) and the authors considered the model successful in predicting the entrainment characteristics of a gas-liquid turbulent annular flow.

2.2.2   Churn Flow Modeling

In comparison with annular flows, there is much less models available in the literature specifically for churn flow. The model of Jayanti and Brauner (1994) is based on force balances for the gas core and for the two-phase mixture, having the pressure gradient and the gas holdup as unknowns. No account was taken of droplet entrainment, and the wall friction was calculated based on the net flow rate using single-phase friction factors (the time-varying characteristics of the liquid film was ignored). The interfacial friction factor was taken as the arithmetic average of the Wallis (1969) and Bharathan and Wallis (1983) correlations, as this approach gave a good prediction of the churn flow data of Owen (1986). The majority of the data points (covering liquid mass

fluxes ranging from 5 to 400 kg m^{-2} s^{-1} in a 0.0318 m ID pipe) was predicted within $\pm$ 20 % for the pressure gradient.

Sawai *et al.* (2004) investigated the interfacial structure (wave velocity and frequency) in churn flow in a vertical 25.8 mm ID pipe using two sets of electrical conductance gas holdup sensors. The frictional pressure gradient was obtained from the total pressure gradient and gas holdup data, without acounting for entrainment in churn flow. Good agreement with empirical correlations for the frictional pressure gradient (FRIEDEL, 1979) was obtained only in the region where the latter increased with the gas superficial velocity. New correlations for the gas holdup and for the frictional pressure gradient were proposed based on the drift-flux model and on a two-phase multiplier for the liquid pressure gradient, respectively. The correlations were not validated against data from other authors.

Ahmad *et al.* (2010) expanded the Hewitt and Govan (1990) correlation to include churn flow using the entrained fraction data of Barbosa *et al.* (2002) at the onset of annular flow. The new correlation for entrainment rate used a linear relation with the dimensionless gas superficial velocity to offset the local value of entrainment rate and include the churn flow region. The authors found that the deposition rate under churn flow should be calculated with the same approach as if the flow was annular, i.e., by multiplying the entrained droplet concentration by the droplet deposition transfer coefficient. Through the introduction of this new correlation, the dependence of the dryout location on the droplet concentration at the onset of annular flow reported by Hewitt and Govan (1990) was shifted to the onset of churn flow. The authors also highlighted that this dependence was still an ongoing investigation, and that by setting the entrained fraction at the onset of churn flow to 90 %, the dryout position was predicted to within $\pm$ 20 % for the experimental data of Bennett *et al.* (1966) and Keys *et al.* (1971), which the authors considered to be a better result than the previous approach.

2.2.3 Numerical Methods

Early attempts to model transient annular flows were made with the codes developed in Harwell in the 1970's and 1980's, which were applied to the calculation of dryout in pressure and flow transients (WHALLEY *et al.*, 1978; JAMES; WHALLEY, 1978; WHALLEY *et al.*, 1984; HEWITT; GOVAN, 1990) and to transient rewetting (HEWITT; GOVAN, 1990). Commercial codes employed in the nuclear industry, such as CO-

BRA/TRAC (THURGOOD *et al.*, 1983), were structured with a three-field formulation for annular flows, which allows the computation of entrainment and deposition rates under non-equilibrium conditions. More recently, the model that originated the commercial code OLGA (BENDIKSEN *et al.*, 1991) contains a conservation equation for the entrained droplets field in annular flow, but takes no account of the churn flow pattern in its modeling framework.

In this thesis, a new transient, one-dimensional, three-field model for upward annular and churn flows is presented. The system of governing equations is hyperbolic in nature, so a finite-difference based solution algorithm (GESSNER, 2010) derived from the Split Coefficient Matrix Method (SCMM) of Chakravarthy *et al.* (1980) was developed to deal with sharp discontinuities in the solution domain from pressure and flow rate induced transients.

The SCMM has been applied successfully in the numerical simulation of a number of two-phase flow problems (DUTTA-ROY, 1984; ROMSTEDT, 1990; LU *et al.*, 1996; OUYANG; AZIZ, 2001; STäDTKE *et al.*, 2005), but to the knowledge of the present author, this is the first time it is employed in the modeling of non-equilibrium churn-annular flows.

The SCMM uses the concept of upwinding, preserving the wave propagation processes through the characteristic directions and allowing for low numerical oscillation and diffusion during the solution of mass, momentum and energy conservation equations in advection problems. The basic idea behind the method is to separate the influence from the positive and negative eigenvalues of the coefficient matrix over the variables of the PDE. Through algebraic manipulation of the coefficient matrix, it is possible to split this matrix into two distinct ones. Each of these matrices accounts for the influence of only one set of eigenvalues; one matrix is associated with the positive eigenvalues and the other with the negative ones. Once that is accomplished, the derivative of the unknown vector (that multiplies the coefficient matrix) can receive adequate numerical treatment.

Romstedt (1990) used a modification of the original SCMM presented by Chakravarthy *et al.* (1980) to solve the two-phase homogeneous equilibrium model for steady state and transient conditions. The main focus of their work was to demonstrate the advantages of using the SCMM with a non-staggered grid over the use of a staggered grid that provides more stability. This was allowed by the fact that the independent backward and forward differencing schemes used in conjunction with the SCMM are more robust than the normal upwind differencing scheme used with the staggered grids. Also the use of a non-staggered

grid requires that the equations of state for the fluid properties be evaluated only in half the points of a staggered grid, resulting in less computational time.

Dutta-Roy (1984) used the SCMM to solve transient two-phase flow problems for homogeneous, stratified and annular flow patterns in a horizontal geometry. The boundary conditions used for the model were the inlet phase flow rates and the outlet pressure. A comparison with experimental data generated by the author in a 420-m long 77.93-mm ID horizontal pipe was performed. During the experiments the facility was operated to match the boundary conditions used in the numerical program. In the comparison the author argued that the representation was reasonable enough and the predicted values were close to each other. However, it was recommended that the intermittent flow patterns (slug/plug flow) should be included in the numerical program before it could have any practical use.

Lu *et al.* (1996) used a time-explicit version of the SCMM to solve the homogeneous equilibrium model during the transient downflow of a two-phase mixture. The model results were compared with experimental data from the literature and the results were considered reasonably accurate by the authors. The boundary conditions used in this scenario were the top pressure and void fraction (at the inlet) and the bottom mass velocity (at the outlet). (LU *et al.*, 1996) presented two main differences in the numerical procedure in comparison with previous models: (i) the explicit time treatment, and (ii) the use of a pressure boundary condition at the inlet while using mass flux at the outlet. This work demonstrated the robustness of the SCMM by dealing with different numerical scenarios while maintaining good agreement with the experimental results.

Ouyang and Aziz (2001) used the SCMM to simulate the transient flow of a gas-liquid mixture in a horizontal pipe. The model was able to account for stratified, annular-mist and dispersed bubble flows, with influx or efflux of both phase through the pipe wall. The numerical formulation was based on an implicit time solution of the equations and the boundary condition were set as in the work of Dutta-Roy (1984). The results were based on the experimental boundary conditions of Dutta-Roy (1984), but no explicit comparison with experimental results were presented. The authors, however, claimed that the results were qualitatively in accordance with the experimental data. Hypothetical scenarios were generated and discussed for impermeable wall, influx of liquid and efflux of liquid.

Gessner (2010) presented solutions for single-phase, two-phase ho-

mogeneous, two-field and three-field (first version of the HyTAF code) formulations using the SCMM. The solution for single-phase flow was validated with the analytical solution of the shock tube problem, generating good results. The other solutions were not compared to experiments or analytical solutions, but the author compared the three-field formulation approach with the GRAMP2 computer code developed by Barbosa and Hewitt (2006). The GRAMP2 code is based on the on a 4th order Runge-Kutta algorithm, solving traditional phenomenological models for bubbly, slug, churn and annular flows.

Both phenomenological approaches (two and three-field formulations) of Gessner (2010) were intended for single pattern simulations, not allowing for flow pattern transitions during transients. The two-field version was specifically devoted to the calculation of mist flows while the three field model could only simulate annular flows. The comparison between GRAMP2 and the first version of the HyTAF code yielded promising results, with most discrepancies being due to the accommodation distance needed to develop annular flow at the inlet. The author also points out that a change in the boundary condition calculation could greatly reduce (or even solve) this issue.

Other numerical methods that could have been used in this work those from the class of Godunov methods (STäDTKE, 2006) such as the FVSM (Flux Vector Splitting Method) and the Roe solver (ROE, 1981).

Munkejord (2005) used the Roe solver to solve several frictionless simplified situations such as the water faucet test case, and the shock tube. Munkejord (2005) also compared this solution using the Roe solver with other methods such as the Flux-Limiter Centered Scheme (FLIC), and the results were reasonably compatible.

2.3   EXPERIMENTAL WORKS

This section presents a detailed description of experimental works on annular and churn flows used to validate the mathematical model. It should be noted that the review is not intended to be extensive and complete, only to give the necessary details to support the model findings.

2.3.1   Owen (1986)

Owen (1986) used the Harwell LOTUS facility illustrated in Fig. 2.2. Air was supplied from an compressed air line at the bottom of the pipe, and water was supplied from a separator. The test section
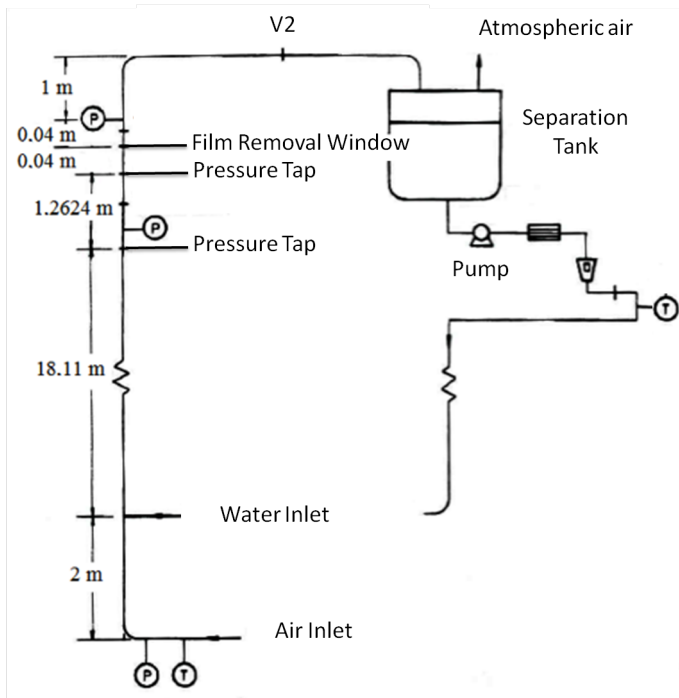
Figure 2.2 – Illustration of the experimental setup used by Owen (1986).

consisted of a copper vertical pipe 23 m long and 31.8 mm ID. The configuration of air and water mixer at the water inlet is a porous sinter section insert flushed with the pipe wall located 2.0 m after the air inlet.

The experiments were performed using gas mass fluxes ranging from 0 to 300 $kgm^{-2}s^{-1}$ and liquid mass fluxes ranging from 0 to 1010 $kgm^{-2}s^{-1}$. The value of absolute pressure at the pipe outlet were: 177, 240, 364, and 377 kPa. The pressure gradient was measured with a differential pressure cell positioned at 18.11 m from the water mixer.

2.3.2 Govan *et al.* (1991)

Govan *et al.* (1991) performed experiments on flooding and churn flow. The experiments provided measurements of pressure gradient and liquid holdup for churn flow with (post flooding regime) and without the presence of a falling film. By comparing the results of both sit-

uations the author concluded that the falling film region (below the water injector) and the churn flow region (above the injector) are essentially decoupled and do not influence each other. The experimental data also revealed that the minimum pressure gradient point would not coincide with the zero wall shear stress as suggested by the laminar flow analysis presented byHewitt and Hall-Taylor (1970). The experimental wall shear stress data was compared to the codes TRAC (WALLIS, 1969) and RELAP (BHARATHAN *et al.*, 1978) revealing the the RELAP yielded more reasonable results.

The test section used by Govan *et al.* (1991) (Fig. 2.3) was comprised of flanged sections of 31.8 mm ID acrylic resin pipe (copper in the case of the water injection and removal sections). The air entered the test section through a short section of 10 mm ID (to prevent water drainage). Two porous sections were available at the facility: the first was located 1.0 m above the air inlet (at the bottom of the test section); and the second was 2.093 m above the air inlet (at the top of the test section). The facility was used for two distinct purposes: flooding experiments and churn flow ones. For the flooding experiments (and also for those of churn flow with falling film) water was injected through the top inlet then flow down, being removed at the lower porous sinter and separated in the cyclone. When churn flow with falling film was being studied this removed liquid flow was measured with a rotameter and subtracted from total water injected initially to give the effective upward liquid flow rate. For the churn flow experiments with no falling film liquid could be injected from both porous inserts resulting in two test sections: one with 2.72 m long, and the other with 1.71 m long. In all the experiments the pressure at point P was maintained at 133 kPa using valve V2.

The holdup was measured using two mechanically linked valves that could be closed simultaneously; the water contained between the valves was subsequently drained to a measuring cylinder. The valves were positioned with their center s 0.92 m apart and the total volume of the pipe section trapped between them when closed was measured as 0.000725 m^3.

The pressure gradient was measured using two pressure taps 846 mm apart connected by a differential pressure cell (DP). The maximum uncertainty in the calculated pressure gradient is estimated to be around 60 Pam^{-1} for churn flow, dropping to around 15 Pam^{-1} in the annular pattern where the fluctuations were much smaller. The liquid mass fluxes for experiments in churn flow were 31.8 and 47.7 $kgm^{-2}s^{-1}$.
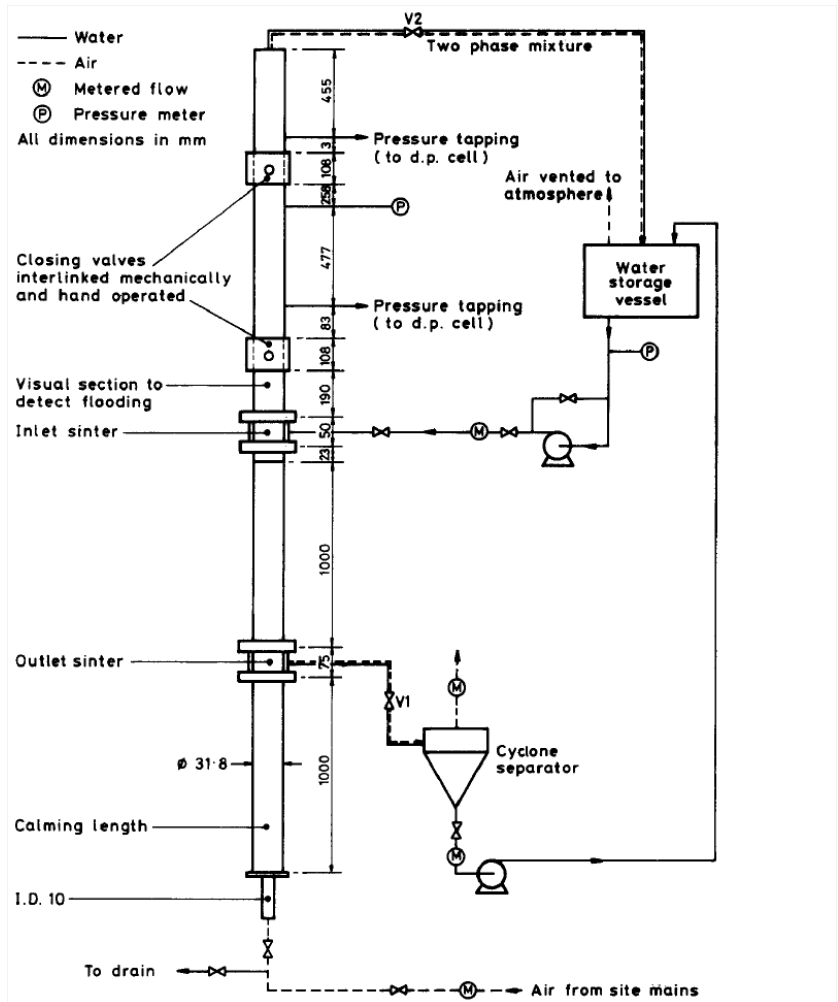
Figure 2.3 – Schematic illustration of the experimental facility used by Govan *et al.* (1991).

2.3.3   Costigan (1997)

Costigan (1997) investigated primarily the slug-churn transition of an air-water mixture in a vertical pipe through experimental observations, however, the experiments rage from the bubble flow to the annular flow patterns. The experimental data indicated that by increasing the gas mass flux while keeping the liquid mass flux constant if the liquid mass fluxes was low the stable slug flow would transition directly to churn flow and if liquid mass fluxes was high no stable slug flow could be achieved. In moderate liquid mass fluxes, however, two different transitions would occur: the first was the degeneration of the Taylor bubbles and the breakup of stable slug flow to an unstable condition, the second one was the transition to churn flow. According to the author no annular flow data was generated. A modified Wallis criterion (WALLIS, 1969) was suggested to correlate the stable to unstable slug transition. The unstable slug to churn transition was correlated by a criterion of constant mean void fraction.

The test facility used by Costigan (1997) is illustrated in Fig. 2.4. It has a test section that received water from a centrifugal pump connected to flow meters. An inlet valve generated a pressure drop between 600 and 100 kPa was used to control the air mass flux so that the liquid mass flux would not be disturbed by the pressure variations in the test section. The inlet temperature is registered by a thermocouple. The air was supplied by a compressed air line with an inlet valve to equalize pressure, this is followed by an orifice plate connected to a water manometer to measure gas volumetric flow rate. Measurements of absolute pressure and temperature allow for density and gas mass flux calculation.

The inlet device is illustrated in Fig 2.5. Water entered the annular chamber radially, and a 0.23 m long deflector was installed downstream of it to reduce turbulence in the inlet section. Air was injected through a centralized 15 mm ID tube. Constant air mass fluxes were ensured by the use of interchangeable critical flow nozzles at the end of the central insert. Strain gauge pressure transducer monitored the inlet pressure.

The test section consisted of several 32 mm ID transparent perspex tube segments. The total length of the test section was of 8.5 m and at the end of it there was a valve to control the system pressure. The two-phase mixture returned to a water tank that also functioned as a separator.

Two identical void fraction probes were used at different positions along the test section. Their construction was based on three pairs of copper electrodes extending 160 ° around the pipe wall and 5 mm apart
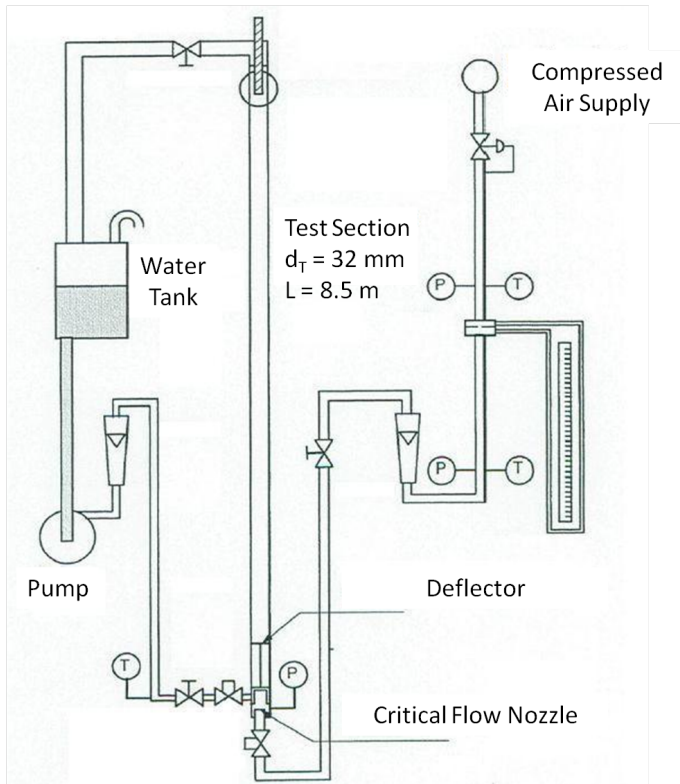
Figure 2.4 – Illustration of the experimental facility used by Costigan (1997).
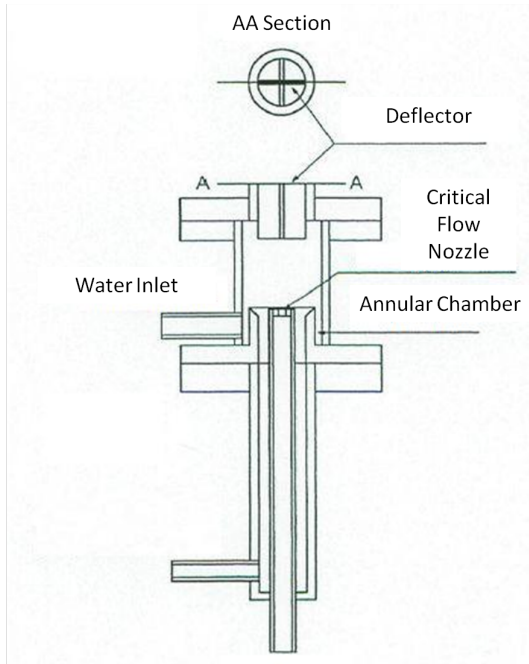
Figure 2.5 – Illustration of inlet device (COSTIGAN, 1997).
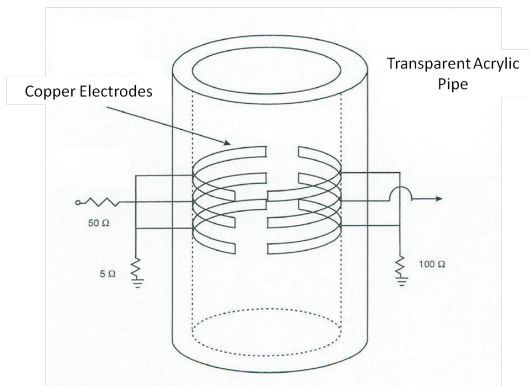
Figure 2.6 – Impedance probe (COSTIGAN, 1997).

(Fig. 2.6). The pressure gradient was calculated from measurements acquired by a differential pressure transducer cell; the schematic dia-
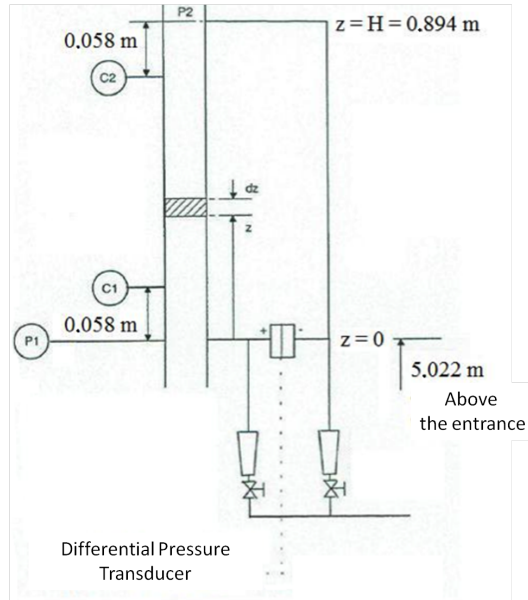
Figure 2.7 – Schematics of test section (COSTIGAN, 1997).

gram is shown in Fig. 2.7 and an illustration of the same section is shown in Fig. 2.8.

The tests were carried out in 100 s long batches for (average) outlet pressures of 110 and 210 kPa. These values represent mean pressures and the nominal pressures varied from 101 to 131 kPa in the first case and from 184 to 231 kPa in the second. The measurements of mean volume fraction and pressure gradient were performed simultaneously.
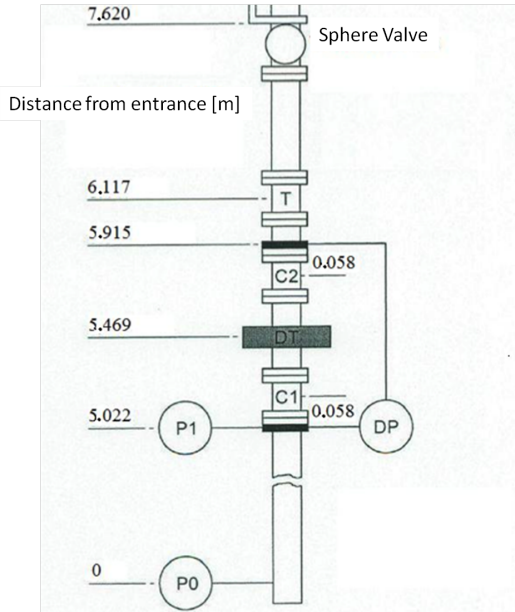
Figure 2.8 – Illustration of the measurement cell for volume fraction and pressure gradient (COSTIGAN, 1997).

2.3.4   Wolf *et al.* (2001)

Wolf *et al.* (2001) performed their experiments in a 10.8 m long test section with 31.8 mm ID (Fig. 2.9). The objective was to characterize the axial development of a two-phase upward flow of an air-water mixture in annular flow. Water was introduced in the test section through a porous insert mounted flush at the pipe wall, 300 mm above the air inlet, which was at the bottom of the pipe.

The inlet pressure was fixed at 238 kPa and the temperature was 25 °C. Liquid mass fluxes ranged from 10 to 120 $kgm^{-2}s^{-1}$ while the gas mass fluxes was set at 71, 97, 124, and 154 $kgm^{-2}s^{-1}$. Air was taken from a compressed air line and the flow rate measured by an orifice plate connected to pressure transducers. The water flow rate was measured by rotameters. Absolute pressures were measured at 0.67, 1.59, 3.2 and 9.74 m along the test section.

The pressure gradient was measured using an electronic differential pressure transducer at 0.67, 1.59, 3.2 and 9.74 m from the water inlet. The liquid film flux was measured directly by sucking off the
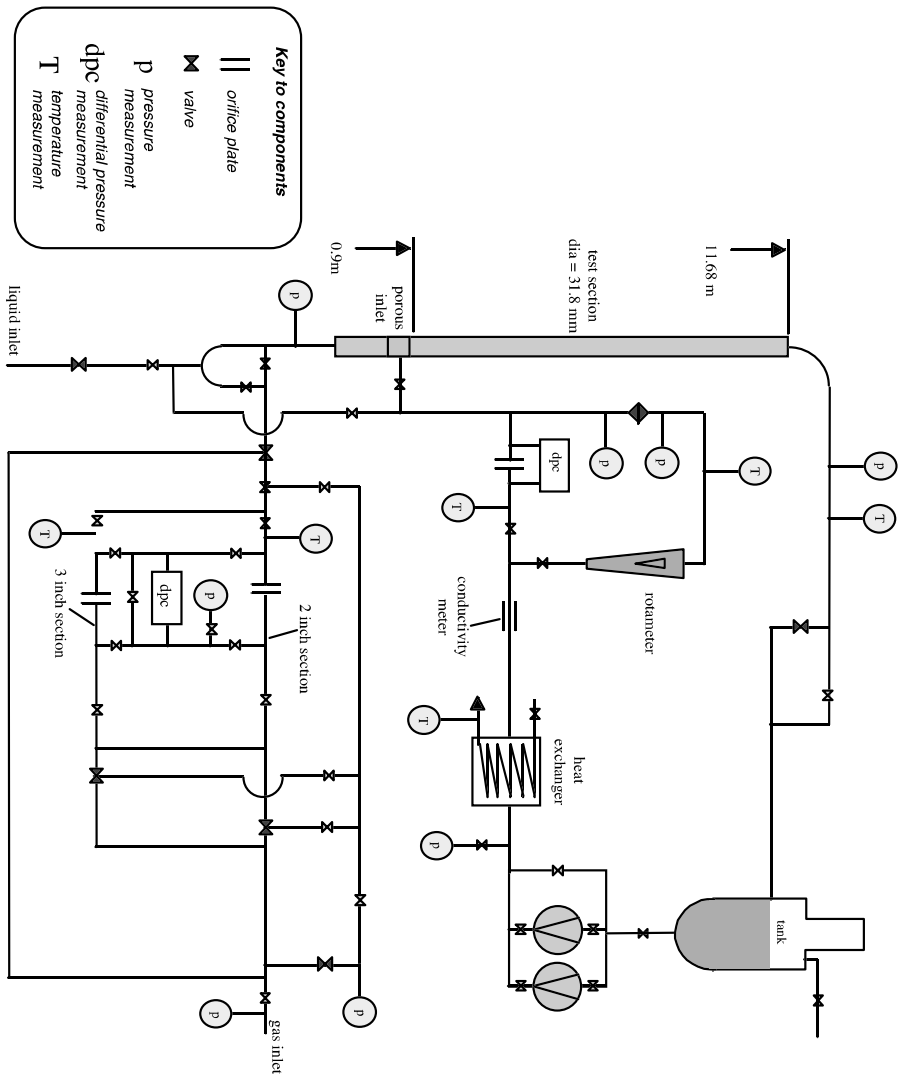
Figure 2.9 – Illustration of the experimental facility used by Wolf *et al.* (2001)

film. The device outlet was connected to a cyclone separator and the accumulated liquid used was to calculate the liquid film flux. This was repeated at 0.45, 1.15, 2.78, and 10.41 m from the water inlet. The liq-

uid film thickness was measured with a concentric conductance probe at distances of 0.05, 0.25, 0.94, 3.85, and 10.41 m from the water inlet.

2.3.5   Belt *et al.* (2009)

Belt *et al.* (2009) presented a modification of the interfacial friction factor correlation initially presented by Wallis (1969) based in a new set of experiments that measured film thickness and pressure gradient. The authors use a different approach to obtain the correlation, instead of fitting a curve using a regression algorithm (usual approach in the literature), they started form the single-phase turbulent friction factor in rough pipes and applied its formulation to annular flow without flow reversal. The authors conclude that the roughness density is the main factor governing the behavior of the friction factor for the fully rough regime, which is encountered in most literature data and industrial applications. However, they also highlight that he density roughness is very difficult to calculate, requiring knowledge about the frequency and amplitude of the roll waves, and so more information about the stability, formation and dynamics of these waves. Following the trend of Wallis (1969) they presented a simple correlation between interfacial friction factor and mean liquid film thickness applicable for the fully rough regime. Belt *et al.* (2009) also highlight that, although simple, the proposed correlation contains in its essence all the information about the roll wave dynamics through the mean liquid film thickness.

The test facility used in the work of Belt *et al.* (2009) was the same employed in the work of van't Westende (2008) and van't Westende *et al.* (2007). The flow loop consisted of a 12 m long, 50 mm ID vertical perspex pipe (Fig. 2.10). Dry air, is supplied at near atmospheric conditions by a compressor. At 1 m downstream from the gas inlet, a water film is created along the circumference using a porous pipe section.

The film thickness was measured 130 diameters downstream of the water inlet using a conductance sensor. The film thickness sensor is an array of 10 measurement points in the axial direction, each with 32 flush-mounted electrodes in the circumferential direction, resulting in 320 measurement points. The accuracy (twice the standard deviation) of the film thickness measured was reported to be about 12% of the film thickness.

The mean axial pressure gradient was measured using a manometer between 80 and 140 diameters downstream of the water inlet. The measurement of the mean axial pressure gradient between 120 and 140
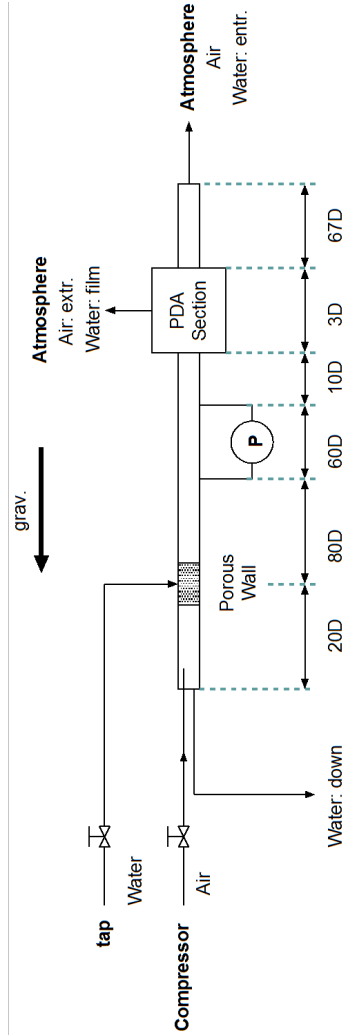
Figure 2.10 – Schematic diagram of flow loop used by Belt *et al.* (2009).

diameters gave the same values, indicating that the flow was developed as far as the mean axial pressure gradient is concerned. The gas superficial velocity u_{gS} was varied between 22 and 42 ms^{-1}, while the liquid superficial velocity u_{lS} was between 0.01 and 0.08 ms^{-1}.

2.3.6   Alamu and Azzopardi (2011)

The experiments of Alamu and Azzopardi (2011) were carried out in a vertical 19 mm ID, 7 m long test section using an air-water mixture at an operating absolute pressure of 150 kPa. The flow facility is shown schematically in Fig. 2.11. The liquid film flow rate was measured using a porous section that sucked off the liquid, synchronized with the conductance ring probes for measurements of film thickness. The pressure drop was monitored with a differential pressure cell connected to two pressure taps. The drop size distribution was measured using a laser beam directed at the flow after the film had been removed.

The flow facility used by Kaji and Azzopardi (2010) was modified to accommodate a special test section, including conductance probes, liquid film extractor and the laser beam. Water was taken from a storage tank and pumped through a bank of calibrated rotameters to monitor flow rate. A dynamic mass flow controller, operating in conjunction with gas rotameters was used to regulate the gas mass flux into a mixer. The mixer consisted of an annular section into which air was introduced through the center. Water emerged into the annulus through a series of 3 mm holes on the wall of the capped central pipe. This mixer was mounted at the bottom of the pipe 310 diameters upstrean of the section where the conductance probes are located.

The two pressure taps were connected to a differential pressure cell; the first located at 230 diameters above the mixer, and the second 82 diameters above the first. The liquid film was extracted via a 19-mm ID, 350-mm long, 0.80-porosity acrylic pipe section. Downstream of the liquid film extractor, only the droplet-laden gas core flows through the chamber, which admits laser beam to illuminate the flow for drop size measurement. The pipe outlet is connected to a separator, the air line being connected to the compressor intake, the liquid being returned to the storage tank.
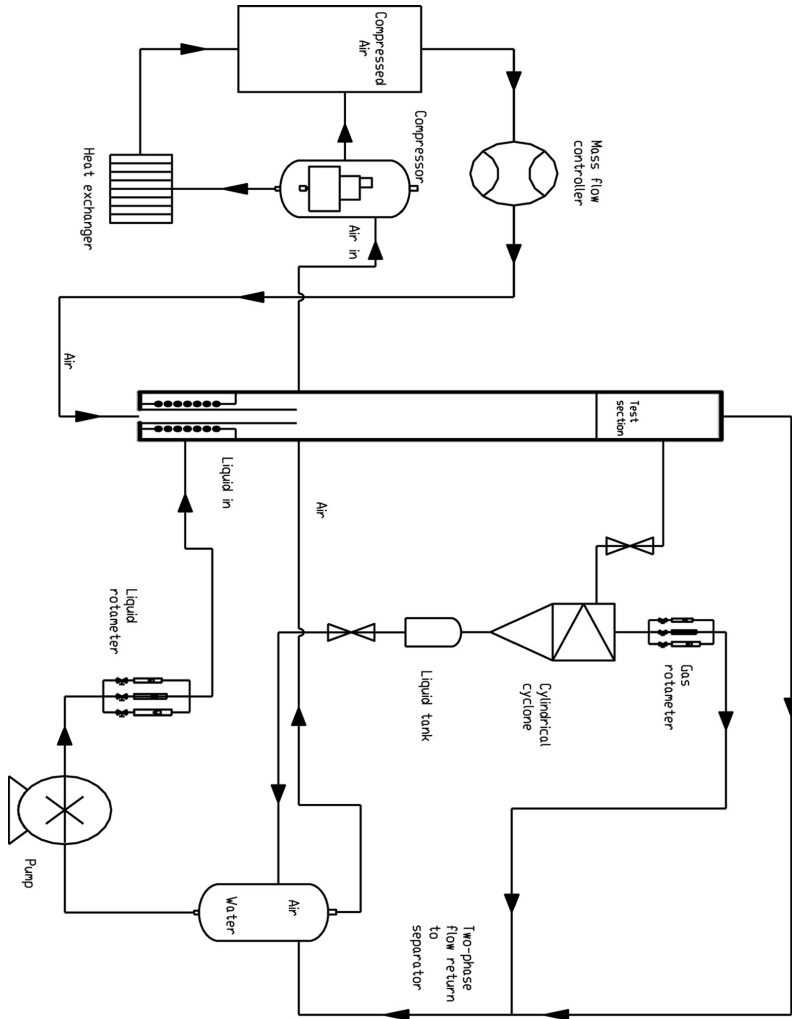
Figure 2.11 – Schematic diagram of flow loop used by Alamu and Az-
zopardi (2011).

2.3.7   Waltrich (2012)

A large-scale air-water experimental two-phase flow loop was built at the Texas A&M University (the TowerLAB facility) to investigate transient gas-liquid flows in a long tube. The test section consisted of a series of 0.049-m ID transparent PVC pipe segments, comprising a total tube length of 42 m (875 diameters) in the vertical position, as shown in Fig. 2.12.
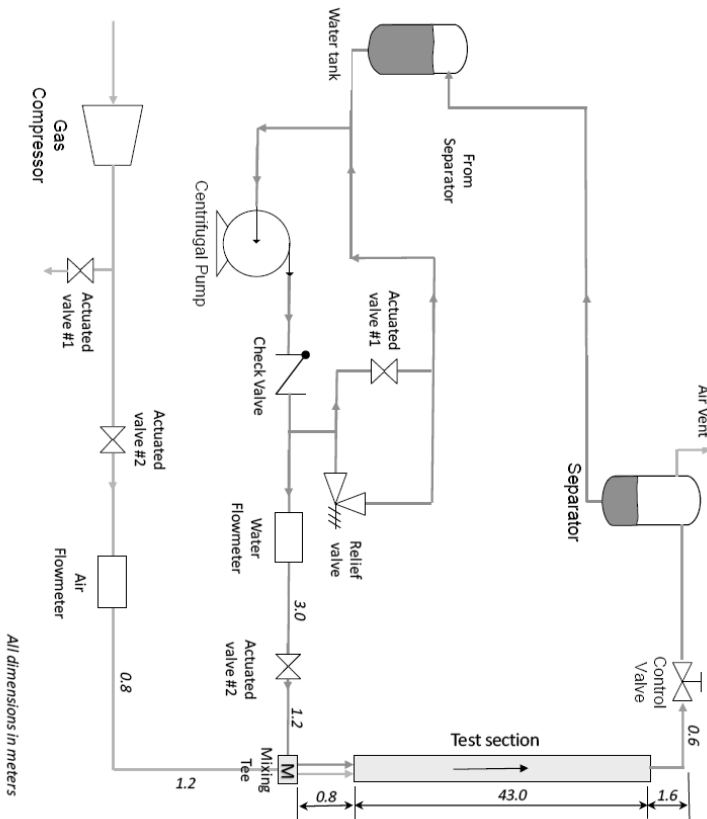
Figure 2.12 – Schematic illustration of the TowerLab facility Waltrich (2012).

A centrifugal pump was used to pump water from a 662 liters water tank to the test section. The water flow rate was controlled using a

variable speed driver and an electronically actuated valve downstream of the water pump. The water mass flow rate was measured using a Coriolis mass flow meter. A water filter, with a 10 μm porous filter element, was also connected just upstream to the mixing tee to keep the water free of particles and impurities.

Compressed air was provided using a screw compressor, and measured using a 38.1-mm vortex meter and a 12.7-mm Coriolis meter. The combination of two actuated valves in the air supply line with a control valve (50.8 mm sphere actuated valve) at the outlet of the test section provided a combined control of the pressure and gas flow rate, allowing to change the outlet pressure without modifying the gas flow rate. Air and water were mixed in a mixing tee, which consisted of a 50.8-mm perforated nipple inserted in a 76.2-mm tee.

In addition to direct visual observation of the flow configuration via digital high-speed cameras, the experimental apparatus enabled measurement of pressure gradient, gas volumetric fraction (via conductivity probes) and slug/wave frequency over a range of pressures and phase flow rates. Absolute pressure measurements were performed at 4 different distances from the mixing tee: 9.2, 20.4, 32.6 and 39.4 m. After calibration, the pressure measurement uncertainty average was estimated as $\pm$ 0.3 kPa. Temperature measurements were taken using T-type thermocouple probes connected to the nylon pressures taps.

The void fraction was measured using three sets of two-wire conductivity probes similar to those described by Zabaras *et al.* (1986) mounted perpendicularly to the flow direction. The cross-sectional void fraction was determined assuming symmetry with respect to the pipe centerline, followed by a calibration procedure explained in detail in Waltrich (2012). The void fraction measurement average uncertainty was estimated as ± 0.02.

2.3.8 Yuan *et al.* (2013)

A schematic diagram of the test facility used by Yuan *et al.* (2013) is shown in Fig. 2.13. The test section could be inclined from horizontal to vertical. A valve and bypass were used to control the flow rate. The outlet of the flow loop was open to atmosphere so no back pressure was imposed at the outlet. A schematic drawing of the test section is shown in Fig. 2.14.

Pressure was measured with three pressure transducers, including two absolute (Rosemount 3051T) and one differential (Rosemount 3051C). Liquid holdup was measured by trapping the fluids between
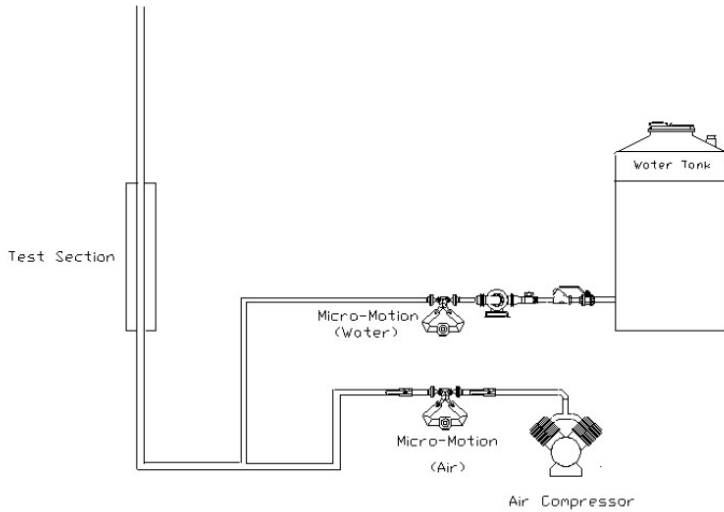
Figure 2.13 – Schematic of multiphase flow loop used by Yuan *et al.* (2013).

quick closing valve sections (two 76.2-mm (3-in.) sphere type quick-closing valves). A drainage valve was installed in the section near the upstream of the loop. To measure the liquid holdup, the trapped fluids were drained through the valve and the liquid volume measured. The flow pattern was identified by recording the flow behavior through a perspex observation window using a high-speed video camera (Photron SA 65-3) recording system.
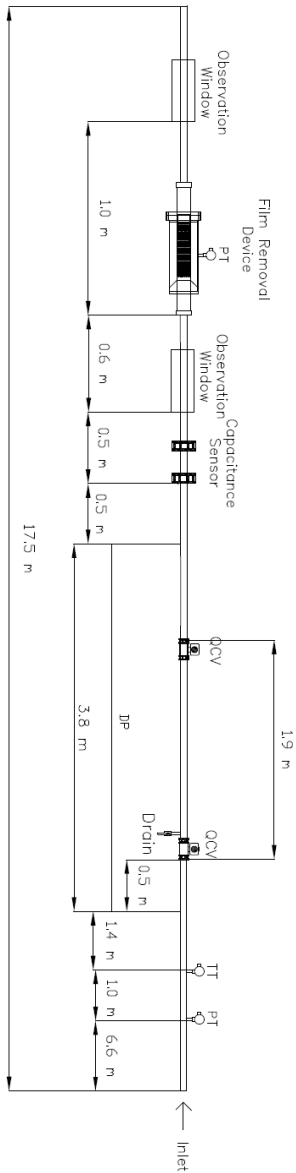
Figure 2.14 – Detail of test section of Yuan *et al.* (2013).

2.4 CONCLUDING REMARKS

Through this literature review it became clear that models for the simulation of transient two-phase flows are scarce in the literature. Most of the available models have not been compared to large experimental datasets and/or do not allow for flow pattern transitions. This justifies the specific objectives of this work, which are: (i) to extend the two and three-field formulations of Gessner (2010), including the transition between annular and churn flows, and (ii) carry out an extensive validation of the new model with experimental data representing the majority of the literature about churn and annular flows in vertical pipes at both steady-state and transient conditions. Another important contribution is the inclusion of better suited boundary conditions, allowing for the reduction (or elimination) of the inlet discrepancies seen in work of Gessner (2010). This will also permit the evaluation of different closure relationships, especially for interfacial friction factors in annular flow. Also, through the numerical analyses of different hypothetical scenarios, it will be possible to gain some understanding of the physical phenomena associated with transient annular and churn flows.

3   MATHEMATICAL MODELING

This chapter presents the mathematical formulation developed in this work for studying transient high gas volume fraction two-phase flows in vertical pipes. The model consists of a hyperbolic three-field model that takes into account the distribution of the phases in annular flow between a continuous liquid film, a gas core and entrained liquid droplets. The three-field model has also been extended to deal with the presence of entrained liquid in churn flow.

3.1   HYPERBOLIC THREE-FIELD MODEL

The main hypotheses of the mathematical model are as follows: (i) one-dimensional flow, (ii) no pressure change across phase interfaces, (iii) adiabatic walls and (iv) no phase change. These are justified based on the large aspect ratio (length/diameter) of the channels encountered in practice, high phase velocities and large density difference between the phases, and on the validation of the model against experimental data for air-water systems without heat transfer. Although these justifications would point for a model without the solution of the energy equation, the energy equation is used in the model with two purposes: the first is to allow the transformation of one of the continuity equations (mass conservation equations) into an equation for the pressure, through the use of thermodynamic relations; the second is that the coupled solution of the hydrodynamic and thermal problems bring stability to the system of algebraic equations.

Figure 3.1 shows the schematic mass balance for the three fields considered (gas core, liquid film and entrained droplets). A_k is the cross-sectional area occupied by field k, and the field area fraction is defined as $\alpha_k = A_k/A$, where A is the channel cross-sectional area. u_k
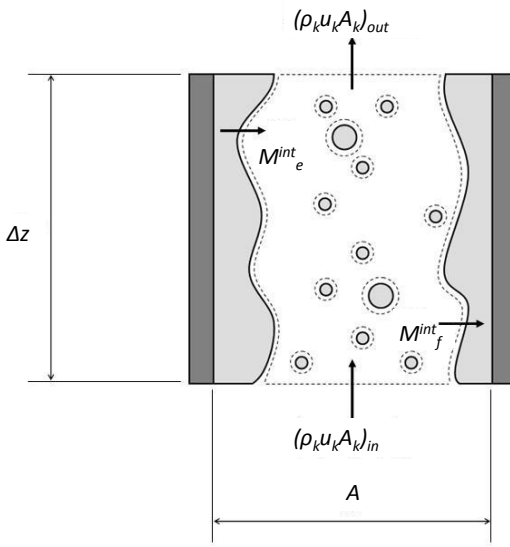
Figure 3.1 – Schematic representation of mass fluxes in annular flow.

is the local *in-situ* velocity of field k.

After some mathematical manipulation, the mass conservation equation in the gas core is given by,

$$\frac{\partial}{\partial t}\left(\alpha_g \rho_g\right) + \frac{\partial}{\partial z}\left(\alpha_g \rho_g u_g\right) = 0 \tag{3.1}$$

Mass conservation in the liquid film and entrained droplets fields are given by,

$$\frac{\partial}{\partial t}\left(\alpha_f \rho_f\right) + \frac{\partial}{\partial z}\left(\alpha_f \rho_f u_f\right) = M_f^{int} - M_e^{int} \tag{3.2}$$

and,

$$\frac{\partial}{\partial t}\left(\alpha_e \rho_e\right) + \frac{\partial}{\partial z}\left(\alpha_e \rho_e u_e\right) = M_e^{int} - M_f^{int} \tag{3.3}$$

where M_e^{int} and M_f^{int} are rates of droplet entrainment and deposition per unit volume, respectively.

Figure 3.2 shows schematically the momentum fluxes and forces in the three fields. Momentum balances result in the following equations for the gas core, entrained liquid and liquid film,
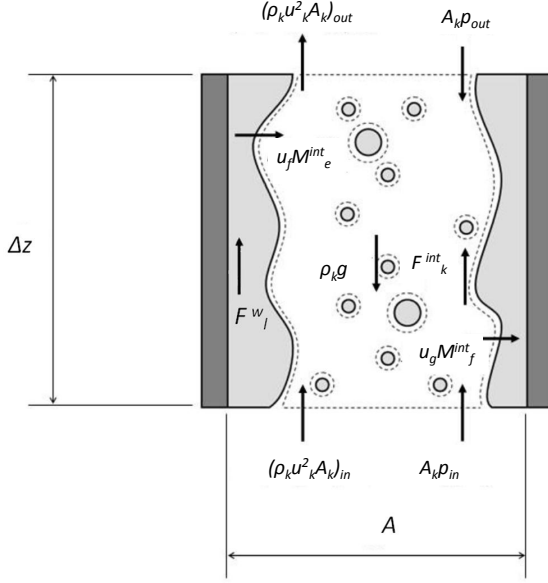
Figure 3.2 – Schematic representation of momentum fluxes in annular flow.

$$\frac{\partial}{\partial t}\left(\alpha_g \rho_g u_g\right) + \frac{\partial}{\partial z}\left(\alpha_g \rho_g u_g^2\right) + \alpha_g \frac{\partial p}{\partial z} = F_g^{nv} + F_g^{int} - \alpha_g \rho_g g_z \quad (3.4)$$

$$\frac{\partial}{\partial t}\left(\alpha_e \rho_e u_e\right) + \frac{\partial}{\partial z}\left(\alpha_e \rho_e u_e^2\right) + \alpha_e \frac{\partial p}{\partial z} =$$
$$F_e^{nv} + F_e^{int} + M_e^{int} u_f - M_f^{int} u_e - \alpha_e \rho_e g_z \quad (3.5)$$

$$\frac{\partial}{\partial t}\left(\alpha_f \rho_f u_f\right) + \frac{\partial}{\partial z}\left(\alpha_f \rho_f u_f^2\right) + \alpha_f \frac{\partial p}{\partial z} =$$
$$F_f^{nv} + F_f^{int} - F_f^{w} - M_e^{int} u_f + M_f^{int} u_e - \alpha_f \rho_f g_z \quad (3.6)$$

In the momentum equations above, the terms $M_i^{int} u_j$ represent the momentum exchange between the two liquid fields via entrainment

and deposition, F_i^{nv} represents the non-viscous interfacial forces, F_i^{int} represents the interfacial friction force between the fields, F_f^w represents the friction force between the liquid film and the wall, and $\alpha_i \rho_i g_z$ is the hydrostatic pressure drop component of each individual field. The expressions for the friction force terms will be presented in Section 3.3.

Munkejord (2005) compared the two and one-pressure versions of the two-fluid model using a Roe type solver (which is a splitting technique similar to the SCMM). The numerical calculations showed that the one and two-pressure schemes converge to the same solution when instantaneous pressure relaxation is employed in the two-pressure model. The two-pressure model was considered to be present more numerical diffusion than the one-pressure model. The diffusion was a strong function of the chosen time step length, the grid size, whether a flux-limiter function is employed or not, and also of the liquid sound speed.

As the pressure relaxation parameter in the two-pressure scheme was increased, the solution gradually approached that obtained using instantaneous pressure relaxation. Furthermore, the results indicate that the approach of two pressures and instantaneous pressure relaxation does not provide an easy way to overcome the problem of complex eigenvalues in the one-pressure two-fluid model. This leads to the conclusion that the use of two-pressure model would bring little contribution to the representation of the physical nature of the annular and churn flows.

Although it is common practice in annular flow modeling to assume homogeneous flow behavior in the gas core and neglect droplet inertia in the flow (GOVAN, 1990; BARBOSA, 2001), some works show that under certain conditions the droplet inertia can represent up to 20% of the total pressure gradient. Solving both momentum equations with a proper correlation for the interfacial friction factor would produce the most physically accurate results however, the solution of the coefficient matrix eigenvalues analytically would became impossible. This is due to the Abel-Ruffini theorem, which forbids the representation of the solution of higher than 4th order polynomial equations as functions of its own coefficients (JACOBSON, 2009). This in turn, would require the numerical solution of the eigenvalues adding complexty and a severe increase in the computational costs. In this way, the homogeneous core momentum balance is given by Gessner (2010),

$$\frac{\partial}{\partial t} \left(\alpha_c \rho_c u_c \right) + \frac{\partial}{\partial z} \left(\alpha_c \rho_c u_c^2 \right) + \alpha_c \frac{\partial p}{\partial z} =$$
$$F_c^{nv} + F_c^{int} + M_e^{int} u_f - M_f^{int} u_c - \alpha_c \rho_c g_z \tag{3.7}$$

where u_c is the homogeneous core mixture velocity, and, α_c and ρ_c are the core void fraction and the homogeneous core density, respectively. These are defined as follows,

$$\alpha_c = \alpha_g + \alpha_e \tag{3.8}$$

$$\rho_c = \frac{\rho_g \alpha_g + \rho_e \alpha_e}{\alpha_c} \tag{3.9}$$

It should be noted that in the homogeneous core formulation u_g and u_e must be replaced by u_c in Eqs. (3.1) and (3.2). Also, Eq. (3.7) replaces Eqs. (3.4) and (3.5) in the momentum balances.

Figure 3.3 show the schematic energy fluxes in annular flow. For the gas core, entrained liquid and liquid film fields, the resulting balance equations are given respectively by,

$$\frac{\partial}{\partial t} \left[\alpha_g \rho_g \left(e_g + \frac{u_c^2}{2} \right) \right] + \frac{\partial}{\partial z} \left[\alpha_g \rho_g u_c \left(h_g + \frac{u_c^2}{2} \right) \right] +$$
$$p \frac{\partial \alpha_g}{\partial t} = F_c^{int} u_f - \alpha_g \rho_g u_c g \tag{3.10}$$

$$\frac{\partial}{\partial t} \left[\alpha_e \rho_e \left(e_e + \frac{u_c^2}{2} \right) \right] + \frac{\partial}{\partial z} \left[\alpha_e \rho_e u_c \left(h_e + \frac{u_c^2}{2} \right) \right] + p \frac{\partial \alpha_e}{\partial t} =$$
$$+ M_e^{int} \left(h_f + \frac{u_f^2}{2} \right) - M_f^{int} \left(h_e + \frac{u_c^2}{2} \right) - \alpha_e \rho_e u_c g \tag{3.11}$$

$$\frac{\partial}{\partial t} \left[\alpha_f \rho_f \left(e_f + \frac{u_f^2}{2} \right) \right] + \frac{\partial}{\partial z} \left[\alpha_f \rho_f u_f \left(h_f + \frac{u_f^2}{2} \right) \right] + p \frac{\partial \alpha_f}{\partial t} =$$
$$F_f^{int} u_c + F_f^w u_f + M_f^{int} \left(h_e + \frac{u_f^2}{2} \right) - M_e^{int} \left(h_f + \frac{u_f^2}{2} \right)$$
$$- \alpha_f \rho_f u_f g \tag{3.12}$$
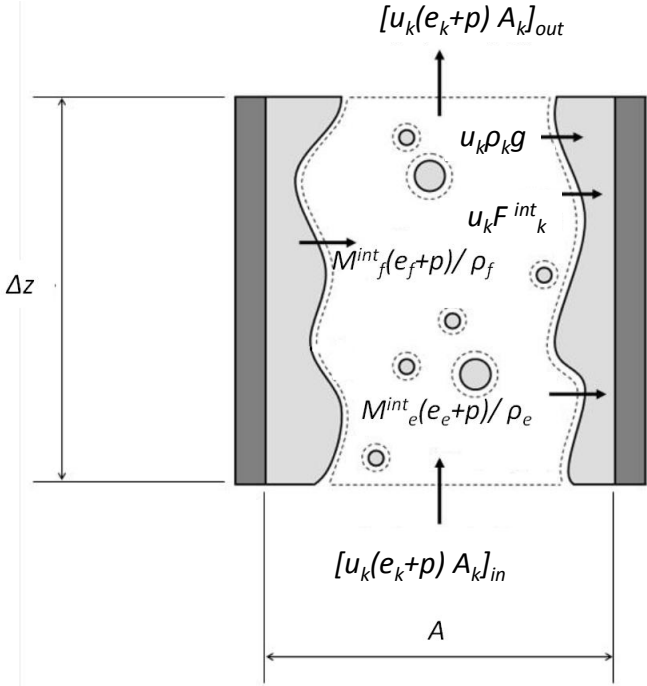
Figure 3.3 – Schematic representation of energy fluxes in annular flow.

where $F_i^{int} u_j$ is the energy generation due to interfacial friction, $F_i^w u_j$ is the energy generation due to wall friction, $M_i \left(h_j + \frac{u_j^2}{2} \right)$ is the energy transport due to mass exchange between the two liquid fields, $p \frac{\partial \alpha}{\partial t}$ is the energy generation due to expansion and compression, and $\alpha_i \rho_i u_i g$ is the energy change associated with the gravitational field.

Städtke (2006) and Gessner (2010) discussed the benefits of using the entropy balance instead of its energy counterpart. In fact, the advantage is purely mathematical as it allows for a more convenient expression of the problem coefficient matrix, generating only real eingenvalues. As can be seen from Städtke (2006), using the energy equation in terms of enthalpy results in complex eigenvalues and a non-hyperbolic system of equations. This, in turn, precludes the application

of the SCMM or other hyperbolic methods.

Entropy and internal energy of phase i are related by the following canonical relationship,

$$de_i = T_i \delta s_i + \frac{p}{\rho_i^2} \delta \rho_i \tag{3.13}$$

The phase density written as a function of pressure and phase entropy is given by,

$$\delta \rho_i = \left(\frac{\partial \rho_i}{\partial s_i} \right)_p \delta s_i + \left(\frac{\partial \rho_i}{\partial p} \right)_{s_i} \delta p \tag{3.14}$$

where introduction of the phase sound velocity, Eq. (3.16), isothermal compressibility coefficient, Eq. (3.17), and isobaric specific heat capacity, Eq. (3.18), results in,

$$\delta \rho_i = \frac{\rho_i \beta_i T_i}{c_{p_i}} \delta s_i - \frac{1}{a_i^2} \delta p \tag{3.15}$$

$$a = \sqrt{\left. \frac{\partial p}{\partial \rho} \right|_s} \tag{3.16}$$

$$\beta = \frac{c_{p_i}}{\rho T} \left. \frac{\partial p}{\partial \rho} \right|_s \tag{3.17}$$

$$c_{p_i} = \left. \frac{\partial h}{\partial T} \right|_p \tag{3.18}$$

As discussed by Städtke (2006) and Gessner (2010), it is convenient to write the balance equations in non-conservative form prior to the application of the Finite Difference-based SCMM. To accomplish this in the context of an entropy-based formulation, Eq. (3.15) is substituted in Eqs. (3.1) to (3.3) and the time and space partial derivatives are expanded using basic differentiation rules. This yields the following set of equations,

$$\frac{\alpha_g}{a_g^2} \left(\frac{\partial p}{\partial t} + u_c \frac{\partial p}{\partial z} \right) + \rho_g \left(\frac{\partial \alpha_g}{\partial t} + u_c \frac{\partial \alpha_g}{\partial z} \right) -$$
$$\alpha_g \left(\frac{\rho_g \beta_g T_g}{c_{p_g}} \right) \left(\frac{\partial s_g}{\partial t} + u_c \frac{\partial s_g}{\partial z} \right) + \alpha_g \rho_g \frac{\partial u_c}{\partial z} = 0 \tag{3.19}$$

$$\frac{\alpha_e}{a_e^2}\left(\frac{\partial p}{\partial t} + u_c\frac{\partial p}{\partial z}\right) + \rho_e\left(\frac{\partial \alpha_e}{\partial t} + u_c\frac{\partial \alpha_e}{\partial z}\right) -$$

$$\alpha_e\left(\frac{\rho_e\beta_e T_e}{c_{p_e}}\right)\left(\frac{\partial s_e}{\partial t} + u_c\frac{\partial s_e}{\partial z}\right) + \alpha_e\rho_e\frac{\partial u_c}{\partial z} = M_f^{int} - M_e^{int} \qquad (3.20)$$

$$\frac{\alpha_f}{a_f^2}\left(\frac{\partial p}{\partial t} + u_f\frac{\partial p}{\partial z}\right) + \rho_f\left(\frac{\partial \alpha_f}{\partial t} + u_f\frac{\partial \alpha_f}{\partial z}\right) -$$

$$\alpha_f\left(\frac{\rho_f\beta_f T_f}{c_{p_f}}\right)\left(\frac{\partial s_f}{\partial t} + u_f\frac{\partial s_f}{\partial z}\right) + \alpha_f\rho_f\frac{\partial u_f}{\partial z} =$$

$$- M_f^{int} + M_e^{int} \qquad (3.21)$$

In non-conservative form, the homogeneous core and liquid film momentum balance equations are given by Gessner (2010),

$$\alpha_c\rho_c\left(\frac{\partial u_c}{\partial t} + u_c\frac{\partial u_c}{\partial z}\right) + \alpha_c\frac{\partial p}{\partial z} = F_c^{nv} +$$

$$F_c^{int} - \alpha_c\rho_c g_z - M_e^{int}\Delta u \qquad (3.22)$$

$$\alpha_f\rho_f\left(\frac{\partial u_f}{\partial t} + u_f\frac{\partial u_f}{\partial z}\right) + \alpha_f\frac{\partial p}{\partial z} = F_f^{nv} +$$

$$F_f^{int} + F_f^w - \alpha_f\rho_f g_z + M_f^{int}\Delta u \qquad (3.23)$$

where, $\Delta u = u_g - u_l$ is the velocity difference between the phases.

Similarly, the entropy balance equations in non-conservative form are given by Gessner (2010),

$$\alpha_g\rho_g\left(\frac{\partial s_g}{\partial t} + u_c\frac{\partial s_g}{\partial z}\right) = -\frac{F_c^{int}\Delta u}{T_g} \qquad (3.24)$$

$$\alpha_e\rho_e\left[\frac{\partial s_e}{\partial t} + u_c\frac{\partial s_e}{\partial z}\right] = \frac{M_e^{int}\left[(h_f - h_e) + \Delta u^2/2\right]}{T_e} \qquad (3.25)$$

$$\alpha_f \rho_f \left[\frac{\partial s_f}{\partial t} + u_f \frac{\partial s_f}{\partial z} \right] = \frac{F_f^{int} \Delta u + F_f^w u_f}{T_f} +$$

$$\frac{M_f^{int} \left[(h_e - h_f) + \Delta u^2/2 \right]}{T_f} \tag{3.26}$$

The right hand side of Eqs. (3.24) to (3.26) can be substituted in Eqs. (3.19) to (3.21) giving the final form of the mass balance equations as follows,

$$\frac{\alpha_g}{a_g^2} \left(\frac{\partial p}{\partial t} + u_c \frac{\partial p}{\partial z} \right) + \rho_g \left(\frac{\partial \alpha_g}{\partial t} + u_c \frac{\partial \alpha_g}{\partial z} \right) +$$

$$\alpha_g \rho_g \frac{\partial u_c}{\partial z} + \left(\frac{\alpha_g \rho_g \beta_g F_g^{int} \Delta u}{c_{p_g}} \right) = 0 \tag{3.27}$$

$$\frac{\alpha_e}{a_e^2} \left(\frac{\partial p}{\partial t} + u_c \frac{\partial p}{\partial z} \right) + \rho_e \left(\frac{\partial \alpha_e}{\partial t} + u_c \frac{\partial \alpha_e}{\partial z} \right) +$$

$$\alpha_e \rho_e \frac{\partial u_c}{\partial z} - \left(\frac{\alpha_e \rho_e \beta_e}{c_{p_e}} \right) \left(M_e^{int} \left[(h_f - h_e) + \Delta u^2/2 \right] \right)$$

$$= M_e^{int} - M_f^{int} \tag{3.28}$$

$$\frac{\alpha_f}{a_f^2} \left(\frac{\partial p}{\partial t} + u_f \frac{\partial p}{\partial z} \right) + \rho_f \left(\frac{\partial \alpha_f}{\partial t} + u_f \frac{\partial \alpha_f}{\partial z} \right) + \alpha_f \rho_f \frac{\partial u_f}{\partial z}$$

$$- \left(\frac{\alpha_f \rho_f \beta_f}{c_{p_f}} \right) \left(F_f^{int} \Delta u + F_f^w u_f M_f^{int} \left[(h_e - h_f) + \Delta u^2/2 \right] \right)$$

$$= M_f^{int} - M_e^{int} \tag{3.29}$$

Although the three-field model was developed originally for annular flow, it can be easily extended to the churn flow regime by introducing closure relationships that are valid in this flow regime, such as the empirical correction due to Ahmad *et al.* (2010) for the droplet entrainment rate in churn flow.

It should be noted that the three-field formulation can easily be converted into a two-field model, for instance, in cases where there

is no entrainment. This two-field model can be used to describe the behavior of the so-called "perfect" or "ideal" annular flow, i.e., that in which the gas core contains no entrained droplets. The two-field formulation is also the traditional approach for modeling churn flow when the operating condition falls out of range of the entrainment and deposition correlation correction. The complete equations for this mathematical formulation are presented in the Apendix C.

Using the following relationship,

$$1 = \alpha_e + \alpha_f + \alpha_g \tag{3.30}$$

the system of equations (3.22) to (3.29) can be written in a more convenient vectorial form as follows,

$$\mathbf{E}\frac{\partial \vec{U}}{\partial t} + \mathbf{F}\frac{\partial \vec{U}}{\partial z} = \vec{C} \tag{3.31}$$

where the unknown variables vector is given by,

$$\vec{U} = \begin{bmatrix} p & \alpha_g & \alpha_f & u_c & u_f & s_g & s_e & s_f \end{bmatrix}^T \tag{3.32}$$

and $\mathbf{E}$ and $\mathbf{F}$ are coefficient matrices detailed in Appendix B.

To obtain the fully non-conservative form, Eq. (3.31) must be multiplied by $\mathbf{E}^{-1}$ to be transformed into,

$$\frac{\partial \vec{U}}{\partial t} + \mathbf{G}\frac{\partial \vec{U}}{\partial z} = \vec{D} \tag{3.33}$$

The coefficient matrix $\mathbf{G}$ and the source term vector $\vec{D}$ (along with the other matrices and source term vectors) are given in Appendix B.

3.2 MODELING NON-VISCOUS INTER-FACIAL FORCES

Non-viscous forces have been introduced by Städtke *et al.* (2005) in their two-fluid model to maintain the hyperbolicity of the system of partial differential equations. Gessner (2010) adopted Städtke's formulation in his model. Non-viscous forces are due to virtual mass F_c^{vm}, pressure difference between interface and phases $F_c^{\Delta p}$, and phase compressibility F_c^{comp}. For the homogeneous core, the resultant force is given by,

$$F_c^{nv} = F_c^{vm} + F_c^{\Delta p} + F_c^{comp} \tag{3.34}$$

The virtual mass effect accounts for the local mass displacements in the case of a relative acceleration between two phases (LAMB, 1932). Thus, when an object immersed in a fluid is accelerated, it also displaces some of the surrounding fluid. Städtke (2006) adopted a specific form of the virtual mass form, which is a generalization of the relationship available in Drew and Passman (2003),

$$F_c^{vm} = \alpha_c \alpha_f \rho \left[k \left(\frac{D^c u_f}{Dt} - \frac{D^f u_c}{Dt} \right) + \frac{\Delta\rho}{\rho} \Delta u \left(\frac{\partial u_c}{\partial z} - \frac{\partial u_f}{\partial z} \right) \right] \quad (3.35)$$

where the $D^c()/D$ and $D^f()/D$ operators denote the material derivatives with respect to the homogeneous core and film velocities, respectively.

In dispersed flow regimes, such as bubbly flow, the virtual mass coefficient, k, approaches the theoretical value for a rigid single sphere, i.e., $1/2$ (STäDTKE, 2006). For completely separated (i.e., stratified) flows, k approaches zero. In the annular and churn flow regimes, the influence of this parameter on the overall value of the virtual mass force is expected to be small (ISHII; HIBIKI, 2006). Thus, the three parts of the non-viscous interfacial forces are given by,

$$F_c^{vm} = \alpha_c \alpha_f \Delta\rho \Delta u \left(\frac{\partial u_c}{\partial z} - \frac{\partial u_f}{\partial z} \right) \quad (3.36)$$

$$F_c^{\Delta p} = \alpha_c \alpha_f \Sigma\rho (\Delta u)^2 \frac{\partial \alpha_f}{\partial z} \quad (3.37)$$

$$F_c^{comp} = -\alpha_c \alpha_f \Sigma\rho \Delta u \left[\frac{\alpha_g}{\rho_c} \left(\frac{\partial \rho_g}{\partial t} + u_c \frac{\partial \rho_g}{\partial z} \right) \right.$$
$$\left. + \frac{\alpha_f}{\rho_c} \left(\frac{\partial \rho_f}{\partial t} + u_f \frac{\partial \rho_f}{\partial z} \right) + \frac{\alpha_e}{\rho_c} \left(\frac{\partial \rho_e}{\partial t} + u_c \frac{\partial \rho_e}{\partial z} \right) \right] \quad (3.38)$$

where,

$$\Delta\rho = \alpha_f \rho_c - \alpha_c \rho_f \quad (3.39)$$

$$\Sigma\rho = \rho_c + \rho_f \quad (3.40)$$

Also, according to Newton's third law,

$$F_f^{nv} = -F_c^{nv} \tag{3.41}$$

The introduction of these non-viscous terms have little physical significance for the model presented here, however, the removal of such terms would render the model non-hyperbolic due to the ill-posedness of the two-fluid model which is the basis for both two and three-field formulations used in this work. The fact that the two-fluid model is ill-posed, i.e., dos not have a complete set of real eigenvaules has the following consequences:

- the model does not represent a well-posed initial-boundary value problem;

- the system of equations cannot be transformed into the characteristic form and, therefore, all numerical techniques developed for fully hyperbolic systems of equations cannot be applied;

- the model does not describe pressure waves realistically, and so, does not provide realistic critical flow predictions;

- short wavelength instabilities require speific dampening mechanisms in order to atain numerical stability;

Without the inclusion of the non-viscous interfacial momentum coupling terms described in this section, one could apply the usual numerical solution methods, based on staggered grids and upwind techniques (donor cell). These methods provide sufficient numerical diffusion so that stable results can be obtainedfor many transient two-phase flow conditions. The application of these techniques severely compromises the accuracy of predicting local flow variables, especially if large density or void fraction gradients exist (STäDTKE, 2006).

3.3   CLOSURE RELATIONSHIPS

3.3.1   Mass Exchange between the Liquid Film and the Homogeneous Core

It is assumed that entrainment and deposition rate correlations formulated based on steady-state data can be applied in the description of transient flows (LANGNER; MAYINGER, 1979). In the present work, use was made of the droplet deposition and entrainment rates of Hewitt and Govan (1990), modified by Ahmad *et al.* (2010) to include the churn

flow region. In this method, if annular flow prevails $\left(u_{gS}^{*} > 1.0\right)$, the
rate of liquid entrainment per unit volume is given by,

$$M_e^{int} = \begin{cases} 0, & \text{if } u_f \leq u_{crit} \\ \frac{23 \times 10^{-5} \alpha_g \sqrt{\alpha_g} u_c \alpha_f^2 \rho_f^3}{\rho_g \sigma} (u_f - u_{crit})^2, & \text{if } u_f > u_{crit} \end{cases} \qquad (3.42)$$

where the critical velocity u_{crit} (the velocity at which disturbance waves
are formed, breakup and release droplets into the gas core) can be
calculated using the following relation,

$$u_{crit} = \frac{\mu_f}{\alpha_f \rho_f d_T} \exp\left(5.8504 + 0.4249 \frac{\mu_g}{\mu_f} \sqrt{\frac{\rho_f}{\rho_g}} \right) \qquad (3.43)$$

where d_T is the pipe diameter.

The droplet deposition rate per unit volume in annular flow ($u_{gS}^{*} > 1.0$) is calculated from,

$$M_f^{int} = \frac{4\sqrt{\alpha_c}}{d_T} k_f C \qquad (3.44)$$

where the deposition coefficient k_f is given by,

$$k_f = \begin{cases} 0.185 \left(\frac{\sigma}{\rho_g d_T} \right)^{0.5}, & \text{if } \frac{C}{\rho_g} < 0.3 \\ 0.185 \left(\frac{\sigma}{\rho_g d_T} \right)^{0.5} \left(\frac{\rho_g}{C} \right)^{0.65}, & \text{if } \frac{C}{\rho_g} \geq 0.3 \end{cases} \qquad (3.45)$$

and the droplet concentration in the gas core is defined as,

$$C = \frac{\alpha_e \rho_e}{\alpha_c} \qquad (3.46)$$

Droplet entrainment in churn flow has been corrected by Ahmad
et al. (2010) applying an empirical factor on the Hewitt and Govan
(1990) correlation as follows,

$$\frac{M_e^{int}\big|_{\text{churn}}}{M_e^{int}\big|_{\text{annular}}} = -8.73 u_{gS}^{*} + 9.73 \qquad (3.47)$$

It follows from Ahmad *et al.* (2010) that deposition rates in churn
flow should be calculated using the same expression proposed for an-
nular flow.

3.3.2   Momentum Transport

The wall shear force on the liquid film can be expressed, per unit volume, as,

$$F_w = \frac{4}{d_T}\tau_w \tag{3.48}$$

where the wall shear stress (τ_w) is defined by,

$$\tau_w = \frac{1}{2}f_w \rho_f u_f \left|u_f\right| \tag{3.49}$$

For annular flow, the wall friction coefficient was calculated using the Kosky and Staub (1971) correlation given by,

$$f_w = \begin{cases} 16/Re_f, & \text{if } Re_f < 50 \\ 12.7937/Re_f^{0.9428}, & \text{if } 50 \leq Re_f \leq 1483 \\ 0.081/Re_f^{0.25}, & \text{if } Re_f > 1483 \end{cases} \tag{3.50}$$

where the liquid film Reynolds number, Re_f, is given by,

$$Re_f = \frac{\alpha_f \rho_f u_f d_T}{\mu_f} \tag{3.51}$$

The interfacial friction force per unit of volume exerted by the homogeneous core on the film, F_c^{int}, can be expressed by,

$$F_c^{int} = \frac{4\sqrt{\alpha_c}}{d_T}\tau_{int} \tag{3.52}$$

where the interfacial shear stress is given by,

$$\tau_{int} = \frac{1}{2}f_{int}\rho_c \alpha_c \left(u_c - u_f\right)\left|u_c - u_f\right| \tag{3.53}$$

Several interfacial friction correlations have been evaluated in the present study. According to Wallis (1969), the interfacial friction coefficient, f_{int}, is given by the following expression for annular flow,

$$f_{int} = f_c \left[1 + 180\left(1 - \sqrt{\alpha_c}\right)\right] \tag{3.54}$$

where,

$$f_c = \frac{0.079}{Re_c^{0.25}} \tag{3.55}$$

and the homogeneous Reynolds number, Re_c, is given by,

$$Re_c = \frac{\alpha_c \rho_c u_c d_T}{\mu_g} \tag{3.56}$$

Whalley and Hewitt (1978) proposed the following annular flow interfacial friction coefficient correlation,

$$f_{int} = f_c \left[1 + 12 \left(\frac{\rho_l}{\rho_g} \right)^{1/3} (1 - \sqrt{\alpha_c}) \right] \tag{3.57}$$

More recently, Belt *et al.* (2009) presented the following correlation for the interfacial friction coefficient in annular flow,

$$f_{int} = 0.0003413 + 0.579 \left(1 - \sqrt{\alpha_c} \right) \tag{3.58}$$

In churn flow, Jayanti and Brauner (1994) suggested single-phase flow relationships for the film-wall friction coefficient,

$$f_w = \begin{cases} 16/Re_f & , \text{ if } Re_f < 2100 \\ 0.079/Re_f^{0.25} & , \text{ if } Re_f \geq 2100 \end{cases} \tag{3.59}$$

Based on comparisons with the experimental data of Govan *et al.* (1991) for churn flow, Jayanti and Brauner (1994) recommended the following relationship for the interfacial friction coefficient, which is the arithmetic average of the correlations due to Bharathan and Wallis (1983) and Wallis (1969),

$$f^{int} = 0.005+$$

$$\frac{1}{2} \left\{ 10^{\left(\frac{9.07}{d_T^*} - 0.56 \right)} \left[\frac{d_T^* (1 - \alpha_c)}{4} \right]^{\left(\frac{4.74}{d_T^*} + 1.63 \right)} + 0.375 (1 - \alpha_c) \right\} \tag{3.60}$$

where,

$$d_T^* = d_T \sqrt{\frac{(\rho_l - \rho_g) g}{\sigma}} \tag{3.61}$$

It should be noted that Newton's third law dictates that,

$$F_f^{int} = -F_c^{int} \tag{3.62}$$

3.3.3 Transition Criteria between the Churn and Annular Flow Patterns

As discussed in Section 2.1.3, starting from a stable annular flow condition, as the gas superficial velocity is decreased, the interfacial shear stress becomes weaker and the liquid film starts to oscillate. A commonly employed criterion for the churn-annular transition is the flow reversal condition, which has been correlated by Hewitt and Wallis (1963) (see also Wallis (1969)) in terms of the following dimensionless velocity,

$$u_{gS}^* = u_{gS} \sqrt{\frac{\rho_g}{g d_T \left(\rho_l - \rho_g\right)}} \qquad (3.63)$$

In the numerical model developed in this work, an adaptation of Wallis flow reversal criterion is considered, exploring the nature of the three-field balance equations. This approach enables a smooth tracking of successive flow pattern transitions (annular to churn and vice-versa), which may occur during transients, without having to change the set of equations being solved. A sharp transition between flow patterns and their respective governing equations is deemed to introduce numerical instabilities that prevent convergence of the iterative calculations. The introduction of a modified transition criterion resulted in a more robust solution process. Therefore, the following transition algorithm is proposed,

- if $u_{gS}^* > 1.0$, the flow is annular;

- if $u_{gS}^* \leq 1.0$, and the residuum $R = \mathrm{abs}\left[\frac{\left(\alpha_e^I - \alpha_e^{I-1}\right)}{\alpha_e^I}\right] < 10^{-2}$ between two consecutive iterations, the flow pattern is churn and the three-field hyperbolic model is used;

- if $u_{gS}^* \leq 1.0$, and the residuum $R = \mathrm{abs}\left[\frac{\left(\alpha_e^I - \alpha_e^{I-1}\right)}{\alpha_e^I}\right] \geq 10^{-2}$ between two consecutive iterations, the flow pattern is churn and the two-field hyperbolic model is used.

where the 'I' represents the current iteration inside any given time step.

The transition criterion between the three and two-field formulation was chosen by observing the behavior of all variables. Though this it was visualised that it was the disappearance of the droplets (in annular flow), and the oscillation in it's volume fraction value fraction (in churn flow), were the governing parameters for the three-field model

to diverge. Once the residuum $R = \text{abs}\left[\frac{\left(\alpha_e^I - \alpha_e^{I-1}\right)}{\alpha_e^I}\right]$ was calculated to be above 10^{-2} the program could not recover from divergence, even if the mathematical formulations were changed. This transition between the three and two-field formulations is a numerical artifice introduced to prevent numerical instabilities associated with the three-field churn flow model for low u_{gS}^*. Once in the churn flow regime, a residuum in α_e greater than 10^{-2} was observed to cause the numerical solution of the three-field model to quickly diverge (specially for lower values of u_{gS}^*). This is possibly due to the lack of generality of the entrainment rate correlation/correction for churn flow. In turn, the two-field formulation eliminates the need for entrainment and deposition rate correlations as there is only one liquid field, and that stabilizes the solution in churn flow.

It should be noted that the annular flow pattern can be described by the three or two-field formulations. The latter is chosen when the film velocity is less than the critical value required to generate entrained droplets (Section 3.3.1). Another important observation is that the numerical model adopts a whole domain formulation and the transition between the mathematical approaches is applied to the full extent of the domain at once, and no subdivision of it is created.

3.4 DETERMINATION OF BOUNDARY CONDITIONS

The balance equations and closure relationships presented in the previous sections are written in terms of local (*in-situ*) velocities and phase fractions. These variables are not often available from experimental input data, which are usually given in terms of phase mass fluxes. These, in turn, have to be converted into velocities and phase fractions to feed the mathematical model. As seen in Fig. 3.4, the flow takes place in a vertical round tube of given length and internal diameter. The boundary conditions are such that at the lower end of the tube the following variables are prescribed: $G_{g,in}$, $G_{l,in}$, $T_{g,in}$, $T_{f,in}$ and $e_{f,in}$. At the top of the tube, the outlet pressure (p_{out}) is also prescribed. This set of boundary conditions was chosen because it corresponds to the majority of practical situations and experimental analyses of two-phase flows, as seen in Section 2.3.

With the mass and momentum boundary conditions stated in terms of mass fluxes, closure relationships are needed to translate them
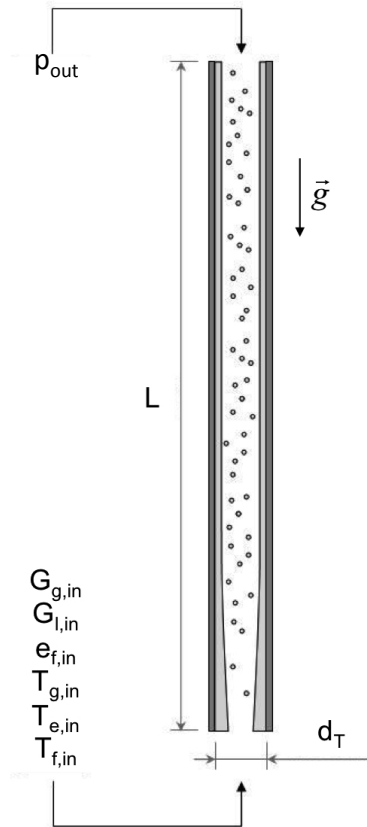
Figure 3.4 – Problem general geometry and boundary condition locations.

into native variables of the balance equations. The following sections discuss how this was accomplished for the annular and churn flow patterns, respectively. The boundary conditions for the entropy equations also need to be converted from temperature and pressure to entropy. This is accomplished via the state functions available in the Fortran source code of the REFPROP 8.0 package (LEMMON *et al.*, 2007).

3.4.1 Determination of the Inlet Parameters in Annular Flow

In annular flow, the conversion from phase mass fluxes to *in-situ* velocities and volumetric fractions is achieved via the "triangular relationship" (HEWITT, 1961) between the liquid film flow rate, the liquid film thickness and the pressure gradient (or wall shear stress). Original forms of the triangular relationship assume that the von Kármán universal velocity profile (UVP) exists in the liquid film. However, the double velocity profile (DVP) showed better results when used (JENSEN, 1987). In terms of dimensionless variables, the liquid film flow rate is given by,

$$\dot{M}_f^+ \equiv \frac{\dot{M}_f}{\pi d_T \mu_l} = \int_0^{\delta^+} u_f^+ \left(1 - \frac{y^+}{Re^+}\right) dy^+ \tag{3.64}$$

where,

$$y^+ = \frac{\rho_l u^* y}{\mu_l} \tag{3.65}$$

$$\delta^+ = \frac{\rho_l u^* \delta}{\mu_l} \tag{3.66}$$

$$Re^+ = \frac{\rho_l u^* d_T}{2\mu_l} \tag{3.67}$$

$$u_f^+ = \frac{u_f}{u^*} \tag{3.68}$$

$$u^* = \sqrt{\frac{\tau_w}{\rho_l}} \tag{3.69}$$

The DVP equals the UVP up to the point where $y^+ = \delta^+/2$, and an inverse reflection of the UVP for $\delta^+/2 \leq y^+ \leq \delta^+$. Thus,

$$u_f^+ = \begin{cases} y^+, & \text{for } y^+ \leq 10 \\ -6.1 + 10.0\ln\left(\frac{y^+}{2}\right), & \text{for } 10 < y^+ \leq 60 \\ 10.92 + 5.0\ln\left(\frac{y^+}{2}\right), & \text{for } y^+ > 60 \end{cases} \tag{3.70}$$

The integration of the above equations according to Eq. (3.64) results in the following relation for the liquid film dimensionless flow

rate,

$$
\dot{M}_f^+ = \begin{cases}
\frac{1}{2}\delta^{+2} - \frac{1}{3}\delta^{+3}, & \text{for } \delta^+ \leq 10 \\
\frac{1}{Re^+}\left[17.22 - 22.26\delta^+ 0.594\delta^{+2} - 2.5\delta^{+2}\ln\left(\frac{\delta^+}{2}\right)\right] \\
+ \left[5\delta^+\ln\left(\delta^+/2\right) - 0.05\delta^+\right], & \text{for } 10 < \delta^+ \leq 60 \\
\frac{1}{Re^+}\left[1146 - 63.9\delta^- 3.688\delta^{+2} - 1.25\delta^{+2}\ln\left(\frac{\delta^+}{2}\right)\right] \\
+ \left[2.5\delta^+\ln\left(\delta^+/2\right) + 5.5\delta^+\right], & \text{for } \delta^+ > 60
\end{cases} \tag{3.71}
$$
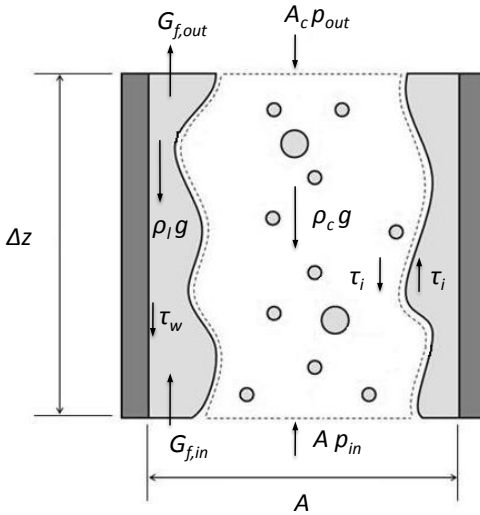
Figure 3.5 – Schematic representation of the momentum balance terms in annular flow.

An expression for the wall shear stress can be calculated by eliminating the total pressure gradient from the liquid film and homogeneous gas core force balances (considering the entrained droplets but neglecting the accelerational pressure gradient) as depicted in Fig. 3.5,

$$
\tau_w = \frac{r^2 - r_{int}^2}{2r}\left[(\rho_l - \rho_c)\, g + \frac{2r\tau_{int}}{r_{int}\left(r^2 - r_{int}^2\right)}\right] \tag{3.72}
$$

where r_{int} is the radius of the interface given by $r - \delta$. Equations (3.65) to (3.72) represent a unique relation between the liquid film flow rate, the film thickness and the wall shear stress. The algorithm employed to calculate the in-situ velocities and phase fractions (u_c, u_f, α_g, α_f) from mass flux input parameters (G_g, G_l, ef) is as follows,

1. With the general inputs (G_g, G_l and ef), calculate the entrained liquid mass flux G_e, the total mass flux G and the film mass flux G_f;

2. Estimate the wall shear stress, τ_w, using the Friedel (1979) correlation;

3. Calculate u^* via Eq. (3.69);

4. Guess δ;

5. Calculate δ^+ via Eq. (3.66);

6. Calculate the new film mass flux, $G_f = \frac{4\mu_l \dot{} M_f^+}{d_T}$, using Eq. (3.71)

7. Calculate the new film thickness, δ^+, via Eq. (3.66);

8. Return to step 6 until $\left| \frac{G_f^I - G_f^{I-1}}{G_f^I} \right| \leq 10^{-4}$;

9. Calculate τ_i using the Wallis (1969) correlation;

10. Calculate the new τ_w using Eq. (3.72);

11. Return to step 3 until $\left| \frac{\tau_w^J - \tau_w^{J-1}}{\tau_w^J} \right| \leq 10^{-4}$;

12. Calculate the final values of α_g, u_c, α_f and u_f using the expressions below,

$$\alpha_c = \left(1 - 2\frac{\delta}{d_T} \right)^2 \tag{3.73}$$

$$x_g = \frac{G_g}{G_g + efG_l} \tag{3.74}$$

$$\alpha_e = 1 - \frac{x_g}{\rho_g} - \frac{1}{\left(\frac{1-x_g}{\rho_l} + \frac{x_g}{\rho_g} \right)} \tag{3.75}$$

$$\alpha_f = 1 - \alpha_c \qquad (3.76)$$

$$\alpha_g = 1 - \alpha_f - \alpha_e \qquad (3.77)$$

$$u_c = \frac{G_g}{\rho_c \alpha_c} \qquad (3.78)$$

$$u_f = \frac{G_f}{\rho_f \alpha_f} \qquad (3.79)$$

3.4.2   Determination of the Inlet Parameters in Churn Flow

The Jayanti and Brauner (1994) model consists of two steady-state balance equations that are used to predict the pressure gradient and the void fraction in churn flow. Considering Fig. 3.6, the force balances on the gas core and on the two-phase mixture are as follows,
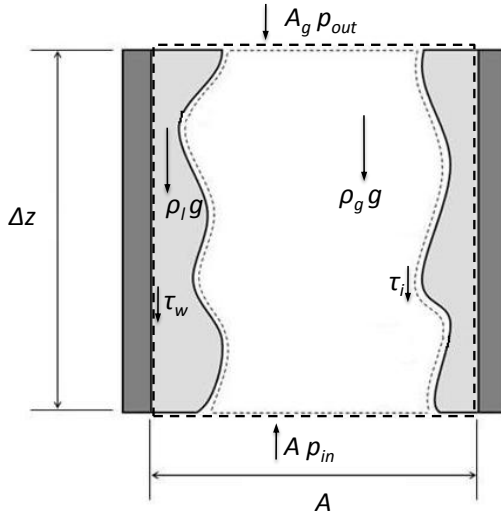
Figure 3.6 – Schematic representation of the momentum balance terms in churn flow.

$$-\frac{dp}{dz} = \frac{4}{d_T}\frac{\tau_{int}}{\sqrt{\alpha_g}} + \rho_g g \tag{3.80}$$

$$-\frac{dp}{dz} = \frac{4}{d_T}\tau_w + [\alpha_g\rho_g + \rho_l (1-\alpha_g)]\, g \tag{3.81}$$

where the wall shear stress is given by,

$$\tau_w = \frac{1}{2}\rho_l f_w \left(\frac{u_{lS}}{1-\alpha_g}\right)^2 \tag{3.82}$$

and the wall friction coefficient, f_w, is calculated from Eq. (3.59). Similarly, the average interfacial shear stress can be written as,

$$\tau_{int} = \frac{1}{2}\rho_g f_{int} \left(\frac{u_{gS}}{\alpha_g}\right)^2 \tag{3.83}$$

where the interfacial friction coefficient, f_{int}, is given by Eq. (3.60).

The main step for converting the variables is to substitute Eq. (3.80) into Eq. (3.81) to generate an implicit equation for α_g as follows,

$$\frac{4}{d_T}\frac{\tau_{int}}{\sqrt{\alpha_g}} + \rho_g g = \frac{4}{d_T}\tau_w + [\alpha_g\rho_g + \rho_l (1-\alpha_g)]\, g \tag{3.84}$$

Equation (3.84) is solved via the Newton-Raphson method (PRESS *et al.*, 1992) using the following algorithm,

1. Guess the void fraction α_g;

2. Calculate the wall and interfacial shear stresses using Eqs. (3.82) and (3.83);

3. Solve Eq. (3.84) for α_g using the Newton-Raphson method (PRESS *et al.*, 1992);

4. Return to step 2 until $\left|\frac{\alpha_g^I - \alpha_g^{I-1}}{\alpha_g^I}\right| \le 10^{-4}$;

5. Calculate final values of: α_g, u_c, α_f and u_f using the expressions below:

$$\alpha_f = 1 - \alpha_g \tag{3.85}$$

$$u_g = \frac{G_g}{\rho_g\alpha_g} \tag{3.86}$$

$$u_f = \frac{G_f}{\rho_f \alpha_f} \tag{3.87}$$

As in annular flow, using the algorithm and equations presented in this section, it is possible to start with mass flux input parameters $(G_g, G_l$ and $ef)$ and convert them into the native variables of the model $(\alpha_g, u_g, \alpha_f$ and $u_f)$. The algorithm presented in this section is based on two-fields only. However, it is also applicable to three-fields, as it is used only to determine the core and film velocities and gas void fraction at the inlet. At the first point of the domain, droplet entrainment in three-filed churn flow is ignored, being calculated for the remainder of the domain via the main solution algorithm.

4 NUMERICAL SOLUTION

This chapter deals with the numerical aspects of the governing equations' solution . It presents the application of the Split Coefficient Matrix Method (SCMM) to the hyperbolic equation system and the processing algorithm adopted to solve the resulting system of algebraic equations. Finally, grid refinement and convergence aspects of the numerical solution are discussed.

The hyperbolic solver was selected mainly due to the PDE's hyperbolicity, but also because of possibility of investigating other phenomena with this same computer code in futures works, such as chock waves and expansions as will be suggested in Section 6.4.

4.1 APPLICATION OF THE SPLIT CO-EFFICIENT MATRIX METHOD

In non-conservative form, the system of mass, momentum and entropy balance equations is given by,

$$\frac{\partial \vec{U}}{\partial t} + \mathbf{G}\frac{\partial \vec{U}}{\partial z} = \vec{D} \tag{4.1}$$

where the unknown variables vector is given by,

$$\vec{U} = \begin{bmatrix} p & \alpha_g & \alpha_f & u_c & u_f & s_g & s_e & s_f \end{bmatrix}^T \tag{4.2}$$

Starting from a non-conservative hyperbolic PDE system of Nth order similar to Eq. 4.1, the eigenvalues of the coefficient matrix $\mathbf{G}$ are defined as the roots of the characteristic polynomial (COOPERSTEIN, 2010),

$$\det\left(\mathbf{G} - \lambda\mathbf{I}\right) = 0 \tag{4.3}$$

The number of roots is equal to the order of the PDE system. The eigenvalues and respective eigenvectors for this particular model are all analytical and are represented by the following expressions.

$$\lambda_1 = u + a \tag{4.4}$$

$$\vec{T}_1 = \begin{bmatrix} \rho_s \rho a_0^2 \\ \alpha_g \left(\rho_f - \frac{\rho_s \rho a_0^2}{\rho_g a_g^2} \right) \\ -\alpha_c \alpha_f \rho a_0^2 \left(\frac{1}{a_f^2} - \frac{1}{a_c^2} \right) \\ \rho_f \left(a - \alpha_f \Delta u \right) \\ \rho_c \left(a + \alpha_c \Delta u \right) \\ 0 \\ 0 \\ 0 \end{bmatrix} \tag{4.5}$$

$$\lambda_2 = u - a \tag{4.6}$$

$$\vec{T}_2 = \begin{bmatrix} \rho_s \rho a_0^2 \\ \alpha_g \left(\rho_f - \frac{\rho_s \rho a_0^2}{\rho_g a_g^2} \right) \\ -\alpha_c \alpha_f \rho a_0^2 \left(\frac{1}{a_f^2} - \frac{1}{a_c^2} \right) \\ -\rho_f \left(a + \alpha_f \Delta u \right) \\ -\rho_c \left(a - \alpha_c \Delta u \right) \\ 0 \\ 0 \\ 0 \end{bmatrix} \tag{4.7}$$

$$\lambda_3 = u_c \tag{4.8}$$

$$\vec{T}_3 = \begin{bmatrix} \alpha_f \rho_f \Delta u^2 \\ 0 \\ \alpha_f \left(1 - \alpha_f \frac{\Delta u^2}{a_f^2} \right) \\ 0 \\ \Delta u \\ 0 \\ 0 \\ 0 \end{bmatrix} \tag{4.9}$$

$$\lambda_4 = u_f \tag{4.10}$$

$$\vec{T_4} = \begin{bmatrix} \alpha_c \rho_c \Delta u^2 \\ 0 \\ -\alpha_c \left(1 - \alpha_c \frac{\Delta u^2}{a_c^2} \right) \\ -\Delta u \\ 0 \\ 0 \\ 0 \\ 0 \end{bmatrix} \tag{4.11}$$

$$\lambda_5 = u_c \tag{4.12}$$

$$\vec{T_5} = \begin{bmatrix} 0 \\ 1 \\ 0 \\ 0 \\ 0 \\ 0 \\ 0 \\ 0 \end{bmatrix} \tag{4.13}$$

$$\lambda_6 = u_c \tag{4.14}$$

$$\vec{T_6} = \begin{bmatrix} 0 \\ 0 \\ 0 \\ 0 \\ 0 \\ 1 \\ 0 \\ 0 \end{bmatrix} \tag{4.15}$$

$$\lambda_7 = u_c \tag{4.16}$$

$$\vec{T_7} = \begin{bmatrix} 0 \\ 0 \\ 0 \\ 0 \\ 0 \\ 0 \\ 1 \\ 0 \end{bmatrix} \tag{4.17}$$

$$\lambda_8 = u_f \tag{4.18}$$

$$\vec{T_8} = \begin{bmatrix} 0 \\ 0 \\ 0 \\ 0 \\ 0 \\ 0 \\ 0 \\ 1 \end{bmatrix} \tag{4.19}$$

$$u = \alpha_c u_c + \alpha_f u_f \tag{4.20}$$

$$a = \sqrt{\tilde{a}^2 - \alpha_c \alpha_f \Delta u^2} \tag{4.21}$$

$$\tilde{a}^2 = \frac{\rho_s \rho a_0^2}{\rho_c \rho_f} \tag{4.22}$$

As all the eigenvalues are real this model (problem) is fully hyperbolic and well-posed, being suitable for solution by the application of a hyperbolic method. The matrix $\mathbf{\Lambda}$ of eigenvalues is given by,

$$\Lambda = \begin{bmatrix} \lambda_1 & 0 & \dots & 0 \\ 0 & \lambda_2 & \dots & 0 \\ \vdots & \vdots & \ddots & \vdots \\ 0 & 0 & \dots & \lambda_N \end{bmatrix} \tag{4.23}$$

In this way each eigenvalue λ_i of the coefficient matrix $\mathbf{G}$ is associated with an eigenvector $\vec{T_i}$ via the following expression,

$$(\mathbf{G} - \lambda \mathbf{I})\, \vec{T_i} = 0 \tag{4.24}$$

The transformation matrix is comprised by the eigenvectors arranged in columns,

$$
\mathbf{T} = \begin{bmatrix}
T_{11} & T_{12} & \dots & T_{1N} \\
T_{21} & T_{22} & \dots & T_{2N} \\
\vdots & \vdots & \ddots & \vdots \\
T_{N1} & T_{N2} & \dots & T_{NN}
\end{bmatrix} \tag{4.25}
$$

The coefficient matrix $\mathbf{G}$ may be reconstructed by,

$$
\mathbf{G} = \mathbf{T\Lambda T^{-1}} \tag{4.26}
$$

The process of eigenvelue decomposition is explained in more detail by Cooperstein (2010). After undergoing this process, the eigenvalue matrix $\mathbf{\Lambda}$ is split in N parts, representing each of the eigenvalues,

$$
\Lambda = \begin{bmatrix}
\lambda_1 & 0 & \dots & 0 \\
0 & 0 & \dots & 0 \\
\vdots & \vdots & \ddots & \vdots \\
0 & 0 & \dots & 0
\end{bmatrix}
+
\begin{bmatrix}
0 & 0 & \dots & 0 \\
0 & \lambda_2 & \dots & 0 \\
\vdots & \vdots & \ddots & \vdots \\
0 & 0 & \dots & 0
\end{bmatrix} + \dots
$$
$$
+
\begin{bmatrix}
0 & 0 & \dots & 0 \\
0 & 0 & \dots & 0 \\
\vdots & \vdots & \ddots & \vdots \\
0 & 0 & \dots & \lambda_N
\end{bmatrix}
= \Lambda_1 + \Lambda_2 + \dots + \Lambda_N \tag{4.27}
$$

Combining Eq. (4.26) and (4.27), results in,

$$
\mathbf{G} = \mathbf{T\Lambda_1 T^{-1}} + \mathbf{T\Lambda_2 T^{-1}} + \dots + \mathbf{T\Lambda_N T^{-1}} = \mathbf{G}_1 + \mathbf{G}_2 + \dots \mathbf{G}_N \tag{4.28}
$$

It is possible to split the coefficient matrix $\mathbf{G}$ into two new matrices one associated with the positive eigenvalues, $\mathbf{G}^+$, and the other associated with the negative ones, $\mathbf{G}^-$, expressed by,

$$
\mathbf{G^+} = \frac{\lambda_1 + |\lambda_1|}{2\lambda_1} \mathbf{G}_1 + \frac{\lambda_2 + |\lambda_2|}{2\lambda_2} \mathbf{G}_2 + \dots + \frac{\lambda_N + |\lambda_N|}{2\lambda_N} \mathbf{G}_N \tag{4.29}
$$

$$
\mathbf{G^-} = \frac{\lambda_1 - |\lambda_1|}{2\lambda_1} \mathbf{G}_1 + \frac{\lambda_2 - |\lambda_2|}{2\lambda_2} \mathbf{G}_2 + \dots + \frac{\lambda_N - |\lambda_N|}{2\lambda_N} \mathbf{G}_N \tag{4.30}
$$

Applying the above definitions to Eq. (4.1) allows it to be rewritten in a more convenient form as follows,

$$\frac{\partial \vec{U}}{\partial t} + \mathbf{G}^+ \frac{\partial \vec{U}}{\partial z} + \mathbf{G}^- \frac{\partial \vec{U}}{\partial z} = \vec{D} \qquad (4.31)$$

When written in this form, i.e., splitting (or separating) the influence of the positive and negative eigenvalues on the PDE's variables, the SCMM not only allows for the derivatives of the variable vector $\vec{U}$ associated with $\mathbf{G}^+$ and $\mathbf{G}^-$ to receive different discretization scheme, which provides good numerical stability (less numerical oscillations), but also permits the use of high order numerical discretization schemes which dampens the effects of numerical diffusion. Also, the matrices $\mathbf{G}^+$ and $\mathbf{G}^-$ can be physically interpreted as being the velocity with which the PDE's variables are influenced by any perturbation in the flow upstream or downstream of the perturbation's position, respectively. For each variable the individual velocity is given by the respective eigenvalue associated with that particular line in matrix $\mathbf{G}$.

Because of the ability to distinguish between the influence of the positive and negative eigenvalues, the SCMM is recognized for its numerical stability when dealing with severe transients. Moreover, the derivatives associated with $\mathbf{G}^+$ and $\mathbf{G}^-$ can be given appropriate discretization treatment to minimize numerical diffusion (STäDTKE, 2006). The process of splitting the $\mathbf{G}$ matrix is analytical, and the resulting matrices, $\mathbf{G}^+$ and $\mathbf{G}^-$, are presented in Appendix B.

4.2   Discretization Scheme

Positive eigenvalues propagate the influence of variables in the downstream direction. This means that, in a numerical grid, this influence is passed from a preceding node, which calls for the use of a backward differencing scheme (BDS) in the discretization of the derivative associated with the matrix $\mathbf{G}^+$. For negative eigenvalues, the situation is the opposite, so a forward differencing scheme (FDS) seems more appropriate to discretize the derivative associated with the matrix $\mathbf{G}^-$. It should be noted that the use of the central differencing scheme (CDS) brings no advantage in either case. Second order discretization schemes for the derivatives associated with the $\mathbf{G}^-$ (FDS) and $\mathbf{G}^-$ (BDS) matrices are given by,

$$\left.\frac{\partial \vec{U}}{\partial z}\right|_{i,j} \approx \frac{\left(\psi^2 - 1\right)\vec{U}_{i,j} - \psi^2\vec{U}_{i-1,j} + \vec{U}_{i-2,j}}{\left(\psi^2 - \psi\right)\Delta z_i} \qquad (4.32)$$

$$\left.\frac{\partial \vec{U}}{\partial z}\right|_{i,j} \approx -\frac{\left(\phi^2 - 1\right)\vec{U}_{i,j} - \phi^2\vec{U}_{i+1,j} + \vec{U}_{i+2,j}}{\left(\phi^2 - \phi\right)\Delta z_{i+1}} \qquad (4.33)$$

where

$$\Delta z_i = z_i - z_{i-1} \qquad (4.34)$$

$$\psi = \frac{\Delta z_i - \Delta z_{i-1}}{\Delta z_i} \qquad (4.35)$$

$$\phi = \frac{\Delta z_{i+1} - \Delta z_{i+2}}{\Delta z_{i+1}} \qquad (4.36)$$

In the above equations, the subscripts i and j are indexes of the spatial and temporal independent variables. The temporal derivative $\partial \vec{U}/\partial t$ was discretized using a first order BDS, due to the characteristics of the marching solution in the variable t. In this way, only the value of $\vec{U}_{i,\,j-1}$ is stored. Thus,

$$\left.\frac{\partial \vec{U}}{\partial t}\right|_{i,j} \approx \frac{\vec{U}_{i,j} - \vec{U}_{i,j-1}}{\Delta t} \qquad (4.37)$$

Using Eqs. (4.32) to (4.37), it is possible to transform the system of partial differential equations given by Eq. (4.31) in the following system of algebraic equations form,

$$\frac{\vec{U}_i - \vec{U}_{i,0}}{\Delta t} + \mathbf{G}_i^+ \frac{\left(\psi^2 - 1\right)\vec{U}_i - \psi^2\vec{U}_{i-1} + \vec{U}_{i-2}}{\left(\psi^2 - \psi\right)\Delta z_i}$$

$$- \mathbf{G}_i^- \frac{\left(\phi^2 - 1\right)\vec{U}_i - \phi^2\vec{U}_{i+1} + \vec{U}_{i+2}}{\left(\phi^2 - \phi\right)\Delta z_{i+1}} = \vec{D}_i \qquad (4.38)$$

where the subscript j was dropped and the $j-1$ vector is marked by the subscript 0.

At the boundaries, the differencing schemes have to be changed. In the first node $(1,\,j)$, it is not possible to use the BDS because there are no preceding nodes. In the second node $(2,\,j)$, the BDS must be

first-order because there is only one preceding node. In the next to last node $(n-1,\ j)$, the FDS must be first-order because there is only one ensuing node. In the last node $(n,\ j)$, it is not possible to use the FDS as there are no ensuing nodes. Moreover, in the first and last nodes, the derivatives associated with the matrices $\mathbf{G}^+$ and $\mathbf{G}^-$ are set to zero, without compromising the solution of the system. The expressions for the discretized equations of these individual points are shown below.

- First node $(1,\ j)$:

$$\frac{\vec{U}_1 - \vec{U}_{1,0}}{\Delta t} - \mathbf{G}_1^- \frac{\left(\phi^2 - 1\right)\vec{U}_1 - \phi^2\vec{U}_2 + \vec{U}_3}{\left(\phi^2 - \phi\right)\Delta z_2} = \vec{D}_1 \qquad (4.39)$$

- Second node $(2,\ j)$:

$$\frac{\vec{U}_2 - \vec{U}_{2,0}}{\Delta t} + \mathbf{G}_2^+ \frac{\vec{U}_2 - \vec{U}_1}{\Delta z_2}$$
$$- \mathbf{G}_2^- \frac{\left(\phi^2 - 1\right)\vec{U}_2 - \phi^2\vec{U}_3 + \vec{U}_4}{\left(\phi^2 - \phi\right)\Delta z_3} = \vec{D}_2 \qquad (4.40)$$

- Next to last node, $(n-1,\ j)$:

$$\frac{\vec{U}_{n-1} - \vec{U}_{n-1,0}}{\Delta t} + \mathbf{G}_{n-1}^+ \frac{\left(\psi^2 - 1\right)\vec{U}_{n-1} - \psi^2\vec{U}_{n-2} + \vec{U}_{n-3}}{\left(\psi^2 - \psi\right)\Delta z_{n-1}}$$
$$- \mathbf{G}_{n-1}^- \frac{\vec{U}_n - \vec{U}_{n-1}}{\Delta z_n} = \vec{D}_{n-1} \qquad (4.41)$$

- Last node $(n,\ j)$:

$$\frac{\vec{U}_n - \vec{U}_{n,0}}{\Delta t} +$$
$$\mathbf{G}_n^+ \frac{\left(\psi^2 - 1\right)\vec{U}_n - \psi^2\vec{U}_{n-1} + \vec{U}_{n-2}}{\left(\psi^2 - \psi\right)\Delta z_n} = \vec{D}_n \qquad (4.42)$$

4.3 SOLUTION OF THE ALGEBRAIC SYSTEM

The system of algebraic equations given by Eq. (4.38) can be written in the more convenient form,

$$\mathbf{A}\vec{X} = \vec{B} \tag{4.43}$$

where $\mathbf{A}$ is a block matrix whose non-zero elements are sub-matrices which are written in terms of the elements of $\mathbf{G}^+$, $\mathbf{G}^-$ and of the unknown variables.

The second-order interpolation scheme resulted in the matrix $\mathbf{A}$ being very sparse (only 21 non-zero elements per block matrix of 64 possible), and its structure is shown in Appendix B. For each point of the domain, five of these block matrices are inserted into the coefficient matrix, $\mathbf{A}$, except for the nodes near the boundaries, which have different structures. Nodes $(2,\ j)$ and $(n-1,\ j)$ are composed of four block matrices, and nodes $(1,\ j)$ and $(n,\ j)$ have three block matrices, as seen in Appendix B.

The linear system of algebraic equations is solved using the PARDISO algorithm of Schenk and co-workers (SCHENK *et al.*, 2000; SCHENK; GARTNER, 2004, 2002). This package uses an implementation of the LU direct solving technique. PARDISO is included in the Intel FORTRAN Compiler 12.0 as part of the Mathematical Kernel Library (Intel MKL), and is used to compile and build the program application. Although an iterative solver would result in a faster solution of the linear system, this type of algorithm could not be used because the coefficient matrix may not be diagonaly dominant for all situations. Diagonal dominace is a prerequisite of the iterative solvers (BURDEN; FAIRES, 2010; TORO, 1999; DAFERMOS, 2005; SHARMA, 2010; COOPERSTEIN, 2010).

The program is written using a "fork-joint" OpenMP paradigm. All but one of its subroutines are parallelized, with the serial subroutine accounting for 15% of the iterative loop computational time. This subroutine has an inherent serial workflow (assembly of the non-zero elements of matrix $\mathbf{A}$ into a format understandable to the PARDISO subroutine) and attempts to create a parallel versions resulted in relative increased computational time comparing with the serial version.

The solution algorithm for the mathematical model (three-field formulation) is as follows:

1. Read all input data: tube length, internal diameter, simulation time, time step, grid size and boundary conditions;

2. Set fields of p, α_g, α_f, u_c, u_f, s_g, s_e and s_f to initial (fictitious) values based on the boundary conditions and the gravitational pressure drop;

3. Calculate the inlet boundary conditions in terms of native variables using the appropriate closure relationship';

4. Calculate all the closure/source variables, such as friction factors and mass exchange through droplet entrainment and deposition (for the three-field model);

5. Based on the latest fields of p, s_g, s_e and s_f, calculate the thermo-dynamic properties of each field in each node. This is performed using the lookup table interpolation scheme established from the state functions and physical properties subroutines available in the FORTRAN source code of the REFPROP 8.0 package (LEM-MON *et al.*, 2007) as described in Apendix A;

6. Calculate the coefficients of the matrix **A** and source vector $\vec{B}$;

7. Solve the system of equations given by Eq. (4.43) using the PAR-DISO algorithm to obtain new values of p, α_g, α_e, α_f, s_g, s_e and s_f;

8. If the following convergence criterion is not met, return to stage 3. The convergence criterion was established based on the nor-malized difference $\left| \left(\vec{U}^I - \vec{U}^{I-1} / \vec{U}^I \right) \right|$ between the values of each variable at two successive iterations, admitting a maximum vari-ation of 10^{-6}, where 'I' is the current iteration;

9. Once convergence is attained, time is advanced and the solution procedure is restarted at stage 3 for a new time step;

10. Once steady-state is observed, the simulation can be either in-terrupted or the boundary conditions changed and the transient behavior tracked for the establishment of a new steady-state con-dition.

Results for all the main simulation and two-phase flow parameters are printed for regular time step intervals determined during the setup of any given simulation.

4.4 Grid and Time Step Refinement Analysis

The quality of the numerical solution of the mathematical model is exemplified using a single transient numerical experiment. This experiment is used to evaluate specific aspects of the numerical solution, such as grid refinement and influence of the size of the time step.

Table 4.1 shows the initial boundary conditions that are feed into the program. The simulation is performed in a 50.0 mm ID, 40-m long vertical tube. At steady state, these conditions are expected to result in annular flow along the entire tube. The transient behavior is triggered by a linear decrease of the inlet gas mass flux between 20 and 30 s into the simulation, when this parameter reaches 40.0 kg m^{-2} s^{-1}. At this point, the mass flux stops decreasing and stays constant until 100.0 s, when the simulation is ended. The gas mass flux boundary condition scenario is expected to trigger a transition from annular to churn flow at some point along the mass flux transient, and the steady-state flow pattern associated with the final condition is expected to be churn flow.

Table 4.1 – Initial boundary conditions for grid refinement analysis.

Inlet gas mass flux [kgm^{-2}s^{-1}]	90.0
Inlet liquid mass flux [kgm^{-2}s^{-1}]	40.0
Inlet liquid entrained fraction [%]	0.0001
Outlet pressure [kPa]	300.0
All inlet temperatures [K]	300.0

Simulations were performed with four different grid refinements (Δz = 0.1, 0.2, 0.5 and 2.0 m) and two time step values (Δt = 1.0, and 20.0 ms). The cases were evaluated with respect to a reference case solved with a Δz = 0.01 m, Δt = 0.1 ms grid. The quantitative parameter used in the evaluation — the combined RMS error — is defined as the sum of individual values of the RMS error for the pressure p, void fraction α, and dimensionless superficial gas velocity, u_{gS}^*. The individual RMS error, in turn, is defined as,

$$\text{RMS} = \frac{1}{N}\sqrt{\sum_{i=1}^{N}\left(\frac{test_i - ref_i}{ref_i}\right)^2} \qquad (4.44)$$

where ref_i is the value of the calculated parameter using the reference grid, while $test_i$ is the value of the calculated parameter using

the coarser (spatial/temporal) grids. N is the number of individual values compared. The comparison starts from 15 s which is 5 s before the boundary condition starts to change and the annular flow was already developed. In the present analysis, four different positions were evaluated, $z = 0$, 13.3, 20.0 and 26.7 m.

Figure 4.1 shows the combined RMS associated with the numerical simulation as a function of the spatial and temporal grid refinements. As can be seen, the combined RMS tends to a constant value as the size of the spatial grid is reduced, demonstrating the consistency of the numerical algorithm based on the finite difference scheme (MALISKA, 2004; SHARMA, 2010). For the time transient used in the example, which is characteristic of those performed experimentally by Waltrich (2012), the time step size is much less influential on the value of the combined RMS.
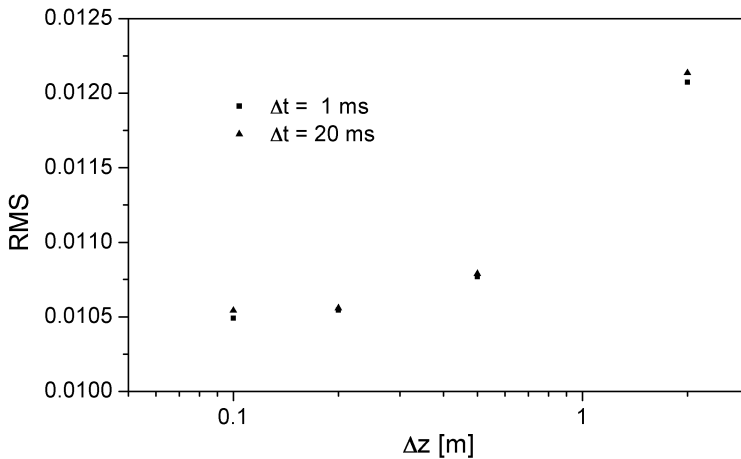
Figure 4.1 – Combined RMS error comparison as a function of the grid refinement.

Tables 4.2 to 4.4 show the specific results for the interest variables, wich are: the pressure difference between the inlet and the outlet of the pipe; the gas and liquid velocities at the outlet section; and, the gas and liquid volumetric fractions at the outlet section. More specifically Table 4.2 shows the last time step before the transient in the inlet gas mass flux was triggered. It is easy to see that the time step value has little effect on the variables, and as the grid size is reduced the value

Table 4.2 – Comparison of important variables for grid and time step refinement analysis for annular flow pattern.

Δz [m]	0.1	0.2	0.5	1.0	2.0
Δp(1 ms) [kPa]	46.5	46.5	46.2	45.7	44.8
Δp(10 ms) [kPa]	46.5	46.5	46.2	45.8	45.0
Δp(20 ms) [kPa]	46.5	46.5	46.2	45.8	45.1
$u_{g_{out}}$(1 ms) [m s^{-1}]	25.98	25.93	25.78	25.57	25.20
$u_{g_{out}}$(10 ms) [m s^{-1}]	25.98	25.92	25.74	25.47	25.01
$u_{g_{out}}$(20 ms) [m s^{-1}]	25.98	25.92	25.74	25.46	25.46
$u_{l_{out}}$(1 ms) [m s^{-1}]	1.20	1.20	1.20	1.19	1.18
$u_{l_{out}}$(10 ms) [m s^{-1}]	1.20	1.20	1.20	1.19	1.17
$u_{l_{out}}$(20 ms) [m s^{-1}]	1.20	1.20	1.20	1.19	1.17
$\alpha_{g_{out}}$(1 ms) [-]	0.9824	0.9824	0.9823	0.9822	0.9822
$\alpha_{g_{out}}$(10 ms) [-]	0.9824	0.9824	0.9823	0.9822	0.9819
$\alpha_{g_{out}}$(20 ms) [-]	0.9824	0.9824	0.9823	0.9822	0.9819
$\alpha_{l_{out}}$(1 ms) [-]	0.0168	0.0169	0.0169	0.0171	0.0173
$\alpha_{l_{out}}$(10 ms) [-]	0.0168	0.0168	0.0170	0.0171	0.0173
$\alpha_{l_{out}}$(20 ms) [-]	0.0168	0.0168	0.0169	0.0171	0.0173

Table 4.3 – Comparison of important variables for grid and time step refinement analysis for churn flow pattern.

Δz [m]	0.1	0.2	0.5	1.0	2.0
Δp(1 ms) [kPa]	36.6	37.3	38.9	40.5	37.1
Δp(10 ms) [kPa]	36.7	37.3	38.9	40.6	36.9
Δp(20 ms) [kPa]	36.7	37.3	39.0	40.7	36.8
$u_{g_{out}}$(1 ms) [m s^{-1}]	8.87	8.99	8.93	8.78	7.80
$u_{g_{out}}$(10 ms) [m s^{-1}]	8.94	8.97	8.89	8.67	7.90
$u_{g_{out}}$(20 ms) [m s^{-1}]	9.02	8.97	8.88	8.66	7.90
$u_{l_{out}}$(1 ms) [m s^{-1}]	0.463	0.464	0.481	0.486	0.450
$u_{l_{out}}$(10 ms) [m s^{-1}]	0.468	0.466	0.479	0.482	0.450
$u_{l_{out}}$(20 ms) [m s^{-1}]	0.468	0.464	0.478	0.478	0.450
$\alpha_{g_{out}}$(1 ms) [-]	0.9374	0.9202	0.9133	0.9091	0.94
$\alpha_{g_{out}}$(10 ms) [-]	0.9289	0.9201	0.9133	0.9091	0.94
$\alpha_{g_{out}}$(20 ms) [-]	0.9206	0.9202	0.9133	0.9091	0.94
$\alpha_{l_{out}}$(1 ms) [-]	0.0178	0.0178	0.0179	0.0181	0.06
$\alpha_{l_{out}}$(10 ms) [-]	0.0178	0.0178	0.0180	0.0181	0.06
$\alpha_{l_{out}}$(20 ms) [-]	0.0178	0.0178	0.0179	0.0181	0.06

Table 4.4 – Values of important variables for reference grid and time
step for churn and annular flow patterns.

Flow Pattern	Annular	Churn
Δp [kPa]	46.6	36.7
$u_{g_{out}}(1 \text{ ms})$ [m s^{-1}]	26.03	8.87
$u_{l_{out}}(1 \text{ ms})$ [m s^{-1}]	1.20	0.462
$\alpha_{g_{out}}(1 \text{ ms})$ [-]	0.9824	0.937
$\alpha_{l_{out}}(1 \text{ ms})$ [-]	0.0168	0.0179

of each observed variable tends to stability. The so called reference
simulation (Table 4.4) presents a much more refined grid size and time
step. Table 4.3 shows the values for the same variables for the last
time step simulated once again the time step has little effect on the
variables, while as the grid size diminishes the values tend to stability,
reaching the same values as the reference simulation shown in Table
4.4. This leads to the conclusion that the numerical code is consistent,
stable and convergent. This is reinforced by the results obtained earlier
by Gessner (2010) with the homogeneous and single-phase versions of
the same algorithm which were able to reproduce analytical solutions
of the shock tube problem as presented by Städtke (2006).

5   RESULTS

This chapter presents the main results of this work, via an extensive comparison between the numerical model predictions and experimental data obtained from the literature, covering wide ranges of liquid and gas mass fluxes, pipe lengths and diameters. The first section presents a validation of the model under steady-state conditions, which represent the largest proportion of the available data. The second section presents results of transient simulations of the churn-annular transition and compares them with the experimental data of Waltrich (2012). The third section presents hypothetical simulations to evaluate the prediction capabilities of the numerical method. Through these simulations, the boundary conditions discussed in Section 3.4 can be isolated and their influence on the flow can be studied separately.

The steady-state comparison includes data for the main parameters, such as pressure gradient, gas volumetric fraction (void fraction), liquid mass flux and entrained liquid fraction. The experimental data of Wolf *et al.* (2001), because they give a rather complete description of annular flow development in terms of local parameters, were compared with the numerical model using three different correlations for the interfacial friction factor for annular flow (WALLIS, 1969; WHALLEY; HEWITT, 1978; BELT *et al.*, 2009). As it will be seen, the best results were obtained with the Whalley and Hewitt (1978) correlation and, for this reason, this correlation was chosen for the comparison with the other annular flow databases. The Jayanti and Brauner (1994) interfacial friction relationship was used for all the churn flow model simulations.

The comparison with the transient experimental data of Waltrich (2012) comprises two different test procedures: the first set analyses the response to a change in outlet pressure generated by closing the outlet choke valve; the second set analyses the system response to a change in the mass flux of gas, liquid or both. Time-dependent boundary conditions derived from the experimental data are used as input

parameters in the model.

According to the grid sensitivity analysis performed in Section 4.4 a grid size of $\Delta z = 0.2$ m was considered sufficiently accurate for the conditions of Waltrich (2012). However, to accomodate the shorter test sections without needing a variable grid size, $\Delta z = 0.01$ m was used in all analyses, which also facilitated the comparison with the data at specified positions along the test sections. For the time step, $\Delta t = 1$ ms was used for all transient and steady-state simulations unless indicated otherwise.

Due to the considerable amount of simulations that had to be done the computer code was run in a Supercomputing facility at the National Centre of High Performance Computing (CENAPAD) at the State University of Campinas, SP. The machine used was a SGI Altix ICE 8400 LX cluster with 32 nodes, accounting for a total of 384 3.33GHz Intel Xeon 5680 processing cores, and 1152 GB of RAM memory, with a theoretical performance of 5 TFlops. The processing cores were arranged into several processing queues, containing from 1 to 128 processors. The simulations were performed using a queue with 12 processors (single node) and 12 simulations could be scheduled at any given time (4 running and 8 waiting execution). The performance gains from single core up to 12 cores were linear, meaning that the same simulation running in single core would take 12 times as much time to run as if it was run in 12 cores. More than 12 cores would implicate in using more than a single node, and so using the network messaging signals which are much slower than the signalling inside the node, and performance would became compromised.

All comparisons are made in terms of three statistical parameters as follows: the Absolute Average Deviation (AAD), the Root Mean Squared (RMS) error and the systematic error (Bias), which are defined respectively by the following expressions.

$$\text{AAD} = \frac{1}{n}\sum_{i=1}^{n}\left|\frac{cal_i - exp_i}{exp_i}\right| \tag{5.1}$$

$$\text{RMS} = \frac{1}{n}\sqrt{\sum_{i=1}^{n}\left(\frac{cal_i - exp_i}{exp_i}\right)^2} \tag{5.2}$$

$$\text{Bias} = \frac{1}{n}\sum_{i=1}^{n}\left(\frac{cal_i - exp_i}{exp_i}\right) \tag{5.3}$$

where exp_i is the value of the experimental variable, while cal_i is the

value of the calculated variable. n is the number of data points. The percentage of data points that fall inside a specified deviation range is also presented.

5.1 COMPARISON WITH STEADY-STATE DATA

This section evaluates the ability of the model in predicting the steady-state experimental data. All the facilities are described in Section 2.3. All film thickness and liquid holdup data were converted to homogeneous core volumetric fraction (core fraction) and to gas volumetric fraction (void fraction), respectively, wherever applicable (except indicated otherwise). The inlet droplet entrained fraction was considered to be 0.01% for all simulations. This is because the injection of liquid in the test facilities was mostly through porous inserts at the pipe walls or through means that facilitate the development of annular flow.

5.1.1   Wolf *et al.* (2001) data

Figure 5.1 – Comparison of numerical and experimental core fraction using Wolf *et al.* (2001) test conditions.

Figure 5.2 – Comparison of numerical and experimental liquid film mass flux using Wolf *et al.* (2001) test conditions.
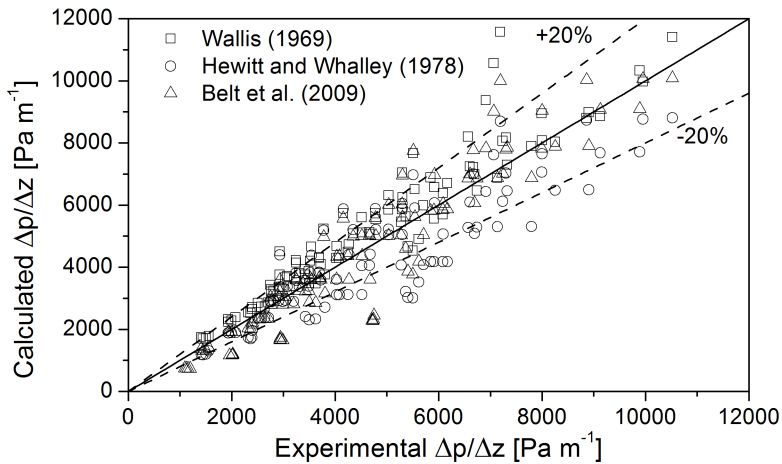
Figure 5.3 – Comparison of numerical and experimental pressure gradient using Wolf *et al.* (2001) test conditions.

Figures 5.1 to 5.3 show the predictions of all simulated conditions of Wolf *et al.* (2001) data set using the three interfacial friction factor correlations presented in Section 3.3.2. The prediction of the experimental data can be considered satisfactory for the three expressions tested, as most of the results lie within $\pm20\%$ deviation from the experimental data. All three correlations of the interfacial friction factor presented nearly equivalent results, with the Whalley and Hewitt (1978) correlation presenting better numerical stability, less iterations per time step, and, thus, lower computational cost. Table 5.1 shows a comparison of the statistical parameters for the three main variables: pressure gradient (dp/dz); core fraction (α_c) and liquid film flux (G_f). The last column shows the computational time needed to run 10 random steady-state simulations from the database conditions.

Table 5.1 – Comparison of interfacial friction factor correlations used

Correlation		AAD (%)	RMS (%)	Bias (%)	Time (s)
Wallis (1969)	dp/dz	14.53	1.898	12.917	613
	α_c	18.99	2.115	-18.995	
	G_f	0.743	0.075	0.735	
Whalley and Hewitt (1978)	dp/dz	14.89	1.949	-5.801	548
	α_c	18.93	2.016	-18.932	
	G_f	0.521	0.052	0.735	
Belt *et al* (2009)	dp/dz	16.51	2.082	-8.188	623
	α_c	20.28	2.223	-20.28	
	G_f	0.728	0.069	0.696	

The Wallis (1969) correlation resulted in 80.2% of the points falling inside the $\pm20.0\%$ band for the pressure gradient, 73.8% of the points within the $\pm1.0\%$ band for the core fraction and 57.3% of the points within the $\pm20.0\%$ band for the film mass flux. The Whalley and Hewitt (1978) resulted in 75.0% of the points falling inside the $\pm20.0\%$ band for the pressure gradient, 86.7% of the points within the $\pm1.0\%$ band for the core fraction, and, 53.6% of the points within the $\pm20.0\%$ band for the film mass flux. The Belt *et al.* (2009) correlation resulted in 62.5% of the points falling inside the $\pm20.0\%$ band for the pressure gradient, 75.6% of the points within the $\pm1.0\%$ band for the core fraction, and, 43.8% of the points within the $\pm20.0\%$ band for the film mass flux.

Figures 5.4 to 5.6 present a comparison of the experimental and numerical axial profiles for three parameters, namely: core fraction, liquid film mass flux, and pressure. This comparison was generated using

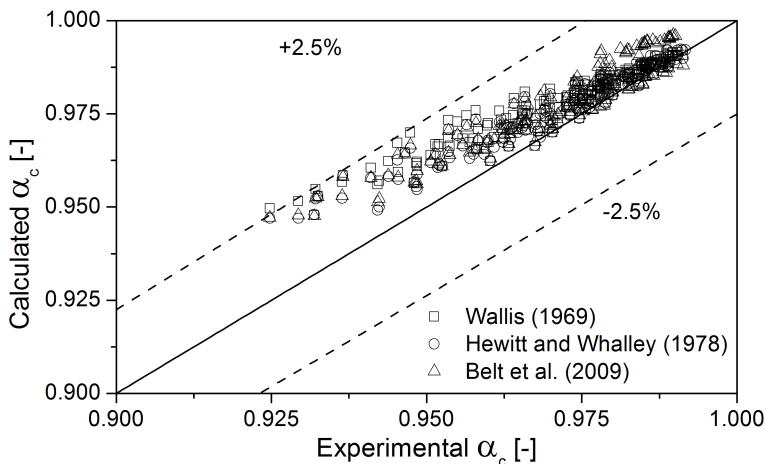the Whalley and Hewitt (1978) interfacial friction factor correlation.

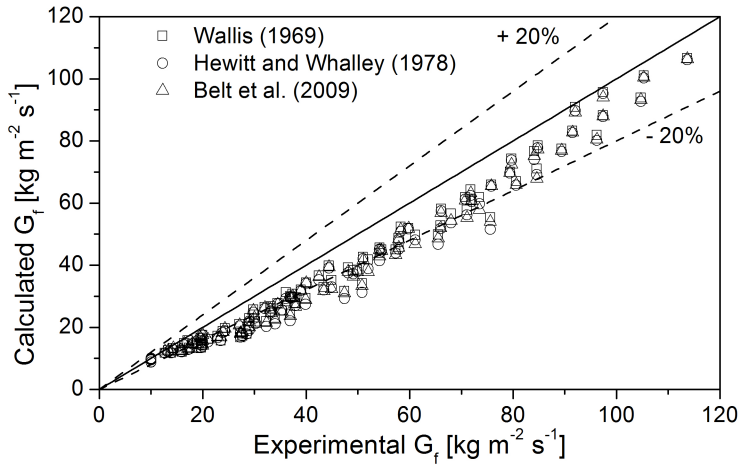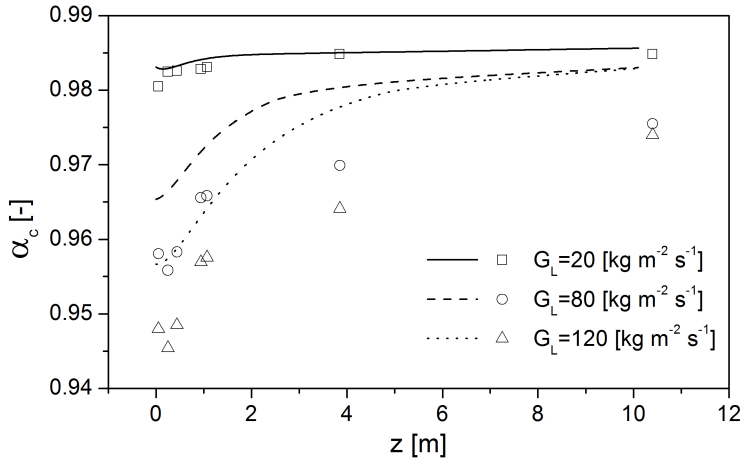Figure 5.4 – Comparison of numerical and experimental core fraction profile using the Wolf *et al.* (2001) data.
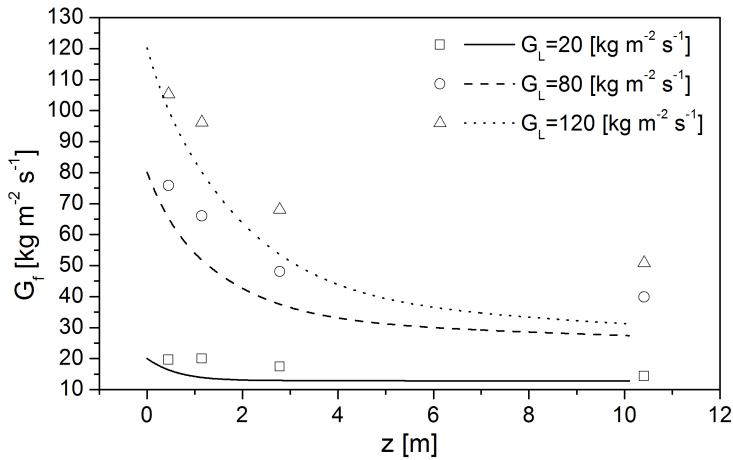
Figure 5.5 – Comparison of numerical and experimental liquid film flux profile using the Wolf *et al.* (2001) data.
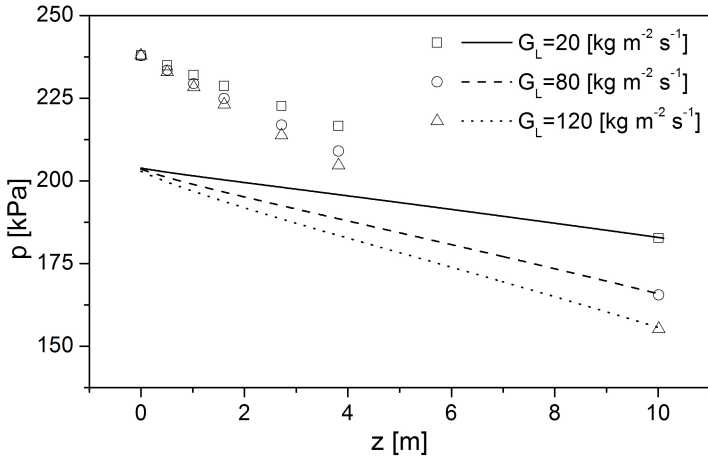
Figure 5.6 – Comparison of numerical and experimental absolute pressure profile using the Wolf *et al.* (2001) data.

Figure 5.4 shows that the model captures the increase in the core fraction with distance from the inlet due to the liquid phase redistribution in the channel. Analogous conclusions can be drawn for the liquid film flux (5.5), whose decrease with distance from a condition of near zero entrained fraction to a condition of hydrodynamic equilibrium (equal rates of droplet entrainment and deposition) is well predicted by the numerical model.

The discrepancies between model and data in Fig. 5.6 can be explained by the fact that the numerical model requires the outlet pressure to be kept fixed, while the inlet pressure is a model output. In the experiments, however, the inlet pressure was controlled, as can be seen from the figure. This difference in approaches generated a discrepancy between the experimental and calculated inlet densities, and so the pressure profile was shifted to the lower values.

5.1.2   Owen (1986) data

Figure 5.7 presents a comparison of the calculated and experimental pressure gradients using the data of Owen (1986). Despite the observed scatter almost 72.0% of the data lie within ±20% deviation, with values of AAD, RMS and Bias equal to 17.9%, 1.15%, and 6.77%, respectively. As it will be seen, the data are more or less equally well
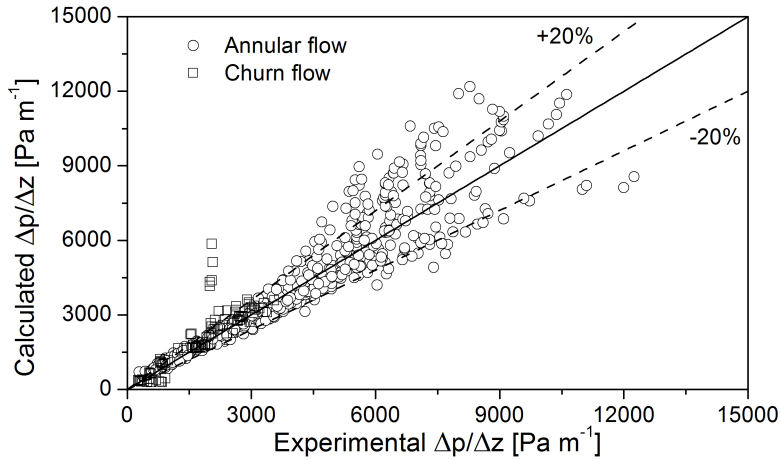
Figure 5.7 – Comparison of numerical and experimental pressure gradient using Owen (1986) data.

Figure 5.8 – Comparison of numerical results and experimental pressure gradient data of Owen (1986) for a nominal outlet pressure of 240 kPa.

predicted in both the annular and churn flow regimes, but large deviations occur for higher values of gas superficial velocity, where the annular flow regime is completely established. The data points below the -20% trend line correspond to high gas mass fluxes with liquid mass fluxes that allowed for the occurrence of wisps in the gas core, as described by Owen (1986) and more recently by Azzopardi (2012). The set of data above +20% trend line (at an experimental pressure gradient of around 2 kPa m^{-1}) correspond to very low gas mass fluxes (typically 1 to 50 kg m^{-2}s^{-1}), near the transition to slug flow.
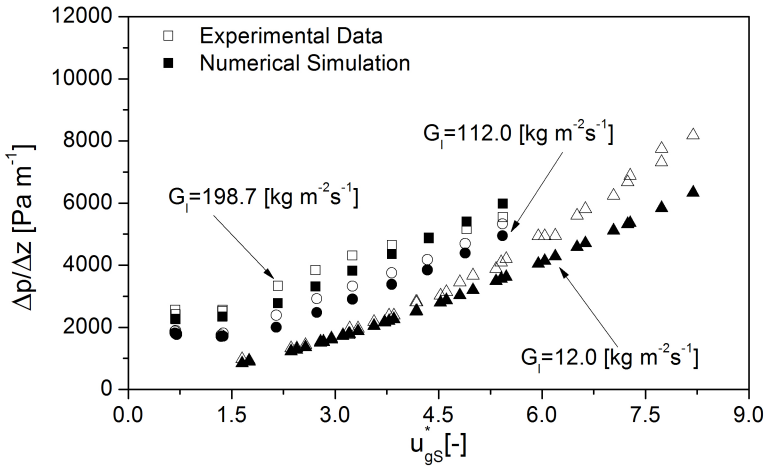
Figure 5.9 – Comparison of numerical results and experimental pressure gradient data of Owen (1986) for a nominal outlet pressure of 370 kPa.

Figure 5.8 shows results of two test conditions with an outlet pressure of 240 kPa. The agreement between the numerical model and the data is good for values of u_{gS}^* below and above unity (churn and annular flows). At this comparatively low value of test section pressure, the minimum pressure gradient occurs at $u_{gS}^* \approx 1.0$. On the other hand, at the higher outlet pressure of 370 kPa (nominal), the minimum pressure gradient is shifted toward higher values of u_{gS}^* (Fig. 5.9), but the agreement with the numerical model remains satisfactory, especially for the lower values of u_{gS}^*.

Figures 5.10 to 5.12 show comparisons between the numerical model and the experimental data of Owen (1986) for the liquid film thickness. Figure 5.10 shows the overall comparison between the dataset and the

model. The comparison is reasonably good and 65% of the data points lies in the $\pm20.0\%$ range, with values of AAD, RMS and Bias equal to 24.0%, 2.41%, and 16.5%, respectively.
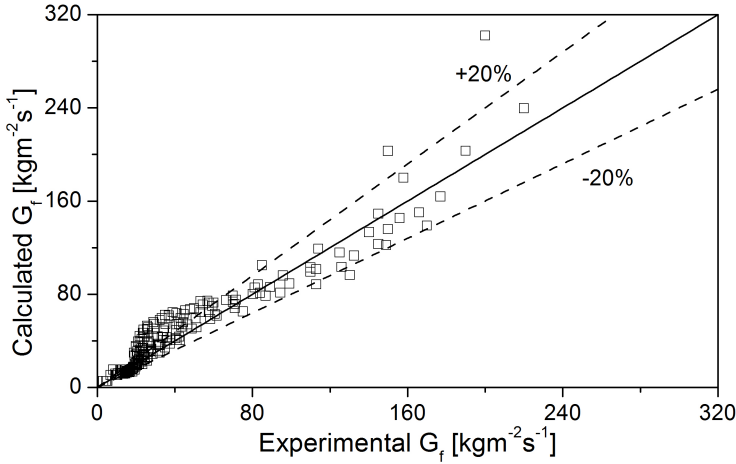
Figure 5.10 – Comparison of numerical results and experimental liquid film mass flux using Owen (1986) data.

Figures 5.11 and 5.12 show film mass flux results for different test conditions with outlet pressures of 240 kPa and 370 kPa (nominal) as function of u_{gS}^*. The conditions are similar to those presented in the pressure gradient comparison. Although some minor discrepancies arise at higher velocities (especially for the higher inlet liquid mass fluxes) the agreement is mostly good.

The comparison between the numerical model and this set of experimental data resulted in 71.7% of the points falling inside the $\pm20.0\%$ range for the pressure gradient and 65.1% of the points within the $\pm20.0\%$ range for the film mass flux.
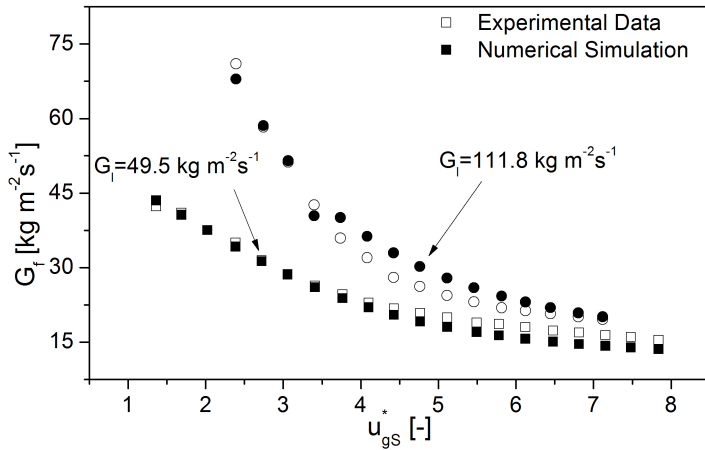
Figure 5.11 – Comparison of numerical results and experimental liquid film mass flux data of Owen (1986) for a nominal outlet pressure of 240 kPa.
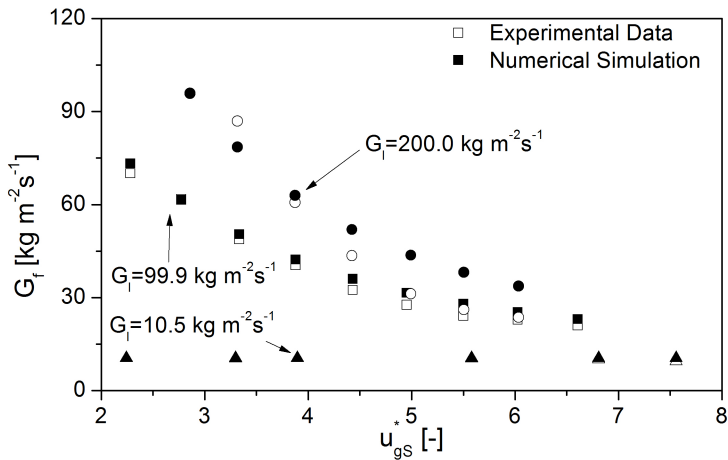
Figure 5.12 – Comparison of numerical results and experimental liquid film mass flux data of Owen (1986) for a nominal outlet pressure of 370 kPa.

5.1.3   Govan *et al.* (1991) data

Figures 5.13 and 5.14 show the overall comparison of pressure gradient and void fraction for the Govan *et al.* (1991) test conditions, respectively. Although, some discrepancies exist, most of the pressure gradient data stay in the $\pm 20\%$ range and the totality of the void fraction prediction lie within the $\pm 10\%$ margin, which can be considered a good prediction of the data. The model predicts the pressure gradient data with AAD=14.4%, RMS=2.82% and Bias= 9.90%, while the void fraction data is predicted with AAD=3.17%, RMS=0.51% and Bias=3.11%.
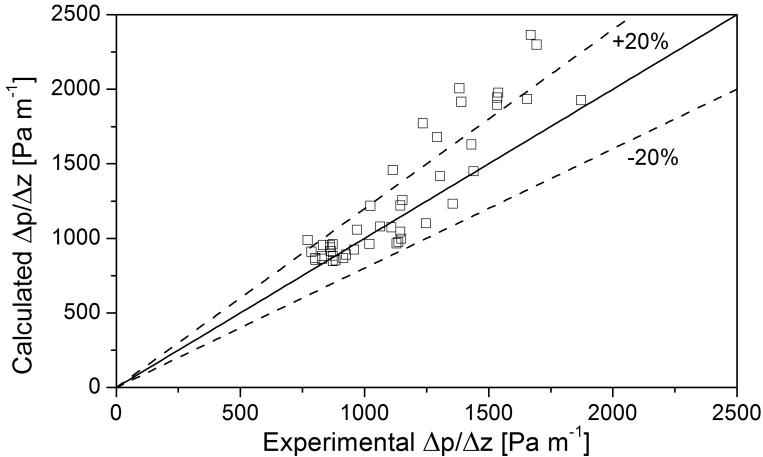
Figure 5.13 – Comparison of numerical results and experimental pressure gradient data of Govan *et al.* (1991).

Figures 5.15 to 5.17 show the model predictions of the churn-annular region for different flow conditions. A generally good agreement is observed, apart from the low u_{gS}^* region (< 0.6), which was predicted using a two-field formulation. These discrepancies can be explained by the fact that the two-field model does not account for the transport of droplets, which in turn results in a higher void fraction (thinner liquid film) and thus higher pressure gradient. As can be seen, the minimum pressure gradient occurs at the vicinity of $u_{gS}^* = 1.0$.

A comparison between the numerical model and the void fraction data of Govan *et al.* (1991) is presented in Figs. 5.18 to 5.20. The
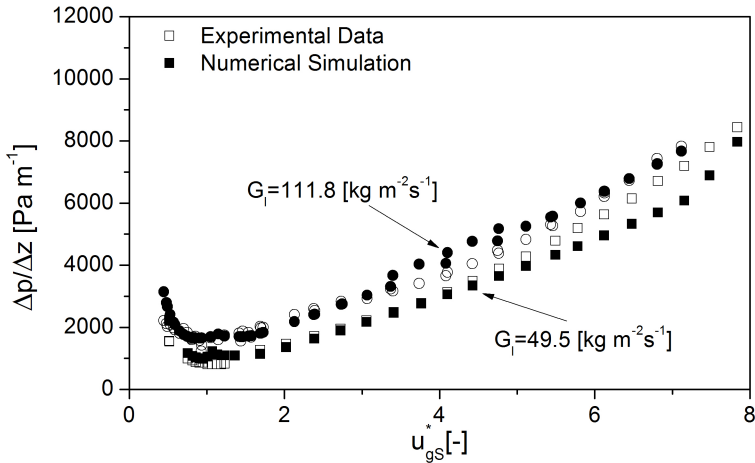
Figure 5.14 – Comparison of numerical results and experimental void fraction data of Govan *et al.* (1991).
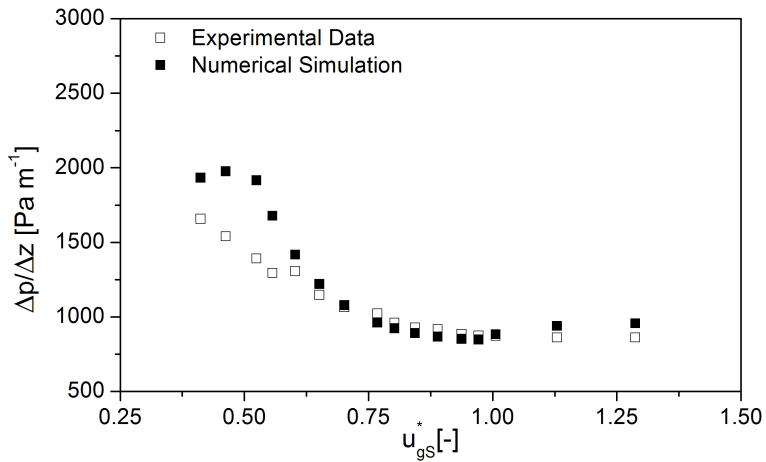
Figure 5.15 – Comparison of numerical results and experimental pressure gradient data of Govan *et al.* (1991) for $G_l = 38.1$ kgm^{-2}s^{-1} and $l = 2.80$ m.
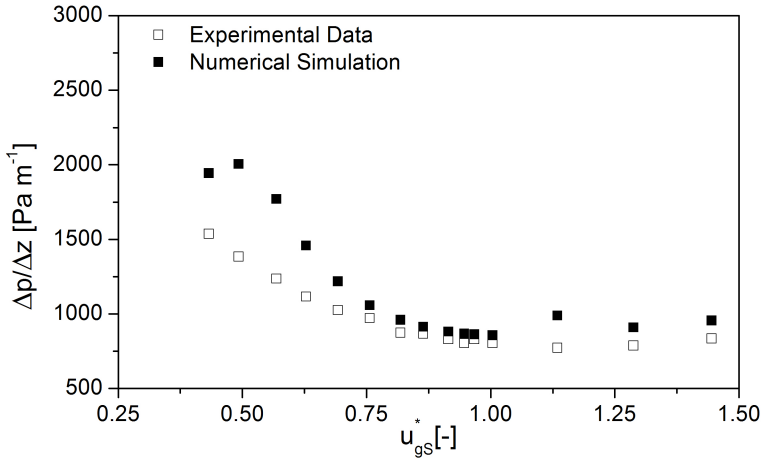
Figure 5.16 – Comparison of numerical results and experimental pressure gradient data of Govan *et al.* (1991) for $G_l = 38.1$ kgm^{-2}s^{-1} and $l = 1.71$ m.
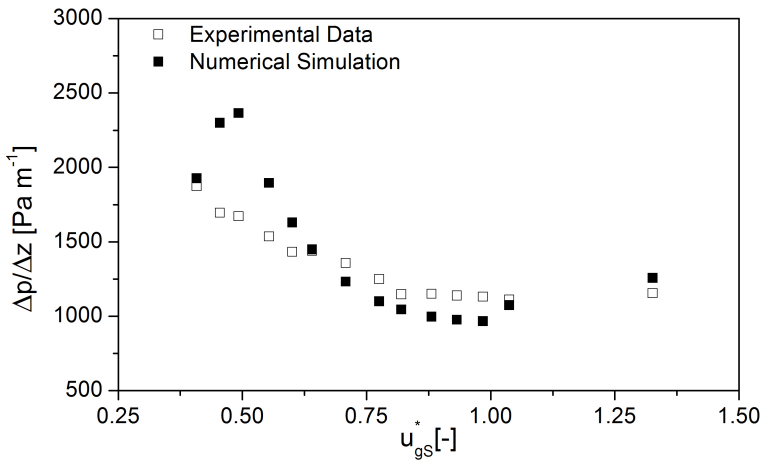
Figure 5.17 – Comparison of numerical results and experimental pressure gradient data of Govan *et al.* (1991) for $G_l = 47.1$ kgm^{-2}s^{-1} and $l = 1.71$ m.

agreement can be considered satisfactory, with the greatest discrepancies around $u_{gS}^* = 0.95$.
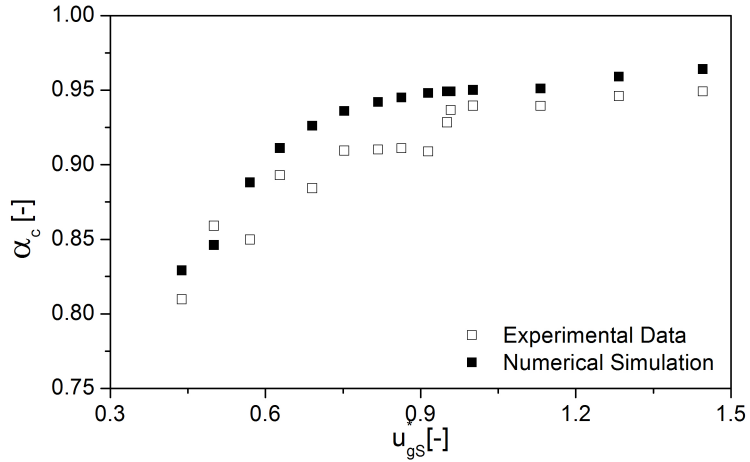
Figure 5.18 – Comparison of numerical results and experimental void fraction data of Govan *et al.* (1991) for $G_l = 38.1$ kgm^{-2}s^{-1} and $l = 2.80$ m.

The comparison between the numerical model and this set of experimental data resulted in 75.6% of the points falling inside the $\pm 20.0\%$ range for the pressure gradient, and, 84.5% of the points stay within the $\pm 1.0\%$ range for the void fraction.
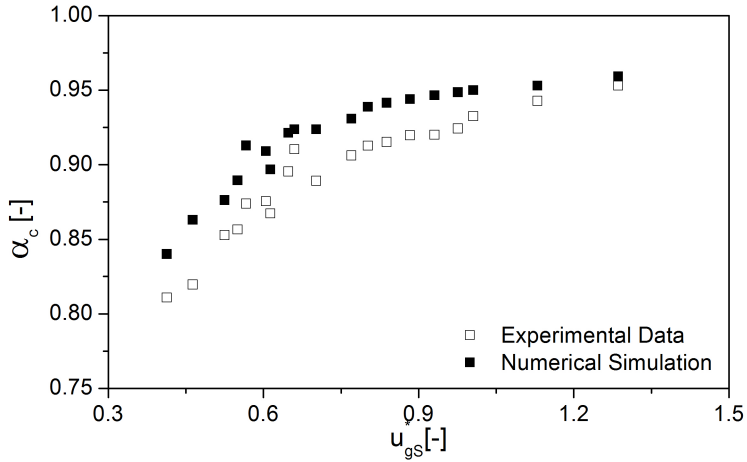
Figure 5.19 – Comparison of numerical results and experimental void fraction data of Govan *et al.* (1991) for $G_l = 38.1$ kgm^{-2}s^{-1} and $l = 1.71$ m.
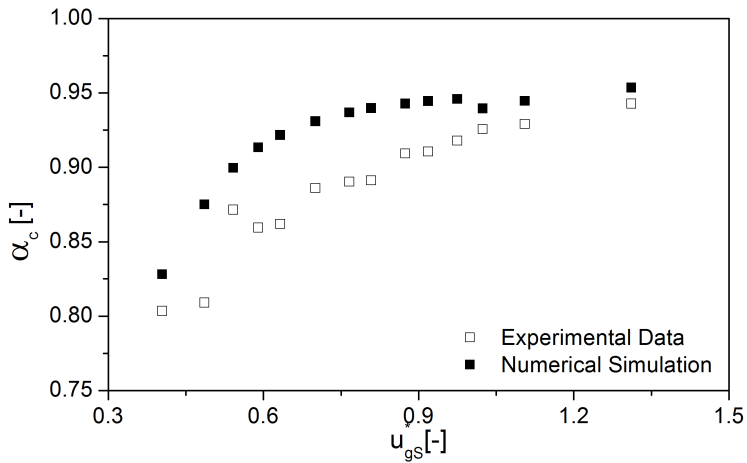
Figure 5.20 – Comparison of numerical results and experimental void fraction data of Govan *et al.* (1991) for $G_l = 47.1$ kgm^{-2}s^{-1} and $l = 1.71$ m.

5.1.4 Costigan (1997) data

In this section the model is compared against the experimental work of Costigan (1997). According to the author's visual observations most points in this dataset lie in the churn flow region close to the transition to slug flow, the numerical prediction however, have detected a few in annular flow points.
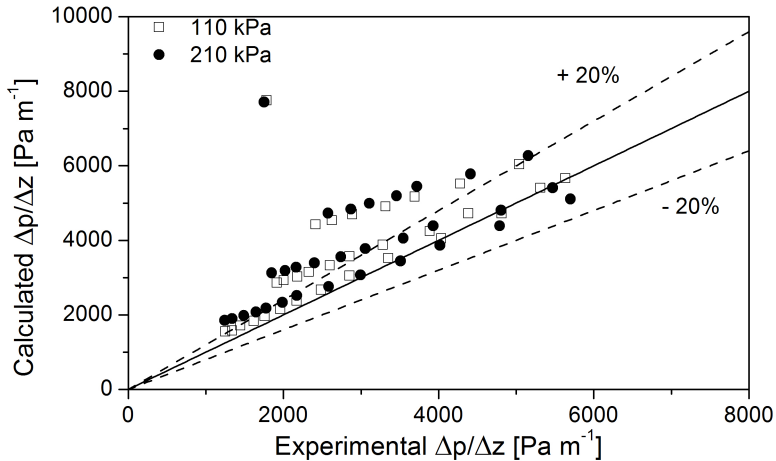
Figure 5.21 – Comparison of numerical results and experimental pressure gradient data of Costigan (1997).

Figure 5.21 shows the overall comparison of the pressure gradient for the two outlet pressure conditions. The somewhat poorer agreement can be explained by the much lower gas velocities employed by Costigan (1997), which resulted in flow conditions closer to slug flow. The mathematical model presented some convergence issues at conditions near the transition to slug flow. The pressure gradient data were predicted with AAD=34.3%, RMS=12.0% and Bias=34.2% for an outlet pressure of 110 kPa and AAD=40.1%, RMS=12.9% and Bias=38.5% for an outlet pressure of 210 kPa.

Figures 5.22 and 5.23 show comparisons of void fraction at two different locations. As can be seen, some points fall outside the $\pm 20\%$ range indicated by the lines. This reflects the application of the model at conditions of gas and liquid mass flow rates closer to the transition to slug flow as indicated by visual observations (COSTIGAN, 1997). The
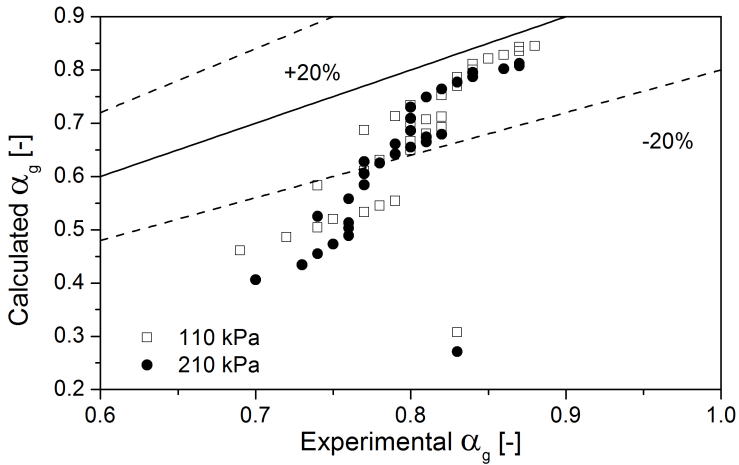
Figure 5.22 – Comparison of numerical results and experimental void fraction data of Costigan (1997) at $z = 5.08$ m.
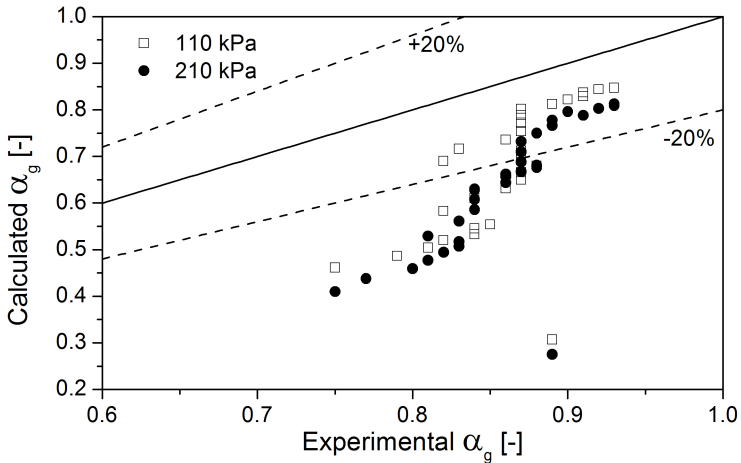
Figure 5.23 – Comparison of numerical results and experimental void fraction data of Costigan (1997) at $z = 5.858$ m.

void fraction data at z =5.08 m were predicted with AAD=16.9%, RMS=3.85% and Bias=-16.9% for the outlet pressure of 210 kPa and AAD=21.3%, RMS=4.58% and Bias=-21.3% for the outlet pressure of 110 kPa. The void fraction for z =5.858 m was predicted with AAD=22.3%, RMS=4.66% and Bias=-22.3% for the outlet pressure of 110 kPa and AAD=26.9%, RMS=5.37% and Bias=-26.9% for the outlet pressure of 210 kPa.

The comparison between the numerical model and this set of experimental data resulted in 54.8% of the points falling inside the ±20.0% range for the pressure gradient and 41.9% of the points stay within the ±20.0% range for the void fraction.

5.1.5   Belt *et al.* (2009) data

Figures 5.24 and 5.25 present a comparison of the numerical model with the experimental results of Belt *et al.* (2009) for annular and churn flows. As can be seen, both flow patterns are equally well described by the model, as far as the pressure gradient behavior is concerned. Figure 5.25 demonstrates the good capability of the model in predicting the experimental core fraction (film thickness). It should be mentioned that Belt *et al.* (2009) did not present film thickness data for the churn flow pattern. Therefore, the core fraction predictions of their data cover only the annular flow pattern. The numerical model predicted this database with AAD=0.40%, RMS=0.11% and Bias=0.19% for the core fraction, AAD=8.33%, RMS=1.44% and Bias=-0.50% for pressure gradient in annular flow and AAD=18.43%, RMS=9.15% and Bias=-1.15% for pressure gradient in churn flow.

Figure 5.26 shows the pressure gradient data prediction in the churn-annular flow transition region. The numerical model captures the minimum pressure gradient region with reasonable accuracy, although it is important to mention that for the Belt *et al.* (2009) experiments this did not correspond to the $u_{gS}^* = 1.0$ condition. The discontinuity in the numerical curve at approximately $u_{gS}^* = 0.7$ for the higher liquid superficial velocity, and approximately $u_{gS}^* = 0.9$ for the lower one can be explained by the transition from a three-field formulation to a two-field one. Although this has no physical justification, it allowed the program to be used under conditions nearer to the transition to slug flow.

Figure 5.27 shows the behavior of the annular flow core fraction as function of u_{gS}^* for three liquid superficial velocities. Although, the data are only for annular flow condition (as observed by the authors), the
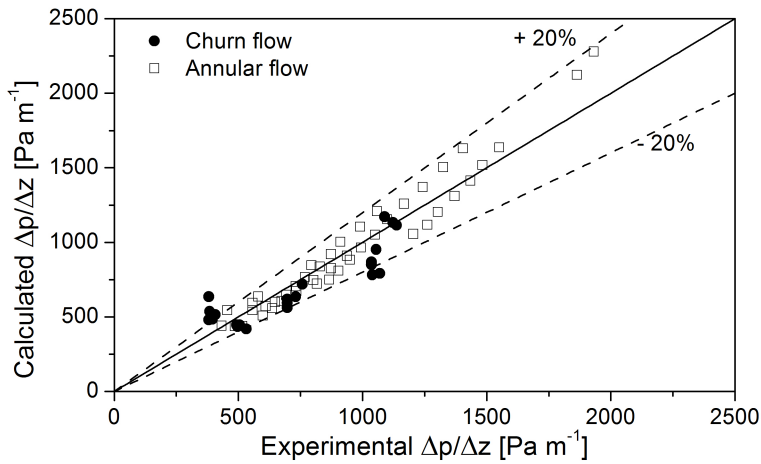
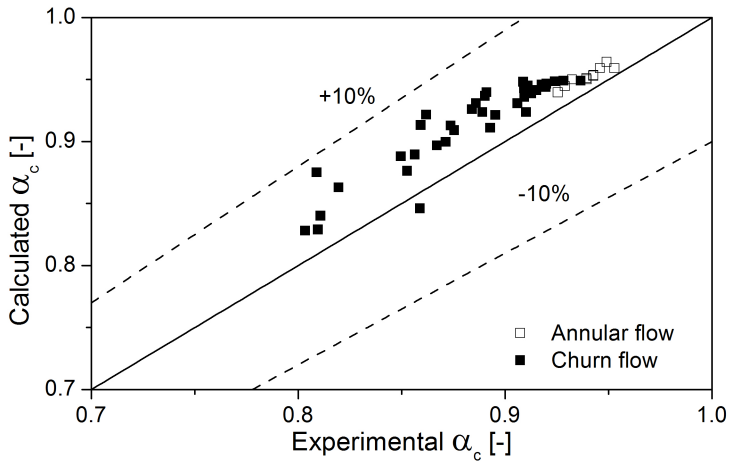Figure 5.24 – Comparison of numerical results and experimental pressure gradient data of Belt *et al.* (2009).

Figure 5.25 – Comparison of numerical results and experimental core fraction data of Belt *et al.* (2009).
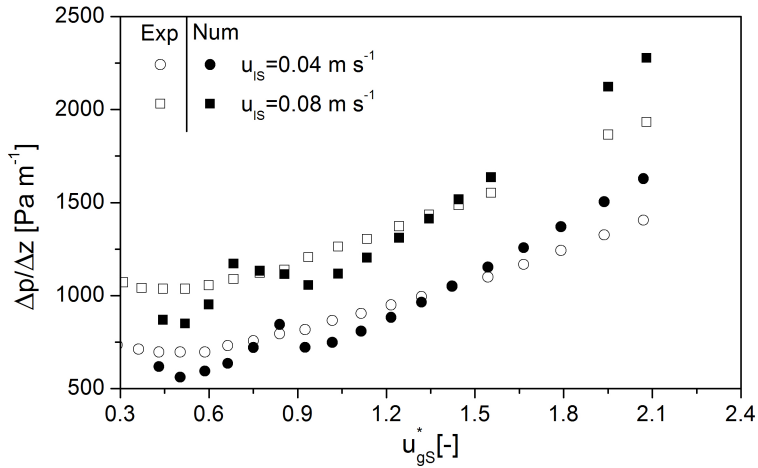
Figure 5.26 – Comparison of numerical results and experimental pressure gradient as function of u_{gS}^* using Belt *et al.* (2009).

Figure 5.27 – Comparison of numerical results and experimental core fraction as function of u_{gS}^* using Belt *et al.* (2009).

present model has predicted the occurrence of churn flow for $u_{gS}^* \approx 0.9$.
The agreement with the data is satisfactory for all conditions. The
comparison between the numerical model and this set of experimental
data resulted in 88.1% of the points falling inside the $\pm 20.0\%$ range for
the pressure gradient and 80.0% range of the points within the $\pm 1.0\%$
for the core fraction.

5.1.6 Alamu and Azzopardi (2011) data

Figure 5.28 shows a comparison of the calculated pressure gradi-
ent with the annular flow experimental data of Alamu and Azzopardi
(2011). The largest deviations are possibly due to an influence of the
pipe diameter, which is smaller than those for which the model clo-
sure relationships (friction factor and droplet interchange) have been
derived. Nevertheless, the core fraction and the film mass flux were
predicted with reasonable accuracy (Figs. 5.29 and 5.30). The values
of AAD, RMS and Bias for the pressure gradient are 28.0, 5.36 and
9.12%. For the core fraction these are 1.01, 0.22 and 0.98%, and for
the film mass flux 10.9, 2.18 and 10.2%, respectively.

Figures 5.31 to 5.33 illustrate the evolution of the pressure gradi-
ent, core fraction and film mass flux as a function of u_{gS}^* for a particular
annular flow run ($u_{lS} = 0.10\mathrm{ms}^{-1}$) of Alamu and Azzopardi (2011).

The comparison between the numerical model and this set of exper-
imental data resulted in 36.11% of the points falling inside the $\pm 20.0\%$
range for the pressure gradient, 66.7% of the points within the $\pm 1.0\%$
range for the core fraction and 88.9% of the points within the $\pm 20.0\%$
range for the film mass flux.
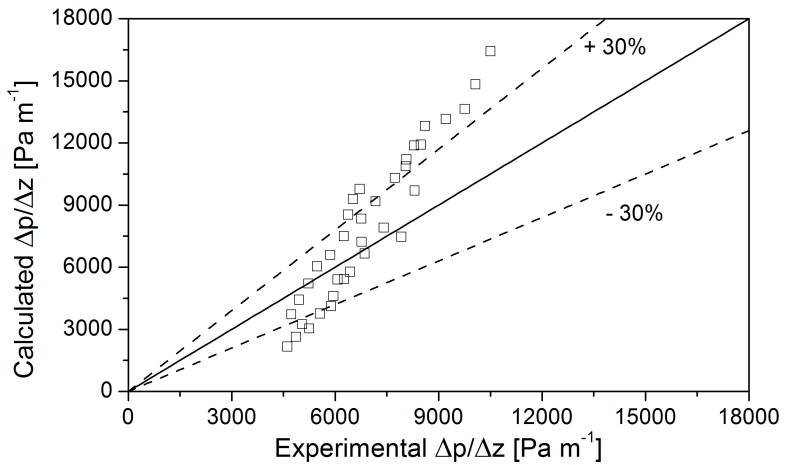
Figure 5.28 – Comparison of numerical results and experimental pressure gradient data of Alamu and Azzopardi (2011).
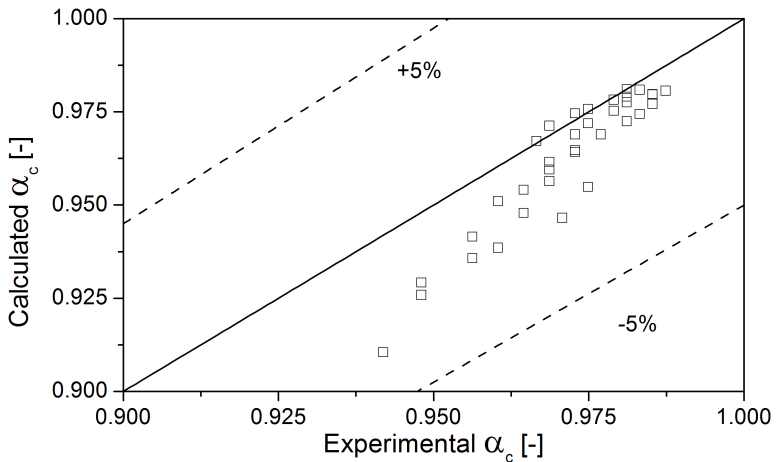
Figure 5.29 – Comparison of numerical results and experimental core fraction data of Alamu and Azzopardi (2011).
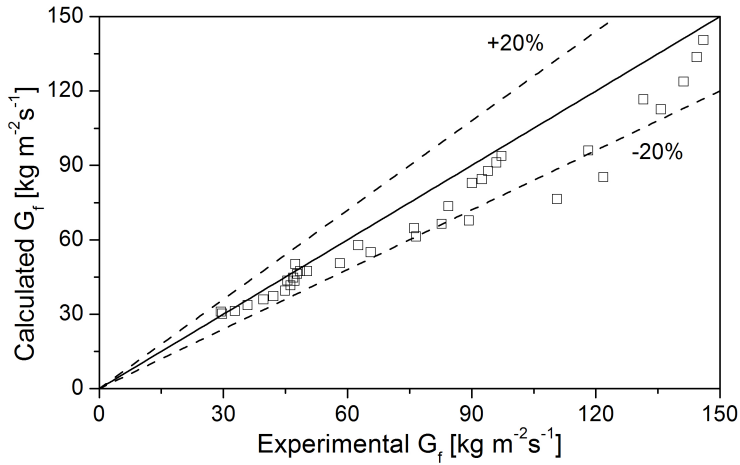
Figure 5.30 – Comparison of numerical results and experimental film mass flux data of Alamu and Azzopardi (2011).
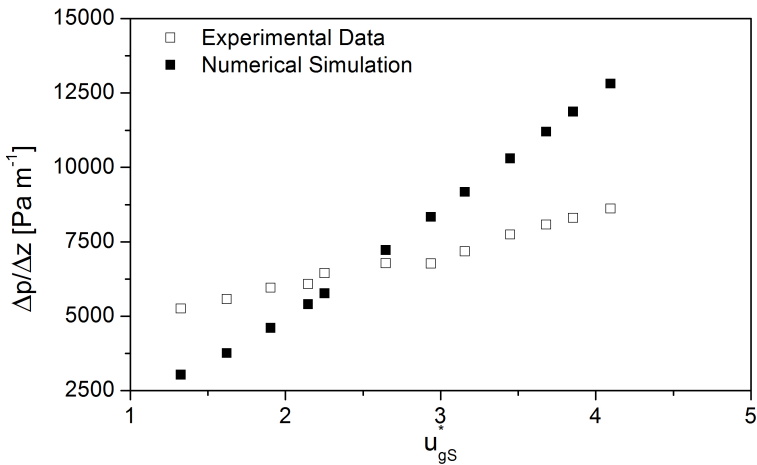
Figure 5.31 – Comparison of numerical results and experimental pressure gradient as function of u_{gS}^* using Alamu and Azzopardi (2011) data for $u_{lS} = 0.10 \mathrm{ms}^{-1}$.
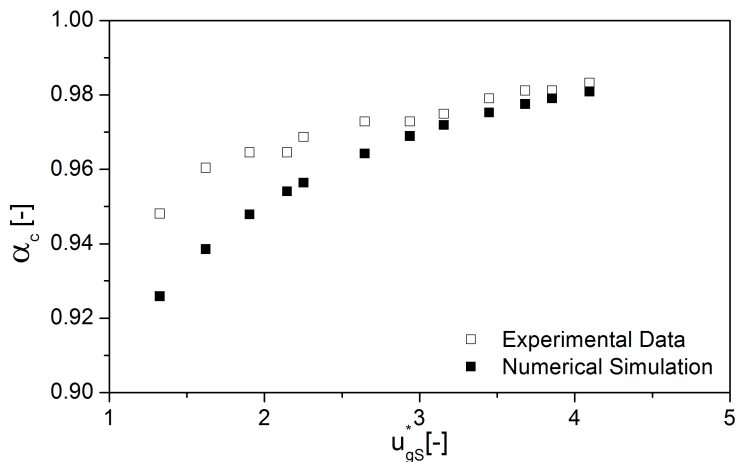
Figure 5.32 – Comparison of numerical results and experimental core fraction as function of u_{gS}^* using Alamu and Azzopardi (2011) data for $u_{lS} = 0.10 \mathrm{ms}^{-1}$.
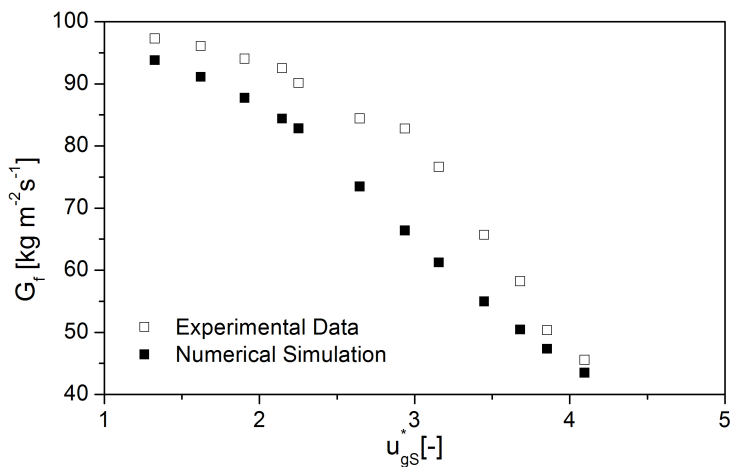
Figure 5.33 – Comparison of numerical results and experimental film mass flux as function of u_{gS}^* using Alamu and Azzopardi (2011) data for $u_{lS} = 0.10 \mathrm{ms}^{-1}$.

5.1.7   Waltrich (2012) data

Figures 5.34 and 5.35 show overall comparisons of the numerical results with the steady-state data of Waltrich (2012). The data cover both the churn and annular flow patterns, which are well predicted by the numerical model, except for some data points that lie in the churn-annular transition and are affected by the transition from two-field to three-field formulation. It is worth mentioning that differentiation between the churn and annular flow data shown in the figure was made by Waltrich (2012) by visual observation. However, the observed flow patterns are in good agreement with the transition criteria adopted in the numerical model (WALTRICH *et al.*, 2013).
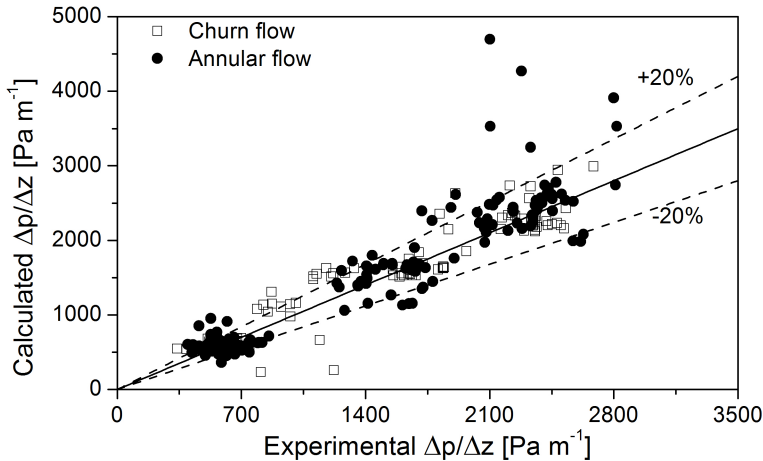
Figure 5.34 – Comparison of numerical results and experimental pressure gradient data of Waltrich (2012).

Figures 5.36 to 5.39 present the pressure gradient behavior in the churn-annular transition region for $G_l = 19$ kg m^{-2}s^{-1} and axial positions indicated in the figure captions. Three nominal outlet pressures are represented in these figures: 110, 300 and 500 kPa. The effect of pressure on the pressure gradient is quite small. The figures also reveal that the minimum pressure gradient occurred at $u_{gS}^* = 1.0$ and the axial position had little influence on the minimum pressure gradient. However, in the region of low u_{gS}^* the influence is clear; the lower the position the higher the pressure gradient. Figures 5.40 to 5.42 show

comparisons of void fraction for the same conditions. Again, the influ-
ence of the outlet pressure and axial position is quite small, as will be
shown next for the axial profiles.

Figures 5.43 and 5.44 show, respectively, comparisons between nu-
merical and experimental results of absolute pressure and void fraction
as a function of inlet distance.

The comparison between the numerical model and this set of exper-
imental data resulted in 71.7% of the points falling inside the $\pm 20.0\%$
range for the pressure gradient and 92.1% of the points within the
$\pm 5.0\%$ range for the void fraction. The statistical parameters for pres-
sure gradient are as follows: AAD=16.1%, RMS=1.37% and Bias=4.95%.
The comparison for void fraction resulted in the following statistical pa-
rameters: AAD=4.88%, RMS=0.44% and Bias=-4.63%.
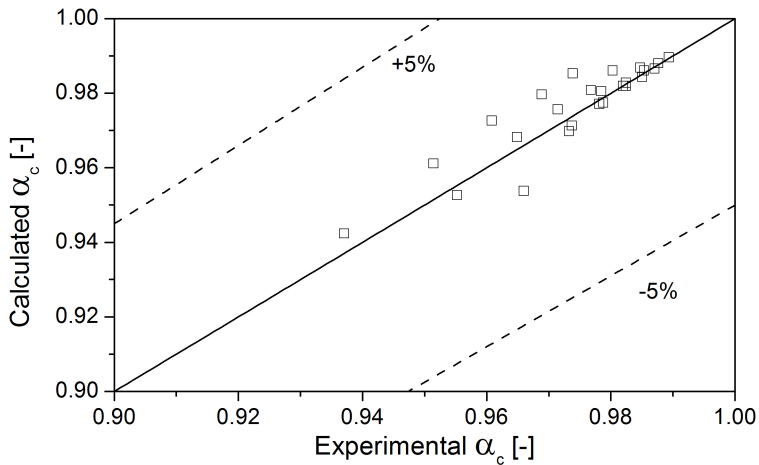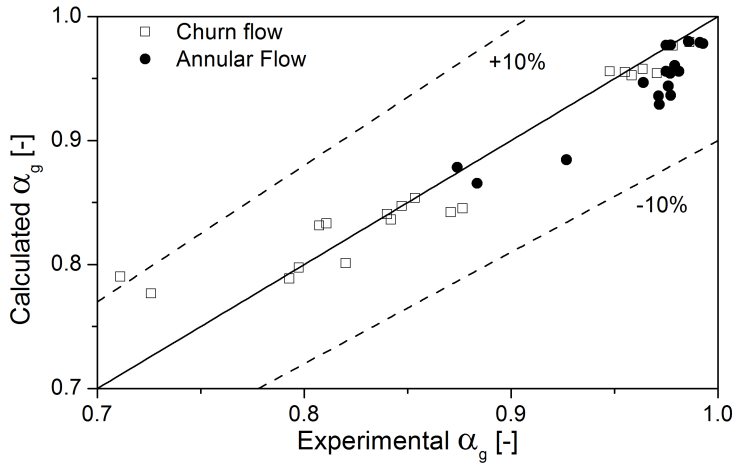
Figure 5.35 – Comparison of numerical results and experimental void fraction data of Waltrich (2012).
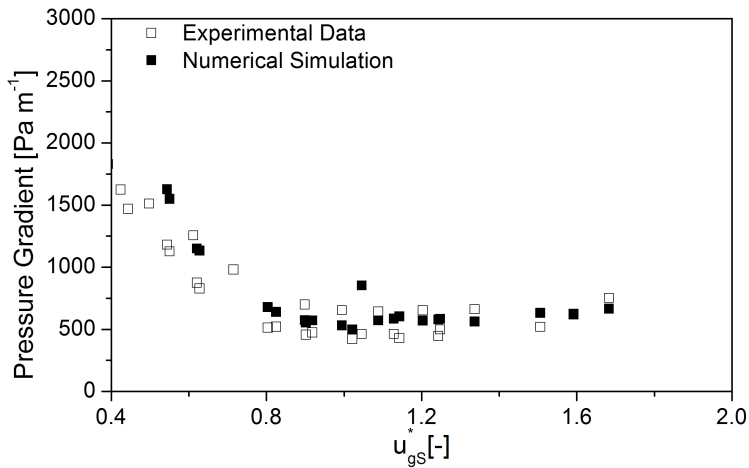
Figure 5.36 – Comparison of numerical and experimental pressure gradient as a function of u_{gS}^* using the Waltrich (2012) data for $z = 9.17$ m with $G_l = 19$ kg m^{-2}s^{-1}.
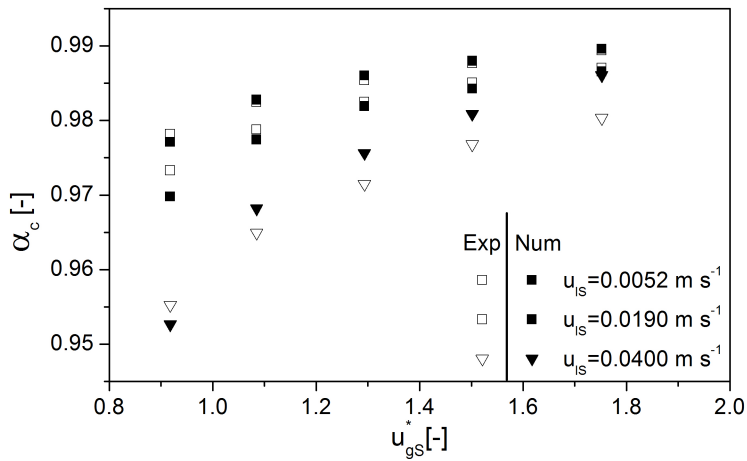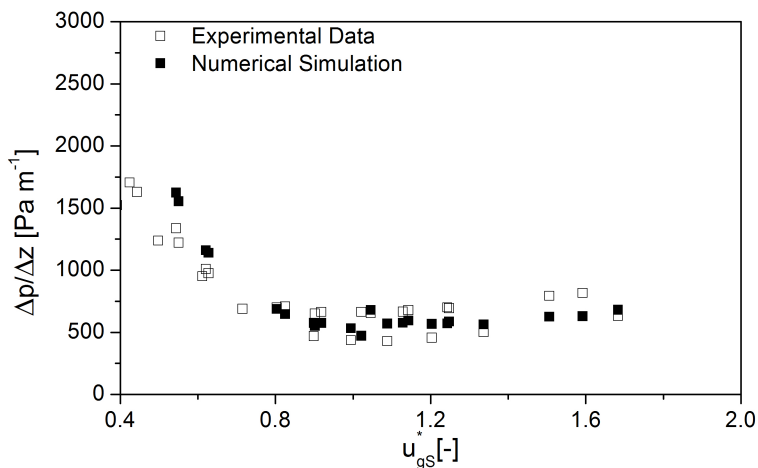
Figure 5.37 – Comparison of numerical and experimental pressure gradient as a function of u_{gS}^* using the Waltrich (2012) data for $z = 20.37$ m with $G_l = 19$ kg m^{-2}s^{-1}.
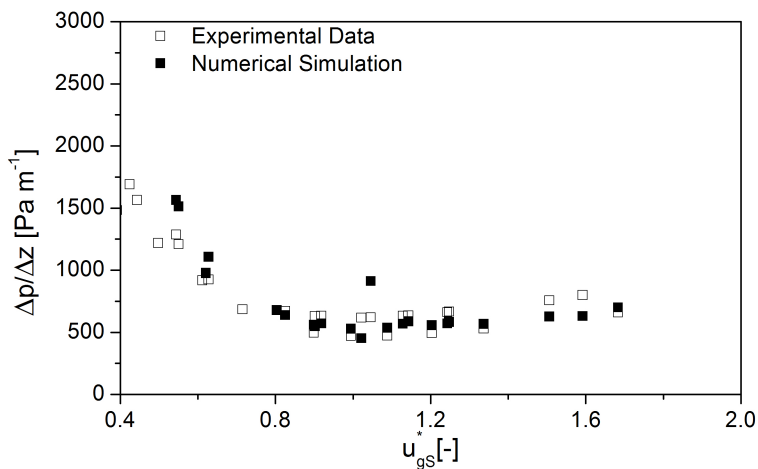
Figure 5.38 – Comparison of numerical and experimental pressure gradient as a function of u_{gS}^* using the Waltrich (2012) data for $z = 32.59$ m with $G_l = 19$ kg m^{-2}s^{-1}.
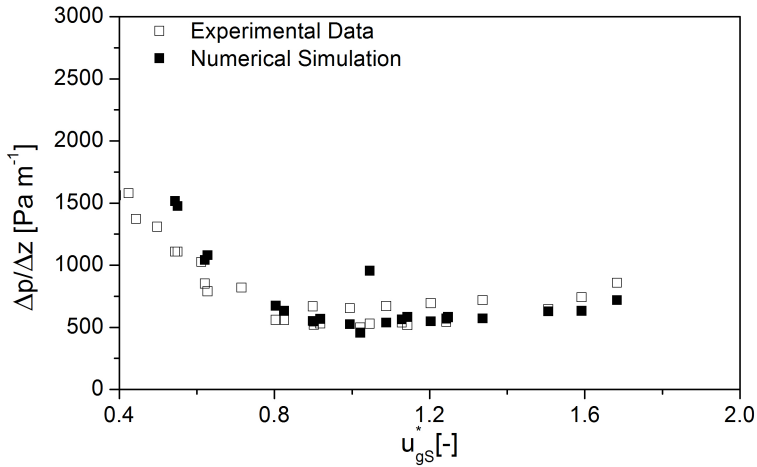
Figure 5.39 – Comparison of numerical and experimental pressure gradient as a function of u_{gS}^* using the Waltrich (2012) data for $z = 39.73$ m with $G_l = 19$ kg m^{-2}s^{-1}.
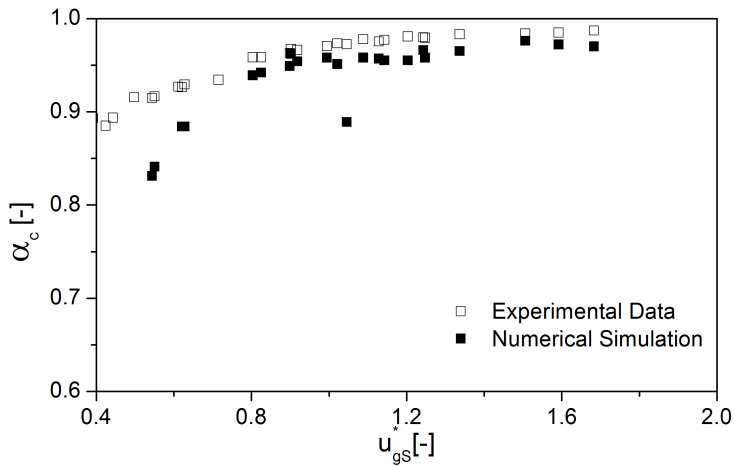
Figure 5.40 – Comparison of numerical and experimental void fraction as a function of u_{gS}^* using the Waltrich (2012) data for $z = 4.08$ m with $G_l = 19$ kg m^{-2}s^{-1}.
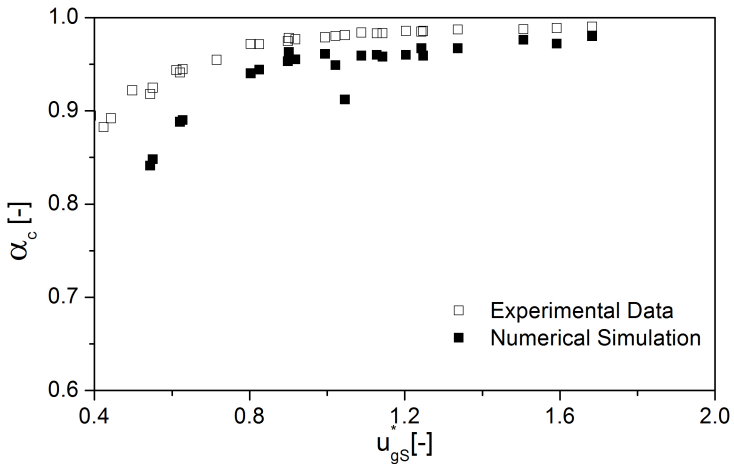
Figure 5.41 – Comparison of numerical and experimental void fraction as a function of u_{gS}^* using the Waltrich (2012) data for $z = 24.59$ m with $G_l = 19$ kg m^{-2}s^{-1}.
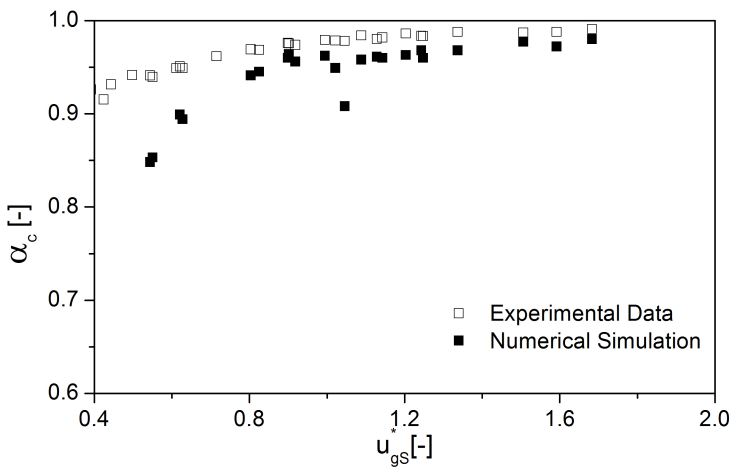
Figure 5.42 – Comparison of numerical and experimental void fraction as a function of u_{gS}^* using the Waltrich (2012) data for $z = 37.8$ m with $G_l = 19$ kg m^{-2}s^{-1}.
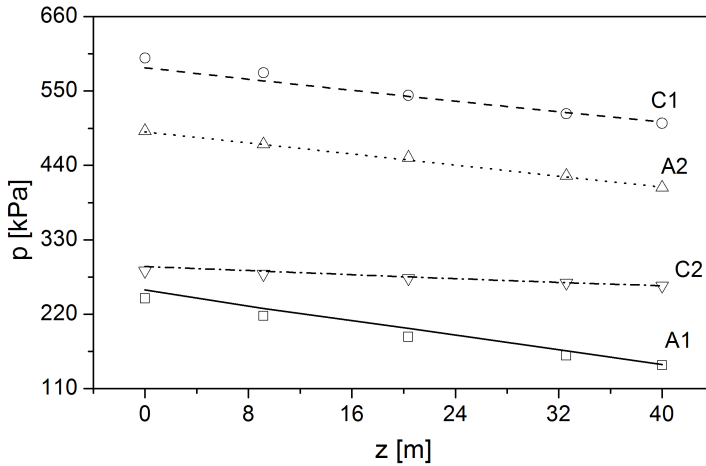
Figure 5.43 – Comparison of experimental and calculated static pressures as a function of distance for steady-state conditions. ANNULAR FLOW CONDITIONS: A1: $G_l = 387.7\text{kgm}^{-2}\text{s}^{-1}$, $G_g = 50.7\text{kgm}^{-2}\text{s}^{-1}$, $p_{out} = 144.2\text{kPa}$. A2: $G_l = 18.9\text{kgm}^{-2}\text{s}^{-1}$, $G_g = 43.0\text{kgm}^{-2}\text{s}^{-1}$, $p_{out} = 261.8\text{kPa}$. CHURN FLOW CONDITIONS: C1: $G_l = 290.3\text{kgm}^{-2}\text{s}^{-1}$, $G_g = 32.1\text{kgm}^{-2}\text{s}^{-1}$, $p_{out} = 502.4\text{kPa}$. C2: $G_l = 285.4\text{kgm}^{-2}\text{s}^{-1}$, $G_g = 38.0\text{kgm}^{-2}\text{s}^{-1}$, $p_{out} = 407.1\text{kPa}$.
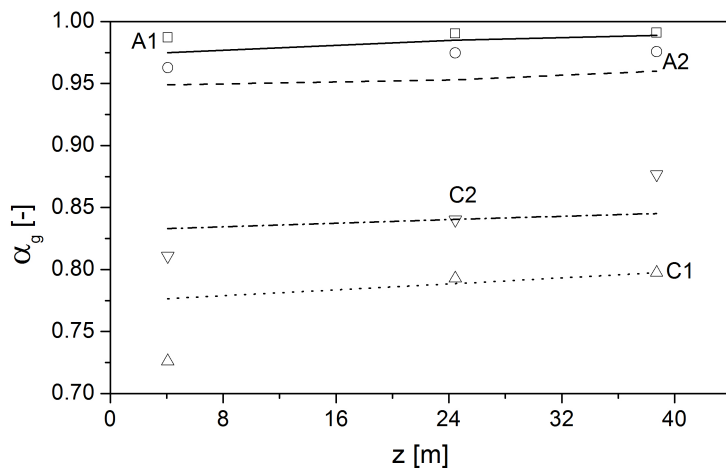
Figure 5.44 – Comparison of experimental and calculated static pressures as a function of distance for steady-state conditions. ANNULAR FLOW CONDITIONS: A1: $G_l = 19.0\text{kgm}^{-2}\text{s}^{-1}$, $G_g = 42.0\text{kgm}^{-2}\text{s}^{-1}$, $p_{out} = 110.0\text{kPa}$. A2: $G_l = 19.0\text{kgm}^{-2}\text{s}^{-1}$, $G_g = 33.0\text{kgm}^{-2}\text{s}^{-1}$, $p_{out} = 238.5\text{kPa}$. CHURN FLOW CONDITIONS: C1: $G_l = 18.0\text{kgm}^{-2}\text{s}^{-1}$, $G_g = 21.7\text{kgm}^{-2}\text{s}^{-1}$, $p_{out} = 103.0\text{kPa}$. C2: $G_l = 285.4\text{kgm}^{-2}\text{s}^{-1}$, $G_g = 38.0\text{kgm}^{-2}\text{s}^{-1}$, $p_{out} = 407.1\text{kPa}$.

5.1.8   Yuan *et al.* (2013) data

Figure 5.45 shows the comparison of pressure gradient between the numerical method and the experimental data for annular and churn flows. Some data points are ore severely over predicted by the model, but the majority of the data is within the $\pm 20\%$ range. Figure 5.46 shows the void fraction comparison.
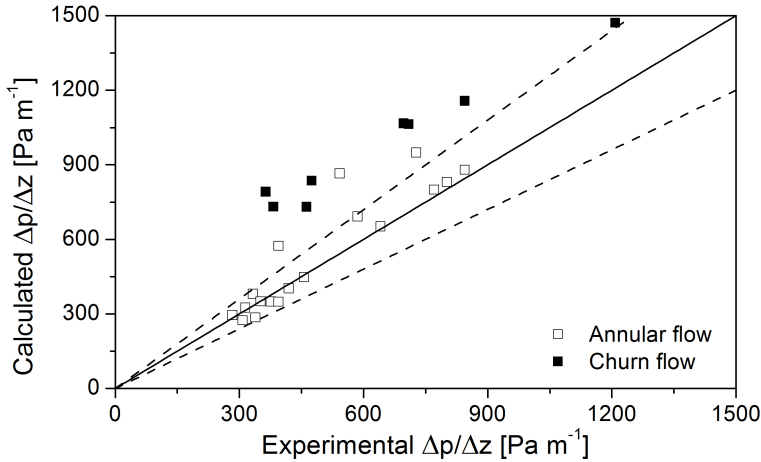
Figure 5.45 – Comparison of the pressure gradient numerical results with Yuan *et al.* (2013) experimental data.

Figures 5.47 and 5.48 show the variation of pressure gradient and void fraction with u_{gS}^*. The trends are well picked up by the model, but some notable aspects must be highlighted. First, the discontinuity at $u_{gS}^* = 1.0$ is due to the transition form the two to the three-field formulation. This discontinuity is more evident in the void fraction comparison. The minimum pressure gradient point is not very well reproduced by the model, as the discontinuity in the curve (due to formulation change) occurs near that point. It is also in this region that the greatest discrepancies between numerical model and experimental data arise. By observing the experimental data alone, it can be seen that the minimum pressure gradient point is shifted from $u_{gS}^* \approx 1.0$ to $u_{gS}^* \approx 0.9$.

The comparison between the numerical model and this set of experimental data resulted in 57.7% of the points falling inside the $\pm 20.0\%$
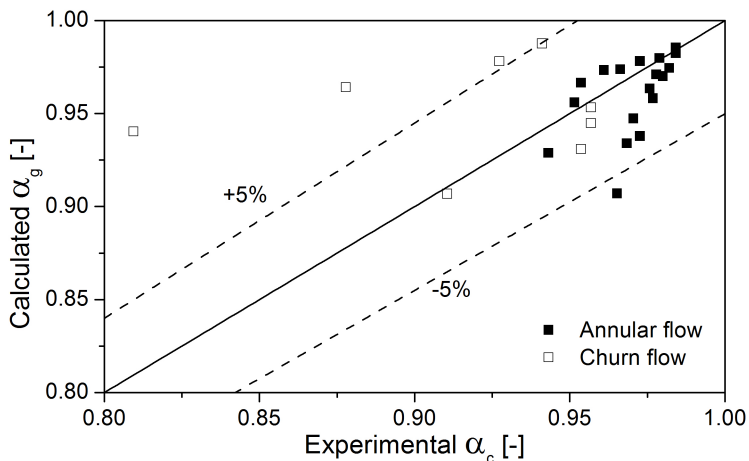
Figure 5.46 – Comparison of the void fraction numerical results with Yuan *et al.* (2013) experimental data.
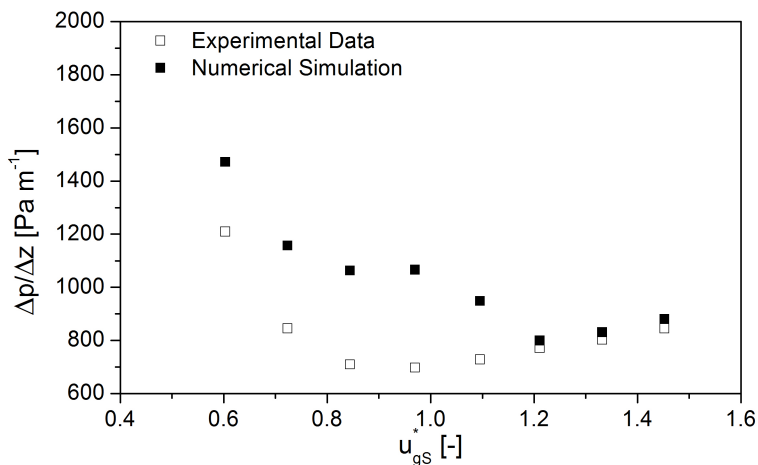
Figure 5.47 – Comparison of numerical and experimental pressure gradient as a function of u_{gS}^* using the Yuan *et al.* (2013) data for $u_{lS} = 0.1 \text{m}^{-1}$.

range for the pressure gradient and 84.6% of the points stay within the ±5.0% range for the void fraction. The statistical parameters obtained for this dataset are: AAD=28.6%, RMS=8.58% and Bias=24.5% for pressure gradient and AAD=2.63%, RMS=0.87% and Bias=0.52% for void fraction.
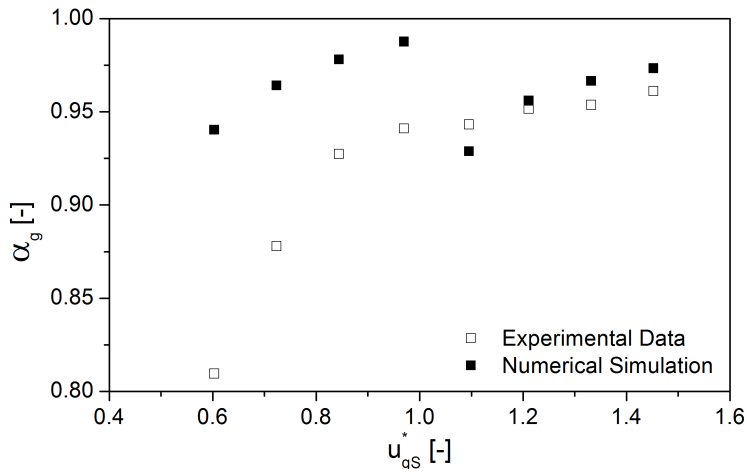
Figure 5.48 – Comparison of numerical and experimental void fraction as a function of u_{gS}^* using the Yuan *et al.* (2013) data for $u_{lS} = 0.1\mathrm{m}^{-1}$.

5.1.9   Overall statistical comparison

This section presents an overall comparison between the numerical model and the steady-state experimental data. Figure 5.49 shows all annular flow pressure gradient for the 552 data points. For this comparison the AAD, RMS and Bias are: 16.2%, 0.92%, 3.84%, respectively. The churn flow pressure gradient comparison is show in Fig. 5.50 for 293 data points. The statistical parameters are AAD=18.5%, RMS=1.56% and Bias=11.2%. A reasonably good agreement can be observed for both flow regimes, with 72.8% and 68.3% of the points within the the ±20% range for annular for churn flows, respectively.
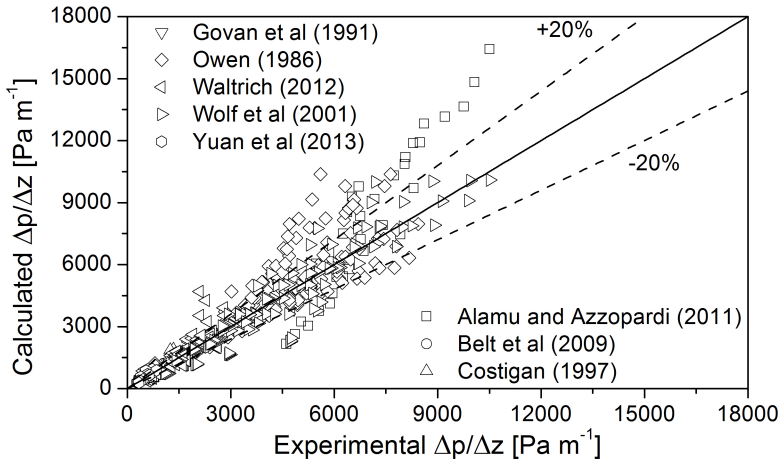
Figure 5.49 – Overall evaluation of the annular flow pressure gradient prediction.

The overall comparison of the liquid film mass flux in annular flow is presented in Fig. 5.51 for the 360 data points. The resulting statistical parameters are AAD=21.1%, RMS=1.57% and Bias=2.81%, with 55.0% of the points in the ±20% range.

The comparison of the void/core fraction in annular flow is presented in Fig. 5.52 for 406 data points which results in AAD=1.86%, RMS=0.16% and Bias=-1.23%, with 89.4% of the data points falling in the ±5.0% range. The comparison for void/core churn flow is depicted in Fig. 5.53, resulting in AAD=12.4%, RMS=1.08% and Bias=-10.8%, with 77.6% of the 245 data points falling in the ±20% range.
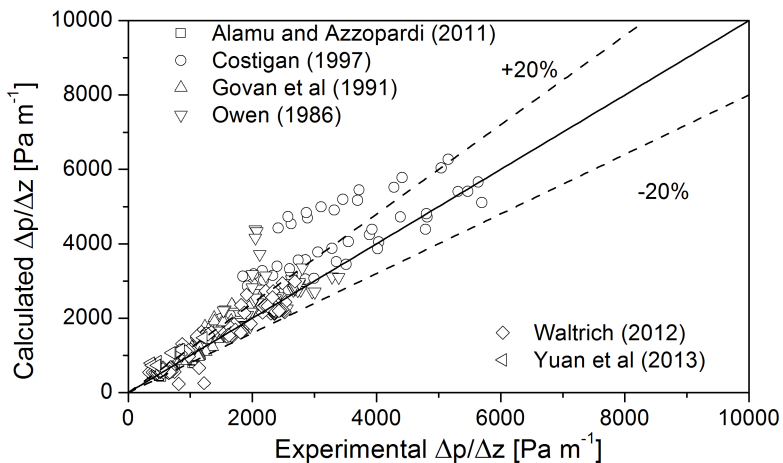
Figure 5.50 – Overall evaluation of the churn flow pressure gradient prediction.
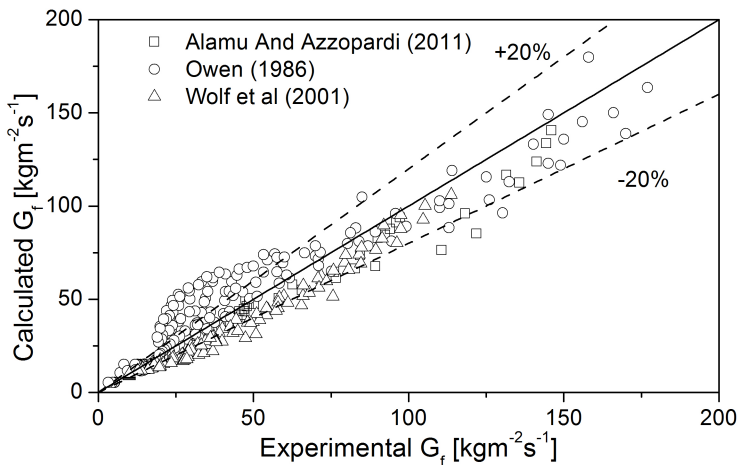
Figure 5.51 – Overall evaluation of the annular flow liquid film mass flux prediction.
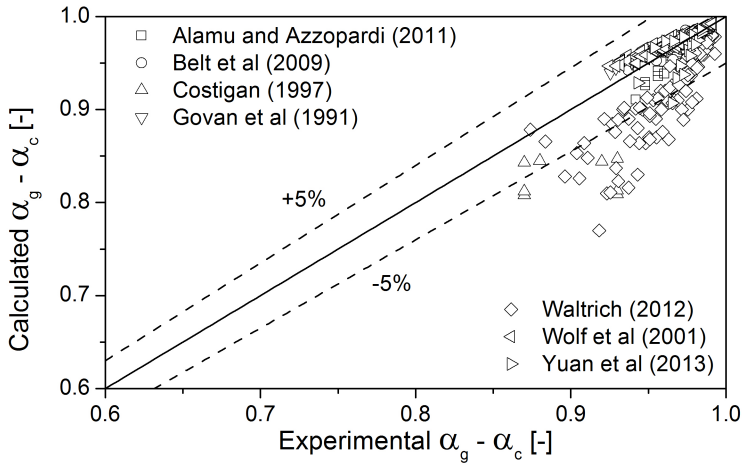
Figure 5.52 – Overall evaluation of the annular flow void/core fraction prediction.
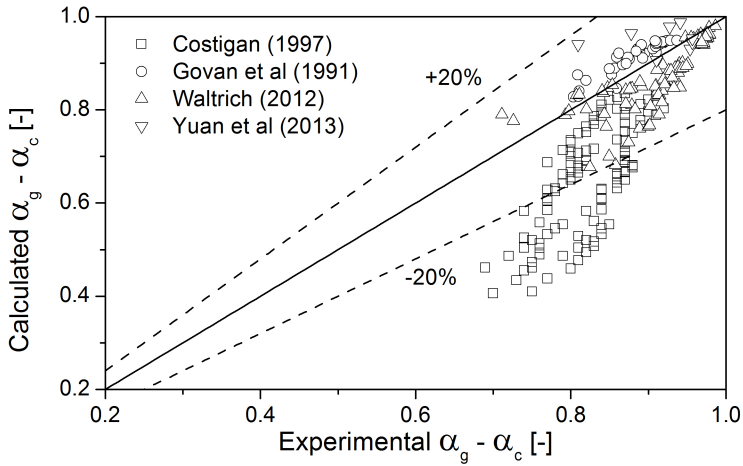
Figure 5.53 – Overall evaluation of the churn flow void/core fraction prediction.

At the end of the steady-state comparison some preliminary conclusion may be drawn about how the program behaves with respect to the experimental data presented so far. First there is a clear tendency of better representing annular flow data with larger diameter pipes such as Belt *et al.* (2009),Waltrich (2012) and Yuan *et al.* (2013). For the churn flow the deviations are larger, as is the scatter in the experimental data, this is due to the larger fluctuations characteristic of this flow pattern. The pressure gradient data tends to be overestimated by the numerical model in both churn and annular flows as is the liquid film flux (this one measured only for the annular flow). For the void/core fraction the deviations are much smaller under annular flow. For Churn flow, however, the experimental data of Costigan (1997) shows a much larger deviation and this relates to the experiments being conducted with lower gas superficial velocities (closer to slug flow). The experimental data of Govan *et al.* (1991), Waltrich (2012) and Yuan *et al.* (2013) present much smaller deviations, in consonance with the other variables compared (pressure gradient and liquid film mass flux).

5.2 COMPARISON WITH TRANSIENT DATA

This section presents the results of a comparison of the numerical model with the experimental data for transient churn and annular flows obtained by Waltrich (2012) in the TowerLab facility. The interfacial friction factor relationships used in the numerical simulations were those of Whalley and Hewitt (1978) and Jayanti and Brauner (1994) for the annular and churn flow patterns respectively.

For all simulations an initial flow was generated starting from the nominal values of the initial boundary conditions, and the simulation was run, with constant boundary conditions, until a stable solution was reached. After this initial stable condition was attained, the transient experimental boundary conditions for the initial steady state started to be used. This was then followed either by a change of mass flux at the bottom of the test section (mass flux-induced transient) or by choking the flow at the top of the test section (pressure-induced transient). In both cases, the flow pattern transits between churn and annular flows along the test section until a new stable condition is reached. It must be mentioned that the initial developing period is necessary to initialize all variable fields with values that are physically consistent, providing a basis for the transient, where the boundary conditions oscillate heavily.

5.2.1   Pressure-induced transients

In this section the pressure-induced transient modeling results are compared with experimental data. In these tests the outlet pressure is the only variable controlled, and fluctuations or changes in other variables such as inlet mass fluxes are a response to that pressure change. Five different cases are discussed based on the transient pressure drop behavior at four different pipe locations and on the transient void fraction behavior at two different pipe locations. Table 5.2 shows the initial and final boundary conditions of the pressure-induced transients. The last two lines show also the expected flow pattern to be encountered in the beginning of each simulation and at the end, where (A) stands for annular flow and (C) for churn flow.

Table 5.2 – Nominal values of the initial (I) and final (F) steady-state parameters of the pressure-induced transients.

	Case 1	Case 2	Case 3	Case 4	Case 5
$G_g(I)$ [kg m^{-2}s^{-1}]	50	39	42	40	49
$G_g(F)$ [kg m^{-2}s^{-1}]	34	29	40	40	47
$G_l(I)$ [kg m^{-2}s^{-1}]	390	20	20	20	313
$G_l(F)$ [kg m^{-2}s^{-1}]	290	12	17	18	295
$p_{out}(I)$ [kPa]	150	110	112	117	138
Flow Pattern (I)	(A)	(A)	(A)	(A)	(A)
Flow Pattern (F)	(C)	(C)	(C)	(C)	(C)

Figures 5.54 to 5.56 show the instantaneous experimental outlet pressure, inlet liquid mass flux and inlet gas mass flux during the Case 1 transient test. The pressure increase in the test section, as well as the decrease in the liquid and gas mass fluxes, result from the constriction imposed by the outlet choke. These three profiles are used as boundary conditions in the hyperbolic numerical model.

Figure 5.57 shows the behavior of the calculated u_{gS}^* at different distances from the inlet along with the Wallis criterion (WALLIS, 1969) for the churn-annular transition ($u_{gS}^* = 1.0$). The model predicts a flow transition from annular to churn flow at around 15 seconds into the test, which is seen to occur more or less uniformly along the test section, i.e., with very little delay between the different positions. The distinct values of u_{gS}^* at the beginning of the test, visible during the annular flow period, result from the steady-state axial pressure gradient, which causes a significant variation of density and superficial velocity as a function of distance. Figure 5.58 depicts the transition region in

Figure 5.54 – Transient outlet pressure boundary condition for Case 1.
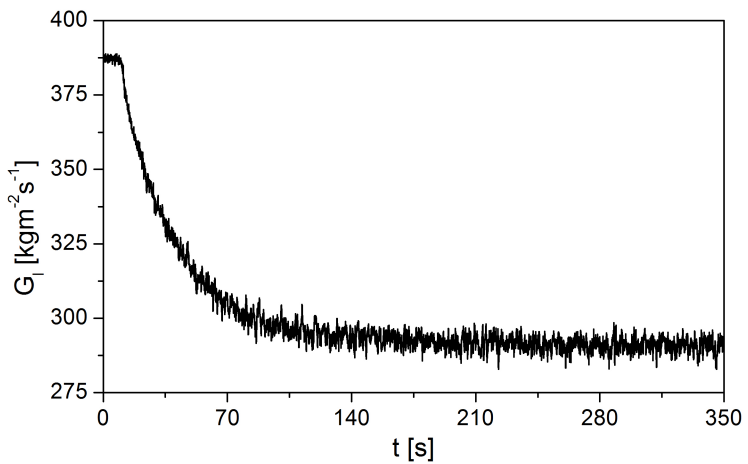
Figure 5.55 – Transient inlet liquid mass flux boundary condition for Case 1.

more detail in order to illustrate the time delay between the different transitions.

A distinct feature of the experimental data (boundary condition), which is reflected on the model results, is the strong temporal fluctuations of the pressure and flow rate signals in the churn flow region. These are clearly associated with the oscillatory nature of the liquid film flow in this flow pattern.

Figures 5.59 and 5.60 show the variation of pressure drop between the outlet pressure measurement and the positions indicated in the figures for Case 1. This pressure drop is calculated by subtracting the outlet pressure from the pressure at the positions indicated in the figures. The agreement between the model and data is generally good, with a certain tendency for the model to overpredict the data in annular flow. In the churn flow region, however, the scatter inherently associated with the data precludes any detailed visual comparison with the model in this region.

Figures 5.61 and 5.62 show the variation of the void fraction as a function of time for $z = 4.08$ m and $z = 38.73$ m, respectively. Violent fluctuations in the void fraction signal of Waltrich (2012) are observed for both positions. The amplitude of the oscilations is much higher in churn flow (see Fig. 5.70) due to the large waves that characterize this flow pattern. In order to allow a better assesment of the numerical model, the experimental data were smoothened using an adjacent averaging technique (PRESS *et al.*, 1992) with an 100 points window. Again, the agreement between the model and the smoothened data is satisfactory, as the model is capable of picking up the trends associated with the annular-churn transition.

For Case 1, the statistical analysis resulted in values of AAD, RMS and Bias for the pressure difference equal to 12.3%, 0.13%, and -3.63%, respectively. For the void fraction the overall AAD, RMS and Bias were calculated as 12.9%, 0.12% and -10.6%, respectively.

Figure 5.56 – Transient inlet gas mass flux boundary condition for Case 1.
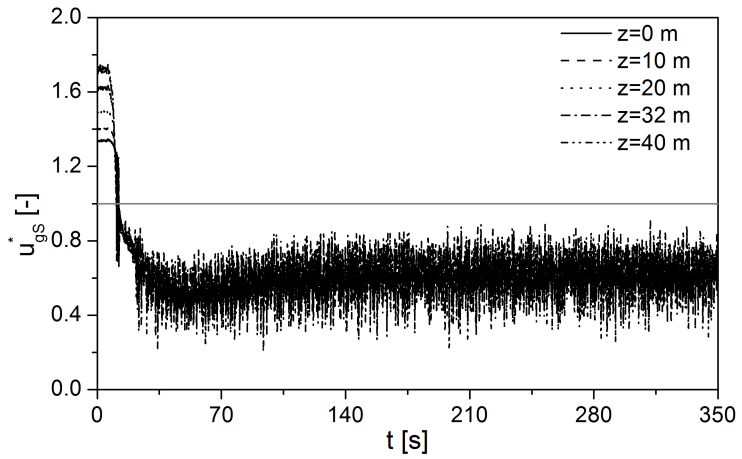
Figure 5.57 – Transient numerical dimensionless gas superficial velocity for Case 1.
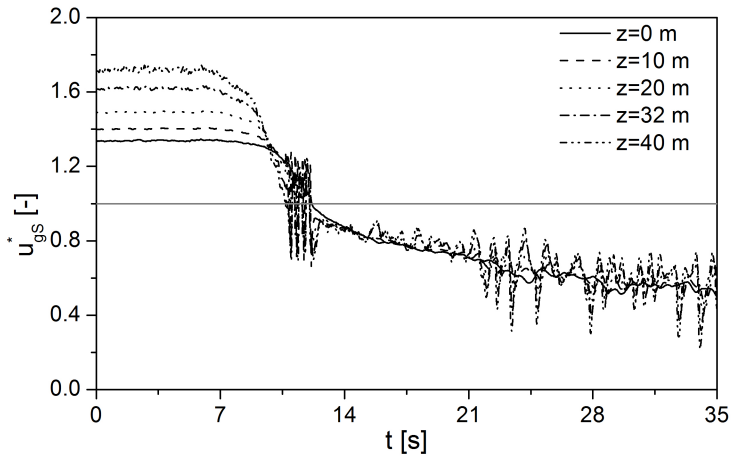
Figure 5.58 – Detail of transition region of Fig. 5.57.

Figure 5.59 – Comparison between transient experimental and numerical pressure drop at $z = 0.0$ m and $z = 20.37$ m for Case 1.
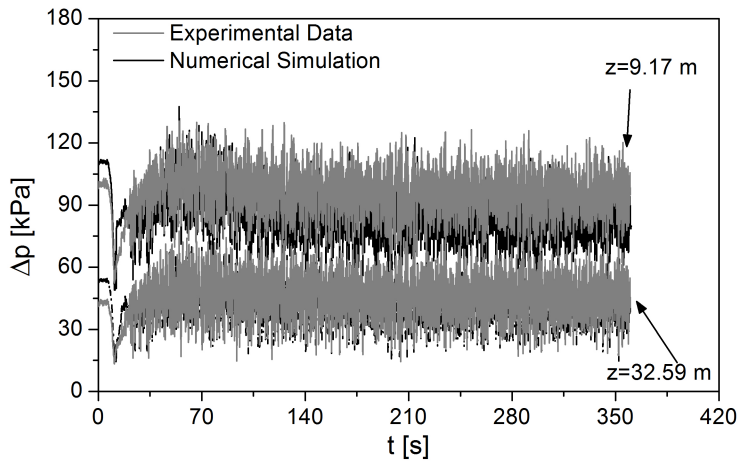
Figure 5.60 – Comparison between transient experimental and numerical pressure drop at $z = 9.17$ m and $z = 32.59$ m for Case 1.
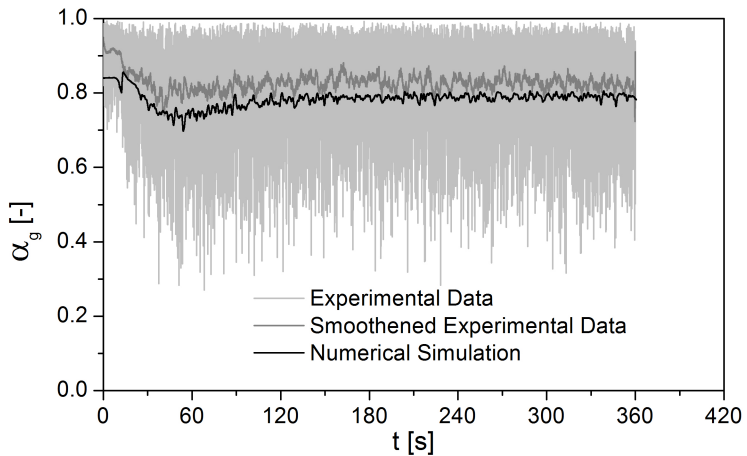
Figure 5.61 – Comparison between transient experimental and numerical void fraction at $z = 4.08$ m for Case 1.

Figure 5.62 – Comparison between transient experimental and numerical void fraction $z = 38.73$ m for Case 1.

Figures 5.63 to 5.65 show the input experimental data used as boundary conditions for the numerical simulation of the pressure-induced transient test Case 2. The most interesting feature of this boundary condition is the smoothness of the pressure distribution in Fig. 5.63. Although not explicitly mentioned in Waltrich (2012), this is most probably related to the low values of the liquid mass flux during the transient, which makes the high frequency fluctuations relatively small in amplitude, even in the presence of liquid film flow reversals.
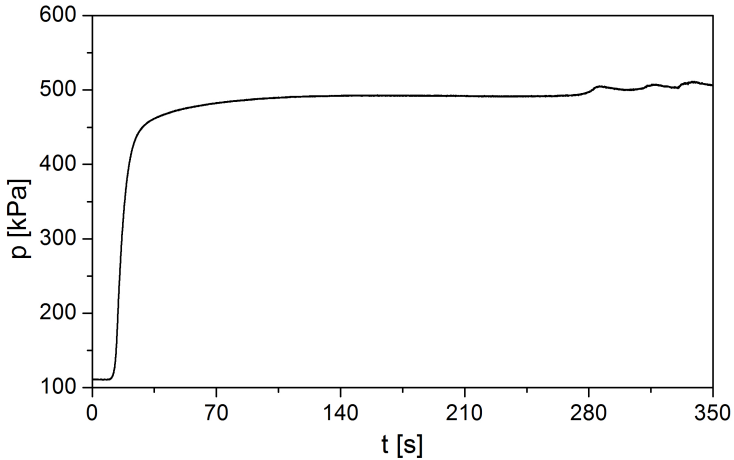
Figure 5.63 – Transient outlet pressure boundary condition for Case 2.

Figure 5.66 shows the calculated dimensionless gas superficial velocity at different pipe distances from the inlet. In this case, the transition is also instantaneous, occurring almost at the same time throughout the pipe length. The annular-churn transition take place at around 15 to 20 seconds.

Figures 5.67 and 5.68 show pressure difference data between the outlet position and the positions indicated in the figures for Case 2. Although the results are reasonably accurate during the initial instants (first 25 seconds), the model performance severely deteriorates after the breakdown of annular flow. According to the visual observations of Waltrich (2012), immediate drainage of the liquid phase to the bottom of the test section occurred after the partial closure of the choke valve. Therefore, instead of a continuous film flow pattern (churn flow) along the test section (as predicted by the model), what actually took place
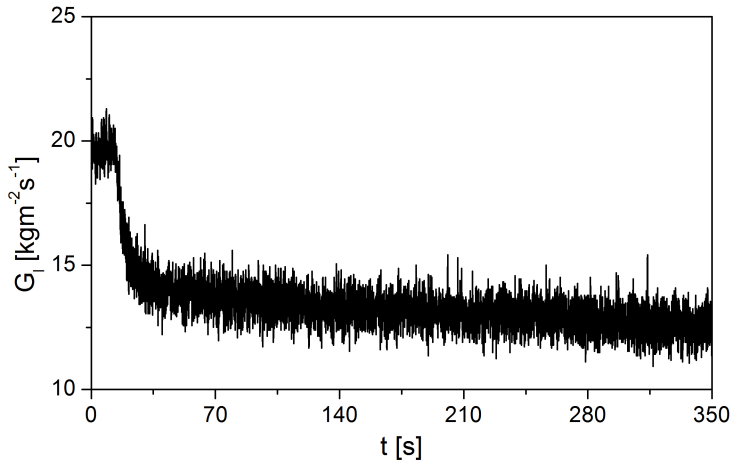
Figure 5.64 – Transient inlet liquid mass flux boundary condition for Case 2.
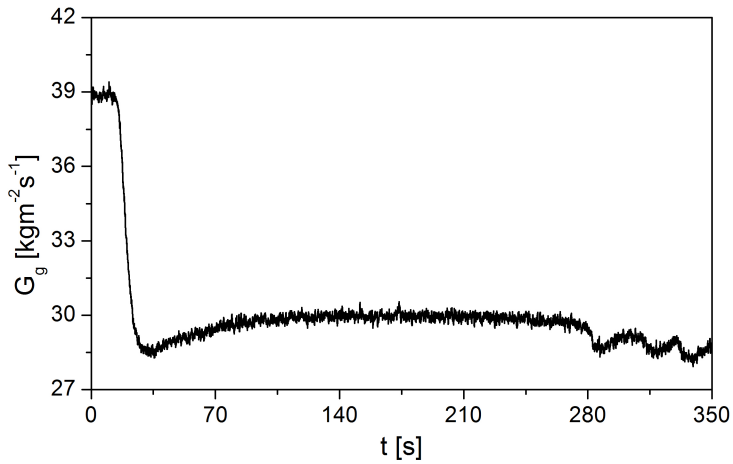
Figure 5.65 – Transient inlet gas mass flux boundary condition for Case 2.

after the valve closure was a complete segregation of the phases followed by an oscillating film front that gradually climbed along the test section. The advancing of the liquid front can be clearly perceived from the pressure gradient experimental data, due to change of slope from a constant pressure difference to an approximately linear profile, which indicates an increase of the gravitational head at a given position as a function of time.

The void fraction behavior at $z = 4.08$ m and $z = 38.73$ m is illustrated in Figs. 5.69 and 5.70, respectively. The experimental data (smoothened) following the transition from annular flow follows a somewhat chaotic behavior that is not picked up by the model. Nevertheless, it should be noted that while the void fraction after the transition is always lower than the value in annular flow (before the transition) for $z = 4.08$ m (which indicates the existence of churn flow in the bottom part) it reaches values close to unity, though oscillating severely at $z = 38.73$ m.

For Case 2, the statistical analysis resulted in values of AAD, RMS and Bias for the pressure difference equal to 427.04%, 118.57%, and -293.57%, respectively. For the void fraction, the AAD, RMS and Bias were calculated as 9.32%, 0.073% and -9.30%, respectively. These large deviations were expected due to the discrepancies in the pressure difference curves.

Figure 5.66 – Transient numerical dimensionless gas superficial velocity for Case 2.

Figure 5.67 – Comparison between transient experimental and numerical pressure drop at $z = 0.0$ m and $z = 20.37$ m for Case 2.

Figure 5.68 – Comparison between transient experimental and numerical pressure drop at $z = 9.17$ m and $z = 32.59$ m for Case 2.

Figure 5.69 – Comparison between transient experimental and numerical void fraction at $z = 4.08$ m for Case 2.
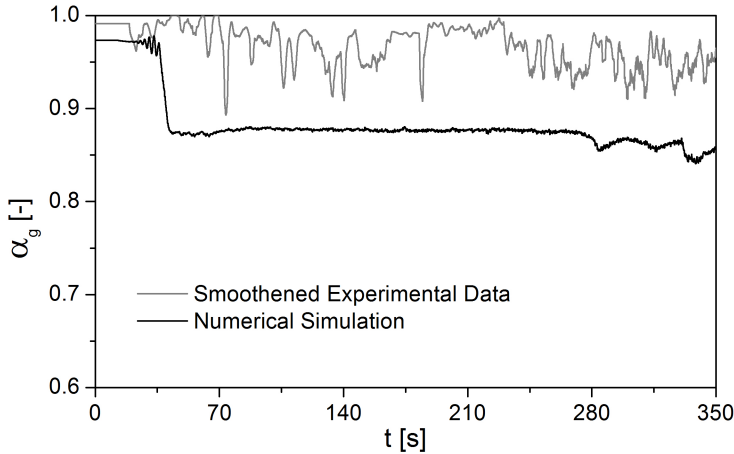
Figure 5.70 – Comparison between transient experimental and numerical void fraction $z = 38.73$ m for Case 2.

Figures 5.71 to 5.73 show the experimental boundary conditions of pressure and mass fluxes associated with Case 3. Qualitatively, this condition is very similar to Case 2. However, the final outlet pressure is not as high, indicating that the choke valve restriction was not as severe as in Case 2. As a result, the gas mass flux after the transition is still high enough to re-establish and sustain a continuous film flow after the transition from upward steady-state annular flow.

Figure 5.74 shows the variation of u_{gS}^* as a function of time. As in previous cases, the annular-churn transition occurs almost at the same time (with little delay) throughout the entire pipe. It should be noted that, in comparison with Case 2, the lower restriction (choking) of Case 3 caused the gas mass flux after the transition to be high enough to grant values of u_{gS}^* closer to unity.

Figures 5.75 and 5.76 show a comparison between the calculated and experimental difference between the outlet pressure and the pressure at the positions indicated in the figures as previously. As can be seen, both initial and final steady-state conditions are well represented. However, during the "accommodation" period a time lag is created between the two time traces. As the choke valve closes and the two-phase flow along the pipe decelerates, the frictional component of the pressure gradient becomes less important and the total pressure gradient is
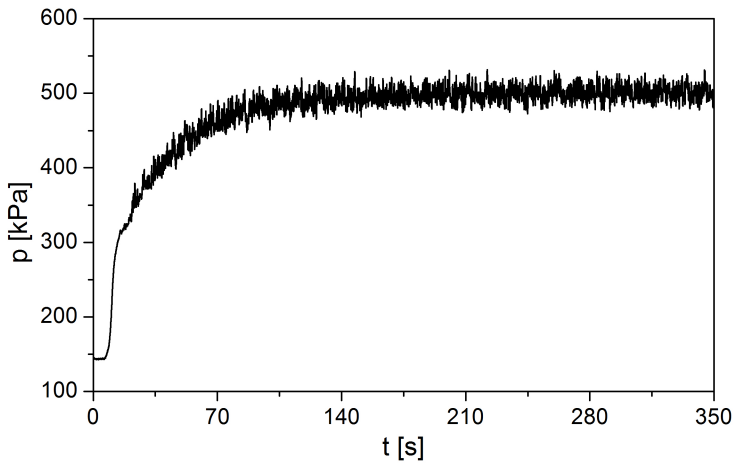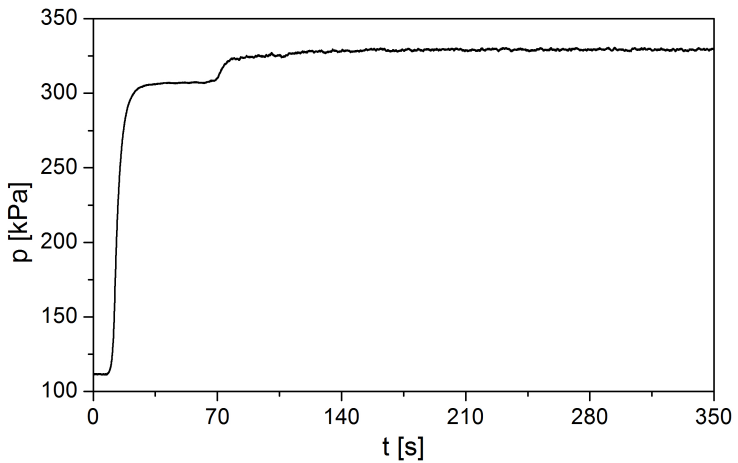
Figure 5.71 – Transient outlet pressure boundary condition for Case 3.

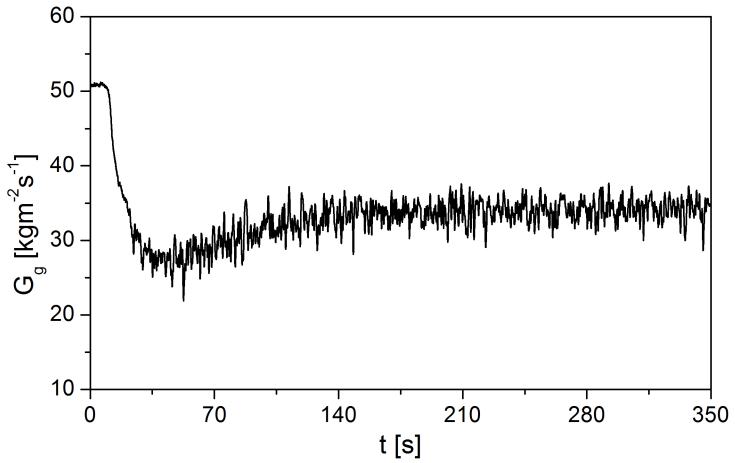Figure 5.72 – Transient inlet liquid mass flux boundary condition for Case 3.

Figure 5.73 – Transient inlet gas mass flux boundary condition for Case 3.
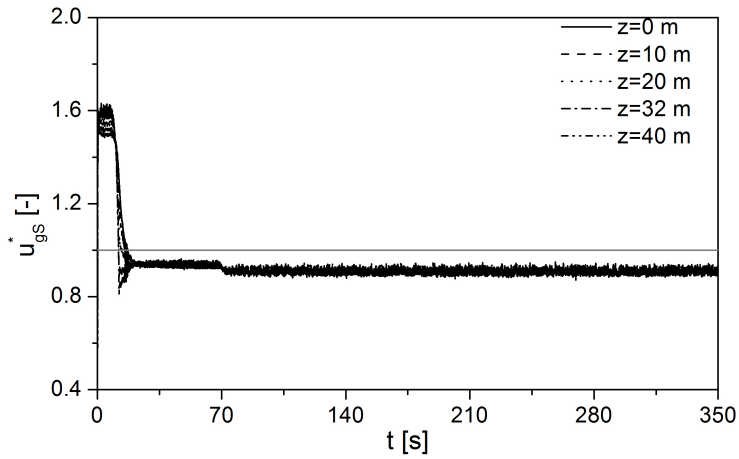
Figure 5.74 – Transient numerical dimensionless gas superficial velocity for Case 3.

almost only due to the static (gravitational) head. The positive slope in the pressure drop curves at $t < 70$ s is a manifestation of the liquid phase redistribution in the pipe following the breakdown of annular flow.
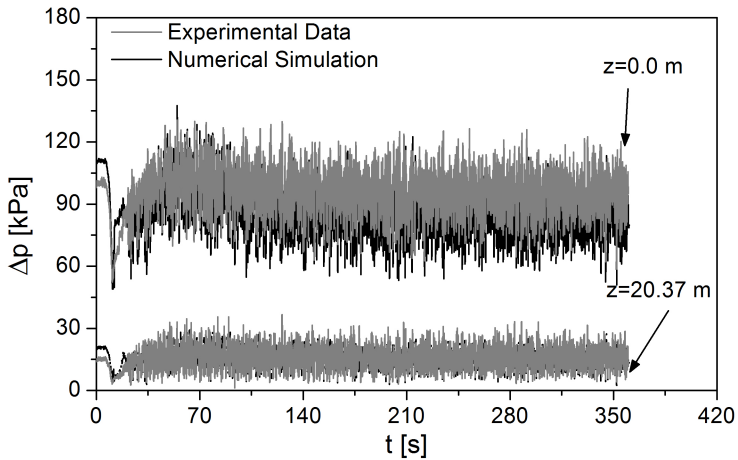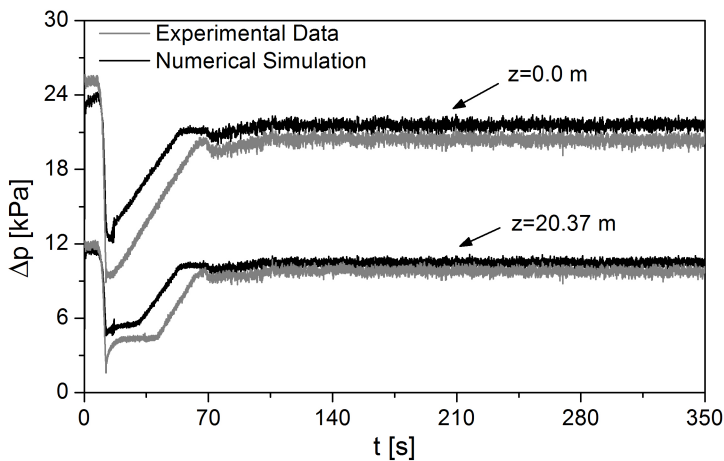

Figure 5.75 – Comparison between transient experimental and numerical pressure drop at $z = 0.0$ m and $z = 20.37$ m for Case 3.

Since the pressure wave travels at a high velocity, the increase in gas density and the reduction of the gas velocity are felt almost instantaneously along the test section (see Fig. 5.74). Liquid accumulation starts at the bottom of the pipe (due to the lower local gas velocity and proximity to the liquid inlet) and a slow moving liquid holdup wave advances upward along the pipe. The velocity of this holdup wave (i.e., the slope of the pressure drop curves in the transient regions) is well predicted by the numerical model. A kind of waiting period (before the front reaches a certain position and the pressure starts to increase linearly) is also reasonably well predicted. As a matter of fact, what seems to be the cause of the time lag in the "accommodation" period is the value of the void fraction predicted immediately after the breakdown of annular flow (at $t \approx 15$ s).

A similar type of liquid redistribution/accumulation can also be inferred from the experimental data of Case 2, where an upward-moving front and waiting periods at each position are clearly visible. In Case 2, however, the numerical model was not successful at predicting the

pressure drop because of the poor suitability of the closure relationships at such small values of u_{gS}^* (≈ 0.6), which are among the lowest values verified against steady-state data. The advancement of the holdup wave along the pipe is illustrated in Fig. 5.77 for the conditions of Case 3. This figure shows an unexpected behavior at $z = 0$ m indicating that the void fraction would be first affected by the boundary condition change at $z = 4.1$ m and at $z = 10$ m than in the inlet position. This happens because this position is the boundary condition (calculated through the "triangular relationship" along with *in situ* velocities), and at this point the phase redistribution has not yet fully developed. When the annular to churn transition takes place (between 15 to 20 s) the value of void fraction at the inlet undergo a sudden elevation, revealing that the transition has happened at that location.

The model results are compared with the experimental void fraction data for z=4.08 m and for z=38.73 m (Figs. 5.78 and 5.79, respectively), with reasonable level of agreement considering the scatter in the experimental data. It is interesting to observe that the experimental void fraction reaches levels very close to unity at z=38.73 m during the instants immediately after the breakdown of annular flow at $t \approx 15$s. This is an indication of a breakdown of the film flow structure at that position. A similar behavior, but in a much larger scale was observed for Case 2.

For Case 3 the statistical parameters were calculated and resulted in an overall AAD, RMS and Bias for the pressure difference equal to 19.29 %, 0.271 %, and 17.47 %, respectively. For the void fraction the overall AAD, RMS and Bias were calculated as 2.1%, 0.02 % and -0.952 %, respectively.
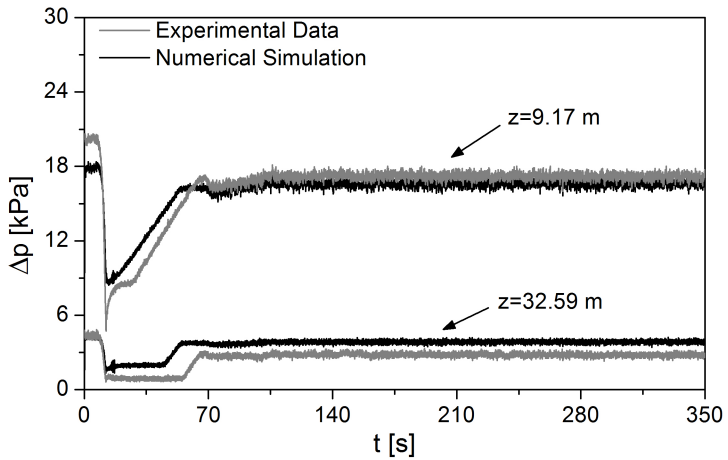
Figure 5.76 – Comparison between transient experimental and numerical pressure drop at $z = 9.17$ m and $z = 32.59$ m for Case 3.

Figure 5.77 – Detail of void fraction wave advancement for Case 3.

Figure 5.78 – Comparison between transient experimental and numerical void fraction at $z = 4.08$ m for Case 3.
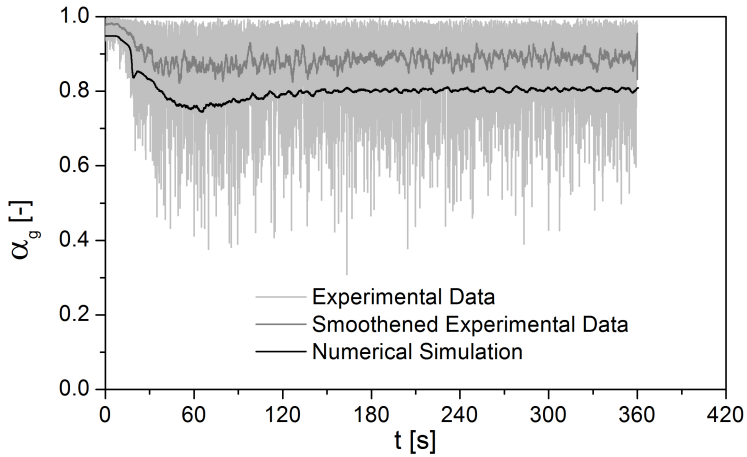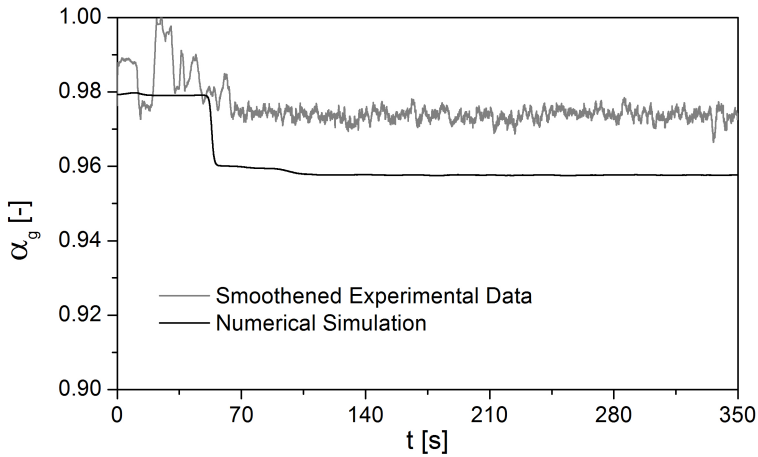

Figure 5.79 – Comparison between transient experimental and numerical void fraction $z = 38.73$ m for Case 3.

Figures 5.80 to 5.82 show the input experimental data/boundary conditions used in the numerical simulations of Case 4. In this case, the choke valve imposes a much smaller pressure change (around 120 kPa) in comparison with the previous cases (all greater than 200 kPa). As a result, the inlet liquid and gas mass fluxes changed much less during the course of the experimental run.
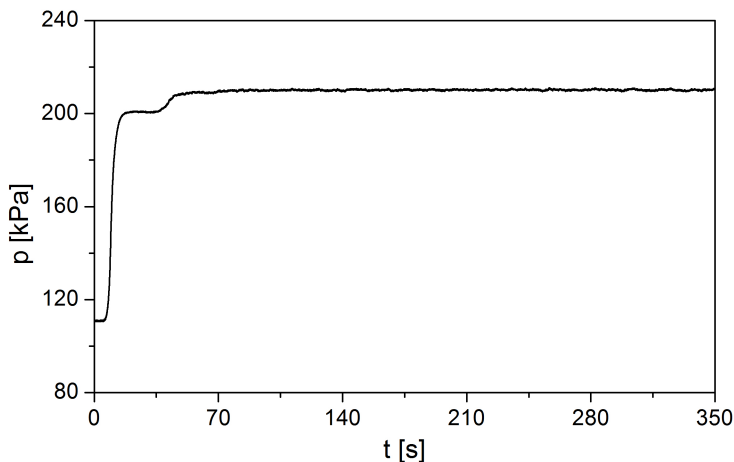
Figure 5.80 – Transient outlet pressure boundary condition for Case 4.

Figure 5.83 shows the calculated dimensionless gas velocity as a function of time. The model once again predicts a fast transient (little delay), however, it is important to note that the numerical model predicts annular flow throughout the whole duration of the experiment. This contradicts the visual observations of Waltrich (2012), who confirmed the existence of annular flow at the beginning of the experimental run and churn flow at the end.

Figures 5.84 and 5.85 present a comparison of the pressure difference between the outlet pressure and those at the different positions along the pipe (as indicated in the figures). Although the qualitative agreement is reasonable, the first station at $z = 0.0$ m still presents a deviation of the order of 30% with respect to the experimental data.
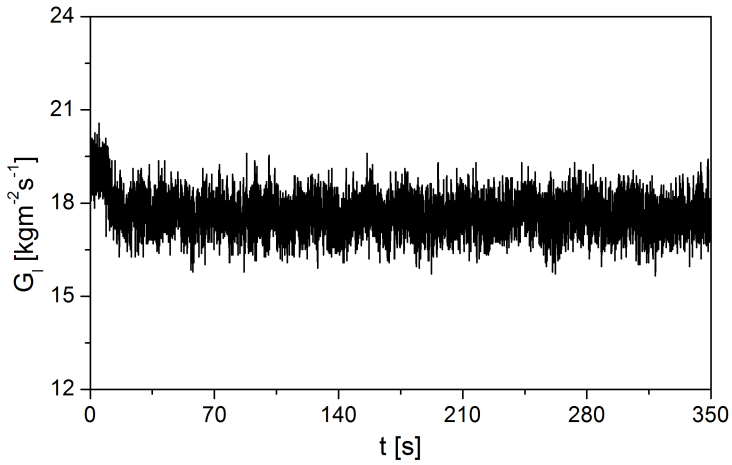
Figure 5.81 – Transient inlet liquid mass flux boundary condition for Case 4.
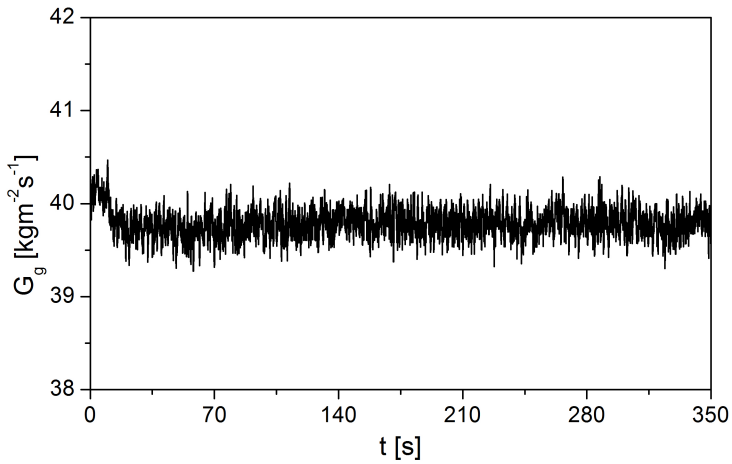
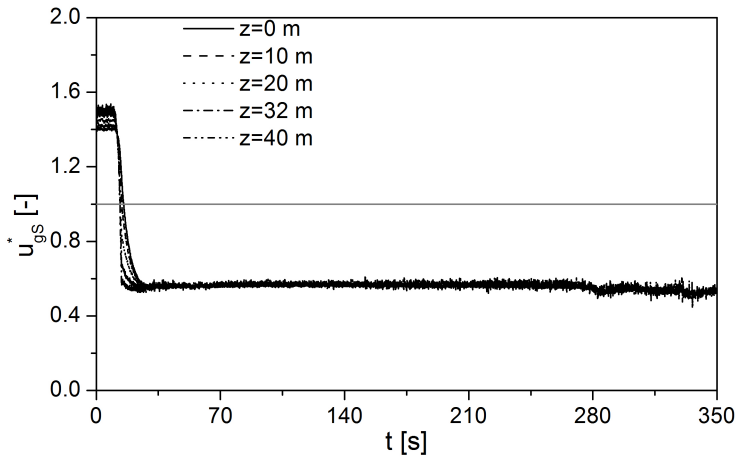Figure 5.82 – Transient inlet gas mass flux boundary condition for Case 4.
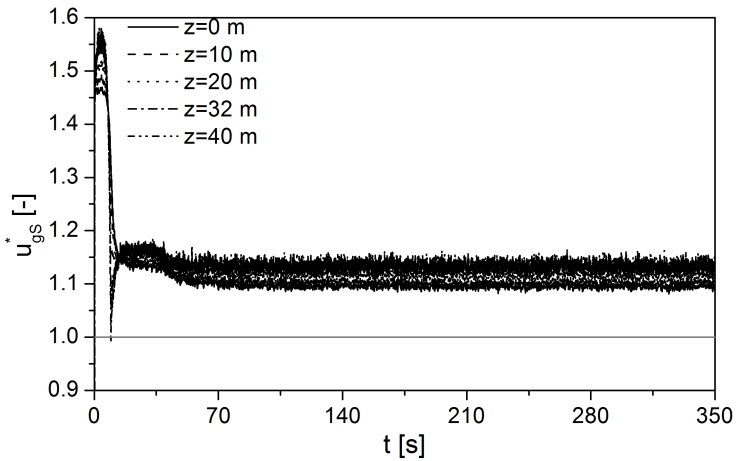
Figure 5.83 – Transient numerical dimensionless gas superficial velocity for Case 4.
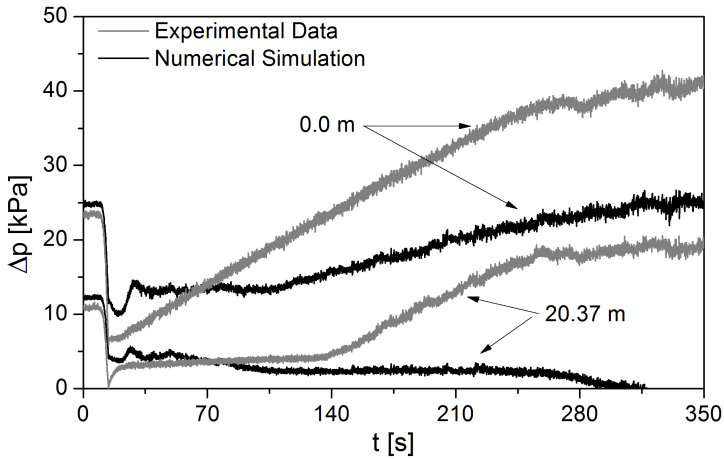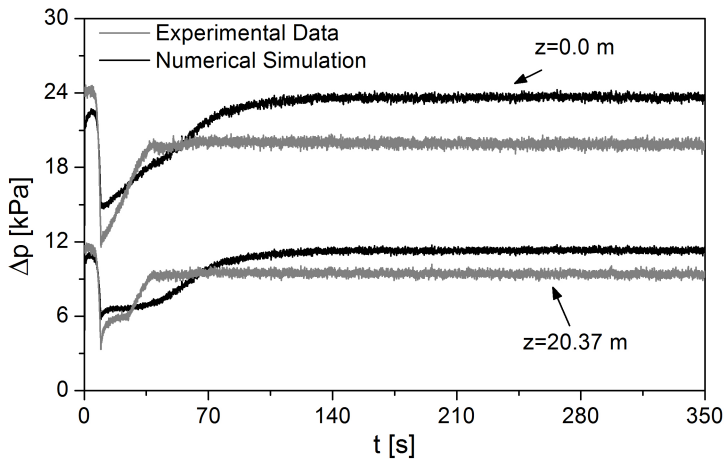

Figure 5.84 – Comparison between transient experimental and numerical pressure drop at $z = 0.0$ m and $z = 20.37$ m for Case 4.
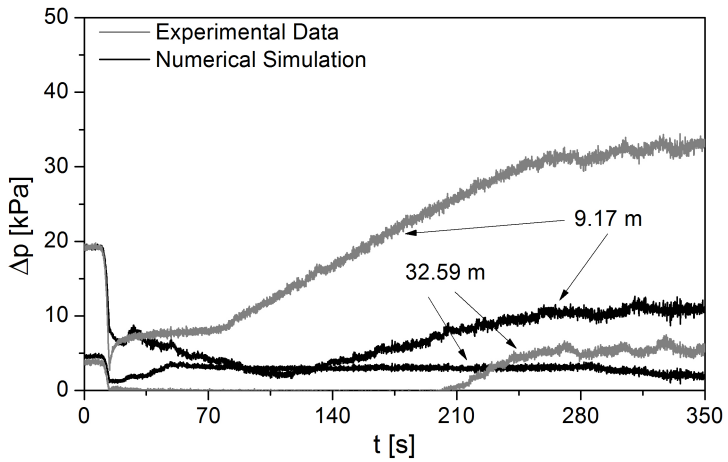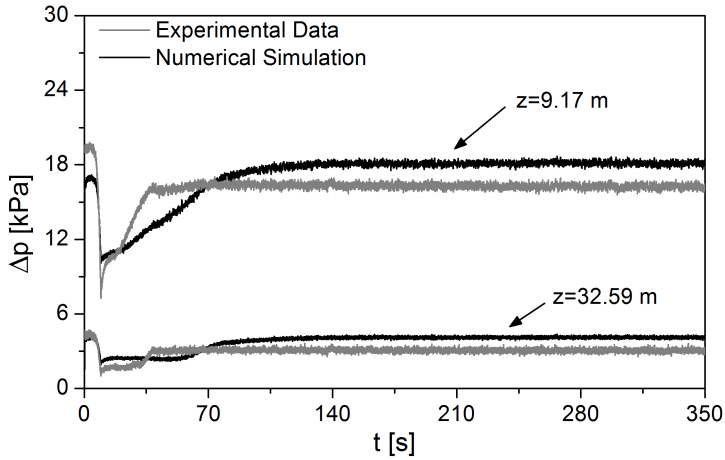
Figure 5.85 – Comparison between transient experimental and numerical pressure drop at $z = 9.17$ m and $z = 32.59$ m for Case 4.
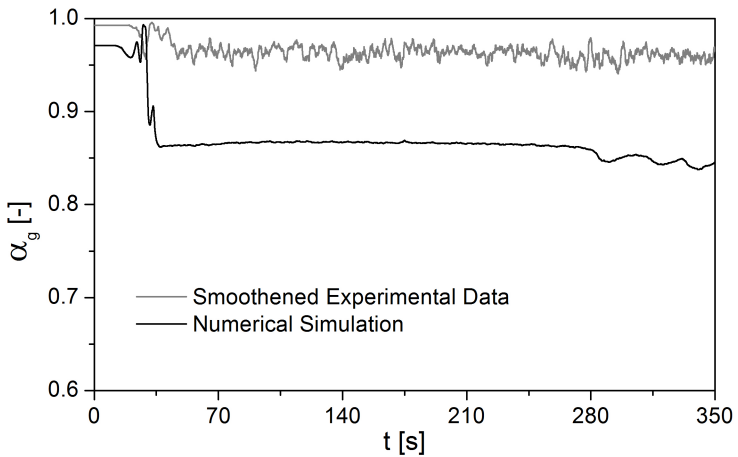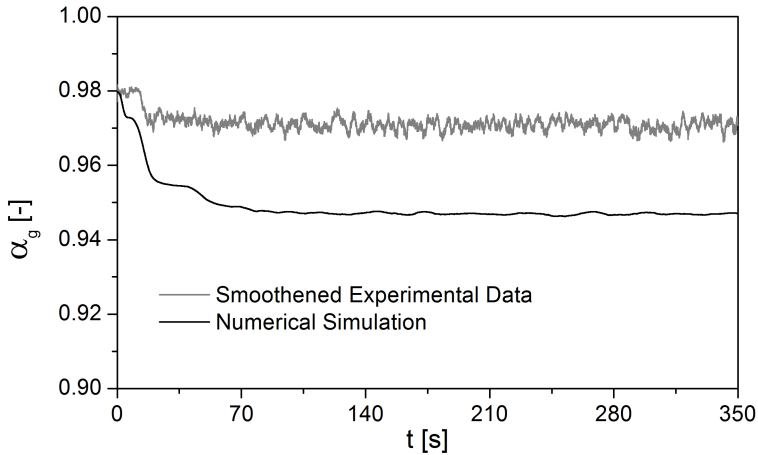

Figure 5.86 – Comparison between transient experimental and numerical void fraction at $z = 4.08$ m for Case 4.

The model predicts rather poorly the slopes of the pressure drop curves for Case 4. As can be seen, larger pressure gradients are predicted in the transient region (i.e., steeper slopes of the pressure drop curves), which can be attributed to the lower values of void fraction calculated by the model over the entire course of the simulation (see Figs. 5.86 and 5.87). Clearly, lower values of void fraction increase the gravitational pressure gradient (main component) due to the higher predicted liquid content.
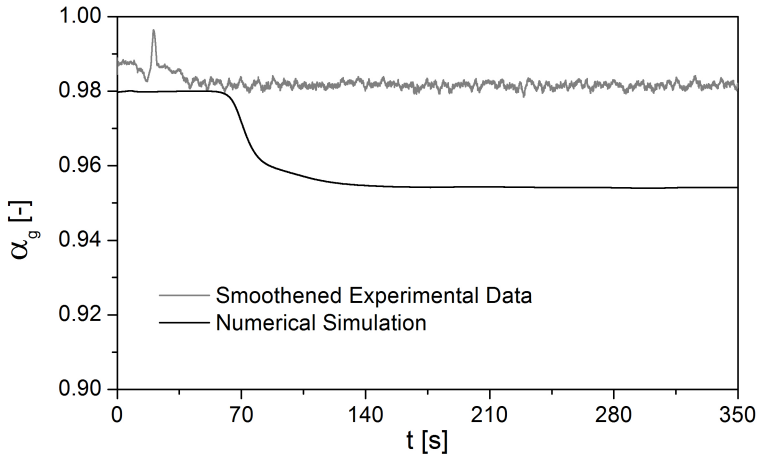
Figure 5.87 – Comparison between transient experimental and numerical void fraction $z = 38.73$ m for Case 4.

For Case 4 the analysis resulted in values of AAD, RMS and Bias for the pressure difference equal to 18.5%, 0.16%, and 15.7%, respectively. For the void fraction the overall AAD, RMS and Bias were calculated as 2.58%, 0.021% and -2.26%, respectively.

As mentioned above, the prediction of annular flow for the entire duration of Case 4 contradicts the experimental observations of Waltrich (2012), who observed the occurrence of churn flow at the end of the test.

In order to investigate the behavior of the model at conditions qualitatively in accordance with the visual observations of Waltrich (2012), the churn-annular transition criterion has been modified to $u_{gS}^* = 1.25$ for Case 4. The effect of the temporal fluctuations of the boundary conditions on the numerical predictions has also been investigated through

the application of an adjacent-averaging filter (PRESS *et al.*, 1992) with a 250 point window to the outlet pressure, inlet liquid and gas mass fluxes signals. The smoothened boundary conditions are presented in Figs. 5.88 to 5.90, most of the high frequency oscillations have been dampened, especially for the mass fluxes.
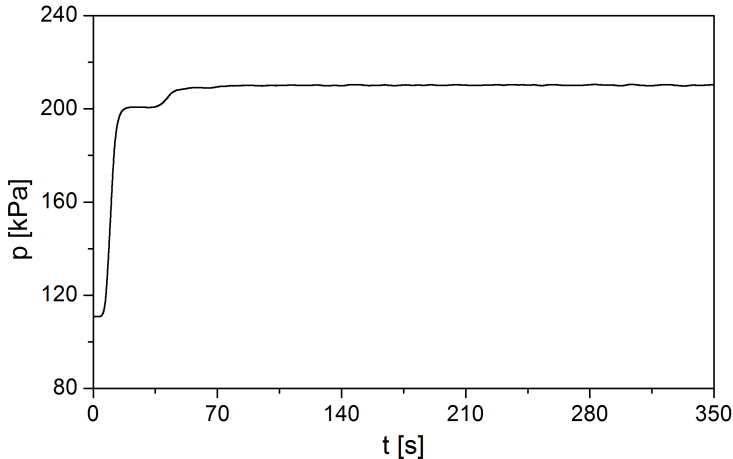
Figure 5.88 – Transient outlet pressure boundary condition for Case 4 (smoothened).

Figure 5.91 shows the calculated dimensionless gas superficial velocity as a function of time for several positions. With the modification in the Wallis (1969) criterion, the transition from annular to churn flow takes place between 10 and 15 s into the test, which is in better agreement with the visual observations of Waltrich (2012). Much less oscillation is observed in comparison with Fig 5.83 due to the smoothening of the boundary conditions.

Figures 5.92 and 5.93 show the pressure difference comparison as for Case 4 with the smoothened boundary conditions. The numerical results exhibit less oscillations and, although the fall in the pressure curves have been underpredicted during the instants where the flow regime transition has now occurs (between 10 and 15 s), the steady-state values are better represented than when the annular flow regime was predicted during the entire run.

Figures 5.94 and 5.95 show the void fraction comparison for the smoothened Case 4. Again, a reasonable agreement with the smoothened
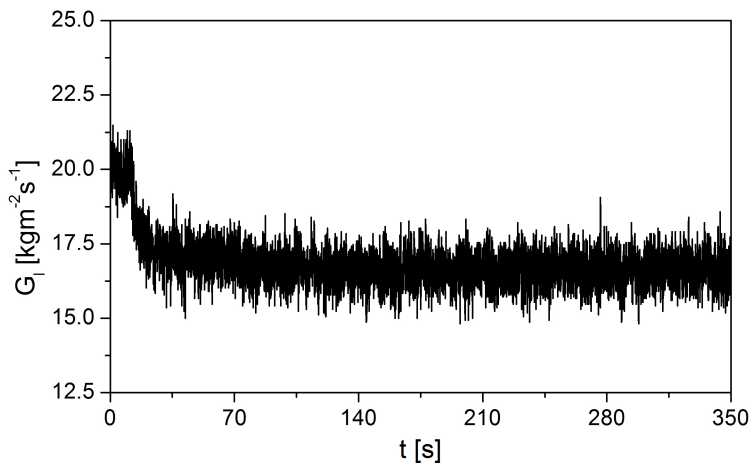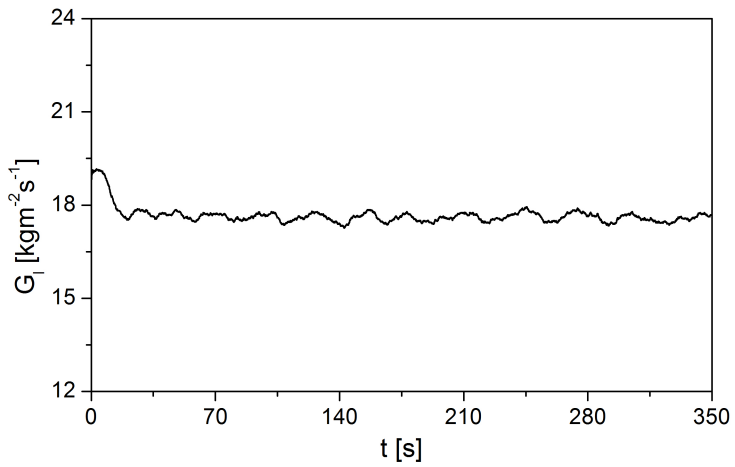
Figure 5.89 – Transient inlet liquid mass flux boundary condition for Case 4 (smoothened).
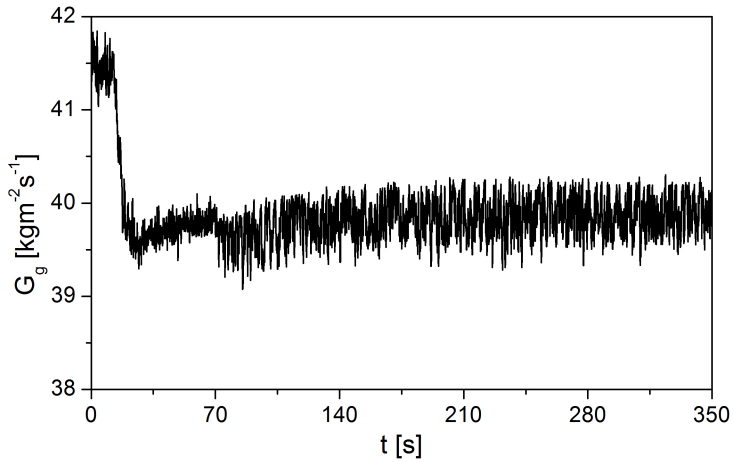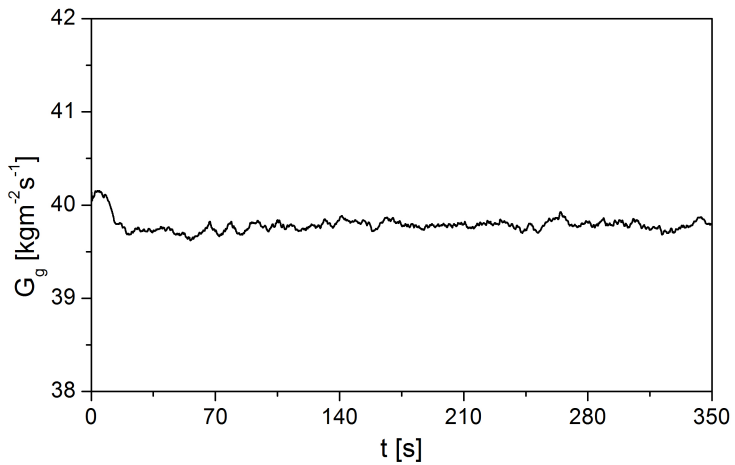

Figure 5.90 – Transient inlet gas mass flux boundary condition for Case 4 (smoothened).

Figure 5.91 – Transient numerical dimensionless gas superficial velocity for Case 4 (smoothened).
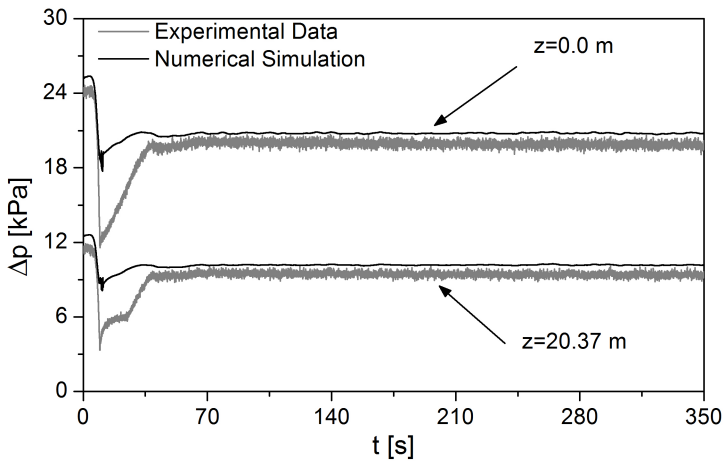
Figure 5.92 – Comparison between transient experimental and numerical pressure drop at $z = 0.0$ m and $z = 20.37$ m for Case 4 (smoothened).

experimental data for void fraction is observed, with differences between the model and the data smaller than 5%.

The statistical analysis of the smoothened Case 4 resulted in the following parameters for the pressure difference: AAD=12.53%, RMS=0.16% and Bias=11.79%. For the void fraction the overall AAD, RMS and Bias were calculated as 1.44%, 0.014% and -0.74%, respectively.

Figure 5.93 – Comparison between transient experimental and numerical pressure drop at $z = 9.17$ m and $z = 32.59$ m for Case 4 (smoothened).

Figure 5.94 – Comparison between transient experimental and numerical void fraction at $z = 4.08$ m for Case 4 (smoothened).
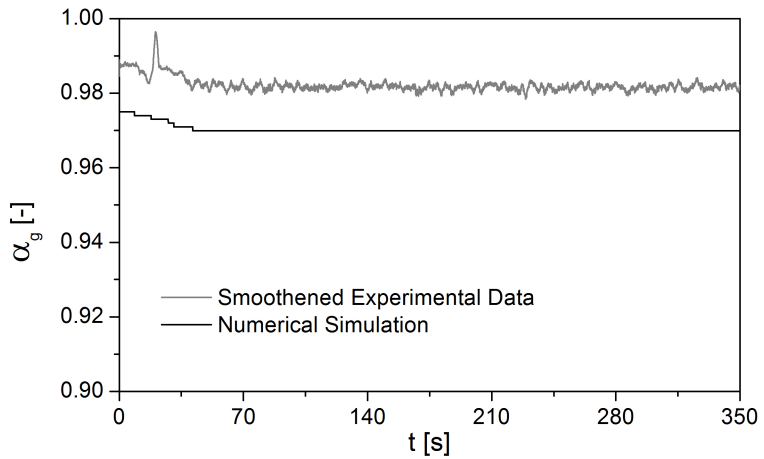
Figure 5.95 – Comparison between transient experimental and numerical void fraction $z = 38.73$ m for Case 4 (smoothened).

The experimental data used as boundary conditions for the numerical simulation of Case 5 are depicted in Figs 5.96 to 5.98. In this case the rise in the outlet pressure is also small (like in Case 4), but the values of the liquid mass flux are quite high (see Fig. 5.97). As a result, the high frequency fluctuations in outlet pressure are significant.
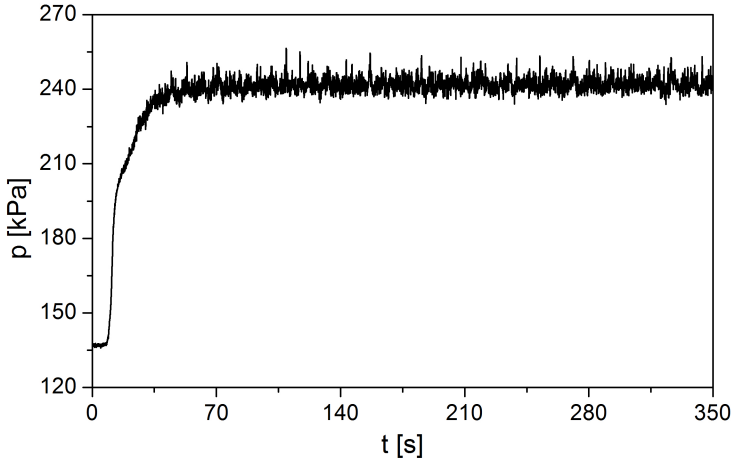
Figure 5.96 – Transient outlet pressure boundary condition for Case 5.

Figure 5.99 shows the calculated u_{gS}^* for different positions as a function of time for the whole simulation. As can be seen, except for a few individual points, due to severe fluctuations of outlet pressure, the calculated dimensionless superficial gas velocity is always greater than unity. This goes against the visual observations of Waltrich (2012), who observed that this case started as annular flow and ended as churn flow.

As can be seen from Figs. 5.100 and 5.101, which show the pressure drop variation (calculated as previously), the mismatch between observed and calculated flow patterns does not impact negatively the model results to a great extent. The largest deviations occur for $z = 0.0$ m, for which the liquid holdup, and consequently the gravitational pressure drop component are more severely over predicted. Although there is no direct measurement of void fraction at $z = 0.0$ m, this can be inferred from Fig. 5.102, which shows the void fraction at $z = 4.08$ m. At $z = 38.73$ m (Fig. 5.103), the numerical void fraction is much closer to the experimental data, which improves the model prediction.

Figure 5.97 – Transient inlet liquid mass flux boundary condition for Case 5.
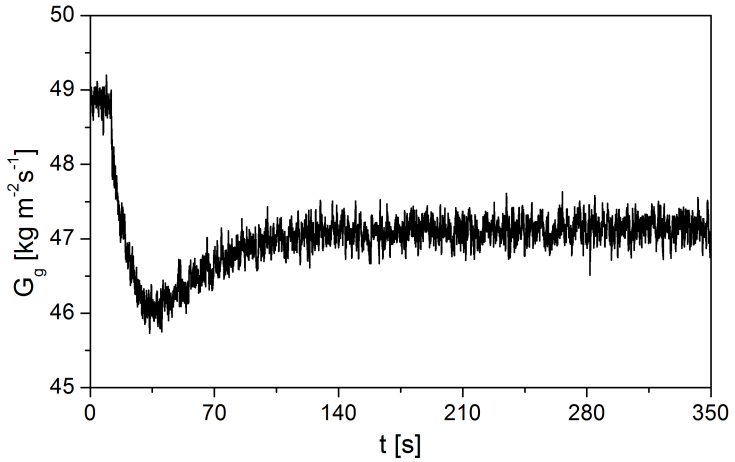
Figure 5.98 – Transient inlet gas mass flux boundary condition for Case 5.
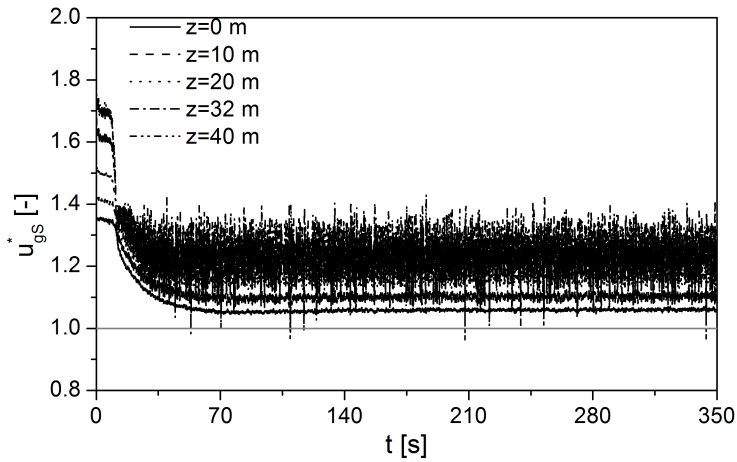
Figure 5.99 – Transient numerical dimensionless gas superficial velocity for Case 5.
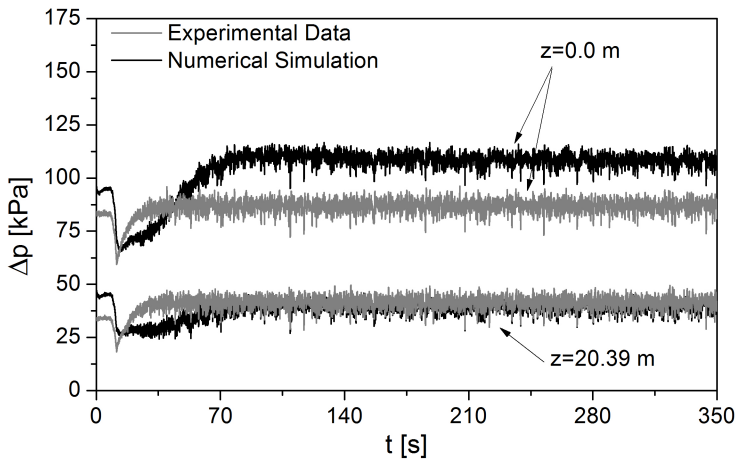
Figure 5.100 – Comparison between transient experimental and numerical pressure drop at $z = 0.0$ m and $z = 20.37$ m for Case 5.

Figure 5.101 – Comparison between transient experimental and numerical pressure drop at $z = 9.17$ m and $z = 32.59$ m for Case 5.
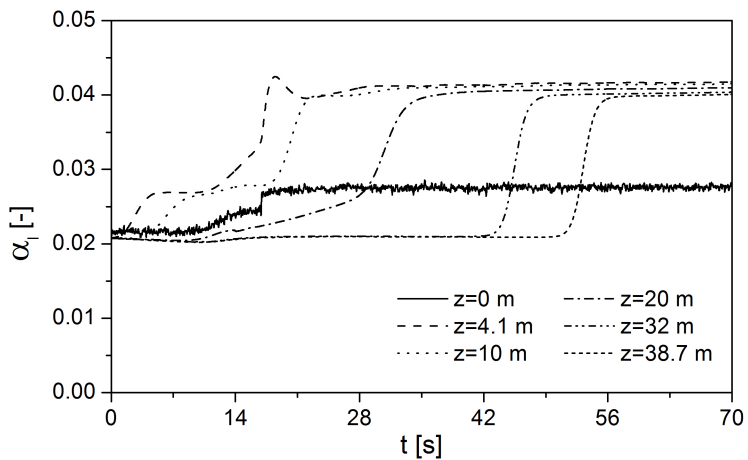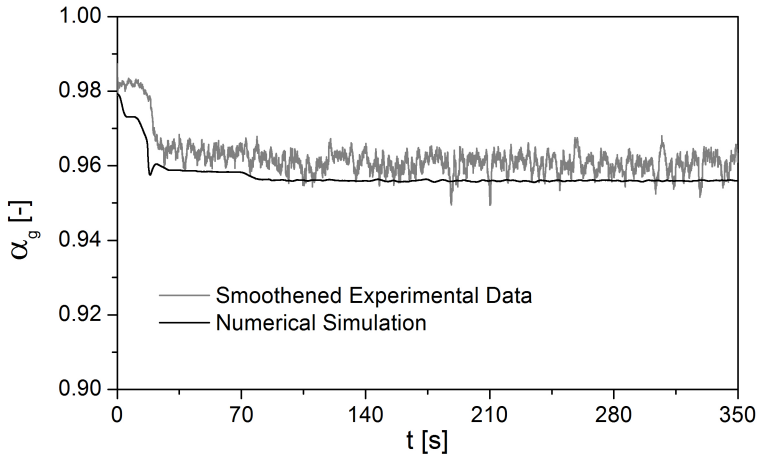

Figure 5.102 – Comparison between transient experimental and numerical void fraction at $z = 4.08$ m for Case 5.

The statistical analysis of Case 5 resulted in following parameters for the pressure difference: AAD=13.58%, RMS=0.123% and Bias=4.86%; and, AAD=14.91%, RMS=0.131% and Bias=-14.62% for void fraction.
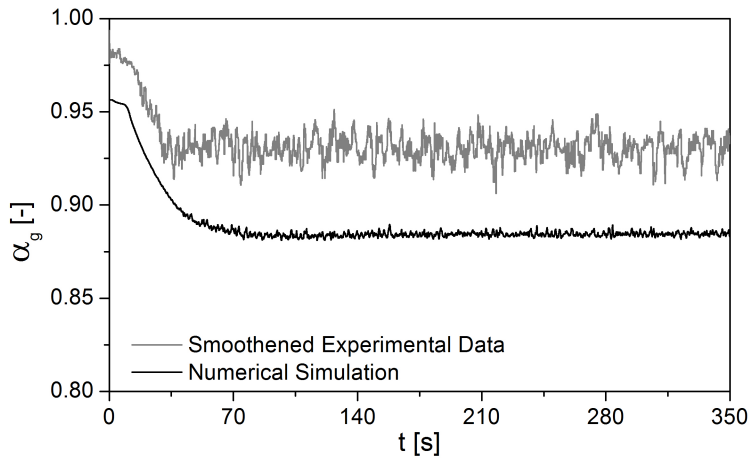
Figure 5.103 – Comparison between transient experimental and numerical void fraction $z = 38.73$ m for Case 5.

As in Case 4, annular flow was predicted for the whole duration of Case 5 ($u_{gS}^* > 1.0$), despite the visual observation of flow reversals by Waltrich (2012). In order to evaluate the sensitivity of the model to a change in the critical dimensionless gas flow rate (Wallis criterion), as done for Case 4, the churn-annular transition criterion was changed to $u_{gS}^* = 1.25$ so that the churn flow governing equations could be solved for part of the experimental run. Again, as in Case 4, the boundary conditions are smoothened using an adjacent-averaging algorithm with a 250-point window (PRESS *et al.*, 1992).

Figure 5.104 shows the calculated dimensionless gas velocity as a function of time for different axial positions using the smoothened Case 5 boundary conditions. The transition form annular to churn flow occurs between 15 and 25 s according to the redefined criterion. The results for pressure drop and void fraction for the smoothened Case 5 are in good qualitative agreement with the original Case 5. Nevertheless, the occurrence of churn flow in the smoothened Case 5 led to lower values of the void fraction (thicker films), which resulted in larger gravitational pressure gradients and higher pressure drops than those predicted with the original transition criterion. For this reason, the statistical parameters for the smoothened Case 5 were AAD=27.4%, RMS=0.2% and Bias= 27.3% for the pressure drop, and AAD=17.4%, RMS=0.31% and Bias=-17.3% for the void fraction, which are all larger than fr the original Case 5.

It should be mentioned that it was necessary to apply an under-relaxation factor equal to 0.8 on the source terms in order to guarantee the numerical convergence of smoothened Case 5 due to instabilities associated with transition to and from the two-filed and trhee-field churn flow models at around 70 s.
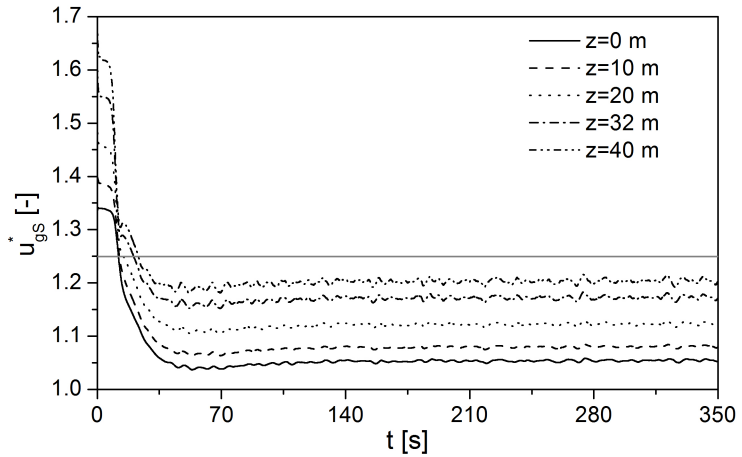
Figure 5.104 – Transient numerical dimensionless gas superficial velocity for Case 5 (smoothened).

5.2.2 Mass flux-induced transients

In this section, the mass flux-induced transient modeling results are compared with the experimental data. In these tests the inlet liquid mass flux is the only variable controlled. Any fluctuations or changes in other variables such as inlet gas mass flux or pressure outlet are a response to that liquid mass flux alteration. Three different cases are discussed in the light of the transient pressure drop behavior at four different pipe locations (calculated in the same way as in Section 5.2.1) and of the transient void fraction behavior at three different pipe locations. Table 5.3 shows the initial and final boundary conditions of the mass flux-induced transients.

Table 5.3 – Nominal values of the initial (I) and final (F) steady-state parameters of the pressure-induced transients.

	Case 6	Case 7	Case 8
$G_g(I)$ [kg m^{-2}s^{-1}]	28	43	37
$G_g(F)$ [kg m^{-2}s^{-1}]	33	37	43
$G_l(I)$ [kg m^{-2}s^{-1}]	289	19	285
$G_l(F)$ [kg m^{-2}s^{-1}]	19	285	19
$p_{out}(I)$ [kPa]	383	262	400
$p_{out}(F)$ [kPa]	240	400	260
Flow Pattern (I)	(C)	(A)	(C)
Flow Pattern (F)	(A)	(C)	(A)

Figures 5.105 to 5.107 show the instantaneous outlet pressure, inlet liquid and inlet gas mass fluxes during the Case 6 transient test. The decrease in the outlet pressure results directly from the instantaneous reduction of the inlet liquid mass flux from almost 300 kg m^{-2}s^{-1} to approximately 20 kg m^{-2}s^{-1}. This causes an increase of the gas mass flux (see Fig. 5.107).

Figure 5.108 shows the behavior of the calculated u_{gS}^* as a function of time for different positions from the inlet. In this case, the transient occurs in the opposite direction compared to the pressure-induced tests, i.e., starting with a lower u_{gS}^* and accelerating to a higher u_{gS}^*. Nevertheless, the fluctuations associated with the outlet pressure conceal the evolution of u_{gS}^* for $z < 40.0$ m. According to the visual observations of Waltrich (2012), the flow started as churn flow but later developed into annular flow. The oscillations in the initial steady-state are characteristic of churn flow, while the smoother behavior in the final steady-state is more typical of annular flow at low liquid fractions.
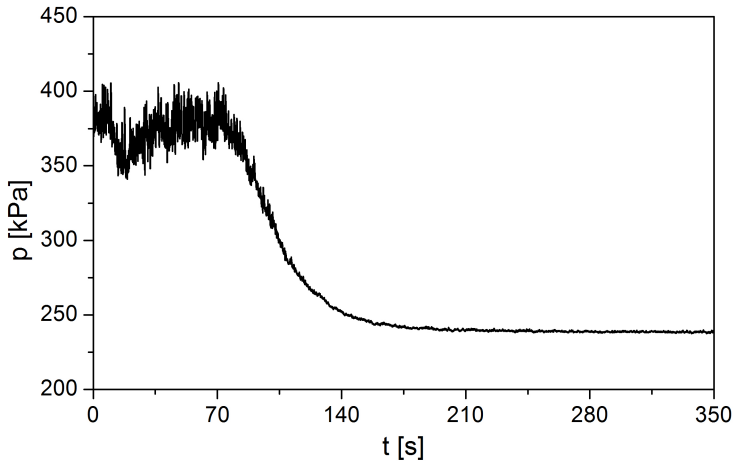
Figure 5.105 – Transient outlet pressure boundary condition for Case 6.
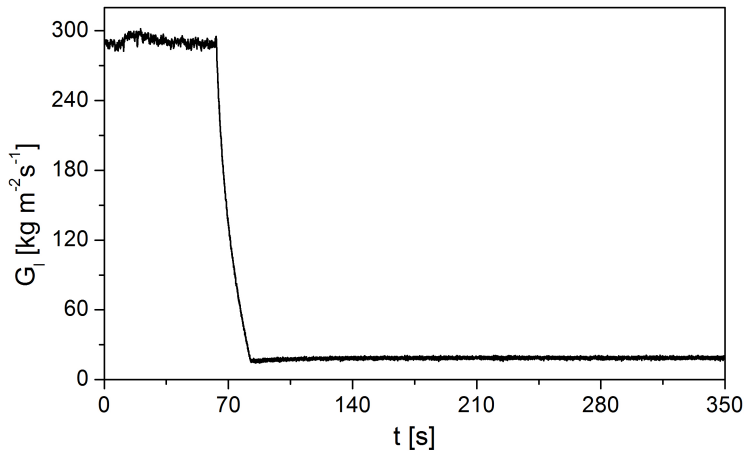
Figure 5.106 – Transient inlet liquid mass flux boundary condition for Case 6.

Figure 5.108 does not show a transition to annular flow, as predicted
by the model according to the Wallis criterion (WALLIS, 1969). How-
ever, in this particular case, the program starts under the two-field
formulation (to be able to deal with the high oscillations of the low
u_{gS}^* churn flow pattern) and then transitions to the more physically
sound three-field formulation allowing for droplet interchange between
the two liquid fields. This was the only case in which this mathematical
formulation transition happened in this order, illustrating the robust-
ness of the numerical model in being able to deal with changes in the
number of governing equations in both ways.

Figures 5.109 and 5.110 show the transient variation of pressure
difference between the outlet pressure and those measured at the points
indicated in the figures (calculated as in the previous pressure-induced
transient cases) for Case 6. The agreement is quite remarkable as the
numerical model consistently reproduces the data for the entire run.

Figures 5.111 to 5.113 present a comparison of the numerical and
experimental void fraction at different pipe locations. Very good agree-
ment is also observed, which adds to the conclusion that the prediction
of the liquid phase distribution along the channel is of great significance
in these flows due to the importance of the gravitational pressure drop.

The statistical analysis of Case 6 resulted in the following cal-
culated overall parameters for the pressure difference: AAD=4.02%,
RMS=0.047% and Bias=-2.64%. The statistical parameters for the
void fraction were: AAD=11.23%, RMS=0.138% and Bias=4.26% for
void fraction.

Numerical simulations of Case 6 with smoothened boundary con-
ditions – 250-point window using the Press *et al.* (1992) adjacent-
averaging algorithm – resulted in a very similar model performance
for a churn-annular transition criterion of $u_{gS}^* = 1.0$. The statisti-
cal parameters for the smoothened Case 6 (AAD=7.8%, RMS=0.13%
and Bias=-1.4% for pressure drop and AAD=5.5%, RMS=0.06% and
Bias=-3.7% for the void fraction) were, however, slightly worse than
the original Case 6 due to a small underestimation of the experimental
data at $z = 0.0$ m in the smoothened case. It should be mentioned that
attempts to redefine the Wallis criterion (WALLIS, 1969) to $u_{gS}^* = 0.9$
resulted in severe divergence of the numerical solution at around 85
seconds, even after the introduction of a source term under-relaxation
of 0.55. This was caused by the transition from two-field formulation to
the three-field formulation and back to the two-field formulation under
different flow patterns.
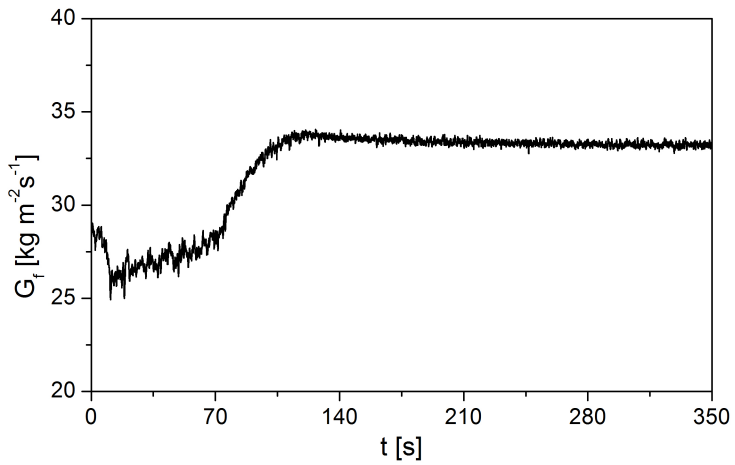
Figure 5.107 – Transient inlet gas mass flux boundary condition for Case 6.
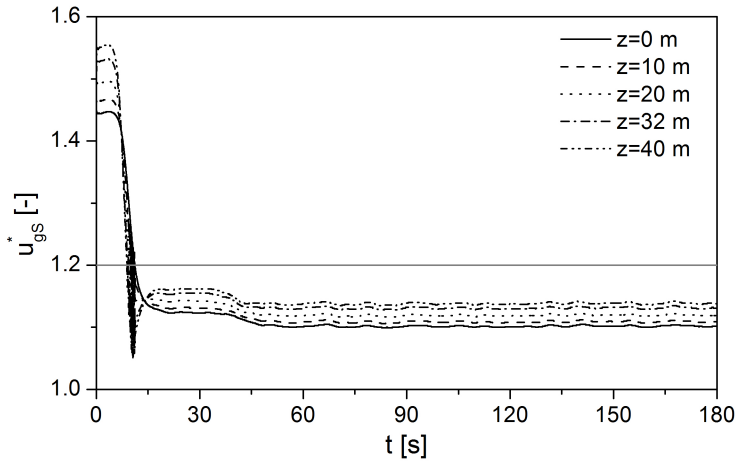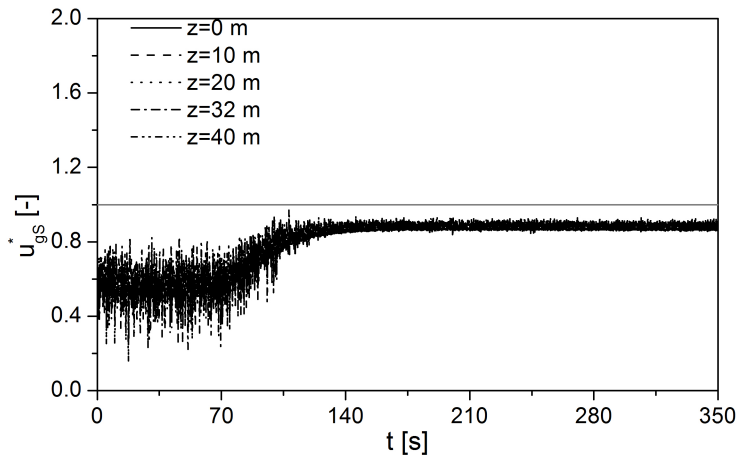

Figure 5.108 – Transient numerical dimensionless gas superficial velocity for Case 6.

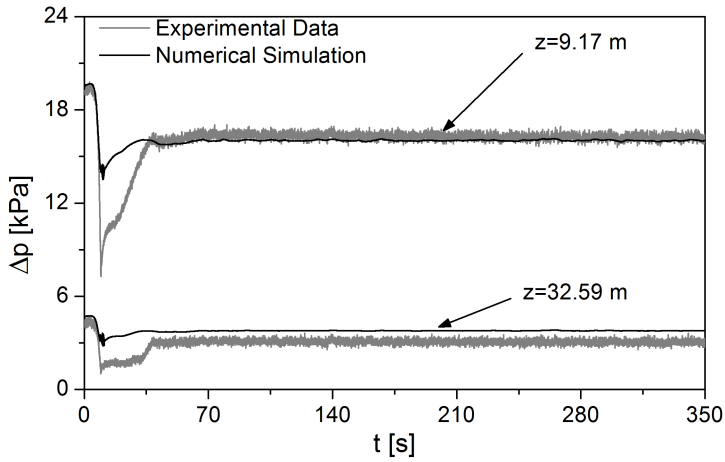Figure 5.109 – Comparison between transient experimental and numerical pressure drop at $z = 0.0$ m and $z = 20.37$ m for Case 6.
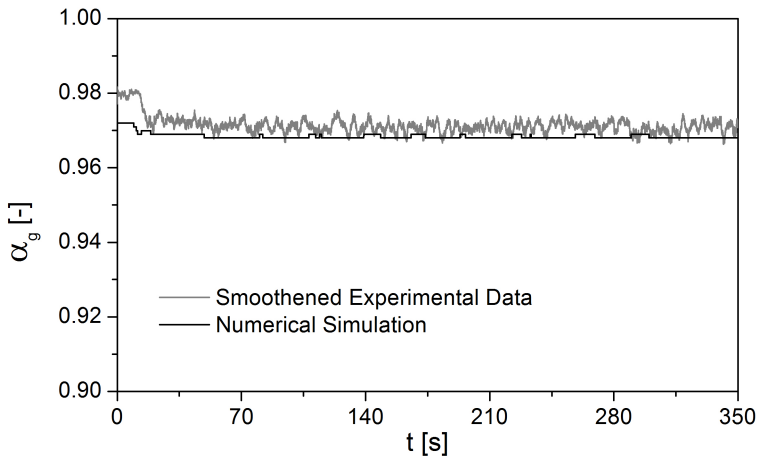

Figure 5.110 – Comparison between transient experimental and numerical pressure drop at $z = 9.17$ m and $z = 32.59$ m for Case 6.
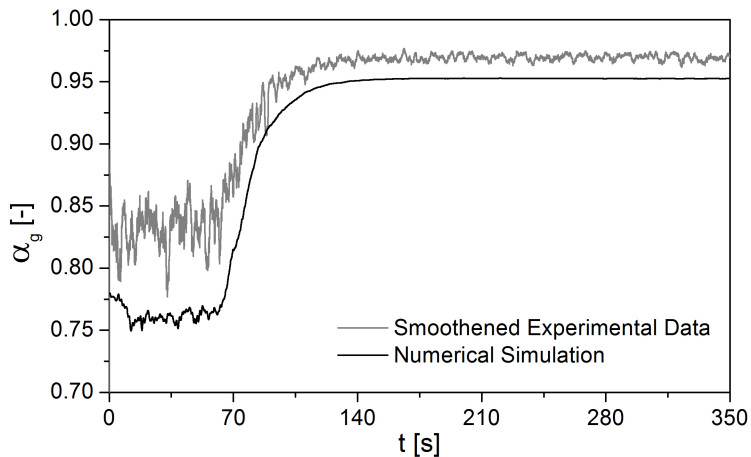
Figure 5.111 – Comparison between transient experimental and numerical void fraction at $z = 4.08$ m for Case 6.
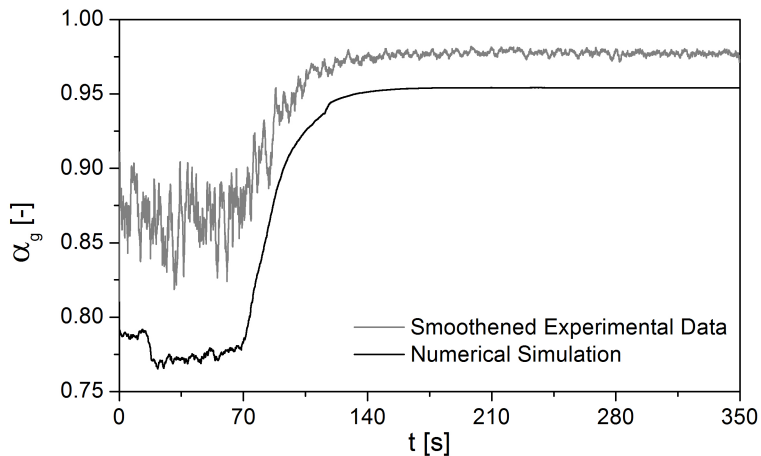
Figure 5.112 – Comparison between transient experimental and numerical void fraction $z = 24.46$ m for Case 6.

Figure 5.113 – Comparison between transient experimental and numerical void fraction $z = 38.73$ m for Case 6.

Figures 5.114 to 5.116 show the input experimental data/ boundary conditions used in the numerical simulation of Case 7. In this case the transient behavior is triggered by a sudden increase of the inlet liquid mass flux. This represents an opposite scenario in relation to Case 6. According to the visual observations of Waltrich (2012), the flow started as stable annular flow, but suffered a transition to churn flow following the liquid mass flux increase.
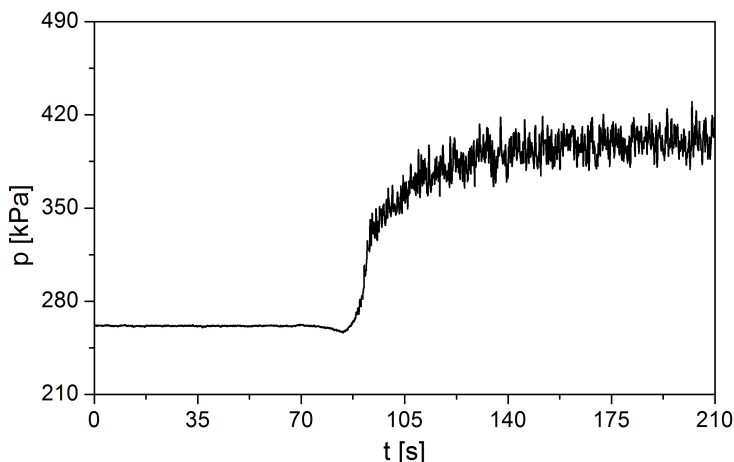
Figure 5.114 – Transient outlet pressure boundary condition for Case 7.

Figure 5.117 shows the calculated u_{gS}^* as a function of time for different pipe locations, showing that according to the Wallis (1969) flow reversal criterion, the flow passes from annular to churn at approximately 90 seconds into the run. After the program reaches a somewhat stable churn flow pattern, a few instabilities (due to elevated residuum triggering the two-field formulation) indicate transition to annular flow and back to churn flow. The change in formulation along with the already highly oscillating gas mass flux boundary condition generates peaks in the local instantaneous gas velocity and the program, oscillates between the two and three-field formulations. Once the three-field formulation is re-established, the local instantaneous gas velocity diminishes and the flow returns to the churn pattern. The transitions occur throughout the pipe and are not a localized phenomenon. These are also unrealistic and should be neglected. When the smoothened
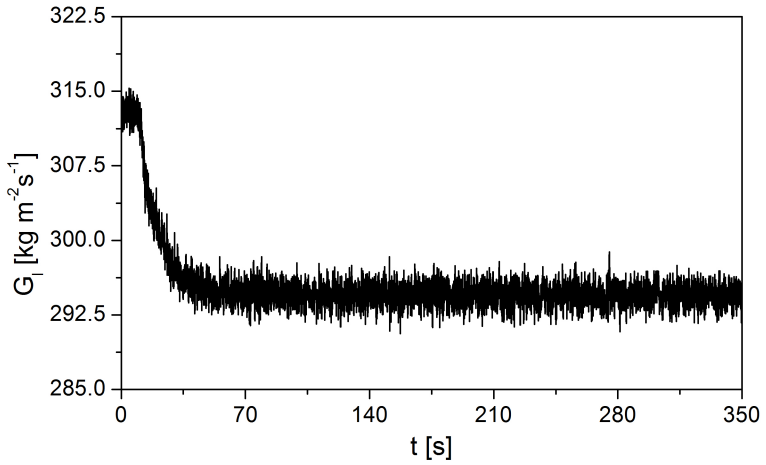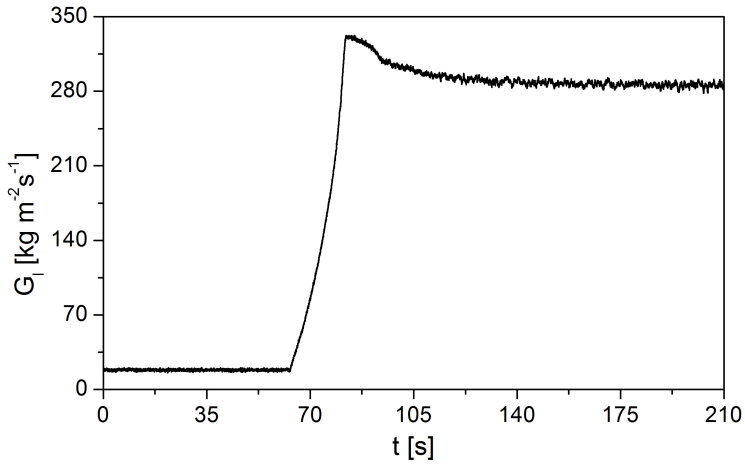
Figure 5.115 – Transient inlet liquid mass flux boundary condition for Case 7.
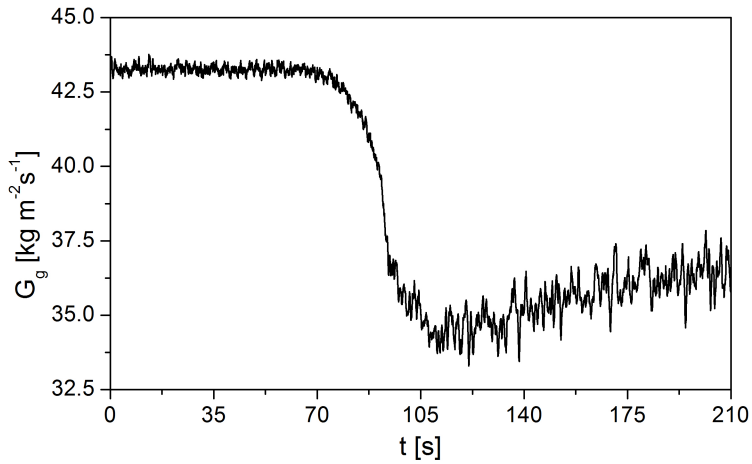
Figure 5.116 – Transient inlet gas mass flux boundary condition for Case 7.

boundary conditions are used, only the strong oscillations at $u^*_{gS} \approx 1.0$ persisted, as a result of the substantial rise in liquid velocity (see Fig. 5.118).
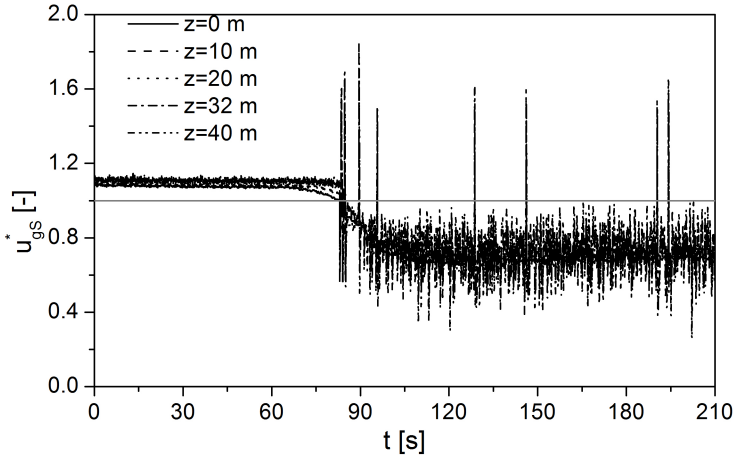
Figure 5.117 – Transient numerical dimensionless gas superficial velocity for Case 7.

Figures 5.119 and 5.120 show a comparison of the pressure differences between the outlet pressure and the pressure measurements at the positions indicated in the figures (calculated as in previous cases) for Case 7. Good agreement is observed between the model and the data in both the annular and churn flow regions. In the model, the flow pattern transition point, taking place at around 90 s is marked by a strong oscillation that is not actually observed in the experimental data. A detailed observation of the void fraction profiles in Figs. 5.121 to 5.123 reveals that those are caused by a sharp decrease in void fraction predicted by the model at the transition point, which gives rise to a localized inverted peak in the gravitational component of the total pressure gradient along the entire test section. The sharp decrease in void fraction, in turn, is due to the increase in liquid flow rate that triggers the flow regime transition. Despite the slight under prediction of the void fraction in the first part of the test (steady-state annular flow), the general agreement between the model and the data can be considered satisfactory for the conditions of Case 7.

The statistical analysis for Case 7 resulted in the following pa-
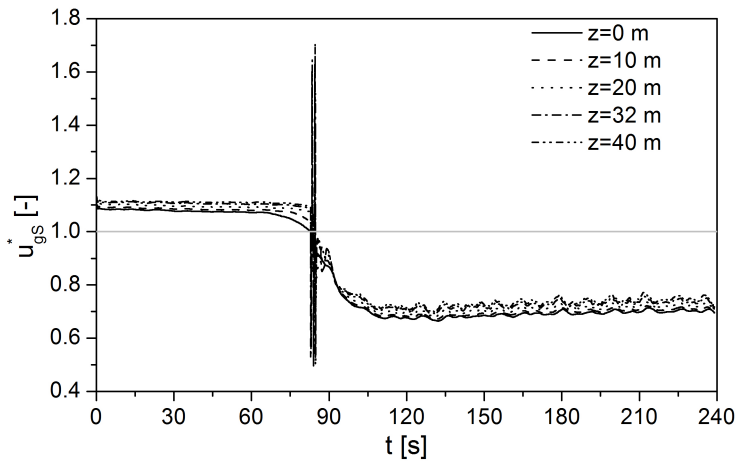
Figure 5.118 – Transient numerical dimensionless gas superficial velocity for Case 7 (smoothened).
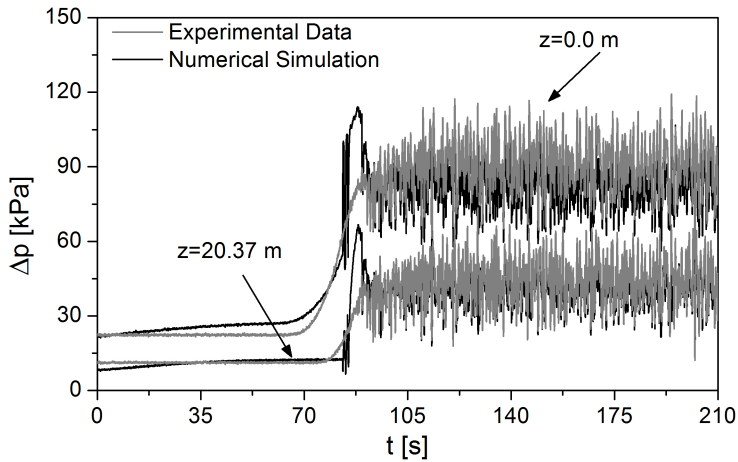
Figure 5.119 – Comparison between transient experimental and numerical pressure drop at $z = 0.0$ m and $z = 20.37$ m for Case 7.
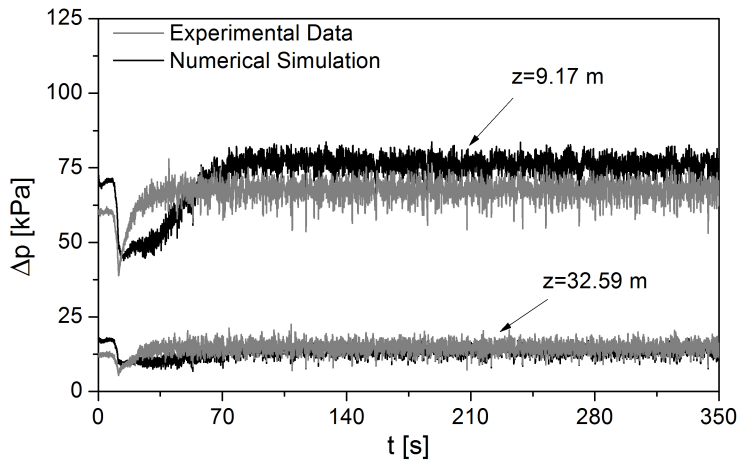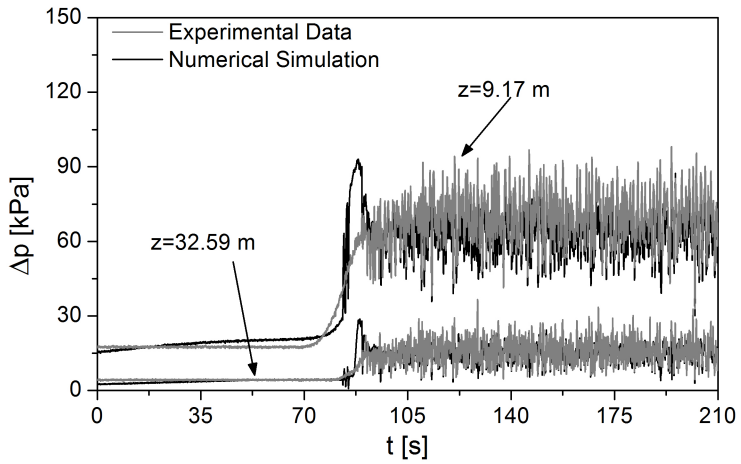
Figure 5.120 – Comparison between transient experimental and numerical pressure drop at $z = 9.17$ m and $z = 32.59$ m for Case 7.
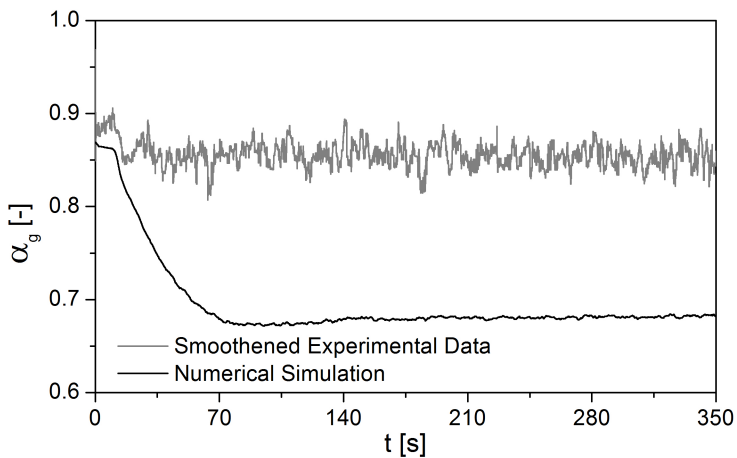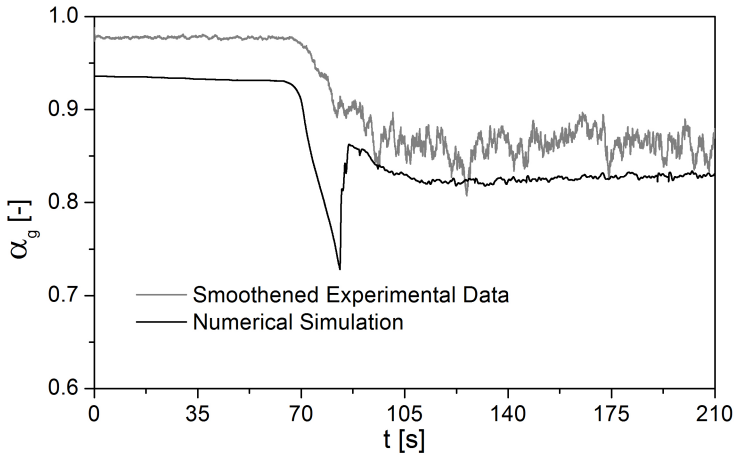

Figure 5.121 – Comparison between transient experimental and numerical void fraction at $z = 4.08$ m for Case 7.
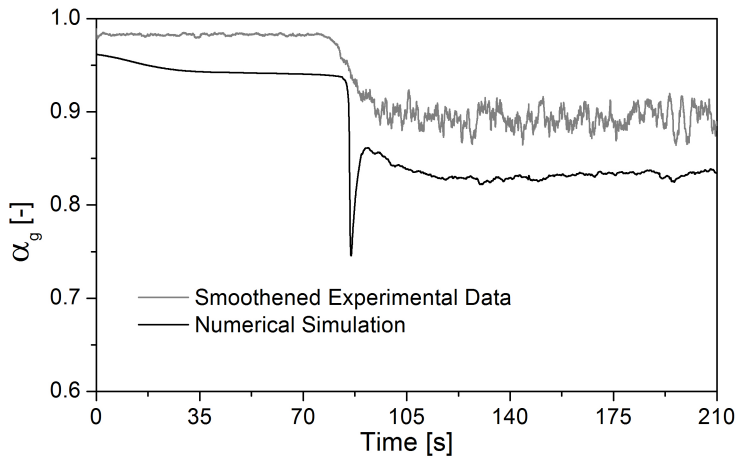
Figure 5.122 – Comparison between transient experimental and numerical void fraction $z = 24.46$ m for Case 7.
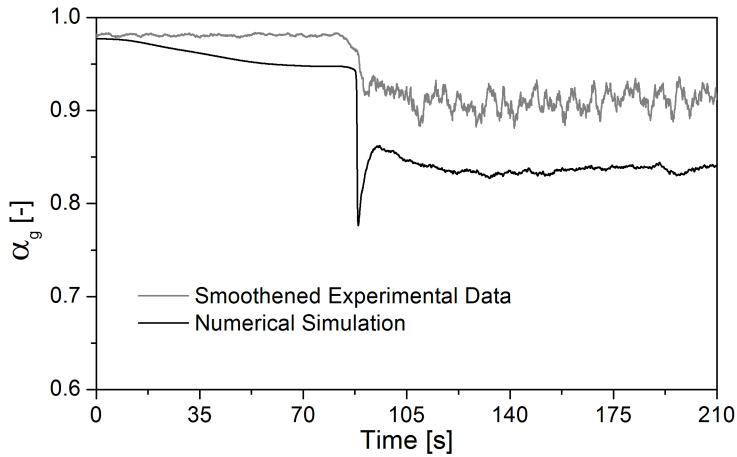
Figure 5.123 – Comparison between transient experimental and numerical void fraction $z = 38.73$ m for Case 7.

rameters for the pressure difference: AAD=11.88%, RMS=0.153% and Bias=-3.10%; and, For void fraction the statistical parameters were: AAD=7.94%, RMS=0.093% and Bias=-4.88%.

As discussed in some of the previous cases (Cases 5 and 7) during the boundary condition change, and consequently the annular to churn transition, the program oscillates heavily (even when the boundary conditions had been smoothened). This is not a desired behavior, and to investigate its cause, two additional simulations were performed. It was hypothesized that two main aspects could be contributing to the oscillation: the change in closure relationships for annular and churn flows and the change between the three and two-field formulations, which were occurring almost simultaneously. Therefore, Case 7 was simulated again (with smoothened boundary conditions), however, this time the program was locked in the two-field simulation, but still allowed to transition between the flow patterns. As can be seen in Fig. 5.118, the oscillations during the annular to churn transition persisted, but the output results were fairly similar to the ones obtained initially. the simulation of Case 7 with the same restrictions as above, but considering the interfacial and wall friction factor correlations to be that of churn flow (JAYANTI; BRAUNER, 1994) made the oscillations in the dimensionless gas superficial velocity disappear (see Fig. 5.124). The nominal values of the initial and final steady-states, however, remained unchanged.

The pressure difference behavior for this all-churn flow case is shown in Figs. 5.125 and 5.126. The representation of the initial and final steady-states is almost identical to the original simulation. The difference that arises during the transition, however, almost disappears and the overall agreement with the experimental curve in this region is greatly improved. The void fraction behavior is shown in Figs 5.127 to 5.129 and similarly to the pressure difference the steady-states are in good agreement with the original simulation. The most noticable difference is the absence of the marked void fraction decrease during the transition. Once again, the representation of this region was greatly improved by considering churn flow only during the entire simulation.

Through the analysis of this simulation (two-field formulation and churn flow closure relationships only) it is clear that for the transition region, when the change in liquid mass fluxes is high, the use of annular flow closure relationships is not advised. A different correlation must be used and the mathematical model must be able to cope with the extreme redistribution and oscillation of the variables when it transits between annular and churn flow. When the flow was considered to be
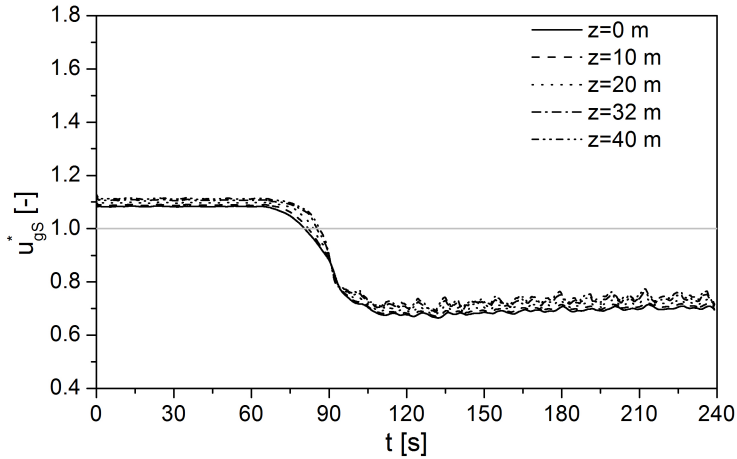
Figure 5.124 – Transient numerical dimensionless gas superficial velocity for Case 7 (smoothened and with modified interfacial friction factor).
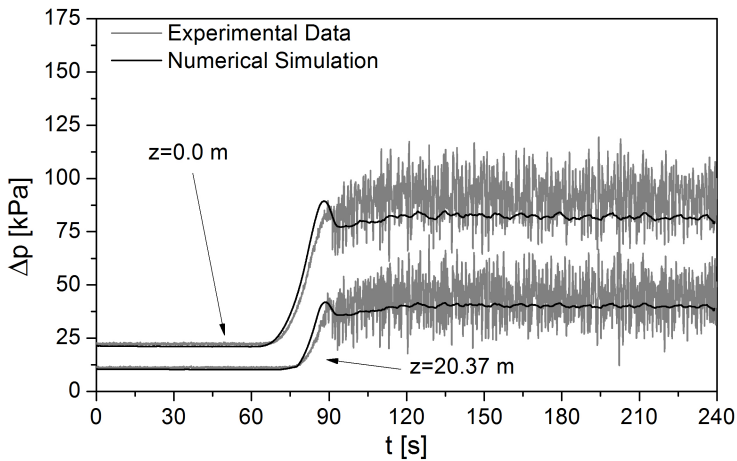
Figure 5.125 – Comparison between transient experimental and numerical pressure drop at $z = 0.0$ m and $z = 20.37$ m for Case 7 (smoothened and with modified interfacial friction factor).
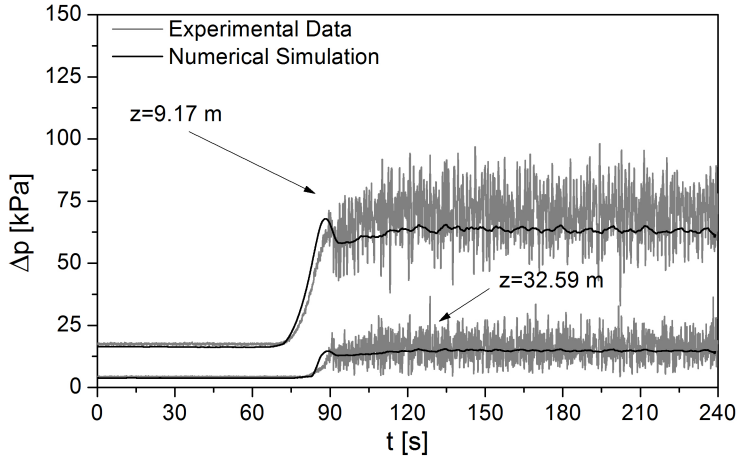
Figure 5.126 – Comparison between transient experimental and numerical pressure drop at $z = 9.17$ m and $z = 32.59$ m for Case 7 (smoothened and with modified interfacial friction factor).
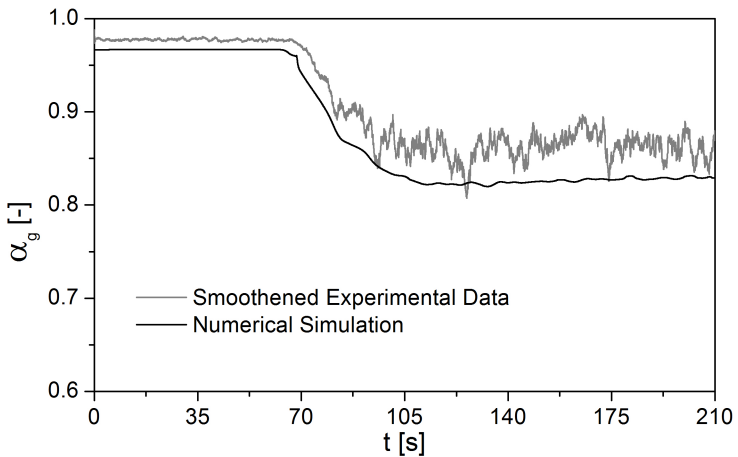
Figure 5.127 – Comparison between transient experimental and numerical void fraction at $z = 4.08$ m for Case 7 (smoothened and with modified interfacial friction factor).
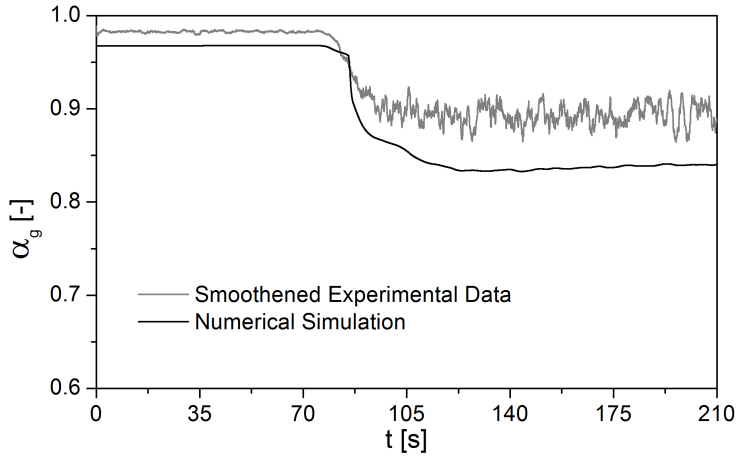
Figure 5.128 – Comparison between transient experimental and numerical void fraction $z = 24.46$ m for Case 7 (smoothened and with modified interfacial friction factor).
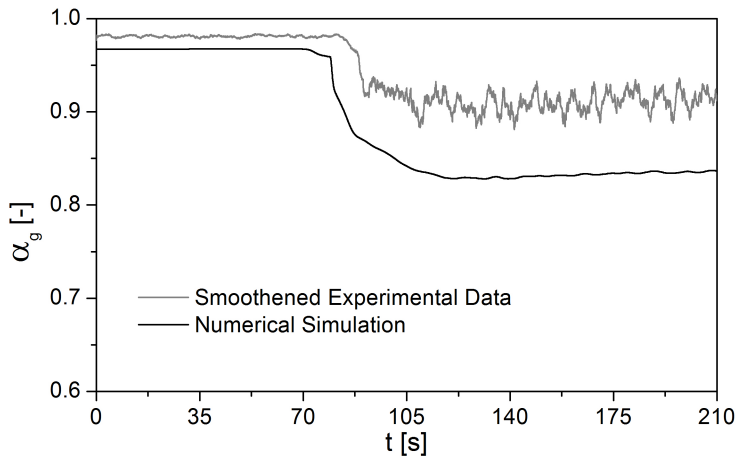
Figure 5.129 – Comparison between transient experimental and numerical void fraction $z = 38.73$ m for Case 7 (smoothened and with modified interfacial friction factor).

only churn flow, the calculated friction factor was increased (the shear stresses in churn flow are higher) and so the oscillations created by the change in the boundary condition could be dampened.

Figures 5.130 to 5.132 show the input experimental data used as boundary conditions for the numerical simulation of Case 8, which is qualitatively very close to Case 6. The abrupt decrease in the liquid mass flux takes place between 70 and 90 seconds into the test.
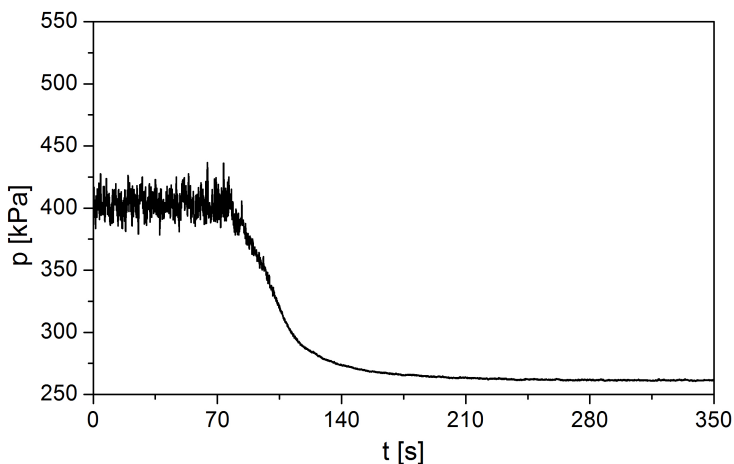
Figure 5.130 – Transient outlet pressure boundary condition for Case 8.

Figure 5.133 shows the calculated u_{gS}^* distributions as a function of time and position for Case 8. A major difference between this case and Case 6 is that a transition to annular flow was not predicted in the latter due to the divergence that occurs when the Wallis criterion (WAL-LIS, 1969) was recalibrated. The model predicts severe fluctuations in the churn flow region and during the transition. These oscillations take place throughout the pipe and are basically due to oscillations in pressure brought into the model by the boundary conditions. Although the pressure oscillations are a real aspect of the churn flow pattern at high liquid mass fluxes, when combined with the mass flux oscillations, they bring about the instabilities (false flow pattern transitions) observed in the model. Again, as in Case 7, when the oscillations in the boundary conditions are numerically filtered using a 250-point window adjacent-averaging algorithm (PRESS *et al.*, 1992),only the instabilities around
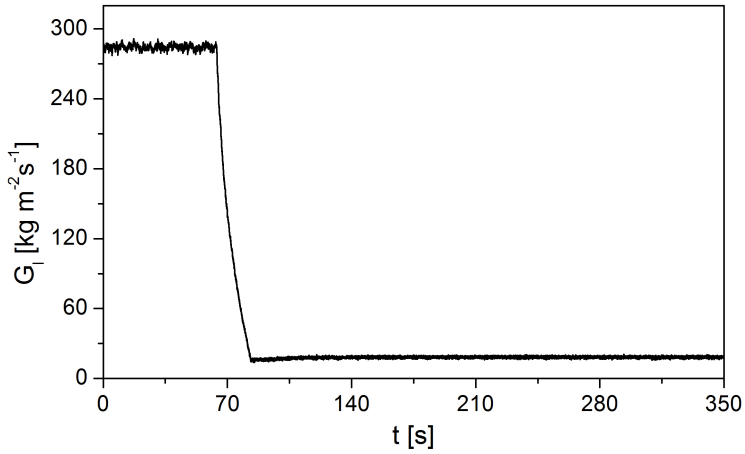
Figure 5.131 – Transient inlet liquid mass flux boundary condition for Case 8.
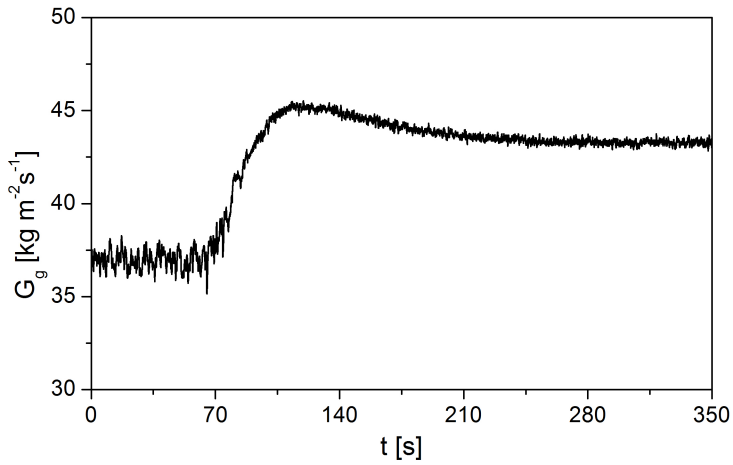
Figure 5.132 – Transient inlet gas mass flux boundary condition for Case 8.

the instant of flow transition are observed, as can be seen from Fig. 5.134. These are, however, quickly transported downstream as in Case 7.

Voltar aqui!
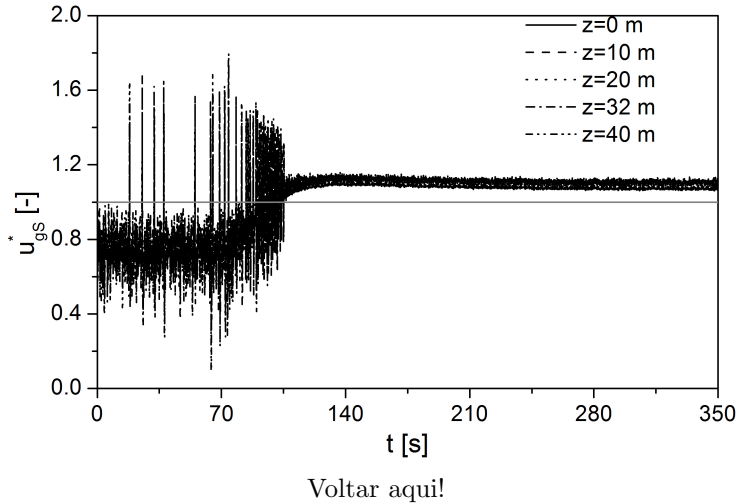
Figure 5.133 – Transient numerical dimensionless gas superficial velocity for Case 8.

Figures 5.135 and 5.136 show a comparison between the calculated and experimental transient pressure difference between the outlet pressure and the positions indicated in the figures for Case 8. The numerical model predicts the initial steady-state interval quite consistently and the transition to the final steady-state is also well represented, with only minor discrepancies due to the sharp flow regime transition calculated by the model.
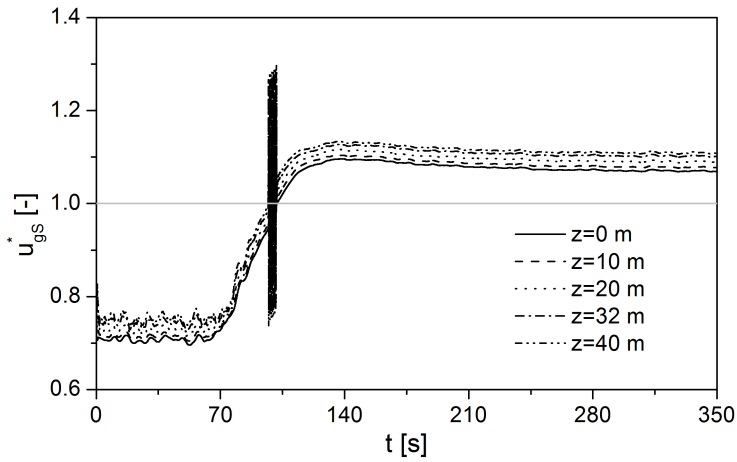
Figure 5.134 – Transient numerical dimensionless gas superficial velocity for the smoothed Case 8.
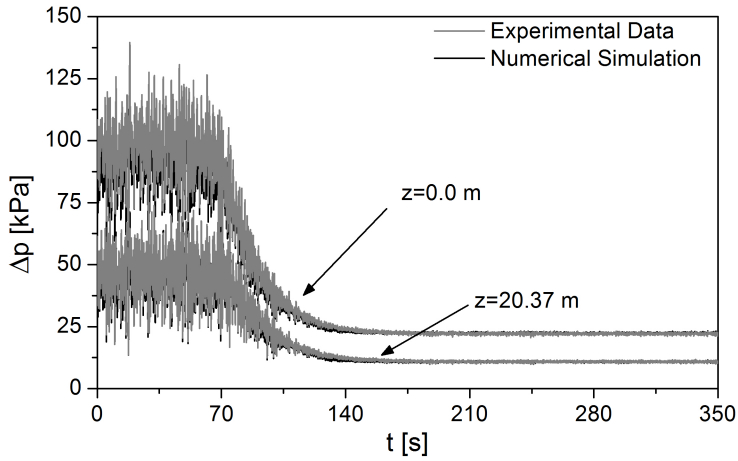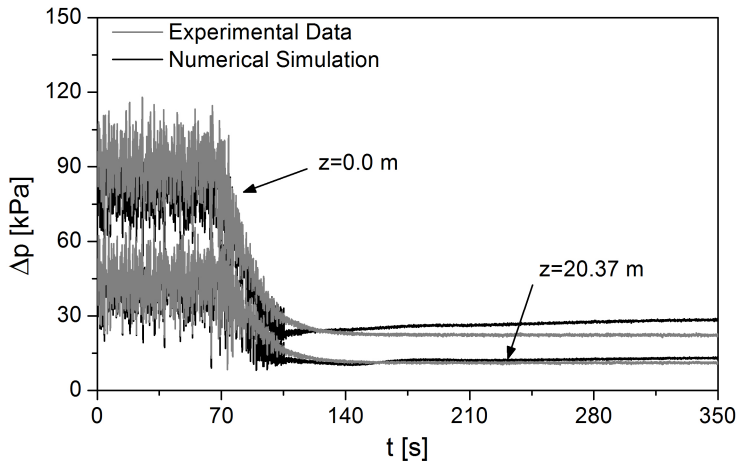

Figure 5.135 – Comparison between transient experimental and numerical pressure drop at $z = 0.0$ m and $z = 20.37$ m for Case 8.
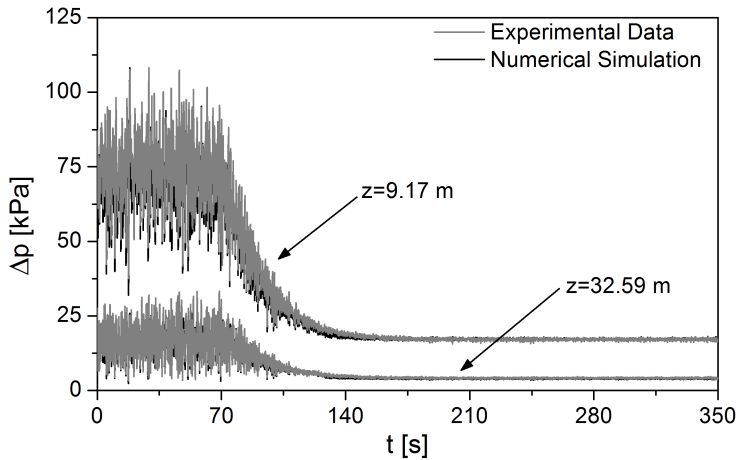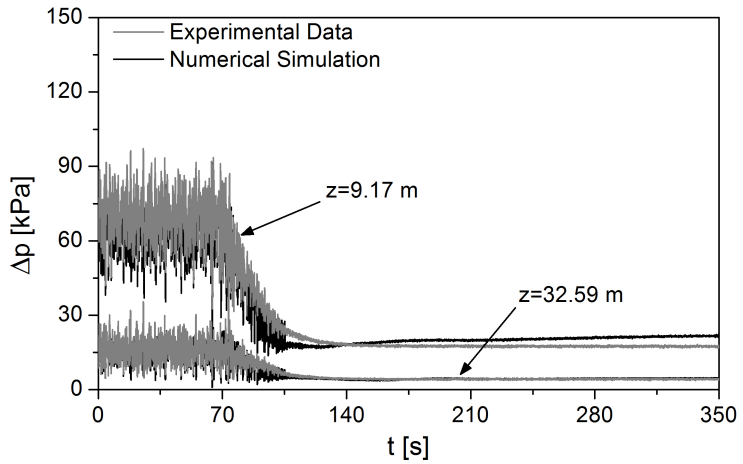
Figure 5.136 – Comparison between transient experimental and numerical pressure drop at $z = 9.17$ m and $z = 32.59$ m for Case 8.

Figures 5.137 to 5.139 show the comparison between calculated and experimental void fractions as a function of time for three different locations. The numerical representation is better for the initial churn flow period at $z = 4.08$ m, but improves for annular flow as the distance from the inlet increases. It should be noted that the three-field formulation was used throughout the simulation, in both the churn and annular flow patterns.
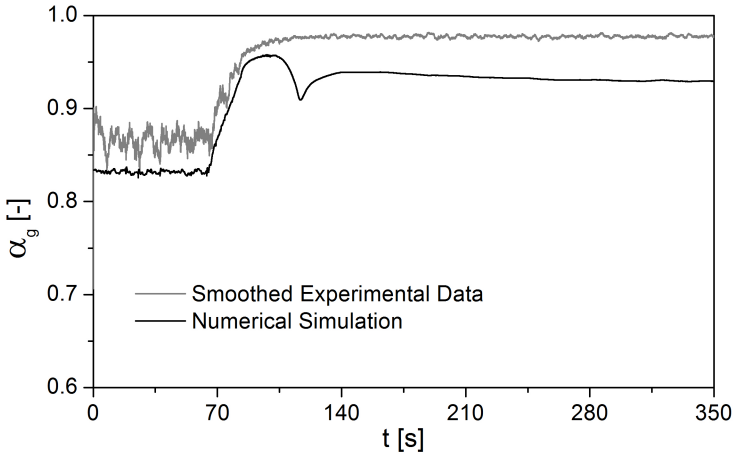
Figure 5.137 – Comparison between transient experimental and numerical void fraction at $z = 4.08$ m for Case 8.

The statistical analysis of Case 8 resulted in following parameters for the pressure difference: AAD=13.00%, RMS=0.115% and Bias=4.39%. For the void fraction the statistical parameters were: AAD=5.39%, RMS=0.050% and Bias=-4.22%.
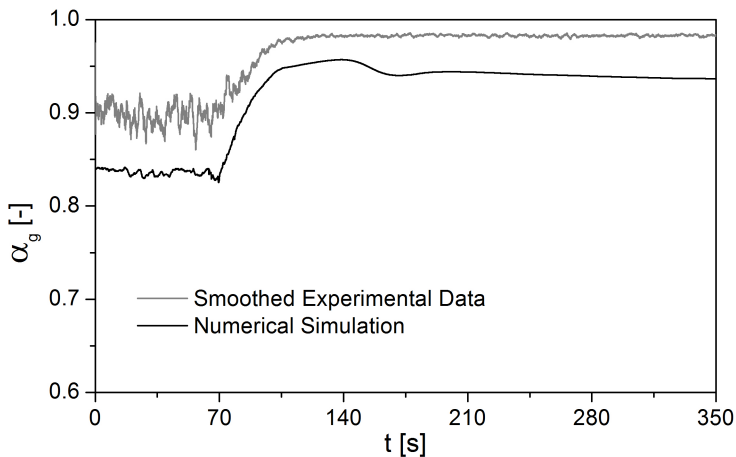
Figure 5.138 – Comparison between transient experimental and numerical void fraction $z = 24.46$ m for Case 8.

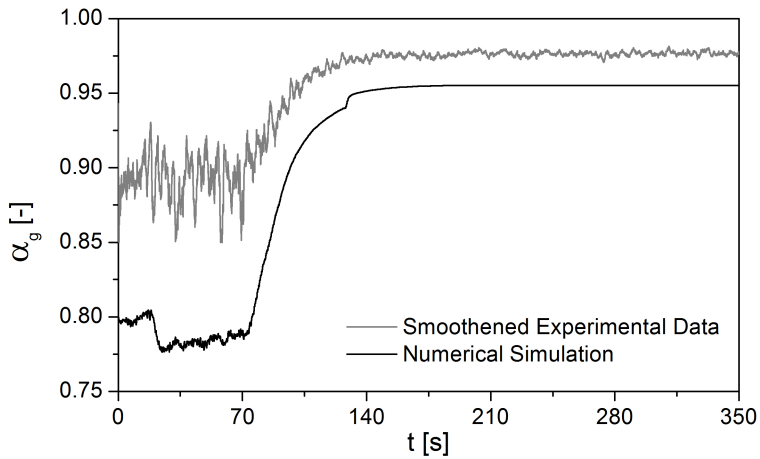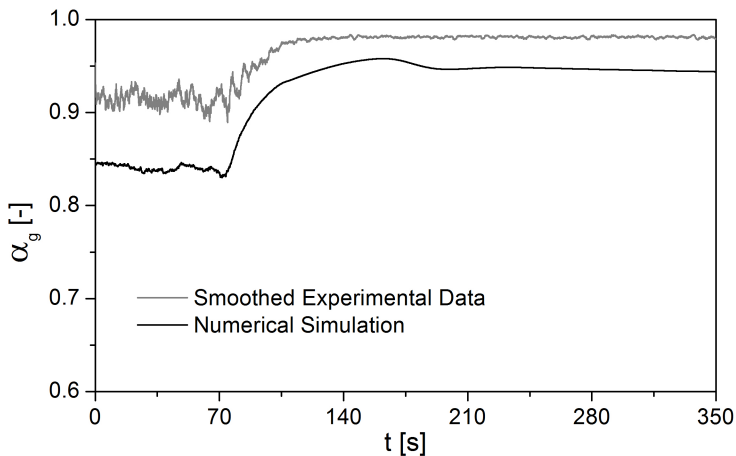Figure 5.139 – Comparison between transient experimental and numerical void fraction $z = 38.73$ m for Case 8.

An overall statistical analysis of all transient cases (Cases 1 to 8) provides the following parameters for the pressure difference AAD=46.2 %,RMS=9.26 %, and Bias=-17.0 %, while for void fraction the values are AAD=7.98%, RMS=0.09%, and Bias=-5.62%. The particularly high values of pressure difference parameters are due to the inability of the model in predicting the severe film breakup that occurs in Case 2. When Case 2 is removed from the statistical analysis, the new values of the statistical parameters are: AAD=14.5%,RMS=0.156%, and Bias=6.02% (for pressure difference) and AAD=7.87%,RMS=0.092%, and Bias=-5.31% (void fraction). Base on this body of data, a more accurate conclusion can be drawn, which indicates that the model is reasonably successful in predicting the transient churn-annular testes of Waltrich (2012), provided that a film flow pattern prevails during the transient test. In the event of a film breakup, the physical consistency of the model is lost, along with its ability to describe high gas fraction transient two-phase flows (as was the case in Case 2).

5.3   HYPOTHETICAL TRANSIENTS

This section presents three hypothetical transient simulations to demonstrate some further capabilities of the program. These scenarios are set to represent situations somewhat difficult to reproduce in an experimental setup. The geometric parameters are the same as those of TowerLab facility (WALTRICH, 2012)

The first hypothetical case (Case H1) is based on the change of only one boundary condition while keeping the others constant. The initial and final values of the boundary conditions are shown in Table 5.4. In this simulation, only the gas mass flux is changed, keeping the other boundary conditions constant. For all simulations, the initial fields are set to values based on the boundary conditions alone and are constant throughout the pipe (for initialization purposes), holding little physical consistency. Therefore, an initial period of 35 seconds is allowed for annular to develop into the real solution the the given set of boundary conditions. After this initialization process, the gas mass flux is decreased linearly from 71.9 to 39.7 kgm^{-2}s^{-1} in 25 s (see Fig. 5.140), before allowing a stable churn flow condition to be reached.

Figure 5.141 presents u_{gS}^* as a function of time at different locations along the pipe. The transition to churn flow according to the Wallis (1969) (u_{gS}^*=1.0) criterion occurs at approximately 48 s. In this hypothetical case, the three-field formulation is utilized throughout the whole simulation, and the transition point is characterized by oscilla-

Table 5.4 – Boundary conditions for Case H1.

Variable	Initial Value (Annular flow)	Final Value (Churn flow)
$G_{g,in}$ [kg m^{-2}s^{-1}]	71.90	39.70
$G_{l,in}$ [kg m^{-2}s^{-1}]	50.93	50.93
$e_{f,in}$	0.0001	0.0001
$T_{g,in}$ [K]	300	300
$T_{e,in}$ [K]	300	300
$T_{f,in}$ [K]	300	300
p_{out} [kPa]	520	520
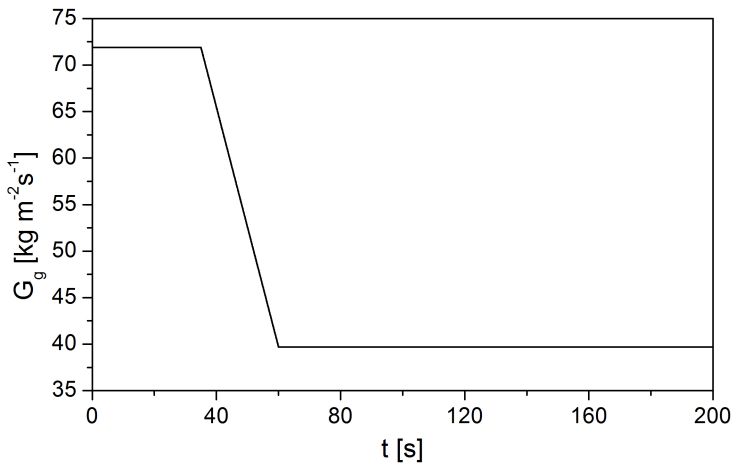
Figure 5.140 – Transient gas mass flux boundary condition for Case H1.

tions associated with the switching in the closure relationships for the two flow patterns.
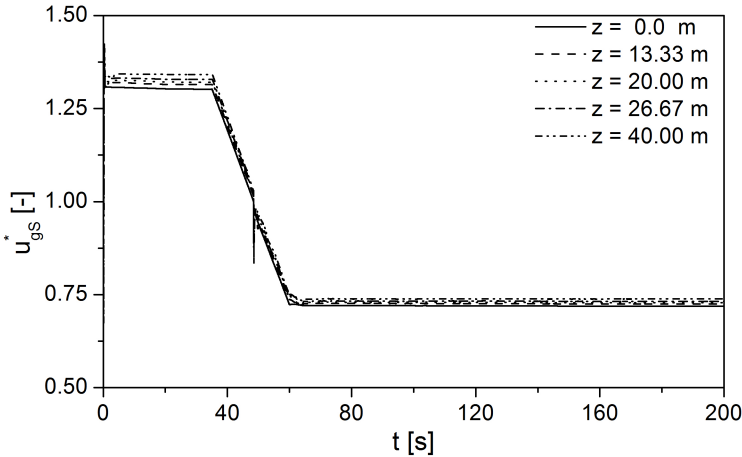
Figure 5.141 – Transient dimensionless gas superficial velocity for Case H1.

Figure 5.142 presents the absolute pressure as a function of time and the transition between annular and churn flow is clearly visible as the simulated time approaches 48 s. Here, the instantaneous peak in local absolute pressure that characterizes the transition is fast and stabilizes quickly along the pipe by propagating itself at the local two-phase mixture sound speed.

As can be seen from the figures detailing this simulation, the pressure stabilizes quickly after the flow transition and stabilization of the inlet gas mass flux. However, the void fraction takes much longer to reach steady-state. This is due to the fact that the variation in void fraction is transported with the liquid film velocity (Fig. 5.143), which is much lower than the sound speed that accounts for pressure propagation. In other words, after the transition to churn flow takes place, which is characterized by a sharp pulse in liquid holdup, a series of instabilities are generated in the lower portion of the pipe (visible at $z=13.33$ m). These instabilities tend to decrease in frequency as a function of time (they cease to exist at around 170 s for $z=13.33$ m) and disappear as the distance from the inlet increases.

Figures 5.144 and 5.145 show, respectively, pressure and void frac-
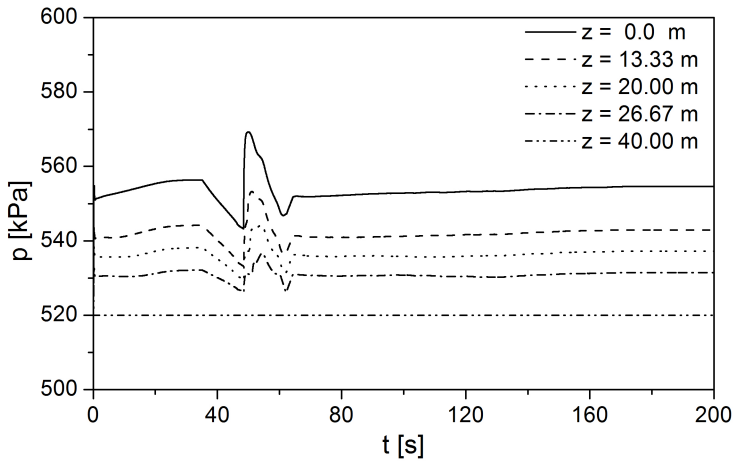
Figure 5.142 – Transient pressure for Case H1.
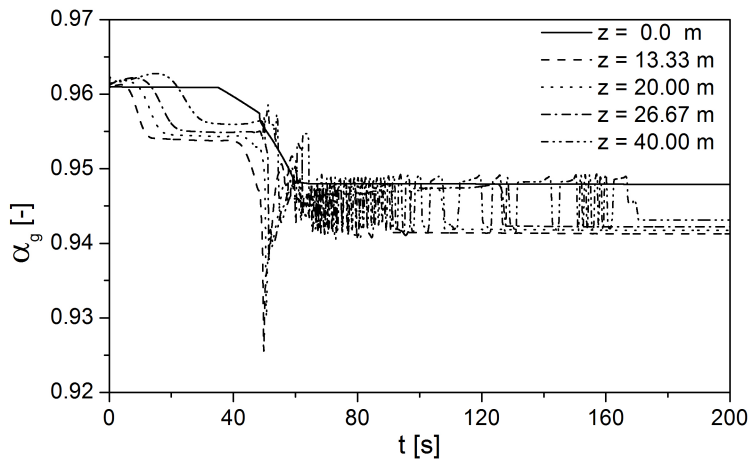
Figure 5.143 – Transient void fraction for Case H1.

tion profiles for different times after the start of the change in the inlet
gas mass flux. Once again it is easy to observe that the pressure stabi-
lizes much faster than the void fraction and with much less oscillation.
In this case only the inlet liquid mass flux is changed. The program is
started once again with constant fields based on the initial conditions
and the annular flow is allowed to develop for 90 s until stabilization,
after which the liquid mass flux is increased linearly during 70 s to
a new steady-state value (see Fig. 5.146). This second steady-state
condition is still under annular flow without a transition to churn flow.
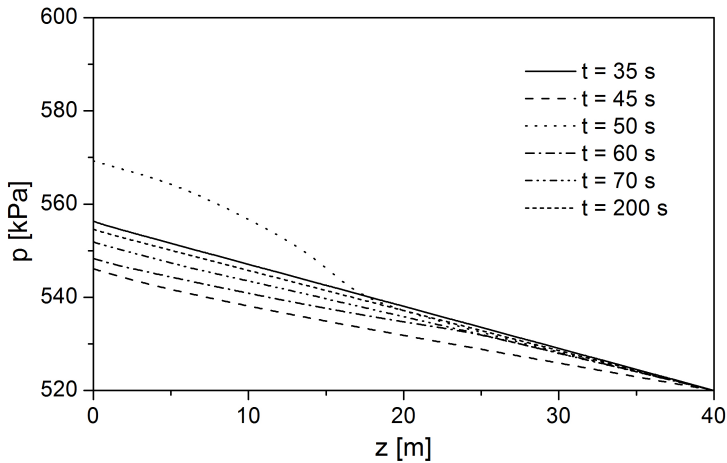
Figure 5.144 – Transient pressure profiles for Case H1.
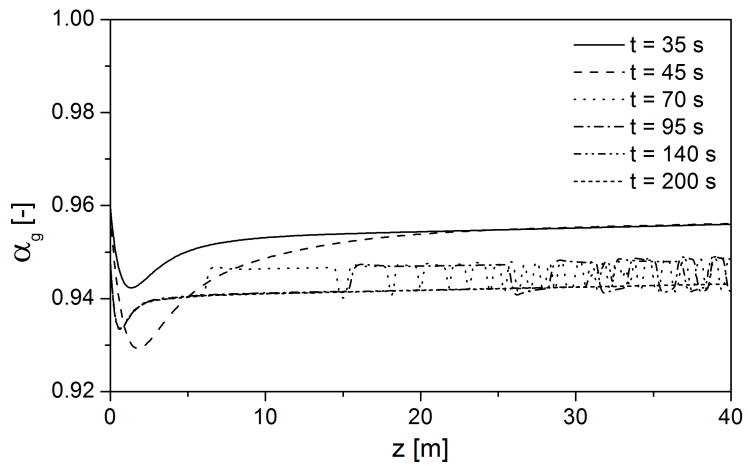
Figure 5.145 – Transient void fraction profiles for Case H1.

The second hypothetical case (Case H2) is also based on changing only one boundary condition while keeping the others constant. The initial and final values of the boundary conditions are shown in Table 5.5.

Table 5.5 – Boundary conditions for Case H2.

Variable	Initial Value (No entrainment)	Final Value (With entrainment)
$G_{g,in}$ [kg m^{-2}s^{-1}]	100.0	100.0
$G_{l,in}$ [kg m^{-2}s^{-1}]	10.0	120.0
$e_{f,in}$	0.0001	0.0001
$T_{g,in}$ [K]	300	300
$T_{e,in}$ [K]	300	300
$T_{f,in}$ [K]	300	300
p_{out} [kPa]	300	300
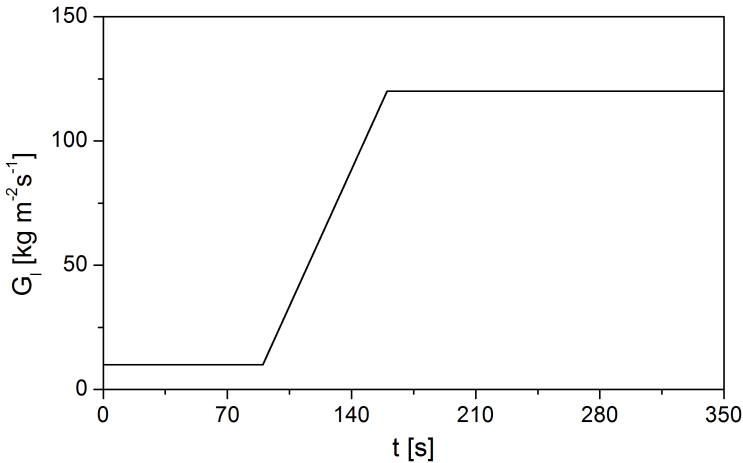
Figure 5.146 – Transient liquid mass flux boundary condition for Case H2.

Figure 5.147 shows the u_{gS}^* as a function of time and distance from the inlet. As shown in Table 5.5, there is no churn-annular transition in this simulation; the goal here is to illustrate the evolution of a liquid entrainment wave. The initial condition is such that the liquid film

flow rate is below the critical film flow rate required for droplet entrainment (GOVAN, 1990). Next, the inlet liquid mass flux is increased past the critical value for entrainment to begin, and the liquid entrainment wave is tracked. As can be seen from Fig. 5.147, u_{gS}^* is always lowest in the bottom region of the pipe since that is the region of highest pressure. As observed in Fig. 5.148, the pressure starts to increase after the beginning of liquid injection, due to the increase of the liquid film thickness, which means a lower void fraction and higher gravitational pressure gradient. The discontinuity in the plot at 95 s is related to the change between a two-field formulation in the region without droplet entrainment to a three-field formulation after the film flux is increased past the critical liquid film flow rate (GOVAN, 1990). The void fraction distribution as a function of time and distance is shown in Fig. 5.149.
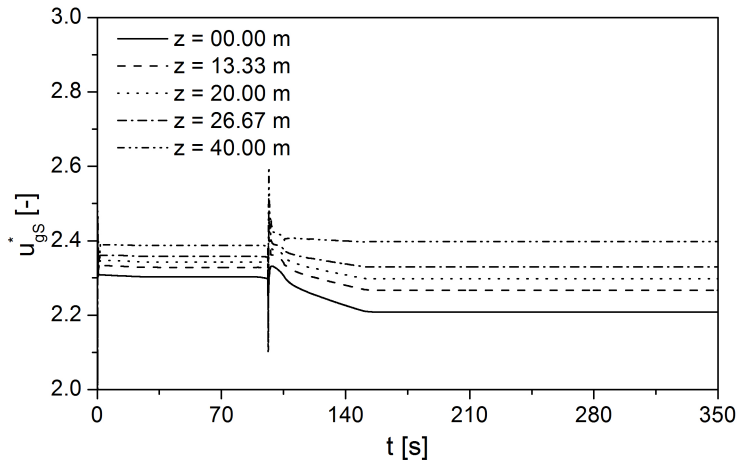
Figure 5.147 – Transient dimensionless gas superficial velocity for Case H2.

Figure 5.150 shows the transient liquid entrained fraction as a function of time and distance. At approximately 95 s a peak in the entrained fraction occurs, which is associated to the transition between the two mathematical formulations, having thus, no physical meaning. The "real" entrainment process is initiated after the numerical disturbance is flushed through the pipe exit.

Figure 5.151 shows the liquid entrained fraction behavior as a function of time for $t > 95$ s (i.e., after the numerical disturbance is flushed
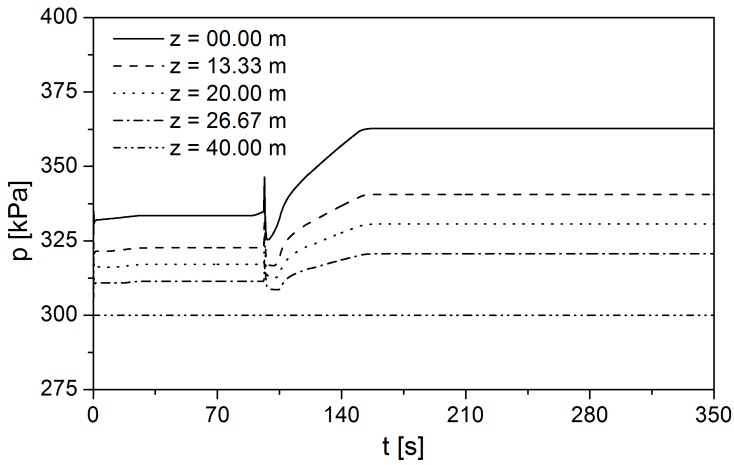
Figure 5.148 – Transient pressure for Case H2.
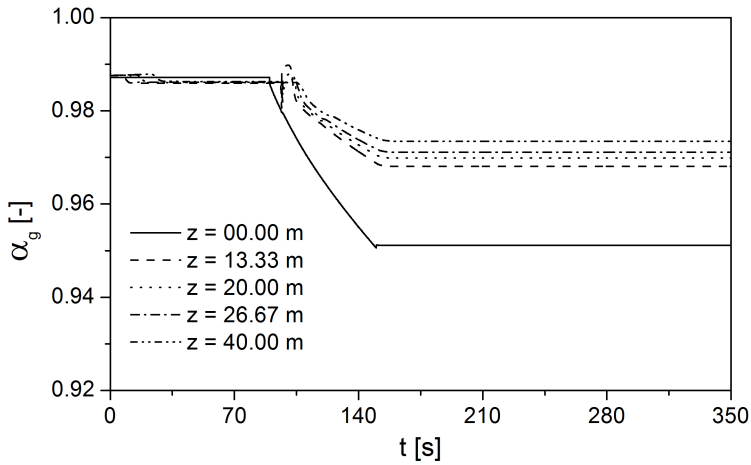
Figure 5.149 – Transient void fraction for Case H2.

out). As can be seen, liquid entrainment starts first at the lowest z, providing a wave front that travels swiftly along the pipe at a velocity close to that of the gas. The entrained fraction increases until $t \approx 160$ s because of the continuous increase of the inlet liquid mass flux up to that point in time (it should be borne in mind that the entrainment rate is directly proportional to the film thickness). After that, hydrodynamic equilibrium is quickly reached, with the liquid entrained fraction highest near the outlet because of the largest superficial gas velocity.

Figures 5.152 and 5.153 show pressure and void fraction profiles at different time instants. These clearly show that the void fraction waves travels at much lower velocities in comparison with pressure disturbances. At steady-state, it can be concluded that there is an increase in pressure gradient and a decrease in void fraction resulting from the inlet mass flux change.

Figure 5.154 shows profiles of liquid entrained fraction at different times. In this figure, the aforementioned unrealistic instantaneous increase in the liquid entrained fraction is not shown. The first curve ($t = 100$ s) shows the initial entrainment wave forming at the bottom of the pipe while the next four curves ($t = 101$ s, $t = 102$ s, $t = 105$ s and $t = 130$ s) show its evolution until it reaches the top of the pipe. This takes a few seconds to occur, because the gas at its local instantaneous velocity transports the entrained liquid upwards. The last curve ($t = 170$ s) represents the final steady-state for this parameter. Around 80 seconds are needed after the initial change in the inlet liquid mass flux for the liquid entrained fraction to stabilize.
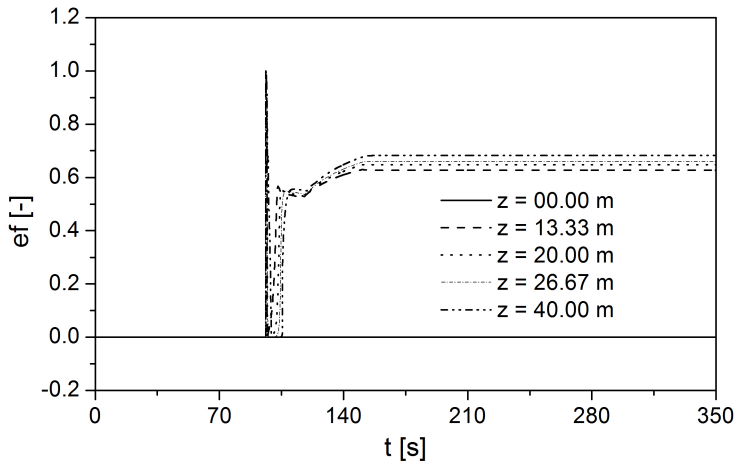
Figure 5.150 – Transient liquid entrained fraction for Case H2.
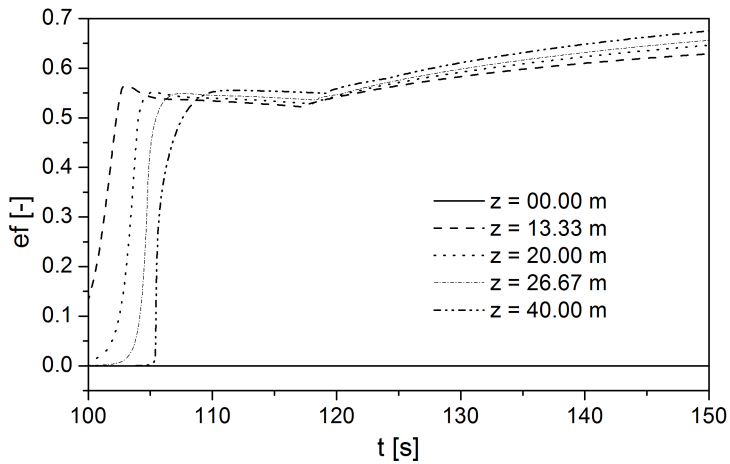
Figure 5.151 – Transient liquid entrained fraction for Case H2 for $t >$ 100 s.
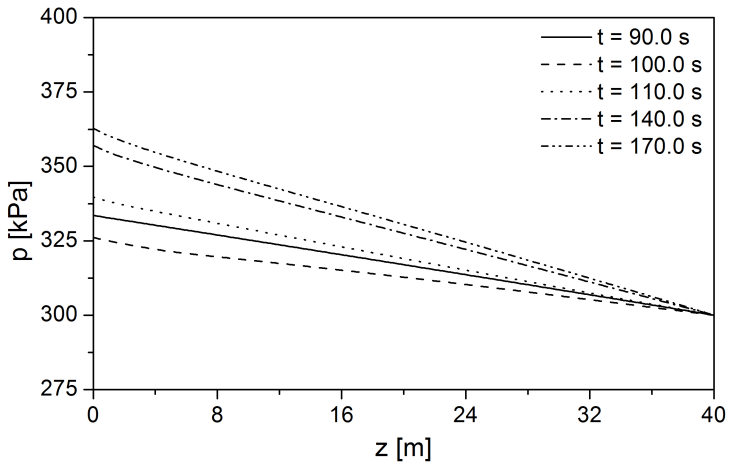
Figure 5.152 – Transient pressure profiles for Case H2.
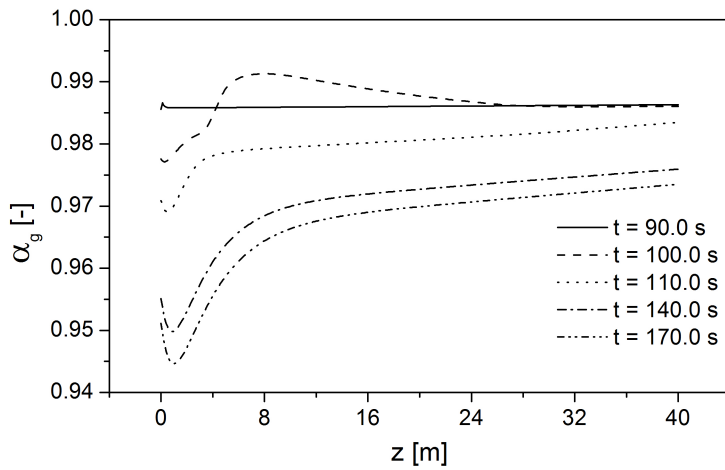
Figure 5.153 – Transient void fraction profiles for Case H2.
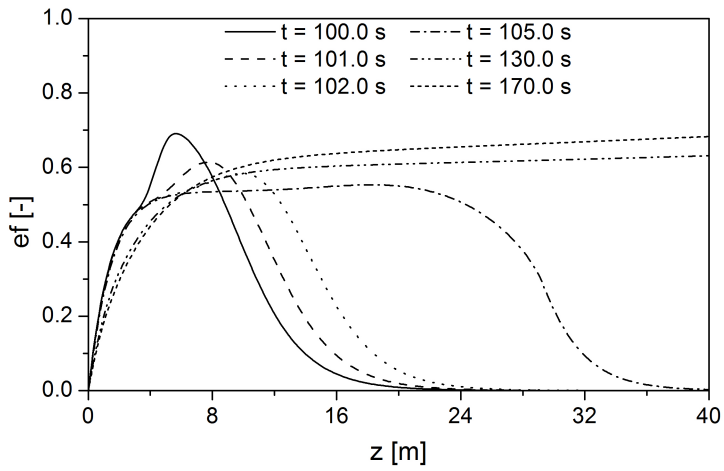
Figure 5.154 – Transient liquid entrained fraction profiles for Case H2.

The third hypothetical case (Case H3) is similar to Case H2 and depicts the evolution of an entrainment wave, however, for this situation only the three-field model is used because the initial condition already has some entrained liquid. The initial and final values of the boundary conditions are shown in Table 5.6.

Table 5.6 – Boundary conditions for Case H3.

Variable	Initial Value (Low entrainment)	Final Value (High entrainment)
$G_{g,in}$ [kg m^{-2}s^{-1}]	85.0	205.0
$G_{l,in}$ [kg m^{-2}s^{-1}]	40.0	40.0
$e_{f,in}$	0.0001	0.0001
$T_{g,in}$ [K]	300	300
$T_{e,in}$ [K]	300	300
$T_{f,in}$ [K]	300	300
p_{out} [kPa]	300	300

As can be inferred from table 5.6 only the inlet gas mass flux is changed in the simulation. An valve opening is simulated and an entrainment wave is followed using the numerical simulation. Figure 5.155 illustrates the change in the inlet gas mass flux imposed to the numerical simulation.

Figures 5.156 to 5.158 show variation of pressure, core fraction and entrained liquid fraction as function of time for different pipe positions. Figure 5.156 shows the gradual rise in pressure following the increase in gas mass flux presenting a linear behavior. All positions face a similar rise in pressure except for the outlet pressure at $z = 40.0$ m which is constant at 300 kPa.

Figure 5.157 shows the core fraction as function of time. As for pressure the rise is gradual with the increase in gas mass flux but this time presents a non-linear behavior. All positions present a very close value of core fraction except the inlet ($z = 0.0$ m) because at this position the boundary condition for the entrained fraction is set to be near zero. This results in a lower value of the core fraction because almost all liquid is in the film.

Figure 5.158 shows the transient entrained fraction for the different pipe positions indicated in the figure. The behavior is similar to the one presented by the other properties with a slight oscillation in the value of the last point ($z = 40.0$ m). The evolution is once again non linear and the value of the first point is undistinguishable from the abscissa due to the low value of the inlet entrainment.
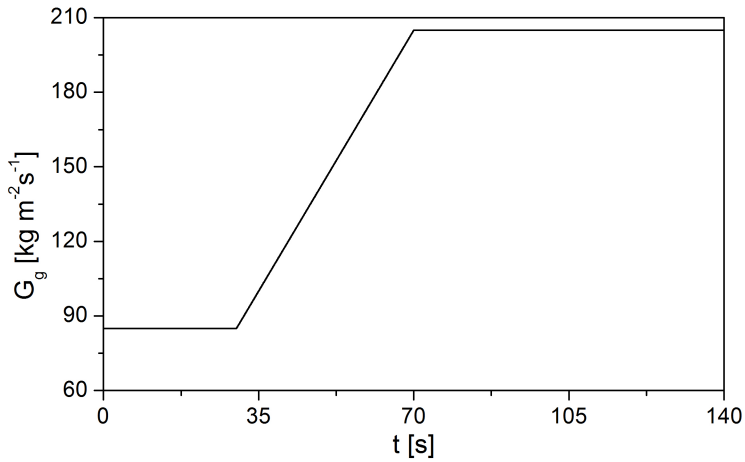
Figure 5.155 – Transient inlet gas mass flux boundary condition for Case H3.
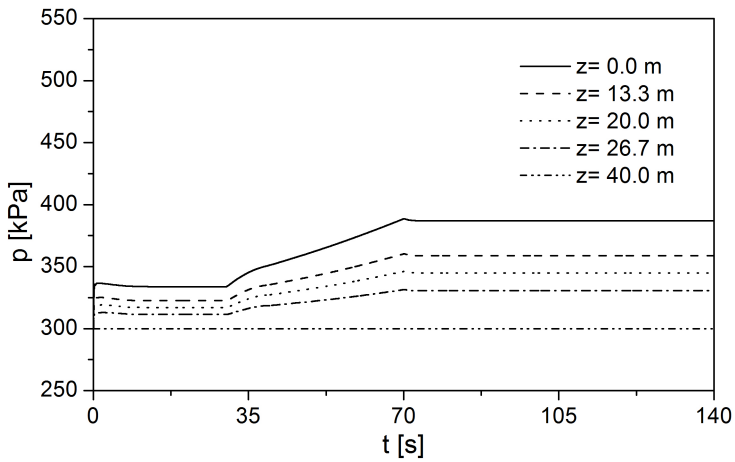
Figure 5.156 – Transient transient pressure for Case H3.
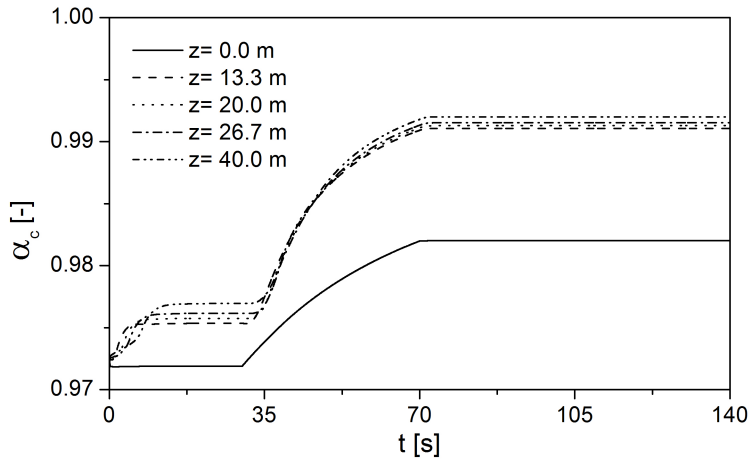
Figure 5.157 – Transient homogeneous core fraction for Case H3.
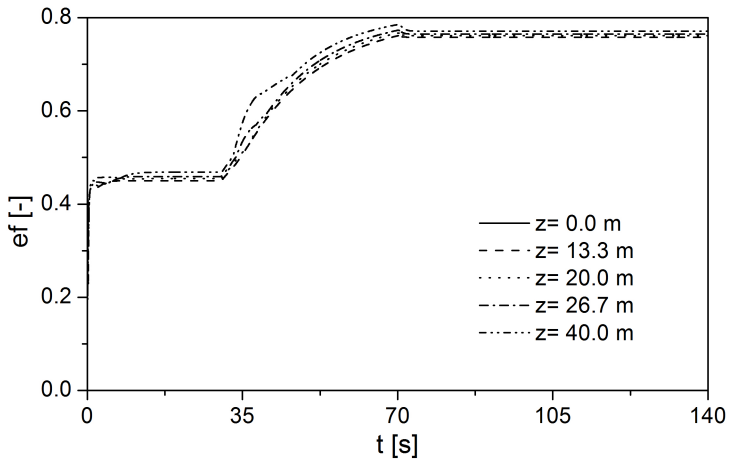
Figure 5.158 – Transient liquid entrained fraction for Case H3.

6 CONCLUSIONS

The main objective of this thesis was to expand and validate a numerical model to simulate annular and churn flows and the transition between them, which is closely connected to the phenomenon of liquid loading in wells. The model was compared with an extensive steady-state database (covering the majority of the available data in the open literature) and to a recently obtained transient dataset (WALTRICH, 2012). Some hypothetical simulations were performed to investigate the effect of individual boundary condition changes. This chapter presents the main conclusions drawn from these extensive comparisons and hypothetical tests. Recommendations for future work are presented at the end of the chapter.

6.1 STEADY-STATE ANALYSIS

The steady-state analysis included data on local pressure gradient, void/core fraction (film thickness) and liquid film mass flux for both the annular and churn flows. Also, the axial development of these flow properties could be analysed for some references. The majority of the numerical simulations performed for each of these properties resulted in a reasonable representation agreement with the experimental data.

Some of the discrepancies between the model and data were due to contrasting boundary condition setup, such as the prediction of axial development in annular flow using the experimental data of Wolf *et al.* (2001). In these tests a constant pressure was maintained at the inlet, but the model considered a fixed pressure boundary condition at the outlet. This generated a mismatch between the numerical and experimental values of the inlet pressure. The pressure gradient however, was reasonably well represented, with the majority of the predictions within the $\pm 20\%$ range. The Wolf *et al.* (2001) dataset was used as benchmark to evaluate three interfacial friction factor correlations, namely the Wallis (1969), Whalley and Hewitt (1978) and Belt

et al. (2009) The Whalley and Hewitt (1978) relationship proved to be the most computationally efficient, but the results were quite similar for the three methods.

Other minor discrepancies were observed in the comparisons with the other databases, however, according to the overall-comparison (Section 5.1.9), the majority of the numerical results for the three parameters were within the $\pm20\%$ margin, which is considered a good representation of the physical phenomena.

The steady-state comparison covered the majority of the data available in the open literature for annular and churn flows. Facilities with internal diameters ranging from 19 to 75 mm and lengths between 1.71 and 40.0 m were simulated with similar degrees of accuracy. It can be concluded that the numerical model in this thesis represents adequately the vertical two-phase annular and churn flows of air and water at steady-state.

6.2   TRANSIENT ANALYSIS

The transient analysis performed in this work was based on the experimental data obtained by Waltrich (2012) in the 42-m long 50-mm ID TowerLab facility at Texas A&M University.

The analysis of the pressure-induced transient cases demonstrated that the numerical model was quite successful in describing the annular to churn transition. The main exception was Case 2, for which a extreme boundary condition change (specifically the outlet pressure) resulted in a breakdown of the film flow topology leading to the poor comparison with the numerical results. This disintegration of the film structure was observed in the experiments of Waltrich (2012) but the model was not able to reproduce it, due to the nature of the interfacial friction relationships (suited for films flows). The remainder of the pressure-induced simulations resulted in reasonably good comparisons in all aspects. The lower void fraction for churn flow was successfully captured, the higher level of oscillations in the pressure drop and void fraction curves for churn flow in relation to annular flow was reproduced. Even when smoothened boundary conditions were considered the natural oscillations of the churn flow pattern was captured, especially for the dimensionless gas velocity.

The simulations of Cases 4 and 5 originally resulted in no transition from annular to churn flow. However, after applying a smoothening process to the boundary conditions and changing the Wallis criterion from $u_{gS}^* = 1.0$ to 1.25, the transition was induced in the simulation.

This change had no impact in the model's ability to represent both annular and churn flow steady-states. In the transition region, however, the predictions became smoother and the model was less accurate in its prediction of the pressure drop due to the use of the churn flow friction factors correlations after the transition, instead of the annular flow closure relationships throughout the simulation.

In addition the pressure-induced transients, three transient cases triggered by a change in the inlet liquid mass flux (which in turn leads to a pressure and gas mass flux variation) were simulated and a generally good agreement was observed. Although the simulation results for Case 6 indicate no churn-annular transition (as observed in the experiments), the results for pressure drop and void fraction were remarkably close to the experimental data. The smoothened simulation for Case 6 gave results that were very similar to the original ones (not smoothened), but the attempt to induce the churn-annular transition were not successful. The simulation of Case 7 also presented a reasonably good agreement with the experimental data, especially in the initial and final steady-states. The curves of dimensionless gas superficial velocity revealed that unrealistic churn-annular transitions took place during the final steady-state. These disappeared after the application of a smoothening process to the boundary conditions. During the transition region, however, there was a more noticeable discrepancy in the pressure drop and void fraction prediction (and also a high amplitude oscillation in the dimensionless gas superficial velocity). The oscillations observed were attributed to the back and forth change in the closure relationships for annular and churn flow which took place during the transition. To obtain a smooth curve for the dimensionless gas superficial velocity, it was necessary to lock the closure relationships as if the flow regime was churn flow during the entire run. This artifice revealed that the higher interfacial friction factor during the transition dampened the oscillations, thus eliminating the discrepancies. Also, this change had no apparent effect on the pressure drop and void fraction curves during the steady-states while improving the representation of the transition region. Case 8 was similar to Case 6 with respect to the order with which changes in flow regime took place (first churn and then annular flow). The simulation results of Case 8 were also in good agreement with the experimental results. As in Case 7, the u_{gS}^* curves for Case 8 present unrealistic churn-annular transitions, which vanished in the simulation of the smoothened boundary conditions. Once again, the smoothening process had little effect on the representation of the experimental data.

Through this analysis a few conclusions can be drawn:

- The numerical model presented in this work was considered successful in reproducing the transient experimental data produced at the TowerLab facility;

- The steady-states were well represented, including the trends of smaller void fraction and higher pressure drop in churn flow;

- The characteristic oscillations of churn flow were reasonably detected in the curves of dimensionless gas velocity, pressure drop and void fraction;

- During the transition period, the description of the transient was compromised by the extreme changes in the boundary conditions, causing oscillations when the closure relationships were changed. These oscillations were removed by the use of a constant set of closure relationships (churn flow correlations) for the entire simulation;

- The experimental data from TowerLab tries to replicate some features of the liquid loading process. In this way, as the model was considered successful in predicting this dataset, it is likely that the numerical model would be a useful tool in predicting the onset of liquid loading.

6.3   HYPOTHETICAL TRANSIENTS

Three hypothetical numerical experiments were performed in order to illustrate the isolated influence of the boundary conditions on the annular to churn transition and also to demonstrate the entrainment wave that takes place when there is an increase in the liquid flow rate or in the gas flow rate. The first simulation was straightforward and very similar to the transient cases compared with the TowerLab data of Waltrich (2012). The oscillations during the transition from annular to churn flow appeared again (as in the mass flow-induced transient Case 7), this time however in a much smaller scale, and then are flushed out the pipe with time. Case H3 shows a different type of entrainment wave, this time created by the increase in the gas flow rate. In this case only the three-field formulation was necessary and no unrealistic predictions were detected.

Based in these observations the main conclusion that can be drawn is that the numerical model can be considered reasonably accurate and reliable in the description of the onset of liquid loading and also of entrainment waves associated with the oscillating mass flow rate.

6.4 RECOMMENDATIONS FOR FUTURE WORK

During the execution of this work, a few key topics of interest were identified for further investigation. The most relevant in terms of application is the development of a coupled wellbore-reservoir model to completely simulate the liquid loading process. Also, the generation of additional transient experimental data in different test facilities would allow the evaluation of the behavior of other variables such as entrained fraction during transients. The application of the model to the current experimental data trying to compare other quantities such as wave velocities (pressure and rarefaction) and the frequency spectrum.

As numerical enhancements it would be interesting to:

- Replace the whole domain transition from the two-field to the three-filed formulations when there is no entrainment or churn flow presents high residuum (this will remove the false entrainment wave seen in Case H2);

- Investigate the influence of the interfacial friction factor correlations in the representation of the churn-annular transition region;

The possible enhancements to the model would be:

- Include heat and mass transfer into the two-phase flow (phase-change) initially for single component and then multicomponent scenarios;

- Include the slug and bubble flow regimes into the modeling using the recent ideas of interfacial drag coefficient for the two-fluid model presented by Brooks *et al.* (2012);

- Evaluate the inclusion of the momentum transfer between entrained droplets and gas modeling into the three-field.

References

AHMAD, M.; PENG, D. J.; HALE, C. P.; WALKER, S. P.; HEWITT, G. F. Droplet Entrainment in Churn Flow. In: *7th International Conference on Multiphase Flow*, 2010. p. 7.

ALAMU, M. B.; AZZOPARDI, B. J. Simultaneous Investigation of Entrained Liquid Fraction, Liquid Film Thickness and Pressure Drop in Vertical Annular Flow. *Journal of Energy Resources Technology*, v. 133, n. 2, p. 10, 2011. ISSN 01950738.

ALEKSEENKO, S.; CHERDANTSEV, A.; CHERDANTSEV, M.; ISAENKOV, S.; KHARLAMOV, S.; MARKOVICH, D. Application of a high-speed laser-induced fluorescence technique for studying the three-dimensional structure of annular gas–liquid flow. *Experiments in fluids*, Springer, v. 53, n. 1, p. 77–89, 2012.

ALIPCHENKOV, V.; ZAICHIK, L.; ZEIGARNIK, Y. The development of a three-fluid model of two-phase flow for a dispersed-annular mode of flow in channels: Size of droplets. *High temperature*, v. 40, n. 4, p. 594–603, 2002.

ALIPCHENKOV, V. M.; NIGMATULIN, R. I.; SOLOVIEV, S. L.; STONIK, O. G.; ZAICHIK, L. I.; ZEIGARNIK, Y. a. A three-fluid model of two-phase dispersed-annular flow. *International Journal of Heat and Mass Transfer*, v. 47, n. 24, p. 5323–5338, nov. 2004.

ANDERSON, D.; TANNEHILL, J.; PLETCHER, R. *Computational fluid mechanics and heat transfer*. McGRALL-HILL BOOK COMPANY, 1984.

AZZOPARDI, B. *Multiphase flow*. 2012. Lecture at the 3rd Brazilian Conference on Boiling, Condensation and Multiphase flow.

AZZOPARDI, B. J. *Gas-Liquid Flows*. New York: Begel House, INC., 2006. 331 p.

AZZOPARDI, B. J.; WHALLEY, P. B. Artificial waves in annular two-phase flow. *Harry Diamond Laboratories (Technical Report) HDL-TR*, p. 1–8, 1980.

BARBOSA JR., J. R. *Phase Change of Single Component Fluids and Mixtures in Annular Flow*. 435 p. PhD Thesis — Imperial College, 2001.

BARBOSA, J. R.; HEWITT, G. F. *Gas-Liquid two-phase flow in vertical pipes (A description of models used in GRAMP2 Programme)*, 2006. 41 p.

BARBOSA, J. R.; HEWITT, G. F.; KöNIG, G.; RICHARDSON, S. M. Liquid entrainment, droplet concentration and pressure gradient at the onset of annular flow in a vertical pipe. *International Journal of Multiphase Flow*, v. 28, n. 6, p. 943–961, 2002.

BARBOSA, J. R.; HEWITT, G. F.; RICHARDSON, S. M. Churn flow: Myth, mystery and magic. In: *39th European Two-Phase Flow Group Meeting, Aveiro, Portugal*, 2001b.

BARBOSA JR., J. R. Aspectos Fenomenológicos e Modelagem de Escoamentos Bifásicos Gás-Líquido. In: *Apostila da 1ª Escola Brasileira de Escoamentos Bifásicos*. 1*st* edition, Publisher ABCM, 2010. p. 73.

BELT, R. J.; van't Westende, J. M. C.; PORTELA, L. M. Prediction

of the interfacial shear-stress in vertical annular flow. *International Journal of Multiphase Flow*, Elsevier Ltd, v. 35, n. 7, p. 689–697, jul. 2009. ISSN 03019322.

BENDIKSEN, K.; MALNES, D.; MOE, R.; NULAND, S. The dynamic two-fluid model OLGA: Theory and application. *SPE Production Engineering*, v. 6, p. 171–180, 1991.

BENNETT, A.; HEWITT, G.; KEARSEY, H.; KEEYS, R. *Heat transfer to steam water mixtures flowing in uniformly heated tubes in which the critical heat flux has been.* [S.l.], 1966.

BHARATHAN, D.; RICHTER, H. J.; WALLIS, G. B. Air-water counter-current annular flow in annular tubes. *Report EPBI-NP-786*, 1978.

BHARATHAN, D.; WALLIS, G. B. Air-water countercurrent annular flow. *International Journal of Multiphase Flow*, v. 9, n. 4, p. 349–366, 1983.

BROOKS, C. S.; HIBIKI, T.; ISHII, M. Interfacial drag force in one-dimensional two-fluid model. *Progress in Nuclear Energy*, Elsevier, v. 61, p. 57–68, 2012.

BURDEN, R. L.; FAIRES, J. D. *Numerical Analysis*: Brooks/Cole, Boston, USA, 2010.

CHAKRAVARTHY, S. R.; ANDERSON, D. A.; SALAS, M. D. The split coefficient matrix method for hyperbolic systems of gasdynamic equations. In: *Proceedings of the AIAA 18th Science Meeting*, 1980. p. Paper 800268.

CIONCOLINI, A.; THOME, J. R. Prediction of the entrained liquid

fraction in vertical annular gas-liquid two-phase flow. *International Journal of Multiphase Flow*, Elsevier Ltd, v. 36, n. 4, p. 293–302, abr. 2010. ISSN 03019322.

CIONCOLINI, A.; THOME, J. R. Algebraic turbulence modeling in adiabatic and evaporating annular two-phase flow. *International Journal of Multiphase Flow*, v. 36, n. 4, p. 805–817, 2011.

COLLIER, J. G.; THOME, J. R. *Convective Boiling and Condensation*. 3rd edition, Publisher: CLAREDON PRESS - OXFORD, 1994. 596 p. ISBN 0198562969.

COOPERSTEIN, B. *Advanced Linear Algebra*. Publisher: CRC Press/Taylor and Francis Group, Boca Raton, Florida USA, 2010.

COSTIGAN, G. *Flow pattern transitions in vertical gas-liquid flows*. 192 p. PhD Thesis — Wolfson College, 1997.

COUSINS, L.; DENTON, W.; HEWITT, G. Liquid mass transfer in annular two-phase fow. In: *in: Sym. on Two-phase Flow*, 1965. vol. 1, paper C4, Exeter, England.

DAFERMOS, C. M. *Hyberbolic conservation laws in continuum physics*. Publisher: Springer, Berlin; New York, USA, 2005.

DALLMAN, J. R. *Investigation of separated flow model in annular gas-liquid two-phase flow*. PhD Thesis — University of Illinois, Urbana, 1978.

DOBRAN, F. Hydrodynamic and heat transfer analysis of two-phase annular flow with a new liquid film model of turbulence. *International Journal of Heat and Mass Transfer*, v. 26, n. 8, p. 1159–1171, 1983.

DREW, D. A.; PASSMAN, S. L. *Theory of Multicomponent Fluids, Applied Mathematical Sciences 135*. Publisher: Springer, New York, 2003.

DUTTA-ROY, K. *Transient phenomena in two-phase horizontal flowlines for the homogeneous, stratified and annular flow patterns*. PhD Thesis — University of Tulsa, 1984.

FALCONE, G.; BARBOSA, J. R. State-of-the-art Review of Liquid Loading in Gas Wells. In: *DGMK/OGEW-Fruhjahrstagung 2013, Fachbereich Aufsuchung und Gewinnung, Germany*, 2013.

FRIEDEL, L. Improved friction pressure drop correlations for horizontal and vertical two-phase pipe flow. In: *European Two-Phase Flow Group Meeting, Ispra, Italy*, 1979. p. paperE2.

FU, F.; KLAUSNER, J. F. A separated flow model for predicting two-phase pressure drop and evaporative heat transfer for vertical annular flow. *International Journal of Heat and Fluid Flow*, v. 18, n. 6, p. 541–549, 1997.

GESSNER, T. *Modelagem Numérica do Escoamento Anular Gás-Líquido Transiente pelo Método da Divisão da Matriz de Coeficientes*. 172 p. Master's Dissertation — Universidade Federal de Santa Catarina, 2010.

GILL, L.; HEWITT, G.; HITCHON, J. *Sampling probe studies of the gas core in annular two-phase flow, Part I: the effect of length on phase and velocity distribution*, 1962.

GOVAN, A.; HEWITT, G.; OWEN, D.; BOTT, T. An improved chf modelling code. In: *IN: PROC. IMECHE SECOND U.K. NAT. CONF. ON HEAT TRANSFER, (GLASGOW, U.K.: SEP. 14-16, 1988)*, 1988. v. 1 , Bury St. Edmunds, U.K., Mech. Engng.

Publications Ltd., 1988, Session 1A, Paper C175, n. 88, p33-48.

GOVAN, A. H. *Modeling of vertical annular and dispersed two-phase flows.* PhD Thesis — Imprerial College, London, 1990.

GOVAN, A. H.; HEWITT, G. F.; RICHTER, H. J.; SCOTT, A. Flooding and Churn Flow in Vertical Pipes. *International Journal of Multiphase Flow*, v. 17, n. I, p. 27–44, 1991.

HEWITT, G. F. *Analysis of annular two-phase flow: application of the Dukler analysis to vertical upward flow in a tube.* , 1961.

HEWITT, G. F. *Flooding and Flow Reversal. In: THERMOPEDIA.* 2010. Disponível em: <http://www.thermopedia.com>.

HEWITT, G. F.; GOVAN, A. H. Phenomenological modelling of non-equilibrium flows with phase change. *International Journal of Heat and Mass Transfer*, v. 33, n. 2, p. 229–242, 1990.

HEWITT, G. F.; HALL-TAYLOR, N. S. *Annular Two-Phase Flow.* Publisher: Pergamon Press., 1970.

HEWITT, G. F.; MARTIN, C. J.; WILKES, N. S. Experimental and modeling studies of annular flow in the region between flow reversal and pressure drop minimum. *PhysicoChemical Hydrodynamics*, v. 69, p. 69–86, 1985.

HEWITT, G. F.; WALLIS, G. B. Flooding and associated phenomena in falling film in a vertical tube. p. 62–74, 1963.

HOLOWACH, M.; HOCHREITER, L.; CHEUNG, F. A model for droplet entrainment in heated annular flow. *International Journal of*

Heat and Fluid Flow, v. 23, n. 6, p. 807–822, 2002.

HUTCHINSON, P.; WHALLEY, P. A possible characterisation of entrainment in annular flow. *Chemical Engineering Science*, v. 28, n. 3, p. 974–975, 1973.

ISHII, M.; GROLMES, M. Inception criteria for droplet entrainment in two-phase concurrent film flow. *AIChE Journal*, v. 21, n. 2, p. 308–318, 1975.

ISHII, M.; HIBIKI, T. *Thermo-fluid dynamics of two-phase flow*, 2006. 469 p. ISBN 9780387283210.

JACOBSON, N. *Basic Algebra I.* Publisher: Dover Publications, 2009. (Basic Algebra). ISBN 9780486471891.

JAMES, P.; WHALLEY, P. The calculation of dryout during flow and pressure transients. In: *2nd CSNI Specialist Meeting on Transient Two-phase Flow*, 1978. p. 281–293.

JAYANTI, S.; BRAUNER, N. Churn Flow. *Multiphase Science and Technology*, v. 8, p. 471–522, 1994.

JENSEN, M. K. The liquid film and the core region velocity profiles in annular two-phase flows. *Int. J. Multiphase Flow*, v. 13, p. 615–628, 1987.

KAJI, R.; AZZOPARDI, B. The effect of pipe diameter on the structure of gas/liquid flow in vertical pipes. *International Journal of Multiphase Flow*, v. 36, n. 4, p. 303–313, 2010.

KATAOKA, I.; ISHII, M.; NAKAYAMA, A. Entrainment and

desposition rates of droplets in annular two-phase flow. *International Journal of Heat and Mass Transfer*, v. 43, n. 9, p. 1573–1589, 2000.

KEEYS, R.; RALPH, J.; ROBERTS, D. *Post burnout heat transfer in high pressure steam-water mixtures in a tube with cosine heat flux distribution*, 1971.

KOSKY, P.; STAUB, F. Local condensing heat transfer coefficients in the annular flow regime. *AIChE Journal*, v. 17, n. 5, p. 1037–1043, 1971.

LAMB, H. *Hydrodynamics. 6th* edition Publisher: Cambridge University Press, Cambridge, 1932.

LANGNER, H.; MAYINGER, F. Entrainment in annular two-phase flow under steady and transient flow conditions. In:*Two-Phase Momentum Heat and Mass Transfer in Chemical, Process, and Energy Systems*. Washington DC: Hemisphere Publishing Co., 1979. v. 2, p. 695–706.

LEA, J.; NICKENS, H. V.; WELLS, M. *Gas Well Deliquification* Publisher: Oxford: Gulf Professional Publishing, 2003. 692 p.

LEMMON, E. W.; HUBER, M. L.; MCLINDEN, M. O. *NIST - Reference Fluid Thermodynamic and Trans- port Properties REFPROP, Version 8.0*, 2007. 123 p.

Lopez de Bertodano, M.; ASSAD, A.; BEUS, S. Experiments for entrainment rate of droplets in the annular regime. *International journal of multiphase flow*, v. 27, n. 4, p. 685–699, 2001.

LU, D. M.; SIMPSON, H. C.; GILCHRIST, A. The application of split coefficient matrix method to transient two-phase flows. *International*

Journal of Numerical Methods in Heat and Fluid Flow, v. 6, p. 63–76, 1996.

MALISKA, C. R. *Transferência de calor and mecânica dos fluidos computacional*, 2004.

MCCOY, D.; HANRATTY, T. Rate of deposition of droplets in annular two-phase flow. *International Journal of Multiphase Flow*, v. 3, n. 4, p. 319–331, 1977.

MUNKEJORD, S. T. *Analysis of the two-fluid modeland the drift-flux model for numerical calculation of two-phase flow*. 275 p. PhD Thesis — Norwegian University of Science and Technology, 2005.

NETUNAEV, S. V. *Gas-liquid medium modelling of local hydrodynamic characteristics of a steam-water flow*. Tese (Doutorado) — VNIIAM, Moscow, 1982.

NIGMATULIN, R.; NIGMATULIN, B.; KHODZAEV, Y.; KROSHILIN, V. Entrainment and deposition rates in a dispersed-film flow. *International Journal of Multiphase Flow*, v. 22, p. 19–30, 1996.

NIMWEGEN, A. T. van; PORTELA, L. M.; HENKES, R. A. W. M. The Effect of Surfactants on Vertical Air/Water Flow for Prevention of Liquid Loading. In: *paper SPE 164095, Presented at the SPE International Symposium on Oilfield Chemistry held in The Woodlands, Texas, USA*, 2013.

OHBA, K.; NAGAE, K. Characteristics and behavior of the interfacial wave on the liquid film in a vertically upward air-water two-phase annular flow. *Nuclear Engineering and Design*, v. 141, n. 1-2, p. 17–25, 1993.

OKAWA, T.; KATAOKA, I. Correlations for the mass transfer rate of droplets in vertical upward annular flow. *International Journal of Heat and Mass Transfer*, Elsevier Ltd, Oxford, United Kingdom, v. 48, n. 23-24, p. 4766–4778, nov. 2005. ISSN 00179310.

OUYANG, L. B.; AZIZ, K. Transient gas-liquid two-phase flow in pipes with radial influx or efflux. *Journal of Petroleum Science and Technology*, v. 30, p. 167–179, 2001.

OWEN, D. G. *An experimental and theoretical analysis of equilibrium annular flows.* 447 p. PhD Thesis — Univesity of Birmingham, 1986.

PRESS, H. W.; TEUKOLSKY, S. A.; VETTERLING, W. T.; FLANNERY, B. P. *Numerical Recipes in FORTRAN 77: The art of scientific computing.* 2*nd* ed. Publisher: Cambridge University Press, UK, 1992.

PUSKINA, O.; SOROKIN, Y. Breakdown of liquid motion in vertical tubes. *Heat Transfer Soviet Research*, v. 1, p. 56–64, 1969.

RACHKOV, V. I. *Experimental research of moisture-transfer processes in steam-water dispersed annular flows.* PhD Thesis — Imperial College, 1979.

ROE, P. L. Approximate riemann solvers, parameter vectors, and difference schemes. *Journal of computational physics*, Elsevier, v. 43, n. 2, p. 357–372, 1981.

ROMSTEDT, T. A split-matrix method for the numerical solution of two-phase flow equations. *Nuclear Science and Engineering*, v. 104, p. 1–9, 1990.

SAWAI, T.; KAJI, M.; KASUGAI, T. Gas-liquid interfacial structure

and pressure drop characteristics of churn flow. *Experimental Thermal and Fluid Science*, Elsevier, v. 28, n. 6, p. 597–606, jun. 2004. ISSN 08941777.

SAWANT, P.; ISHII, M.; MORI, M. Prediction of amount of entrained droplets in vertical annular two-phase flow. *International Journal of Heat and Fluid Flow*, v. 30, n. 4, p. 715–728, 2009.

SCHADEL, S.; LEMAN, G.; BINDER, J.; HANRATTY, T. Rates of atomization and deposition in vertical annular flow. *International Journal of Multiphase Flow*, v. 16, p. 363–374, 1990.

SCHENK, O.; GARTNER, K. Two-level scheduling in pardiso: Improved scalability on shared memory multi-processing systems. *Parallel Computing*, v. 28, p. 187–197, 2002.

SCHENK, O.; GARTNER, K. Solving unsymmetric sparse systems of linear equations with PARDISO. *Journal of Future Generation Computer Systems*, v. 20, p. 475–487, 2004.

SCHENK, O.; GARTNER, K.; FICHTNER, W. Efficient Sparse LU Factorization with Left-right Looking Strategy on Shared Memory Multiprocessors. *BIT*, v. 40, p. 158–176, 2000.

SHARMA, V. D. *Quasilinear hyperbolic systems, compressible flows, and waves* Publisher: CRC Press/Taylor and Francis Group, Boca Raton, Florida USA, 2010.

SKOPICH, A.; PEREYRA, E.; SARICA, C.; KELKAR, M. Pipe Diameter Effect on Liquid Loading in Vertical Gas Wells. *2013 SPE Production and Operations Symposium*, v. 3, p. 1–12, 2013.

STäDTKE, H. *Gasdynamic Aspects of Two-Phase Flow Hyperbolicity*

, *Wave Propagation Phenomena , and Related Numerical Methods.* 1*st* edition Publisher: Wiley-VCH, 2006. 273 p. ISBN 352740578X.

STäDTKE, H.; FRANCHELLO, G.; WORTH, B.; GRAF, U.; ROMSTEDT, P.; KUMBARO, A.; GARCá-CASCALES, J.; PAILLéRE, H.; DECONINCK, H.; RICCHIUTO, M.; SMITH, B.; CACHARD, F. D.; TORO, E. F.; ROMENSKI, E.; MIMOUNI, S. Advanced three-dimensional two-phase flow simulation tools for application to reactor safety (ASTAR). *Nuclear Engineering and Design*, p. 379 400, 2005.

SUTTON, R.; COX, S.; LEA, J.; ROWLAN, O. Guidelines for the proper application of critical velocity calculations. *SPE Production & Operations*, n. May, p. 182–194, 2010.

SUTTON, R. P.; COX, S. A.; WILLIAMS, E. G.; STOLTZ, R. P.; GILBERT, J. V. Gas Well Performance at Subcritical Rates. In: *paper SPE 80887, presented at the SPE Production and Operations Symposium, held in Oklahoma City, Oklahoma, USA*, 2003.

TATTERSON, D. F. *Rates of automization and drop size in annular two phase flow.* PhD Thesis — University of Illinois, Urbana, 1975.

THURGOOD, M. J.; KELLY, M. J.; GUIDOTTI, T. E.; KOHRT, R. J.; CROWELL, K. R. *COBRA/TRAC, a Thermal-hydraulics Code for Transient Analysis of Nuclear Reactor Vessels and Primary Coolant Systems NUREG/CR-3046*, 1983.

TORO, E. F. *Riemann Solvers and Numerical Methods for Fluid Dynamics.* 2*nd* edition Publisher: Springer Berlin / Heidelberg, 1999. 605 p. ISBN 3540659668.

TURNER, R.; HUBBARD, M.; DUKLER, A. Analysis and prediction of minimum flow rate for the continuous removal of liquids from gas

wells. *Journal of Petroleum Technology*, p. 1475–1482, november 1969.

van der Meulen, G. P. *CHURN-ANNULAR GAS-LIQUID FLOWS IN LARGE DIAMETER VERTICAL PIPES*. 226 p. PhD Thesis — University of Notthingham, 2012.

van't Westende, J. *Droplets in annular-dispersed gas-liquid pipe-flows*. 147 p. PhD Thesis — Technishe Universiteit Delft, 2008.

van't Westende, J.; KEMP, H.; BELT, R.; PORTELA, L.; MUDDE, R.; OLIEMANS, R. On the role of droplets in cocurrent annular and churn-annular pipe flow. *International Journal of Multiphase Flow*, v. 33, n. 6, p. 595–615, jun. 2007. ISSN 03019322.

VEEKEN, C. a. M.; BELFROID, S. P. C. New Perspective on Gas-Well Liquid Loading and Unloading. *SPE Annual Technical Conference and Exhibition*, v. 2, n. November, p. 19–22, 2010.

WALLIS, G. *One-dimensional Two-phase Flow*. 1st edition Publisher: McGraw-Hill, New York, 1969. 409 p.

WALTRICH, P. J. *Onset and subsequent transient phenomena of liquid loading in gas wells: experimental investigation using a large scale flow loop*. PhD Thesis — Texas A&M University, 2012.

WALTRICH, P. J.; FALCONE, G.; BARBOSA, J. R. . Axial development of annular, churn and slug flows in a long vertical tube. *International Journal of Multiphase Flow*, v. 57, p. 38–48, 2013.

WATSON, M.; HEWITT, G. Pressure effects on the slug to churn transition. *International Journal of Multiphase Flow*, v. 25, p. 1225–1241, 1999.

WHALLEY, P.; HEWITT, G.; HUTCHINSON, P. Experimental wave and entrainment measurements in vertical annular two-phase flow. In: *Multi-Phase Flow Systems Symposium, Stratclyde.*, 1974.

WHALLEY, P.; HUTCHINSON, P.; JAMES, P. The calculation of critical heat flux in complex situations using an annular flow model. In: *Proccedings of the 6th International Heat Transfer Conference, Toronto* 1978.

WHALLEY, P.; LYONS, A.; SWINNERTON, D. Transient critical heat flux in flow boiling. In: *Proceedings of the 1st UK National Heat Transfer Conference, Leeds*, 1984.

WHALLEY, P. B.; HEWITT, G. F. *The correlation of entrained fraction and entrainment rate in annular two-phase flow*, 1978. 123 p.

WOLF, A.; JAYANTI, S.; HEWITT, G. F. Flow development in vertical annular flow. *Chemical Engineering Science*, v. 56, n. 10, p. 3221–3235, 2001.

YUAN, G.; PEREYRA, E.; SARICA, C.; SUTTON, R. P.; COMPANY, M. O. SPE 164516 An Experimental Study on Liquid Loading of Vertical and Deviated Gas Wells. *SPE Production And Operations Symposium*, v. 3, p. 16, 2013.

ZABARAS, G.; DUKLER, A. E.; MOALEM-MARON, D. Vertical upward cocurrent gas-liquid annular flow. *AIChE Journal*, v. 32, p. 829–843, 1986.

APPENDIX A

Thermodynamic Property Calculation

This appendix explains how the thermodynamic and transport property calculation is performed inside HyTAF. Two reference temperatures and two pressures (high and low) are specified during the setup of a simulation. These informations are based in the boundary conditions and the expected variation range of the simulation. Based on these, the following set of operations is performed to calculate the boundary conditions and the thermodynamic and transport properties for the first time step.

1. Read the data file that contains the equations of state and transport properties correlations constants from the REFPROP 8.0 (LEMMON *et al.*, 2007) database for the air;

2. Set the appropriate values for bulk phase descriptor (equal to 2 for gas) and bulk phase composition (equal to 1 for pure or pseudo pure fluid);

3. Calculate the air density at the four extreme points given by the two reference temperatures and pressures;

4. Calculate the minimum and maximum density among the four extreme points;

5. Calculate the air entropy at four extreme points using the high and low temperature and density;

6. Calculate the minimum and maximum entropy among the four extreme points;

7. Divide the pressure, temperature and entropy intervals into a given number of points that must be in ascending order;

8. Calculate the necessary properties as function of pressure and entropy at the points determined in the previous step;

9. Read the data file that contains the equations of state and transport properties correlations constants from the REFPROP 8.0 (LEMMON *et al.*, 2007) database for the water and set the bulk phase descriptor to 1 (liquid phase);

10. Return to step 2 and recalculate all steps for the liquid;

Once the program has been initialized and the calculation of the first iteration is accomplished, new physical properties must be calculated. This is performed using the tables calculated in the initialization through the following operations.

1. Using a locate subroutine (PRESS *et al.*, 1992) find the interval where the actual entropy and pressure at each grid point is situated;

2. Using the "location" information interpolate (using a bilinear interpolation as discussed in Press *et al.* (1992)) the necessary physical properties for each grid point;

3. Repeat this process for each field involved in the calculation;

APPENDIX B

Coefficient Matrices and Source Vectors

This Appendix presents the matrices and vectors elements and structures that appear during the description of the model and the application of the SCMM in Chapters 3 and 4, respectively.

Considering the original partial differential equation system (repeated below),

$$\mathbf{E}\frac{\partial \vec{U}}{\partial t} + \mathbf{F}\frac{\partial \vec{U}}{\partial z} = \vec{C} \tag{B.1}$$

The two matrices $\mathbf{E}$ and $\mathbf{F}$ along with the vector $\vec{C}$ are the coefficient matrices and source term obtained directly from the three-field formulation in non-conservative form (see Section 3.1), before the fully non-conservative form was obtained. The structure and the element values that were omitted in the text are shown below.

$$\mathbf{E} = \begin{bmatrix} e_{11} & e_{12} & 0 & 0 & 0 & e_{16} & 0 & 0 \\ e_{21} & e_{22} & e_{23} & 0 & 0 & 0 & e_{27} & 0 \\ e_{31} & 0 & e_{33} & 0 & 0 & 0 & 0 & e_{38} \\ e_{41} & 0 & 0 & e_{44} & 0 & e_{46} & e_{47} & e_{48} \\ e_{51} & 0 & 0 & 0 & e_{55} & e_{56} & e_{57} & e_{58} \\ 0 & 0 & 0 & 0 & 0 & e_{66} & 0 & 0 \\ 0 & 0 & 0 & 0 & 0 & 0 & e_{77} & 0 \\ 0 & 0 & 0 & 0 & 0 & 0 & 0 & e_{88} \end{bmatrix} \tag{B.2}$$

where,

$$e_{11} = \frac{\alpha_g}{a_g^2} \tag{B.3}$$

$$e_{12} = \rho_g \tag{B.4}$$

$$e_{16} = -\alpha_g \frac{\rho_g \beta_g T_g}{cp_g} \tag{B.5}$$

$$e_{21} = \frac{\alpha_e}{a_e^2} \tag{B.6}$$

$$e_{22} = -\rho_e \tag{B.7}$$

$$e_{23} = -\rho_e \tag{B.8}$$

$$e_{27} = -\alpha_e \frac{\rho_e \beta_e T_e}{cp_e} \tag{B.9}$$

$$e_{31} = \frac{\alpha_f}{a_f^2} \tag{B.10}$$

$$e_{33} = \rho_f \tag{B.11}$$

$$e_{38} = -\alpha_f \frac{\rho_f \beta_f T_f}{cp_f} \tag{B.12}$$

$$e_{41} = \frac{\alpha_c \alpha_f \Sigma \rho \Delta u}{\rho a_0^2} \tag{B.13}$$

$$e_{44} = \alpha_c \rho_c \tag{B.14}$$

$$e_{46} = -\alpha_c \alpha_f \Sigma \rho \Delta u \frac{\alpha_g \beta_g T_g}{cp_g} \tag{B.15}$$

$$e_{47} = -\alpha_c \alpha_f \Sigma \rho \Delta u \frac{\alpha_e \beta_e T_e}{cp_e} \tag{B.16}$$

$$e_{48} = -\alpha_c \alpha_f \Sigma \rho \Delta u \frac{\alpha_f \beta_f T_f}{cp_f} \tag{B.17}$$

$$e_{51} = -\frac{\alpha_c \alpha_f \Sigma \rho \Delta u}{\rho a_0^2} \tag{B.18}$$

$$e_{55} = \alpha_f \rho_f \tag{B.19}$$

$$e_{56} = \alpha_c \alpha_f \Sigma \rho \Delta u \frac{\alpha_g \beta_g T_g}{cp_g} \tag{B.20}$$

$$e_{57} = \alpha_c \alpha_f \Sigma \rho \Delta u \frac{\alpha_e \beta_e T_e}{cp_e} \tag{B.21}$$

$$e_{58} = \alpha_c \alpha_f \Sigma \rho \Delta u \frac{\alpha_f \beta_f T_f}{cp_f} \tag{B.22}$$

$$e_{66} = \alpha_g \rho_g \tag{B.23}$$

$$e_{77} = \alpha_e \rho_e \tag{B.24}$$

$$e_{88} = \alpha_f \rho_f \tag{B.25}$$

And,

$$\mathbf{F} = \begin{bmatrix} f_{11} & f_{12} & 0 & f_{14} & 0 & f_{16} & 0 & 0 \\ f_{21} & f_{22} & f_{23} & f_{24} & 0 & 0 & f_{27} & 0 \\ f_{31} & 0 & f_{33} & 0 & f_{35} & 0 & 0 & f_{38} \\ f_{41} & 0 & f_{43} & f_{44} & f_{45} & f_{46} & f_{47} & f_{48} \\ f_{51} & 0 & f_{53} & f_{54} & f_{55} & f_{56} & f_{57} & f_{58} \\ 0 & 0 & 0 & 0 & 0 & f_{66} & 0 & 0 \\ 0 & 0 & 0 & 0 & 0 & 0 & f_{77} & 0 \\ 0 & 0 & 0 & 0 & 0 & 0 & 0 & f_{88} \end{bmatrix} \tag{B.26}$$

where,

$$f_{11} = \frac{\alpha_g u_c}{a_g^2} \tag{B.27}$$

$$f_{12} = \rho_g u_c \tag{B.28}$$

$$f_{14} = \alpha_g \rho_g \tag{B.29}$$

$$f_{16} = -\alpha_g u_c \frac{\rho_g \beta_g T_g}{cp_g} \tag{B.30}$$

$$f_{21} = \frac{\alpha_e u_c}{a_e^2} \tag{B.31}$$

$$f_{22} = -\rho_e u_c \tag{B.32}$$

$$f_{23} = -\rho_e u_c \tag{B.33}$$

$$f_{24} = \alpha_e \rho_e \tag{B.34}$$

$$f_{27} = -\alpha_e u_c \frac{\rho_e \beta_e T_e}{cp_e} \tag{B.35}$$

$$f_{31} = \frac{\alpha_f u_f}{a_f^2} \tag{B.36}$$

$$f_{33} = \rho_f u_f \tag{B.37}$$

$$f_{35} = \alpha_f \rho_f \tag{B.38}$$

$$f_{38} = -\alpha_f u_f \frac{\rho_f \beta_f T_f}{cp_f} \tag{B.39}$$

$$f_{41} = \alpha_c + \frac{\alpha_c \alpha_f u_a \Sigma \rho \Delta u}{\rho_c \rho_f} \tag{B.40}$$

$$f_{43} = -\alpha_c \alpha_f \Sigma \rho \Delta u^2 \tag{B.41}$$

$$f_{44} = \alpha_c \rho_c u_c - \alpha_c \alpha_f \Delta \rho \Delta u \tag{B.42}$$

$$f_{45} = \alpha_c \alpha_f \Delta \rho \Delta u \tag{B.43}$$

$$f_{46} = -\alpha_c \alpha_f u_c \Sigma \rho \Delta u \frac{\alpha_g \beta_g T_g}{cp_g} \tag{B.44}$$

$$f_{47} = -\alpha_c \alpha_f u_c \Sigma \rho \Delta u \frac{\alpha_e \beta_e T_e}{cp_e} \tag{B.45}$$

$$f_{48} = -\alpha_c \alpha_f u_f \Sigma \rho \Delta u \frac{\alpha_f \beta_f T_f}{cp_f} \tag{B.46}$$

$$f_{51} = \alpha_f - \frac{\alpha_c \alpha_f u_a \Sigma \rho \Delta u}{\rho_c \rho_f} \tag{B.47}$$

$$f_{53} = \alpha_c \alpha_f \Sigma \rho \Delta u^2 \tag{B.48}$$

$$f_{54} = \alpha_c \alpha_f \Delta \rho \Delta u \tag{B.49}$$

$$f_{55} = \alpha_f \rho_f u_f - \alpha_c \alpha_f \Delta \rho \Delta \tag{B.50}$$

$$f_{56} = \alpha_c \alpha_f u_c \Sigma \rho \Delta u \frac{\alpha_g \beta_g T_g}{cp_g} \tag{B.51}$$

$$f_{57} = \alpha_c \alpha_f u_c \Sigma \rho \Delta u \frac{\alpha_e \beta_e T_e}{cp_e} \tag{B.52}$$

$$f_{58} = \alpha_c \alpha_f u_f \Sigma \rho \Delta u \frac{\alpha_f \beta_f T_f}{cp_f} \tag{B.53}$$

$$f_{66} = \alpha_g \rho_g u_c \tag{B.54}$$

$$f_{77} = \alpha_e \rho_e u_c \tag{B.55}$$

$$f_{88} = \alpha_f \rho_f u_f \tag{B.56}$$

The source term is,

$$\vec{C} = \begin{bmatrix} 0 \\ M_e - M_f \\ M_f - M_e \\ -M_e \Delta u + F_c^{int} - \alpha_c \rho_c g_x \\ M_f \Delta u + F_f^{int} - F_f^w - \alpha_f \rho_f g_x \\ S_g \\ S_e \\ S_f \end{bmatrix} \tag{B.57}$$

where,

$$u_a = \frac{\alpha_c \rho_f u_c}{a_c^2} + \frac{\alpha_f \rho_c u_f}{a_f^2} \tag{B.58}$$

$$\rho = \alpha_c \rho_c + \alpha_f \rho_f \tag{B.59}$$

$$a_0 = \sqrt{\frac{\rho_c a_c^2 \rho_f a_f^2}{\rho \left(\alpha_c \rho_f a_f^2 + \alpha_f \rho_c a_c^2 \right)}} \tag{B.60}$$

$$S_g = -\frac{F_c^{int} \Delta u}{T_g} \tag{B.61}$$

$$S_e = \frac{M_e^{int} \left[(h_f - h_e) + \Delta u^2/2 \right]}{T_e} \tag{B.62}$$

$$S_f = \frac{F_f^{int} \Delta u + F_f^w u_f}{T_f} + \frac{M_f^{int} \left[(h_e - h_f) + \Delta u^2/2 \right]}{T_f} \tag{B.63}$$

The coefficient matrix and source term vector for the fully non-conservative form (Eq. (B.64)), obtained after the multiplication of the initial system ((B.1)) by $\mathbf{E}^{-1}$, are as follows.

$$\frac{\partial \vec{U}}{\partial t} + \mathbf{G} \frac{\partial \vec{U}}{\partial z} = \vec{D} \tag{B.64}$$

$$\mathbf{G} = \begin{bmatrix} g_{11} & 0 & g_{13} & g_{14} & g_{15} & 0 & 0 & 0 \\ g_{21} & g_{22} & g_{23} & g_{24} & g_{25} & 0 & 0 & 0 \\ g_{31} & 0 & g_{33} & g_{34} & g_{35} & 0 & 0 & 0 \\ g_{41} & 0 & 0 & g_{44} & g_{45} & 0 & 0 & 0 \\ g_{51} & 0 & 0 & g_{54} & g_{55} & 0 & 0 & 0 \\ 0 & 0 & 0 & 0 & 0 & g_{66} & 0 & 0 \\ 0 & 0 & 0 & 0 & 0 & 0 & g_{77} & 0 \\ 0 & 0 & 0 & 0 & 0 & 0 & 0 & g_{88} \end{bmatrix} \tag{B.65}$$

where,

$$g_{11} = (\varepsilon_c u_c + \varepsilon_f u_f) \rho a_0^2 \tag{B.66}$$

$$g_{13} = -\rho a_0^2 \Delta u \tag{B.67}$$

$$g_{14} = \alpha_c \rho a_0^2 \tag{B.68}$$

$$g_{15} = \alpha_f \rho a_0^2 \tag{B.69}$$

$$g_{21} = \varepsilon_g \varepsilon_f \rho a_0^2 \Delta u \tag{B.70}$$

$$g_{22} = u_c \tag{B.71}$$

$$g_{23} = \varepsilon_g \rho a_0^2 \Delta u \tag{B.72}$$

$$g_{24} = \varepsilon_g \left(\rho_g a_g^2 - \alpha_c \rho a_0^2 \right) \tag{B.73}$$

$$g_{25} = -\varepsilon_g \alpha_f \rho a_0^2 \tag{B.74}$$

$$g_{31} = -\varepsilon_c \varepsilon_f \rho a_0^2 \Delta u \tag{B.75}$$

$$g_{33} = \left(\varepsilon_f u_c + \varepsilon_c u_f \right) \rho a_0^2 \tag{B.76}$$

$$g_{34} = -\varepsilon_f \alpha_c \rho a_0^2 \tag{B.77}$$

$$f_{35} = \varepsilon_c \alpha_f \rho a_0^2 \tag{B.78}$$

$$f_{41} = \frac{1}{\rho_c} \tag{B.79}$$

$$f_{44} = \alpha_c u_c + \alpha_f u_f \tag{B.80}$$

$$f_{45} = -\frac{\alpha_f \rho_f}{\rho_c} \Delta u \tag{B.81}$$

$$f_{51} = \frac{1}{\rho_f} \tag{B.82}$$

$$f_{54} = \frac{\alpha_c \rho_c}{\rho_f} \Delta u \tag{B.83}$$

$$f_{55} = \alpha_c u_c + \alpha_f u_f \tag{B.84}$$

$$f_{66} = u_c \tag{B.85}$$

$$f_{77} = u_c \tag{B.86}$$

$$f_{88} = u_f \tag{B.87}$$

The source term is,

$$\vec{D} = \begin{bmatrix} d_1 \\ d_2 \\ d_3 \\ d_4 \\ d_5 \\ d_6 \\ d_7 \\ d_8 \end{bmatrix} \tag{B.88}$$

where,

$$\frac{d_1}{\rho a_0^2} = \kappa_g S_g + \kappa_e S_e + \frac{M_e - M_f}{\rho_e} + \kappa_f S_f - \frac{M_e - M_f}{\rho_f} \tag{B.89}$$

$$\frac{d_2}{\rho a_0^2} = (\varepsilon_e + \varepsilon_f)\,\kappa_g S_g - \varepsilon_g \left(\kappa_e S_e + \frac{M_e - M_f}{\rho_e} \right) - \varepsilon_g \left(\kappa_f S_f - \frac{M_e - M_f}{\rho_f} \right) \tag{B.90}$$

$$\frac{d_3}{\rho a_0^2} = -\varepsilon_f \kappa_g S_g - \varepsilon_f \left(\kappa_e S_e + \frac{M_e - M_f}{\rho_e} \right) + (\varepsilon_g + \varepsilon_e) \left(\kappa_f S_f - \frac{M_e - M_f}{\rho_f} \right) \tag{B.91}$$

$$d_4 \alpha_c \rho_c = F_c^{int} - M_e \Delta u$$
$$+ \alpha_c \alpha_f \Sigma \rho \Delta u \left(\frac{1}{\rho_f} - \frac{1}{\rho_e} \right) \left(M_e - M_f \right) - g_x \tag{B.92}$$

$$d_5 \alpha_f \rho_f = F_f^{int} - F_f^w + M_f \Delta u$$
$$- \alpha_c \alpha_f \Sigma \rho \Delta u \left(\frac{1}{\rho_f} - \frac{1}{\rho_e} \right) \left(M_e - M_f \right) - g_x \tag{B.93}$$

$$d_6 = \frac{S_g}{\alpha_g \rho_g} \tag{B.94}$$

$$d_7 = \frac{S_e}{\alpha_e \rho_e} \tag{B.95}$$

$$d_8 = \frac{S_f}{\alpha_f \rho_f} \tag{B.96}$$

$$\kappa_i = \frac{\beta_i T_i}{\rho_i c_{p_i}} \tag{B.97}$$

$$\varepsilon_i = \frac{\alpha_i}{\rho_i a_i^2} \tag{B.98}$$

After obtaining the coefficient matrix, this is subjected to a eigenvalue analysis, which results in the following pairs of eigenvalues and associated eigenvectors.

$$\lambda_1 = u + a \tag{B.99}$$

$$\vec{T}_1 = \begin{bmatrix} \rho_s \rho a_0^2 \\ \alpha_g \left(\rho_f - \frac{\rho_s \rho a_0^2}{\rho_g a_g^2} \right) \\ -\alpha_c \alpha_f \rho a_0^2 \left(\frac{1}{a_f^2} - \frac{1}{a_c^2} \right) \\ \rho_f \left(a - \alpha_f \Delta u \right) \\ \rho_c \left(a + \alpha_c \Delta u \right) \\ 0 \\ 0 \\ 0 \end{bmatrix} \tag{B.100}$$

$$\lambda_2 = u - a \tag{B.101}$$

$$
\vec{T}_2 =
\begin{bmatrix}
\rho_s \rho a_0^2 \\
\alpha_g \left(\rho_f - \frac{\rho_s \rho a_0^2}{\rho_g a_g^2} \right) \\
-\alpha_c \alpha_f \rho a_0^2 \left(\frac{1}{a_f^2} - \frac{1}{a_c^2} \right) \\
-\rho_f \left(a + \alpha_f \Delta u \right) \\
-\rho_c \left(a - \alpha_c \Delta u \right) \\
0 \\
0 \\
0
\end{bmatrix}
\tag{B.102}
$$

$$\lambda_3 = u_c \tag{B.103}$$

$$
\vec{T}_3 =
\begin{bmatrix}
\alpha_f \rho_f \Delta u^2 \\
0 \\
\alpha_f \left(1 - \alpha_f \frac{\Delta u^2}{a_f^2} \right) \\
0 \\
\Delta u \\
0 \\
0 \\
0
\end{bmatrix}
\tag{B.104}
$$

$$\lambda_4 = u_f \tag{B.105}$$

$$
\vec{T}_4 =
\begin{bmatrix}
\alpha_c \rho_c \Delta u^2 \\
0 \\
-\alpha_c \left(1 - \alpha_c \frac{\Delta u^2}{a_c^2} \right) \\
-\Delta u \\
0 \\
0 \\
0 \\
0
\end{bmatrix}
\tag{B.106}
$$

$$\lambda_5 = u_c \tag{B.107}$$

$$\vec{T}_5 = \begin{bmatrix} 0 \\ 1 \\ 0 \\ 0 \\ 0 \\ 0 \\ 0 \\ 0 \end{bmatrix} \tag{B.108}$$

$$\lambda_6 = u_c \tag{B.109}$$

$$\vec{T}_6 = \begin{bmatrix} 0 \\ 0 \\ 0 \\ 0 \\ 0 \\ 1 \\ 0 \\ 0 \end{bmatrix} \tag{B.110}$$

$$\lambda_7 = u_c \tag{B.111}$$

$$\vec{T}_7 = \begin{bmatrix} 0 \\ 0 \\ 0 \\ 0 \\ 0 \\ 0 \\ 1 \\ 0 \end{bmatrix} \tag{B.112}$$

$$\lambda_8 = u_f \tag{B.113}$$

$$\vec{T_8} = \begin{bmatrix} 0 \\ 0 \\ 0 \\ 0 \\ 0 \\ 0 \\ 0 \\ 1 \end{bmatrix} \tag{B.114}$$

$$u = \alpha_c u_c + \alpha_f u_f \tag{B.115}$$

$$a = \sqrt{\tilde{a}^2 - \alpha_c \alpha_f \Delta u^2} \tag{B.116}$$

$$\tilde{a}^2 = \frac{\rho_s \rho a_0^2}{\rho_c \rho_f} \tag{B.117}$$

After the coefficient matrix is separated using the SCMM, one individual matrix associated with each eigenvalue is created (see Section 4.1). These are more easily displayed in terms of cross products, as follows,

$$\mathbf{G_1} = \varphi_1 \begin{bmatrix} \rho_s \rho a_0^2 \\ \frac{\alpha_g}{\rho_g a_g^2}\left(\rho_f \rho_g a_g^2 - \rho_s \rho a_0^2\right) \\ \alpha_c \alpha_f \left(\frac{1}{a_c^2} - \frac{1}{a_f^2}\right)\rho a_0^2 \\ \rho_f \left(a - \alpha_f \Delta u\right) \\ \rho_c \left(a + \alpha_c \Delta u\right) \\ 0 \\ 0 \\ 0 \end{bmatrix} \times \begin{bmatrix} \rho_s a + \rho_s \Delta u \Delta a \\ 0 \\ -\rho_s \rho a_0^2 \Delta u \\ \alpha_c \rho_c \left(\rho_f a_2^2 + \rho_s a \Delta u\right) \\ \alpha_f \rho_f \left(\rho_c a_1^2 - \rho_s a \Delta u\right) \\ 0 \\ 0 \\ 0 \end{bmatrix}^T \tag{B.118}$$

$$\mathbf{G_2} = \varphi_2 \begin{bmatrix} \rho_s \rho a_0^2 \\ \frac{\alpha_g}{\rho_g a_g^2}\left(\rho_f \rho_g a_g^2 - \rho_s \rho a_0^2\right) \\ \alpha_c \alpha_f \left(\frac{1}{a_c^2} - \frac{1}{a_f^2}\right)\rho a_0^2 \\ \rho_f \left(-a - \alpha_f \Delta u\right) \\ \rho_c \left(-a + \alpha_c \Delta u\right) \\ 0 \\ 0 \\ 0 \end{bmatrix} \times \begin{bmatrix} -\rho_s a + \rho_s \Delta u \Delta a \\ 0 \\ -\rho_s \rho a_0^2 \Delta u \\ \alpha_c \rho_c \left(\rho_f a_2^2 - \rho_s a \Delta u\right) \\ \alpha_f \rho_f \left(\rho_c a_1^2 + \rho_s a \Delta u\right) \\ 0 \\ 0 \\ 0 \end{bmatrix}^T \tag{B.119}$$

$$
\mathbf{G}_3 = \varphi_3
\begin{bmatrix}
\alpha_f \rho_f \Delta u^2 \\
0 \\
\alpha_f \left[1 - \dfrac{\alpha_f (\Delta u)^2}{a_f^2} \right] \\
0 \\
\Delta u \\
0 \\
0 \\
0
\end{bmatrix}
\times
\begin{bmatrix}
\dfrac{\alpha_c \Delta u}{a_c^2} \\
0 \\
-\rho_c \Delta u \\
\alpha_c \rho_c \\
-\alpha_c \rho_f \\
0 \\
0 \\
0
\end{bmatrix}^T
\tag{B.120}
$$

$$
\mathbf{G}_4 = \varphi_4
\begin{bmatrix}
\alpha_c \rho_c \Delta u^2 \\
\alpha_g \left[1 - \dfrac{\alpha_c \rho_c (\Delta u)^2}{\rho_g a_g^2} \right] \\
-\alpha_c \left[1 - \dfrac{\alpha_c (\Delta u)^2}{a_c^2} \right] \\
-\Delta u \\
0 \\
0 \\
0 \\
0
\end{bmatrix}
\times
\begin{bmatrix}
\dfrac{\alpha_f \Delta u}{a_f^2} \\
0 \\
\rho_f \Delta u \\
\alpha_f \rho_c \\
-\alpha_f \rho_f \\
0 \\
0 \\
0
\end{bmatrix}^T
\tag{B.121}
$$

$$
\mathbf{G}_5 = \varphi_5
\begin{bmatrix}
0 \\
\alpha_g \\
0 \\
0 \\
0 \\
0 \\
0 \\
0
\end{bmatrix}
\times
\begin{bmatrix}
\alpha_e \rho_f \Delta u \left(\dfrac{1}{\rho_g a_g^2} - \dfrac{1}{\rho_e a_e^2} \right) + \dfrac{\alpha_f \rho_c \Delta u}{\rho_g a_g^2} \left[1 - \dfrac{\alpha_f \Delta u^2}{a_f^2} \right] \\
1 \\
\rho_f \Delta u \left[1 - \dfrac{\alpha_f \rho_c \Delta u^2}{\rho_g a_g^2} \right] \\
\alpha_f \rho_c - \alpha_f \rho_c \rho_f \left(\dfrac{1}{\rho a_0^2} - \dfrac{\alpha_c}{\rho_g a_g^2} \right) \Delta u^2 \\
-\alpha_f \rho_f + \alpha_f \rho_f^2 \left(\dfrac{1}{\rho a_0^2} - \dfrac{\alpha_c}{\rho_g a_g^2} \right) \Delta u^2 \\
0 \\
0 \\
0
\end{bmatrix}^T
\tag{B.122}
$$

$$
\mathbf{G}_6 = u_c
\begin{bmatrix}
0 & 0 & 0 & 0 & 0 & 0 & 0 & 0 \\
0 & 0 & 0 & 0 & 0 & 0 & 0 & 0 \\
0 & 0 & 0 & 0 & 0 & 0 & 0 & 0 \\
0 & 0 & 0 & 0 & 0 & 0 & 0 & 0 \\
0 & 0 & 0 & 0 & 0 & 0 & 0 & 0 \\
0 & 0 & 0 & 0 & 0 & 1 & 0 & 0 \\
0 & 0 & 0 & 0 & 0 & 0 & 0 & 0 \\
0 & 0 & 0 & 0 & 0 & 0 & 0 & 0
\end{bmatrix}
\tag{B.123}
$$

$$\mathbf{G}_7 = u_c \begin{bmatrix} 0 & 0 & 0 & 0 & 0 & 0 & 0 & 0 \\ 0 & 0 & 0 & 0 & 0 & 0 & 0 & 0 \\ 0 & 0 & 0 & 0 & 0 & 0 & 0 & 0 \\ 0 & 0 & 0 & 0 & 0 & 0 & 0 & 0 \\ 0 & 0 & 0 & 0 & 0 & 0 & 0 & 0 \\ 0 & 0 & 0 & 0 & 0 & 0 & 0 & 0 \\ 0 & 0 & 0 & 0 & 0 & 0 & 1 & 0 \\ 0 & 0 & 0 & 0 & 0 & 0 & 0 & 0 \end{bmatrix} \tag{B.124}$$

$$\mathbf{G}_8 = u_f \begin{bmatrix} 0 & 0 & 0 & 0 & 0 & 0 & 0 & 0 \\ 0 & 0 & 0 & 0 & 0 & 0 & 0 & 0 \\ 0 & 0 & 0 & 0 & 0 & 0 & 0 & 0 \\ 0 & 0 & 0 & 0 & 0 & 0 & 0 & 0 \\ 0 & 0 & 0 & 0 & 0 & 0 & 0 & 0 \\ 0 & 0 & 0 & 0 & 0 & 0 & 0 & 0 \\ 0 & 0 & 0 & 0 & 0 & 0 & 0 & 0 \\ 0 & 0 & 0 & 0 & 0 & 0 & 0 & 1 \end{bmatrix} \tag{B.125}$$

where,

$$\varphi_1 = (u + a)\,\frac{a^2 - \alpha_c\alpha_f\Delta u^2 + a\Delta u\Delta\alpha}{2a\rho_c\rho_f\rho_s a_3^2 a_4^2} \tag{B.126}$$

$$\varphi_2 = -(u - a)\,\frac{a^2 - \alpha_c\alpha_f\Delta u^2 - a\Delta u\Delta\alpha}{2a\rho_c\rho_f\rho_s a_3^2 a_4^2} \tag{B.127}$$

$$\varphi_3 = -\frac{\rho a_0^2 u_c}{\rho_c\rho_f a_3^2 \Delta u} \tag{B.128}$$

$$\varphi_4 = -\frac{\rho a_0^2 u_f}{\rho_c\rho_f a_4^2 \Delta u} \tag{B.129}$$

$$\varphi_5 = \frac{\rho a_0^2}{\rho_c\rho_f a_3^2 \Delta u}u_c \tag{B.130}$$

$$a_1^2 = a^2 - (\alpha_c\Delta u)^2\,\frac{\rho_f}{\rho_c} \tag{B.131}$$

$$a_2^2 = a^2 - (\alpha_f\Delta u)^2\,\frac{\rho_c}{\rho_f} \tag{B.132}$$

$$a_3^2 = a^2 - (\alpha_f\Delta u)^2 \tag{B.133}$$

$$a_4^2 = a^2 - (\alpha_c \Delta u)^2 \tag{B.134}$$

$$\Delta a = \rho a_0^2 \left(\frac{\alpha_c^2}{\rho_c a_c^2} - \frac{\alpha_f^2}{\rho_f a_f^2} \right) \tag{B.135}$$

$$\Delta \alpha = \alpha_f - \alpha_c \tag{B.136}$$

Finally, the separated coefficient matrices are as follows,

$$
\begin{aligned}
\mathbf{G}^+ &= G_1 + \frac{u_c + |u_c|}{2u_c} (G_3 + G_5 + G_6 + G_7) \\
&+ \frac{u_f + |u_f|}{2u_f} (G_4 + G_8)
\end{aligned} \tag{B.137}
$$

$$
\begin{aligned}
\mathbf{G}^- &= G_2 + \frac{u_c - |u_c|}{2u_c} (G_3 + G_5 + G_6 + G_7) \\
&+ \frac{u_f - |u_f|}{2u_f} (G_4 + G_8)
\end{aligned} \tag{B.138}
$$

The structure of the full coefficient matrix is shown in Fig. B.1 for an example where the numerical grid has 10 points.

Where the individual block matrices inside matrix $\mathbf{A}$ have the following structure,

$$A = \begin{bmatrix}
[p(1)] & [f(1)] & [ff(1)] & [0] & [0] & [0] & [0] & [0] & [0] & [0] \\
[b(i)] & [p(i)] & [f(i)] & [ff(i)] & [0] & [0] & [0] & [0] & [0] & [0] \\
[bb(i)] & [b(i)] & [p(i)] & [f(i)] & [ff(i)] & [0] & [0] & [0] & [0] & [0] \\
[0] & [bb(i)] & [b(i)] & [p(i)] & [f(i)] & [ff(i)] & [0] & [0] & [0] & [0] \\
[0] & [0] & [bb(i)] & [b(i)] & [p(i)] & [f(i)] & [ff(i)] & [0] & [0] & [0] \\
[0] & [0] & [0] & [bb(i)] & [b(i)] & [p(i)] & [f(i)] & [ff(i)] & [0] & [0] \\
[0] & [0] & [0] & [0] & [bb(i)] & [b(i)] & [p(i)] & [f(i)] & [ff(i)] & [0] \\
[0] & [0] & [0] & [0] & [0] & [bb(i)] & [b(i)] & [p(i)] & [f(i)] & [ff(i)] \\
[0] & [0] & [0] & [0] & [0] & [0] & [bb(n)] & [b(n)] & [p(n)] & [f(i)] \\
[0] & [0] & [0] & [0] & [0] & [0] & [0] & [bb(n)] & [b(n)] & [p(n)]
\end{bmatrix}$$

Figure B.1 – Structure of the full linear system coefficient matrix for Eq. (4.43).

For the first and last points the boundary conditions must be considered and so the structure of the global matrix (Fig. B.1) and the value of the elements inside each block matrix are different. For the first point the structure is,

$$
\mathbf{p}(1) =
\begin{bmatrix}
p_{11}(1) & p_{12}(1) & p_{13}(1) & p_{14}(1) & p_{15}(1) & 0 & 0 & 0 \\
0 & 1 & 0 & 0 & 0 & 0 & 0 & 0 \\
0 & 0 & 1 & 0 & 0 & 0 & 0 & 0 \\
0 & 0 & 0 & 1 & 0 & 0 & 0 & 0 \\
0 & 0 & 0 & 0 & 1 & 0 & 0 & 0 \\
0 & 0 & 0 & 0 & 0 & 1 & 0 & 0 \\
0 & 0 & 0 & 0 & 0 & 0 & 1 & 0 \\
0 & 0 & 0 & 0 & 0 & 0 & 0 & 1
\end{bmatrix}
\tag{B.139}
$$

$$
\mathbf{f}(1) =
\begin{bmatrix}
f_{11}(1) & f_{12}(1) & f_{13}(1) & f_{14}(1) & f_{15}(1) & 0 & 0 & 0 \\
0 & 0 & 0 & 0 & 0 & 0 & 0 & 0 \\
0 & 0 & 0 & 0 & 0 & 0 & 0 & 0 \\
0 & 0 & 0 & 0 & 0 & 0 & 0 & 0 \\
0 & 0 & 0 & 0 & 0 & 0 & 0 & 0 \\
0 & 0 & 0 & 0 & 0 & 0 & 0 & 0 \\
0 & 0 & 0 & 0 & 0 & 0 & 0 & 0 \\
0 & 0 & 0 & 0 & 0 & 0 & 0 & 0
\end{bmatrix}
\tag{B.140}
$$

$$
\mathbf{ff}(1) =
\begin{bmatrix}
ff_{11}(1) & ff_{12}(1) & ff_{13}(1) & ff_{14}(1) & ff_{15}(1) & 0 & 0 & 0 \\
0 & 0 & 0 & 0 & 0 & 0 & 0 & 0 \\
0 & 0 & 0 & 0 & 0 & 0 & 0 & 0 \\
0 & 0 & 0 & 0 & 0 & 0 & 0 & 0 \\
0 & 0 & 0 & 0 & 0 & 0 & 0 & 0 \\
0 & 0 & 0 & 0 & 0 & 0 & 0 & 0 \\
0 & 0 & 0 & 0 & 0 & 0 & 0 & 0 \\
0 & 0 & 0 & 0 & 0 & 0 & 0 & 0
\end{bmatrix}
\tag{B.141}
$$

$\mathbf{bb}(n) =$

$$
\begin{bmatrix}
0 & 0 & 0 & 0 & 0 & 0 & 0 & 0 \\
bb_{21}(n) & bb_{22}(n) & bb_{23}(n) & bb_{24}(n) & bb_{25}(n) & 0 & 0 & 0 \\
bb_{31}(n) & bb_{32}(n) & bb_{33}(n) & bb_{34}(n) & bb_{35}(n) & 0 & 0 & 0 \\
bb_{41}(n) & bb_{42}(n) & bb_{43}(n) & bb_{44}(n) & bb_{45}(n) & 0 & 0 & 0 \\
bb_{51}(n) & bb_{52}(n) & bb_{53}(n) & bb_{54}(n) & bb_{55}(n) & 0 & 0 & 0 \\
0 & 0 & 0 & 0 & 0 & bb_{66}(n) & 0 & 0 \\
0 & 0 & 0 & 0 & 0 & 0 & bb_{77}(n) & 0 \\
0 & 0 & 0 & 0 & 0 & 0 & 0 & bb_{88}(n)
\end{bmatrix}
\tag{B.142}
$$

$\mathbf{b}(n) =$

$$
\begin{bmatrix}
0 & 0 & 0 & 0 & 0 & 0 & 0 & 0 \\
b_{21}(n) & b_{22}(n) & b_{23}(n) & b_{24}(n) & b_{25}(n) & 0 & 0 & 0 \\
b_{31}(n) & b_{32}(n) & b_{33}(n) & b_{34}(n) & b_{35}(n) & 0 & 0 & 0 \\
b_{41}(n) & b_{42}(n) & b_{43}(n) & b_{44}(n) & b_{45}(n) & 0 & 0 & 0 \\
b_{51}(n) & b_{52}(n) & b_{53}(n) & b_{54}(n) & b_{55}(n) & 0 & 0 & 0 \\
0 & 0 & 0 & 0 & 0 & b_{66}(n) & 0 & 0 \\
0 & 0 & 0 & 0 & 0 & 0 & b_{77}(n) & 0 \\
0 & 0 & 0 & 0 & 0 & 0 & 0 & b_{88}(n)
\end{bmatrix}
\tag{B.143}
$$

$\mathbf{p}(n) =$

$$
\begin{bmatrix}
1 & 0 & 0 & 0 & 0 & 0 & 0 & 0 \\
p_{21}(n) & p_{22}(n) & p_{23}(n) & p_{24}(n) & p_{25}(n) & 0 & 0 & 0 \\
p_{31}(n) & p_{32}(n) & p_{33}(n) & p_{34}(n) & p_{35}(n) & 0 & 0 & 0 \\
p_{41}(n) & p_{42}(n) & p_{43}(n) & p_{44}(n) & p_{45}(n) & 0 & 0 & 0 \\
p_{51}(n) & p_{52}(n) & p_{53}(n) & p_{54}(n) & p_{55}(n) & 0 & 0 & 0 \\
0 & 0 & 0 & 0 & 0 & p_{66}(n) & 0 & 0 \\
0 & 0 & 0 & 0 & 0 & 0 & p_{77}(n) & 0 \\
0 & 0 & 0 & 0 & 0 & 0 & 0 & p_{88}(n)
\end{bmatrix}
\tag{B.144}
$$

For the inner points $i = 2$ until $i = n - 1$ the block matrices structures are the same, and only the central matrix is shown.

$$\mathbf{p}(i) =$$

$$
\begin{bmatrix}
p_{11}(i) & p_{12}(i) & p_{13}(i) & p_{14}(i) & p_{15}(i) & 0 & 0 & 0 \\
p_{21}(i) & p_{22}(i) & p_{23}(i) & p_{24}(i) & p_{25}(i) & 0 & 0 & 0 \\
p_{31}(i) & p_{32}(i) & p_{33}(i) & p_{34}(i) & p_{35}(i) & 0 & 0 & 0 \\
p_{41}(i) & p_{42}(i) & p_{43}(i) & p_{44}(i) & p_{45}(i) & 0 & 0 & 0 \\
p_{51}(i) & p_{52}(i) & p_{53}(i) & p_{54}(i) & p_{55}(i) & 0 & 0 & 0 \\
0 & 0 & 0 & 0 & 0 & p_{66}(i) & 0 & 0 \\
0 & 0 & 0 & 0 & 0 & 0 & p_{77}(i) & 0 \\
0 & 0 & 0 & 0 & 0 & 0 & 0 & p_{88}(i)
\end{bmatrix}
\tag{B.145}
$$

The values of each element is defined by equations (B.137), (B.138) and the discretization scheme. For more information on this topic see Anderson *et al.* (1984) and Städtke (2006).

APPENDIX C

Equations of the Two-Field Formulation

The two-fluid formulation uses the same closure relations of the three-field one except the entrainment and deposition rates which are not necessary due to the absence of entrained droplets. In this way the conservative form of the conservation equations for mass momentum and energy, are as following,

$$\frac{\partial}{\partial t}\left(\alpha_g \rho_g\right) + \frac{\partial}{\partial z}\left(\alpha_g \rho_g u_g\right) = 0 \qquad \text{(C.1)}$$

$$\frac{\partial}{\partial t}\left(\alpha_l \rho_l\right) + \frac{\partial}{\partial z}\left(\alpha_l \rho_l u_l\right) = 0 \qquad \text{(C.2)}$$

$$\frac{\partial}{\partial t}\left(\alpha_g \rho_g u_g\right) + \frac{\partial}{\partial z}\left(\alpha_g \rho_g u_g^2\right) + \alpha_g \frac{\partial p}{\partial z} = F_g^{nv} + F_g^{int} - \alpha_g \rho_g g_z \qquad \text{(C.3)}$$

$$\frac{\partial}{\partial t}\left(\alpha_l \rho_l u_l\right) + \frac{\partial}{\partial z}\left(\alpha_l \rho_l u_l^2\right) + \alpha_l \frac{\partial p}{\partial z} = F_l^{nv} + F_l^{int} - F_l^{w} - \alpha_l \rho_l g_z \qquad \text{(C.4)}$$

$$\frac{\partial}{\partial t}\left(\alpha_g \rho_g s_g\right) + \frac{\partial}{\partial z}\left(\alpha_g \rho_g u_g s_g\right) = \frac{1}{T_g}\left(F_g^{int}\Delta u\right) \qquad \text{(C.5)}$$

$$\frac{\partial}{\partial t}\left(\alpha_l \rho_l s_l\right) + \frac{\partial}{\partial z}\left(\alpha_l \rho_l u_l s_l\right) = \frac{1}{T_l}\left(F_l^{w}u_l + F_l^{int}\Delta u\right) \qquad \text{(C.6)}$$

Where F_k^{nv} denotes the non-viscous interfacial forces per unity of volume the act in phase k. And, from the Newton's Third Law,

$$F_l^{nv} = -F_g^{nv} \qquad \text{(C.7)}$$

$$\Delta u = u_g - u_l \tag{C.8}$$

Using the same procedure used for the three-field model, the equations (C.1) to (C.6) are transformed to the non-conservative form. Using the thermodynamic relations below and the phase density written as a function of pressure and phase entropy,

$$de_i = T_i \delta s_i + \frac{p}{\rho_i^2} \delta \rho_i \tag{C.9}$$

$$\delta \rho_i = \left(\frac{\partial \rho_i}{\partial s_i} \right)_p \delta s_i + \left(\frac{\partial \rho_i}{\partial p} \right)_{s_i} \delta p \tag{C.10}$$

With introduction of the phase sound velocity, Eq. (C.12), isothermal compressibility coefficient, Eq. (C.13), and isobaric specific heat capacity, Eq. (C.14), results in,

$$\delta \rho_i = \frac{\rho_i \beta_i T_i}{c_{p_i}} \delta s_i - \frac{1}{a_i^2} \delta p \tag{C.11}$$

$$a = \sqrt{\left. \frac{\partial p}{\partial \rho} \right|_s} \tag{C.12}$$

$$\beta = \frac{c_{p_i}}{\rho T} \left. \frac{\partial p}{\partial \rho} \right|_s \tag{C.13}$$

$$c_{p_i} = \left. \frac{\partial h}{\partial T} \right|_p \tag{C.14}$$

In this way, the fully non-conservative form of the two-field formulation is expressed as,

$$\frac{\alpha_g}{a_g^2} \left(\frac{\partial p}{\partial t} + u_g \frac{\partial p}{\partial z} \right) + \rho_g \left(\frac{\partial \alpha_g}{\partial t} + u_g \frac{\partial \alpha_g}{\partial z} \right)$$
$$- \alpha_g \left(\frac{\rho_g \beta_g T_g}{c_{p_g}} \right) \left(\frac{\partial s_g}{\partial t} + u_g \frac{\partial s_g}{\partial z} \right) + \alpha_g \rho_g \frac{\partial u_g}{\partial z} = 0 \tag{C.15}$$

$$\frac{\alpha_l}{a_l^2}\left(\frac{\partial p}{\partial t} + u_l\frac{\partial p}{\partial z}\right) - \rho_l\left(\frac{\partial \alpha_g}{\partial t} + u_l\frac{\partial \alpha_g}{\partial z}\right)$$

$$- \alpha_l\left(\frac{\rho_l\beta_l T_l}{c_{pl}}\right)\left(\frac{\partial s_l}{\partial t} + u_l\frac{\partial s_l}{\partial z}\right) + \alpha_l\rho_l\frac{\partial u_l}{\partial z} = 0 \tag{C.16}$$

$$\alpha_g\rho_g\left(\frac{\partial u_g}{\partial t} + u_g\frac{\partial u_g}{\partial z}\right) + \alpha_g\frac{\partial p}{\partial z} = F_g^{nv} + F_g^{int} - \alpha_g\rho_g g_z \tag{C.17}$$

$$\alpha_l\rho_l\left(\frac{\partial u_l}{\partial t} + u_l\frac{\partial u_l}{\partial z}\right) + \alpha_l\frac{\partial p}{\partial z} = F_l^{nv} + F_l^{int} - F_l^{w} - \alpha_l\rho_l g_z \tag{C.18}$$

$$\alpha_g\rho_g\left(\frac{\partial s_g}{\partial t} + u_g\frac{\partial s_g}{\partial z}\right) = \frac{1}{T_g}\left(F_g^{int}\Delta u\right) \tag{C.19}$$

$$\alpha_l\rho_l\left(\frac{\partial s_l}{\partial t} + u_l\frac{\partial s_l}{\partial z}\right) = \frac{1}{T_l}\left(F_l^{w} u_l + F_l^{int}\Delta u\right) \tag{C.20}$$

Substituting eqs. (C.19) into (C.15) and (C.20) into (C.16), the final form of the conservation equations in fully non conservative form with the mass conservation equation transformed into an equation for gas fraction (C.21) and another for pressure (C.22).

$$\frac{\alpha_g}{a_g^2}\left(\frac{\partial p}{\partial t} + u_g\frac{\partial p}{\partial z}\right) + \rho_g\left(\frac{\partial \alpha_g}{\partial t} + u_g\frac{\partial \alpha_g}{\partial z}\right)$$

$$- \left(\frac{\beta_g}{c_{pg}}\right)\left(F_g^{int}\Delta u\right) + \alpha_g\rho_g\frac{\partial u_g}{\partial z} = 0 \tag{C.21}$$

$$\frac{\alpha_l}{a_l^2}\left(\frac{\partial p}{\partial t} + u_l\frac{\partial p}{\partial z}\right) - \rho_l\left(\frac{\partial \alpha_g}{\partial t} + u_l\frac{\partial \alpha_g}{\partial z}\right)$$

$$- \left(\frac{\rho_l\beta_l}{c_{pl}}\right)\left(F_l^{w} u_l + F_l^{int}\Delta u\right) + \alpha_l\rho_l\frac{\partial u_l}{\partial z} = 0 \tag{C.22}$$

$$\alpha_g\rho_g\left(\frac{\partial u_g}{\partial t} + u_g\frac{\partial u_g}{\partial z}\right) + \alpha_g\frac{\partial p}{\partial z} = F_g^{nv} + F_g^{int} - \alpha_g\rho_g g_z \tag{C.23}$$

$$\alpha_l\rho_l\left(\frac{\partial u_l}{\partial t} + u_l\frac{\partial u_l}{\partial z}\right) + \alpha_l\frac{\partial p}{\partial z} = F_l^{nv} + F_l^{int} - F_l^{w} - \alpha_l\rho_l g_z \tag{C.24}$$

$$\alpha_g\rho_g\left(\frac{\partial s_g}{\partial t} + u_g\frac{\partial s_g}{\partial z}\right) = \frac{1}{T_g}\left(F_g^{int}\Delta u\right) \tag{C.25}$$

$$\alpha_l \rho_l \left(\frac{\partial s_l}{\partial t} + u_l \frac{\partial s_l}{\partial z} \right) = \frac{1}{T_l} \left(F_l^w u_l + F_l^{int} \Delta u \right) \tag{C.26}$$

These equations are then arranged in a compact PDE form as,

$$\mathbf{E} \frac{\partial \vec{U}}{\partial t} + \mathbf{F} \frac{\partial \vec{U}}{\partial z} = \vec{C} \tag{C.27}$$

where the unknown variables vector is given by,

$$\vec{U} = \begin{bmatrix} p & \alpha_g & u_g & u_l & s_g & s_l \end{bmatrix}^T \tag{C.28}$$

To obtain the fully non-conservative form, Eq. (C.27) must be multiplied by $\mathbf{E}^{-1}$ to be transformed into,

$$\frac{\partial \vec{U}}{\partial t} + \mathbf{G} \frac{\partial \vec{U}}{\partial z} = \vec{D} \tag{C.29}$$

The non-viscous forces are modelled in a similar way as for the three-field formulation. Their physical meaning for the annular and churn flow patterns have already been discussed in Section 3.2. The mathematical expressions for the virtual mass, compressibility and interfacial pressure difference terms are presented below.

$$F_g^{vm} = - \alpha_g \alpha_l \rho c_1 \left(\frac{\partial u_g}{\partial t} + u_l \frac{\partial u_g}{\partial z} - \frac{\partial u_l}{\partial t} - u_g \frac{\partial u_l}{\partial z} \right)$$
$$- \alpha_g \alpha_l \rho c_2 \Delta u \left(\frac{\partial u_g}{\partial z} - \frac{\partial u_l}{\partial z} \right) \tag{C.30}$$

$$F_g^{\Delta p} = -c_3 \alpha_g \alpha_l \rho \left(\Delta u \right)^2 \frac{\partial \alpha_g}{\partial z} \tag{C.31}$$

$$F_g^{comp} = - \alpha_g \alpha_l \Delta u c_4 \left(\frac{\partial \rho_g}{\partial t} + u_g \frac{\partial \rho_g}{\partial z} \right)$$
$$- \alpha_g \alpha_l \Delta u c_5 \left(\frac{\partial \rho_l}{\partial t} + u_l \frac{\partial \rho_l}{\partial z} \right) \tag{C.32}$$

Where c_i are fitting parameters presented by Städtke (2006) as:

$$c_1 = k \tag{C.33}$$

$$c_2 = -\frac{\alpha_g \rho_l - \alpha_l \rho_g}{\rho} \tag{C.34}$$

$$c_3 = \frac{\rho_l + \rho_g}{\rho} \tag{C.35}$$

$$c_4 = \alpha_g \frac{\rho_l + \rho_g}{\rho_g} \tag{C.36}$$

$$c_5 = \alpha_l \frac{\rho_l + \rho_g}{\rho_l} \tag{C.37}$$

Where the virtual mass coefficient k is employed in adjusting the momentum transfer in the interfacial coupling for the different flow pattern that can occur. For this work this coefficient is kept equal do zero to be consistent with the three-field formulation that neglects the influence of this parameter. Also, Newton's third law implies that

$$F_l^{nv} = -F_g^{nv} \tag{C.38}$$

The coefficient matrices **E**, **F** and **G** are presented below.

$$\mathbf{E} = \begin{bmatrix} e_{11} & e_{12} & 0 & 0 & e_{15} & 0 \\ e_{21} & e_{22} & 0 & 0 & 0 & e_{26} \\ e_{31} & 0 & e_{33} & e_{34} & e_{35} & e_{36} \\ e_{41} & 0 & e_{43} & e_{44} & e_{45} & e_{46} \\ 0 & 0 & 0 & 0 & e_{55} & 0 \\ 0 & 0 & 0 & 0 & 0 & e_{66} \end{bmatrix} \tag{C.39}$$

$$e_{11} = \frac{\alpha_g}{a_g^2} \tag{C.40}$$

$$e_{12} = \rho_g \tag{C.41}$$

$$e_{15} = -\alpha_g \left(\frac{\rho_g \beta_g T_g}{cp_g} \right) \tag{C.42}$$

$$e_{21} = \frac{\alpha_l}{a_l^2} \tag{C.43}$$

$$e_{22} = -\rho_l \tag{C.44}$$

$$e_{26} = -\alpha_l \left(\frac{\rho_l \beta_l T_l}{cp_l} \right) \tag{C.45}$$

$$e_{31} = \frac{\alpha_g \alpha_l \Sigma \rho \Delta u}{\rho a_0^2} \tag{C.46}$$

$$e_{33} = \alpha_g \left(\rho_g + \alpha_l k \rho \right) \tag{C.47}$$

$$e_{34} = -\alpha_g \alpha_l k \rho \tag{C.48}$$

$$e_{35} = -\alpha_g^2 \alpha_l \Sigma \rho \Delta u \frac{\beta_g T_g}{cp_g} \tag{C.49}$$

$$e_{36} = -\alpha_g \alpha_l^2 \Sigma \rho \Delta u \frac{\beta_l T_l}{cp_l} \tag{C.50}$$

$$e_{41} = -\frac{\alpha_g \alpha_l \Sigma \rho \Delta u}{\rho a_0^2} \tag{C.51}$$

$$e_{43} = -\alpha_g \alpha_l k \rho \tag{C.52}$$

$$e_{44} = \alpha_l \left(\rho_l + \alpha_g k \rho \right) \tag{C.53}$$

$$e_{45} = \alpha_g^2 \alpha_l \Sigma \rho \Delta u \frac{\beta_g T_g}{cp_g} \tag{C.54}$$

$$e_{46} = \alpha_g \alpha_l^2 \Sigma \rho \Delta u \frac{\beta_l T_l}{cp_l} \tag{C.55}$$

$$e_{55} = \alpha_g \rho_g \tag{C.56}$$

$$e_{66} = \alpha_l \rho_l \tag{C.57}$$

$$\mathbf{F} = \begin{bmatrix} f_{11} & f_{12} & f_{13} & 0 & f_{15} & 0 \\ f_{21} & f_{22} & 0 & f_{24} & 0 & f_{26} \\ f_{31} & f_{32} & f_{33} & f_{34} & f_{35} & f_{36} \\ f_{41} & f_{42} & f_{43} & f_{44} & f_{45} & f_{46} \\ 0 & 0 & 0 & 0 & f_{55} & 0 \\ 0 & 0 & 0 & 0 & 0 & f_{66} \end{bmatrix} \tag{C.58}$$

$$f_{11} = \frac{\alpha_g u_g}{a_g^2} \tag{C.59}$$

$$f_{12} = \rho_g u_g \tag{C.60}$$

$$f_{13} = \alpha_g \rho_g \tag{C.61}$$

$$f_{15} = -\alpha_g u_g \left(\frac{\rho_g \beta_g T_g}{cp_g} \right) \tag{C.62}$$

$$f_{21} = \frac{\alpha_l u_l}{a_l^2} \tag{C.63}$$

$$f_{22} = -\rho_l u_l \tag{C.64}$$

$$f_{24} = \alpha_l \rho_l \tag{C.65}$$

$$f_{26} = -\alpha_l u_l \left(\frac{\rho_l \beta_l T_l}{cp_l} \right) \tag{C.66}$$

$$f_{31} = \alpha_g + \frac{\alpha_g \alpha_l u_a \Sigma \rho \Delta u}{\rho_l \rho_g} \tag{C.67}$$

$$f_{32} = \alpha_g \alpha_l \Sigma \rho \Delta u^2 \tag{C.68}$$

$$f_{33} = \alpha_g \rho_g u_g + \alpha_g \alpha_l k \rho u_l - \alpha_g \alpha_l \Delta \rho \Delta u \tag{C.69}$$

$$f_{34} = -\alpha_g \alpha_l k \rho u_g + \alpha_g \alpha_l \Delta \rho \Delta u \tag{C.70}$$

$$f_{35} = -\alpha_g^2 \alpha_l U_g \Sigma \rho \Delta u \frac{\beta_g T_g}{cp_g} \tag{C.71}$$

$$f_{36} = -\alpha_g \alpha_l^2 U_l \Sigma \rho \Delta u \frac{\beta_l T_l}{cp_l} \tag{C.72}$$

$$f_{41} = \alpha_l - \frac{\alpha_g \alpha_l u_a \Sigma \rho \Delta u}{\rho_l \rho_g} \tag{C.73}$$

$$f_{42} = -\alpha_g \alpha_l \Sigma \rho \Delta u^2 \tag{C.74}$$

$$f_{43} = -\alpha_g \alpha_l k \rho u_l + \alpha_g \alpha_l \Delta \rho \Delta u \tag{C.75}$$

$$f_{44} = \alpha_l \rho_l u_l + \alpha_g \alpha_l k \rho u_g - \alpha_g \alpha_l \Delta \rho \Delta u \tag{C.76}$$

$$f_{45} = \alpha_g^2 \alpha_l u_g \Sigma \rho \Delta u \frac{\beta_g T_g}{cp_g} \tag{C.77}$$

$$f_{46} = \alpha_g \alpha_l^2 u_l \Sigma \rho \Delta u \frac{\beta_l T_l}{cp_l} \tag{C.78}$$

$$f_{55} = \alpha_g \rho_g u_g \tag{C.79}$$

$$f_{66} = \alpha_l \rho_l u_l \tag{C.80}$$

$$\mathbf{G} = \begin{bmatrix} g_{11} & g_{12} & g_{13} & g_{14} & 0 & 0 \\ g_{21} & g_{22} & g_{23} & g_{24} & 0 & 0 \\ g_{31} & 0 & g_{33} & g_{34} & 0 & 0 \\ g_{41} & 0 & g_{43} & g_{44} & 0 & 0 \\ 0 & 0 & 0 & 0 & g_{55} & 0 \\ 0 & 0 & 0 & 0 & 0 & g_{66} \end{bmatrix} \tag{C.81}$$

$$g_{11} = u_g - \frac{\alpha_l}{\rho_l a_l^2} \rho a_0^2 \Delta u \tag{C.82}$$

$$g_{12} = \rho a_0^2 \Delta u \tag{C.83}$$

$$g_{13} = \alpha_g \rho a_0^2 \tag{C.84}$$

$$g_{14} = \alpha_l \rho a_0^2 \tag{C.85}$$

$$g_{21} = \frac{\alpha_g}{\rho_g a_g^2} \frac{\alpha_l}{\rho_l a_l^2} \rho a_0^2 \Delta u \qquad \text{(C.86)}$$

$$g_{22} = u_l + \frac{\alpha_l}{\rho_l a_l^2} \rho a_0^2 \Delta u \qquad \text{(C.87)}$$

$$g_{23} = \frac{\alpha_l}{\rho_l a_l^2} \alpha_g \rho a_0^2 \qquad \text{(C.88)}$$

$$g_{24} = -\frac{\alpha_g}{\rho_g a_g^2} \alpha_l \rho a_0^2 \qquad \text{(C.89)}$$

$$g_{31} = \frac{\hat{\rho}_l}{\hat{\rho}^2} \qquad \text{(C.90)}$$

$$g_{33} = \alpha_g \frac{\rho_g \hat{\rho}_l}{\hat{\rho}^2} u_g + \alpha_l \frac{\rho_l \hat{\rho}_g}{\hat{\rho}^2} u_l \qquad \text{(C.91)}$$

$$g_{34} = -\alpha_l \frac{\rho_l \hat{\rho}_l}{\hat{\rho}^2} \Delta u \qquad \text{(C.92)}$$

$$g_{41} = \frac{\hat{\rho}_g}{\hat{\rho}^2} \qquad \text{(C.93)}$$

$$g_{43} = \alpha_g \frac{\rho_g \hat{\rho}_g}{\hat{\rho}^2} \Delta u \qquad \text{(C.94)}$$

$$g_{44} = \alpha_g \frac{\rho_g \hat{\rho}_l}{\hat{\rho}^2} u_g + \alpha_l \frac{\rho_l \hat{\rho}_g}{\hat{\rho}^2} u_l \qquad \text{(C.95)}$$

$$g_{55} = u_g \qquad \text{(C.96)}$$

$$g_{66} = u_l \qquad \text{(C.97)}$$

And the source terms $\vec{C}$ and $\vec{D}$ are:

$$\vec{C} = \begin{bmatrix} 0 \\ 0 \\ F_g^{int} - F_g^w - \alpha_g \rho_g g_z \\ F_l^{int} - F_l^w - \alpha_l \rho_l g_z \\ \frac{1}{T_g}\left(F_g^{int}\Delta u + F_g^w u_g\right) \\ \frac{1}{T_l}\left(F_l^w u_l + F_l^{int}\Delta u\right) \end{bmatrix} \qquad \text{(C.98)}$$

$$\vec{D} = \begin{bmatrix} \rho a_0^2 \left(\frac{\beta_g T_g}{\rho_g cp_g} S_g + \frac{\beta_l T_l}{\rho_l cp_l} S_l \right) \\ \rho a_0^2 \left(\frac{\alpha_l}{\rho_l a_l^2} \frac{\beta_g T_g}{\rho_g cp_g} S_g - \frac{\alpha_g}{\rho_g a_g^2} \frac{\beta_l T_l}{\rho_l cp_l} S_l \right) \\ \frac{1}{\alpha_g \hat{\rho}^2} \left[\rho_l F_g^{int} - \alpha_g k\rho F_l^w \right] - g_x \\ \frac{1}{\alpha_l \hat{\rho}^2} \left[\rho_g \left(F_l^{int} - F_l^w \right) - \alpha_l k\rho F_l^w \right] - g_x \\ \frac{S_g}{\alpha_g \rho_g} \\ \frac{S_l}{\alpha_l \rho_l} \end{bmatrix} \tag{C.99}$$

The newly introduced variables are expressed by:

$$\Sigma\rho = \rho_g + \rho_l \tag{C.100}$$

$$\Delta\rho = \alpha_l \rho_g - \alpha_g \rho_l \tag{C.101}$$

$$u_a = \frac{\alpha_g \rho_l u_g}{a_g^2} + \frac{\alpha_l \rho_g u_l}{a_l^2} \tag{C.102}$$

$$a_0 = \sqrt{\frac{\rho_g a_g^2 \rho_l a_l^2}{\rho \left(\alpha_g \rho_l a_l^2 + \alpha_l \rho_g a_g^2 \right)}} \tag{C.103}$$

$$\hat{\rho}_g = \rho_g + k\rho \tag{C.104}$$

$$\hat{\rho}_l = \rho_l + k\rho \tag{C.105}$$

$$\hat{\rho} = \sqrt{\rho_g \rho_l + k\rho^2} \tag{C.106}$$

$$S_g = \frac{1}{T_g} \left(F_g^{int} \Delta u \right) \tag{C.107}$$

$$S_l = \frac{1}{T_l} \left(F_l^w u_l + F_l^{int} \Delta u \right) \tag{C.108}$$

By applying a characteristic analysis similar to the one demonstrated by Städtke (2006) and Gessner (2010), the eigenvalues and the respective eigenvectors for the two-field formulation are expressed as follows.

$$\lambda_1 = u + a \tag{C.109}$$

$$\vec{T}_1 = \begin{bmatrix} \hat{\rho}_s \rho a_0^2 \\ \alpha_g \alpha_l \rho a_0^2 \left(\frac{\hat{\rho}_l}{\rho_l a_l^2} - \frac{\hat{\rho}_g}{\rho_g a_g^2} \right) \\ \hat{\rho}_l \left(a - \alpha_l \frac{\rho_l \hat{\rho}_g}{\hat{\rho}^2} \Delta u \right) \\ \hat{\rho}_g \left(a + \alpha_g \frac{\rho_g \hat{\rho}_l}{\hat{\rho}^2} \Delta u \right) \\ 0 \\ 0 \end{bmatrix} \tag{C.110}$$

$$\lambda_2 = u - a \tag{C.111}$$

$$\vec{T}_2 = \begin{bmatrix} \hat{\rho}_s \rho a_0^2 \\ \alpha_g \alpha_l \rho a_0^2 \left(\frac{\hat{\rho}_l}{\rho_l a_l^2} - \frac{\hat{\rho}_g}{\rho_g a_g^2} \right) \\ \hat{\rho}_l \left(-a - \alpha_l \frac{\rho_l \hat{\rho}_g}{\hat{\rho}^2} \Delta u \right) \\ \hat{\rho}_g \left(-a + \alpha_g \frac{\rho_g \hat{\rho}_l}{\hat{\rho}^2} \Delta u \right) \\ 0 \\ 0 \end{bmatrix} \tag{C.112}$$

$$\lambda_3 = u_g \tag{C.113}$$

$$\vec{T}_3 = \begin{bmatrix} \alpha_l \rho_l \left(\Delta u \right)^2 \\ -\alpha_l \left(1 - \alpha_l \left(\frac{\Delta u}{a_l} \right)^2 \right) \\ 0 \\ \Delta U \\ 0 \\ 0 \end{bmatrix} \tag{C.114}$$

$$\lambda_4 = u_l \tag{C.115}$$

$$\vec{T}_4 = \begin{bmatrix} \alpha_g \rho_g \left(\Delta u \right)^2 \\ \alpha_g \left(1 - \alpha_g \left(\frac{\Delta u}{a_g} \right)^2 \right) \\ -\Delta u \\ 0 \\ 0 \\ 0 \end{bmatrix} \tag{C.116}$$

$$\lambda_5 = u_g \tag{C.117}$$

$$\vec{T_5} = \begin{bmatrix} 0 \\ 0 \\ 0 \\ 0 \\ 1 \\ 0 \end{bmatrix} \tag{C.118}$$

$$\lambda_6 = u_l \tag{C.119}$$

$$\vec{T_6} = \begin{bmatrix} 0 \\ 0 \\ 0 \\ 0 \\ 0 \\ 1 \end{bmatrix} \tag{C.120}$$

Where,

$$u = \alpha_g \frac{\rho_g \hat{\rho}_l}{\hat{\rho}^2} u_g + \alpha_l \frac{\rho_l \hat{\rho}_g}{\hat{\rho}^2} u_l \tag{C.121}$$

$$a = \sqrt{\tilde{a}^2 - \Delta\tilde{a}^2} \tag{C.122}$$

$$\tilde{a}^2 = \frac{\hat{\rho}_s}{\hat{\rho}^2} \rho a_0^2 \tag{C.123}$$

$$\Delta\tilde{a}^2 = \alpha_g \frac{\rho_g \hat{\rho}_l}{\hat{\rho}^2} \alpha_l \frac{\rho_l \hat{\rho}_g}{\hat{\rho}^2} \left(\Delta u\right)^2 \tag{C.124}$$

$$\hat{\rho}_s = \rho_s + k\rho \tag{C.125}$$

$$\rho_s = \alpha_g \rho_l + \alpha_l \rho_g \tag{C.126}$$

In this way the SCMM is applied in the same way as for the three-field formulation and the decomposition of the coefficient matrix **G** as function of its eigenvalues is written as,

$$G_1 = \varphi_1 \begin{bmatrix} \alpha_g \alpha_l \frac{\hat{\rho}^2 \tilde{a}^2}{\hat{\rho}_s} \left(\frac{\hat{\rho}_l}{\rho_l a_l^2} - \frac{\hat{\rho}_g}{\rho_g a_g^2} \right) \\ \hat{\rho}_l \left(a - \alpha_l \frac{\rho_l \hat{\rho}_g}{\hat{\rho}^2} \Delta u \right) \\ \hat{\rho}_g \left(a + \alpha_g \frac{\rho_g \hat{\rho}_l}{\hat{\rho}^2} \Delta u \right) \\ 0 \\ 0 \end{bmatrix} \times \begin{bmatrix} a\hat{\rho}_s + \hat{\rho}\Delta u\Delta a \\ \hat{\rho}^2 \tilde{a}^2 \Delta u \\ \alpha_g \hat{\rho}^2 \left(a_2^2 + a\frac{\rho_g \hat{\rho}_s}{\hat{\rho}^2} \Delta u \right) \\ \alpha_l \hat{\rho}^2 \left(a_1^2 - a\frac{\rho_l \hat{\rho}_s}{\hat{\rho}^2} \Delta u \right) \\ 0 \\ 0 \end{bmatrix}^T \tag{C.127}$$

$$G_2 = \varphi_2 \begin{bmatrix} \hat{\rho}^2 \tilde{a}^2 \\ \alpha_g \alpha_l \frac{\hat{\rho}^2 \tilde{a}^2}{\hat{\rho}_s} \left(\frac{\hat{\rho}_l}{\rho_l a_l^2} - \frac{\hat{\rho}_g}{\rho_g a_g^2} \right) \\ \hat{\rho}_l \left(-a - \alpha_l \frac{\rho_l \hat{\rho}_g}{\hat{\rho}^2} \Delta u \right) \\ \hat{\rho}_g \left(-a + \alpha_g \frac{\rho_g \hat{\rho}_l}{\hat{\rho}^2} \Delta u \right) \\ 0 \\ 0 \end{bmatrix} \times \begin{bmatrix} -a\hat{\rho}_s + \hat{\rho}\Delta u \Delta a \\ \hat{\rho}^2 \tilde{a}^2 \Delta u \\ \alpha_g \hat{\rho}^2 \left(a_2^2 - a \frac{\rho_g \hat{\rho}_s}{\hat{\rho}^2} \Delta u \right) \\ \alpha_l \hat{\rho}^2 \left(a_1^2 + a \frac{\rho_l \hat{\rho}_s}{\hat{\rho}^2} \Delta u \right) \\ 0 \\ 0 \end{bmatrix}^T \tag{C.128}$$

$$G_3 = \varphi_3 \begin{bmatrix} \alpha_l \rho_l (\Delta u)^2 \\ -\alpha_l \left(1 - \alpha_l \left(\frac{\Delta u}{a_l} \right)^2 \right) \\ 0 \\ \Delta u \\ 0 \\ 0 \end{bmatrix} \times \begin{bmatrix} \frac{\alpha_g \Delta u}{a_g^2} \\ \rho_g \Delta u \\ \alpha_g \rho_g \\ -\alpha_g \frac{\rho_g \hat{\rho}_l}{\hat{\rho}_g} \\ 0 \\ 0 \end{bmatrix}^T \tag{C.129}$$

$$G_4 = \varphi_4 \begin{bmatrix} \alpha_g \rho_g (\Delta u)^2 \\ \alpha_g \left(1 - \alpha_g \left(\frac{\Delta u}{a_g} \right)^2 \right) \\ -\Delta u \\ 0 \\ 0 \\ 0 \end{bmatrix} \times \begin{bmatrix} \frac{\alpha_l \Delta u}{a_l^2} \\ -\rho_l \Delta u \\ \alpha_l \frac{\rho_l \hat{\rho}_g}{\hat{\rho}_l} \\ -\alpha_l \rho_l \\ 0 \\ 0 \end{bmatrix} \tag{C.130}$$

$$G_5 = U_g \begin{bmatrix} 0 & 0 & 0 & 0 & 0 & 0 \\ 0 & 0 & 0 & 0 & 0 & 0 \\ 0 & 0 & 0 & 0 & 0 & 0 \\ 0 & 0 & 0 & 0 & 0 & 0 \\ 0 & 0 & 0 & 0 & 1 & 0 \\ 0 & 0 & 0 & 0 & 0 & 0 \end{bmatrix} \tag{C.131}$$

$$G_6 = U_l \begin{bmatrix} 0 & 0 & 0 & 0 & 0 & 0 \\ 0 & 0 & 0 & 0 & 0 & 0 \\ 0 & 0 & 0 & 0 & 0 & 0 \\ 0 & 0 & 0 & 0 & 0 & 0 \\ 0 & 0 & 0 & 0 & 0 & 0 \\ 0 & 0 & 0 & 0 & 0 & 1 \end{bmatrix} \tag{C.132}$$

Where

$$\varphi_1 = (u+a) \frac{\tilde{a}^2 + a\Delta u \Delta \alpha - 2\Delta a^2}{2a\hat{\rho}_s \hat{\rho}^2 a_3^2 a_4^2} \tag{C.133}$$

$$\varphi_2 = -(u-a) \frac{\tilde{a}^2 - a\Delta u \Delta \alpha - 2\Delta a^2}{2a\hat{\rho}_s \hat{\rho}^2 a_3^2 a_4^2} \tag{C.134}$$

$$\varphi_3 = -\frac{u_g}{\rho_g \Delta u \left[\frac{\hat{\rho}_s}{\hat{\rho}_g} - \frac{\alpha_l \rho_l (\Delta u)^2}{\rho a_0^2} \right]} \tag{C.135}$$

$$\varphi_4 = -\frac{u_l}{\rho_l \Delta u \left[\frac{\hat{\rho}_s}{\hat{\rho}_l} - \frac{\alpha_g \rho_g (\Delta u)^2}{\rho a_0^2} \right]} \tag{C.136}$$

And,

$$a_1^2 = a^2 - \rho_g \rho_l \left(\frac{\alpha_g \hat{\rho}_l \Delta u}{\hat{\rho}^2} \right)^2 \tag{C.137}$$

$$a_2^2 = a^2 - \rho_g \rho_l \left(\frac{\alpha_l \hat{\rho}_g \Delta u}{\hat{\rho}^2} \right)^2 \tag{C.138}$$

$$a_3^2 = \tilde{a}^2 - \alpha_l \frac{\rho_l \hat{\rho}_g}{\hat{\rho}^2} (\Delta u)^2 \tag{C.139}$$

$$a_4^2 = \tilde{a}^2 - \alpha_g \frac{\rho_g \hat{\rho}_l}{\hat{\rho}^2} (\Delta u)^2 \tag{C.140}$$

$$\Delta a = \frac{\hat{\rho}_l}{\hat{\rho}} \left(\frac{\alpha_g \tilde{a}}{a_g} \right)^2 - \frac{\hat{\rho}_g}{\hat{\rho}} \left(\frac{\alpha_l \tilde{a}}{a_l} \right)^2 \tag{C.141}$$

$$\Delta \alpha = \alpha_l \frac{\rho_l \hat{\rho}_g}{\hat{\rho}^2} - \alpha_g \frac{\rho_g \hat{\rho}_l}{\hat{\rho}^2} \tag{C.142}$$

The matrices $\mathbf{G}^+$ and $\mathbf{G}^-$ are then assembled as follows.

$$G^+ = G_1 + \frac{u_g + |u_g|}{2u_g} (G_3 + G_5) + \frac{u_l + |u_l|}{2u_l} (G_4 + G_6) \tag{C.143}$$

$$G^- = G_2 + \frac{u_g - |u_g|}{2u_g} (G_3 + G_5) + \frac{u_l - |u_l|}{2u_l} (G_4 + G_6) \tag{C.144}$$

And, the same algorithm is used to solve the slitted PDE as the systems are similar, and just the number of equations change. The wall and interface forces are calculated using the same correlations as for the three-field formulation.